Driven microparticles interacting with lipid vesicles : from wrapping by optical tweezers to autonomous active particle engulfment

Florent Fessler

To cite this version:

Florent Fessler. Driven microparticles interacting with lipid vesicles : from wrapping by optical tweezers to autonomous active particle engulfment. Physics [physics]. Université de Strasbourg, 2024. English. NNT : 2024STRAE012 . tel-04902607

HAL Id: tel-04902607
https://theses.hal.science/tel-04902607v1
Submitted on 21 Jan 2025

UNIVERSITÉ DE STRASBOURG

ÉCOLE DOCTORALE 182

Institut Charles Sadron, CNRS (UPR-22)

THÈSE présentée par :

Florent FESSLER

soutenue le : **03 Octobre 2024**

pour obtenir le grade de : **Docteur de l'université de Strasbourg**

Discipline/Spécialité : PHYSIQUE

Driven microparticles interacting with lipid vesicles: from wrapping by optical tweezers to autonomous active particle engulfment

Interaction microparticules-vésicules géantes : de l'enveloppement par pinces optiques à l'engloutissement autonome de particules actives

THÈSE dirigée par :

Dr. STOCCO Antonio	Chargé de recherches, Institut Charles Sadron

RAPPORTEURS :

Dr. ABKARIAN Manouk	Directeur de recherches, Centre de Biologie Structurale, Montpellier
Dr. LEOCMACH Mathieu	Chargé de recherches, Institut Lumière Matière, Villeurbanne

---

AUTRES MEMBRES DU JURY :

Dr. BASSEREAU Patricia	Directrice de recherches, Institut Curie, Paris, France
Dr. AGUDO-CANALEJO Jaime	Lecturer, University College London, London, UK
Dr. QUILLIET Catherine	Maître de conférences, Laboratoire Interdisciplinaire de Physique, Grenoble, France
Dr. HEBRAUD Pascal	Directeur de recherches, Institut de Physique et Chimie des Matériaux de Strasbourg

Acknowledgements

First and foremost, I would like to thank the reviewers, Manouk Abkarian and Mathieu Leocmach, as well as all the members of the jury, Patricia Bassereau, Pascal Hébraud, Catherine Quilliet, and Jaime Agudo-Canalejo, for accepting to examine and evaluate this manuscript.

This manuscript is the result of work that could not have been carried out without the guidance of my thesis supervisor, Antonio Stocco, whom I would like to thank warmly. When I was an undecided master's student uncertain about my future, he encouraged me to consider the path of fundamental research by introducing me to his approach to physics and to systems that were unfamiliar to me. Since then, he has consistently been supportive and available, and I am very grateful for the trust and time he has always granted me. His kindness and optimism made these years a period of joyful and enriching learning, and I thank him for all our discussions, whether scientific or otherwise, through which his scientific and human qualities allowed me to learn a lot.

I would also like to thank all the members of the Mcube team, without whom these three years and the work resulting from them—this manuscript—would have been very different. Starting with Fabrice Thalmann, Jean Wolff, and Tatiana Schmatko for the stimulating scientific discussions and the joyful moments in the office/cafeteria/decision room in F.145 or elsewhere. Thank you to Marc Basler for his precious help in setting up experimental setups, to André Schroeder for generously taking the time during his stays in Strasbourg to introduce me to micropipettes, and to Igor Kulic for his enthusiasm and our conversations, always rich in advice and fresh ideas. I would like to extend a special thank you to Pierre Muller for the invaluable assistance he provided me throughout my thesis on so many aspects, as well as for his kindness and enthusiasm. Finally, thank you to Thierry Charitat, whose statistical physics courses have the merit—among others—of being easier to follow than him during a bike climb up a mountain pass. Thank you for always being so kind and attentive, and a guide in many respects.

I would like to thank Juliane Simmchen's group at TU Dresden for hosting me for a couple weeks. In particular, thank you to Martin Wittmann, who was an exceptional host and partner.

My thanks also go to the entire administrative team at ICS, particularly Virginie Oberlé and Odile Lemblé, for their help and kindness.

I would like to thank David Halley and Boris Hippolyte for offering me my first opportunities to teach as a teaching assistant for vibration and wave tutorials over the past three years, for their trust and advice. I must also thank Pierre Muller and Thierry Charitat once again, this time as supervisors of the physics tournament at the Faculty of Physics, for taking the risk of assigning me the role of Team Leader of the Strasbourg team for two consecutive years. I learned a great deal and thoroughly enjoyed working with you and these motivated students. Thank you also to Jean Farago for being my pedagogical advisor in the context of these teaching missions and for our always stimulating and pleasant discussions.

Thanks to all my companions on this journey—interns, PhD students, post-docs, and other permanent members of ICS—for their friendship and for making this period special. Thanks to the friends from the Young Researchers' Bureau for the festive moments and to the baby-foot friends. Thanks to those who warmly welcomed me in the beginning: Eulalie Lafarge, Lisa Berezovska, Fedir Demydiuk, Purusharth Tiwari, Vaibhav Sharma, and to my Mcube comrades and others, Clément Marque, Friedrich Walzel, Ann Rosna George, Thomas Bugnand, Nicolas Mille, and so many others for your joyful company in a lab room as well as around a drink. Finally, thanks to the motivated interns who came to contribute: Thomas Ducatel, Ndeye Saly Diouf, Thomas Dartige, Azeline Hilaire, I really enjoyed working with each of you and wish you all the best for the future. I certainly cannot forget my long-time companion, Swen Helstroffer. These three years of sharing an office are almost nothing compared to all we share elsewhere, but the days would have been much duller without your loyal company.

Pour finir, j'aimerais remercier mes amis proches et ma famille pour leur soutien sans faille depuis tant d'années. Gabin, Sam, Ott, Bastien, Jonas, Schmi, Nina, Amanda, Margot, Gugu, Remi, Lisa et tous les autres ; votre amitié est un soutien permanent que je ne cesserai de chérir. Camille, merci de me rendre heureux, pour ta lumière, et pour toujours m'encourager et me soutenir. Thibaud, merci d'être ce garçon inspirant dont je suis fier d'être le frère. Enfin, merci à Vesna et Thierry, mes parents à qui je dois beaucoup et qui m'ont toujours soutenu. Cette thèse vous est dédiée.

Table of contents

Front matter

List of figures

Abbreviations and notations

b	Intermonolayer friction coefficient
C	Principal curvature
Cu@SiO_2	Copper-Silica Janus colloid
DOPC	1,2-dioleoyl-sn-glycero-3-phosphocholine
d_{up}	Uptake penetration depth
D_r	Rotational diffusion coefficient
D_t	Translational diffusion coefficient
E_{up}	Uptake energy
f	Frequency
$f(h_P)$	Drag modification factor
f, F	Force
fps	Frames per second
GUV	Giant unilamellar vesicle
H_2O_2	Hydrogen peroxide
K_A	Compressibility (or stretching) modulus
k_B	Boltzmann constant
κ_b	Membrane bending modulus
κ_G	Membrane gaussian modulus
κ_i, κ	Trapping stiffness
$\bar{K}$	Gaussian curvature
M	Mean curvature
MF	Melamine formaldehyde
m	Spontaneous curvature
MSAD	Mean squared angular displacement
MSD	Mean squared displacement
N	Number
Ω	Angular velocity
P	Probability density
POPC	1-palmitoyl-2-oleoyl-glycero-3-phosphocholine
PS	Polystyrene
PSD	Position power spectral density
PSD_v	Velocity power spectral density
Pt@SiO_2	Platinum-Silica Janus colloid
R_i	Radius

SiO_2	Silicon dioxide
σ	Membrane tension
$\tilde{\sigma}$	Membrane spontaneous tension
Σ	Membrane mechanical tension
T	Temperature
U	Energy potential
v, V	Velocity
φ	In-plane orientation angle
w	Adhesion energy density
ζ_r	Rotational friction (drag) coefficient
ζ_t	Translational friction (drag) coefficient
Z	Zeta potential
θ	Out-of-plane orientation angle
ω	Angular frequency
$\bar{\tau}$	Torque
η	Bulk shear viscosity
η_m	Membrane shear viscosity

Publications and communications

Publications

- F. Fessler, M. Wittman, J. Simmchen and A. Stocco. *Autonomous engulfment of active colloids by giant lipid vesicles*, Soft Matter (2024)
- V. Sharma, F. Fessler, F. Thalmann, C. M. Marques and A. Stocco. *Rotational and translational drags of a Janus particle close to a wall and a lipid membrane.* Journal of Colloids and Interface Science, 2159-2199, 652 (2023)
- F. Fessler, V. Sharma, P.Muller, A. Stocco, *Entry of microparticles into giant lipid vesicles by optical tweezers*, Phys. Rev. E 107, L052601 (2023)

Communications

- APS March Meeting 2024 (Minneapolis, U.S.A.), 2024 ; talk: *Dynamics of Active Colloid Engulfment by Giant Lipid Vesicles*
- Soft Matter Meeting Strasbourg (Strasbourg, France), 2024 ; talk: *Autonomous Engulfment of Active Colloids by Lipid Vesicles*
- DPG (German Society of Physics) Spring Meeting of the Condensed Matter Section (Dresden, Germany), 2023 ; talk: *Entry of Microparticles into Giant Lipid Vesicles Induced by Optical Force*
- GDR Solliciter La Matière Molle (Roscoff, France), 2022; poster: *Entry of Microparticles into Giant Lipid Vesicles Induced by Optical Force*
- Biomembrane Days (Berlin, Germany), 2022 ; poster: *Dynamics of a colloidal particle interacting with lipid membranes in and out of equilibrium*
- Soft Matter Meeting Strasbourg (Strasbourg, France), 2022 ; talk: *Bare and Lipid-coated Colloidal Particles Interacting with Biomimetic Membranes*
- ITI HiFunMat Annual Conference (Strasbourg, France), 2022 ; talk: *Entry of Microparticles into Giant Lipid Vesicles by Optical Tweezers*
- ITI HiFunMat Summer school (Strasbourg, France), 2022 ; poster: Functional and Hierarchical materials for energy and sustainable development

Chapter 1

Introduction

Microscopic bodies interacting with membranes is an ubiquitous situation at the cellular scale. These interactions play crucial roles in a variety of contexts, including the phagocytic uptake of microbes by immune cells [1, 2] and the cell-to-cell spread of bacterial pathogens [3, 4]. During such processes, the cell membrane deforms upon contact with a foreign body and undergoes shape and topological transitions to achieve internalization. In some instances, the foreign body is an inert microparticle subjected to thermal diffusion, as seen in the cellular uptake of microplastics [5]. In other instances, the particle consumes energy from its surroundings and converts it into directed motion or mechanical forces, maintaining itself out of thermal equilibrium. This property is observed in microorganisms such as bacteria, but can also be replicated in artificial systems. In these systems, it can be challenging to distinguish the contributions of active biological mechanisms from those of physical interactions in determining the uptake outcome. Reproducing the complex remodelling processes occurring in biology in the absence of the biological machinery therefore constitutes a promising approach to evidence and study the role of physical interactions. In this thesis, we use minimal model systems to experimentally investigate the physical principles governing the engulfment of microparticles driven by external or active forces. In this first chapter, essential concepts and terminology are introduced, and a comprehensive review of the current state of the art is provided to contextualize and motivate the investigations presented in the following chapters.

1.1 Biological membranes and lipid bilayers

Biological membranes are highly adaptable structures that can deform and remodel their shape in response to various stimuli, while also acting as barriers to compartmentalize cellular

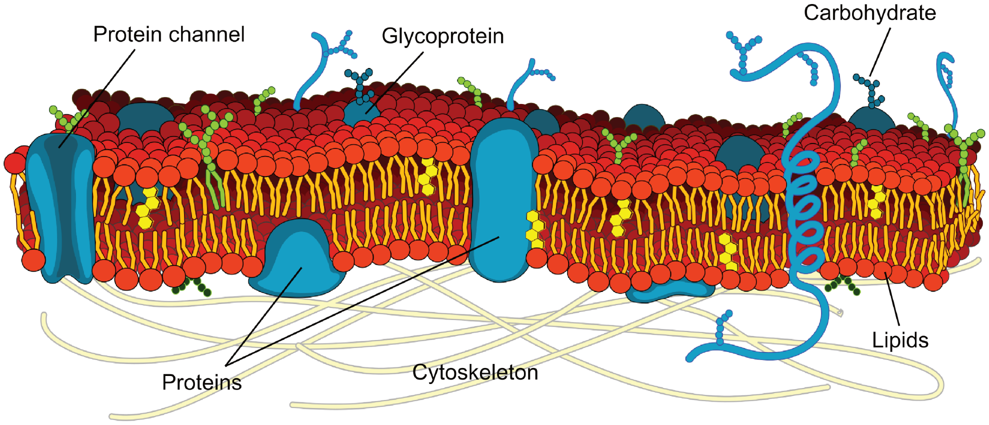

Figure 1.1: Schematic diagram of the plasma membrane in the fluid-mosaic model, describing it as a two-dimensional fluid in which lipids, proteins, and any other embedded molecule can diffuse. Image Wikimedia Commons (public domain).

components [6]. This flexibility is essential for the proper functioning of cells and is due to the structural nature of membranes. Specifically, properties such as fluidity and low bending rigidity originate from the core matrix of biological membranes: the lipid bilayer. Simplifying the complexity of cell membranes, illustrated in Figure 1.1, to their fundamental structural component -a lipid bilayer- allows for the study of a wide range of processes, including fusion and fission, cell adhesion, molecular recognition, membrane trafficking, and shape remodeling.

1.1.1 Lipids and self-assembly

The fundamental building blocks of biological membranes are lipids, which constitute a wide class of molecules. While the lipid type composition of biological membranes greatly varies depending on the type and function, the most abundant structural lipids in cell membranes are phospholipids, containing a phosphate group in the hydrophilic head and two tails made up of saturated or unsaturated carbon chains [7]. The amphiphilic nature of phospholipids is the key property that determines the structures they form. In an aqueous environment, when the concentration of lipids exceeds the critical micelle concentration (CMC), these molecules spontaneously self-assemble into structures that minimize the exposure of their hydrophobic tails to water [6]. The most common resulting structures are lipid bilayers (shown in Figure 1.2) and micelles, depending on the shape of the assembling lipid [8]. In a bulk fluid, finite size planar lipid bilayers are not stable due to the high energetic cost associated to the exposure of the hydrophobic edges to water [9]. For this reason, they tend to form closed bags called vesicles, or liposomes, which are classified depending on their size. Indeed, despite

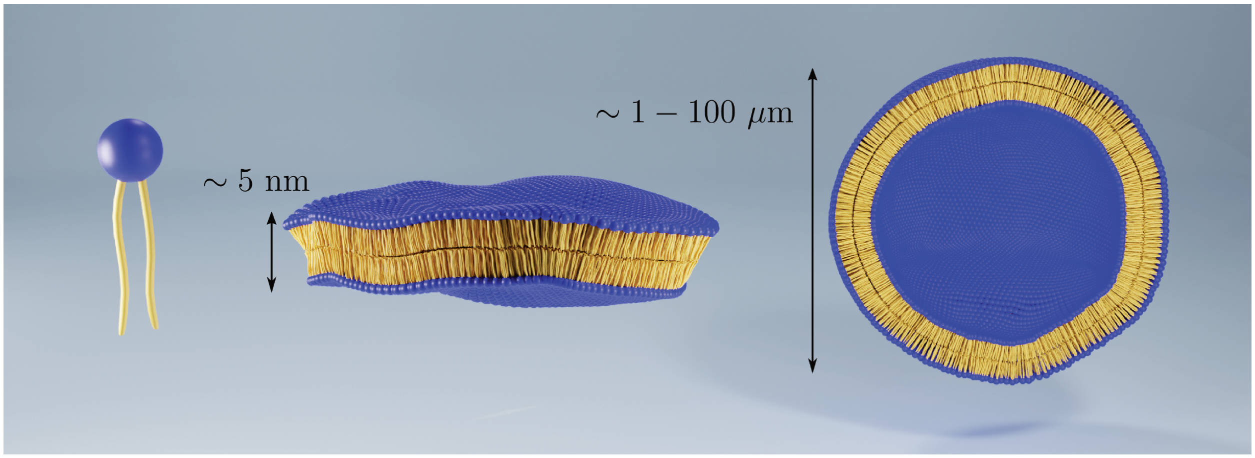

Figure 1.2: Schematic representation of a lipid molecule *(left)* with the hydrophillic head in blue and the fatty acid chains in yellow. *(middle)* Lipid bilayer spontaneously formed by phospholipids in water. *(right)* Cut plane of an unilamellar lipid vesicle, known as giant unilamellar vesicles (GUVs) for sizes ranging between $1 - 100\,\mu$m. It is constituted of a single lipid bilayer closed on itself forming a spherical *balloon* to prevent the exposure of the hydrophobic edges to water.

their nanometric thickness ($\sim 5\,$nm), lipid membranes can form vesicle structures with sizes up to 4-5 orders of magnitude larger. The classes of small and intermediate sized unilamellar vesicles are: SUVs or small unilamellar vesicles (size $< 10\,$nm) and LUVs or large unilamellar vesicles (size $\sim 10 - 1000\,$nm). Giant unilamellar vesicles (GUVs), corresponding to sizes ranging between $1 - 100\,\mu$m, have the great advantage of being visible under an optical microscope, in addition to being in the same size range as cells. They therefore constitute a valuable tool for probing the membrane response and systematically investigating the thermodynamic and mechanical properties of lipid bilayers [10].

1.1.2 Elastic theory of membranes

Curvature elasticity

In order to explain the shape and morphology of fluid membranes structures, a theoretical framework has been developed considering these membranes as continuous 2-dimensional surfaces. This is justified by the separation of lengthscales between the membrane thickness and the distances over which they extend, and allows to describe them using standard mathematical tools to describe curved surfaces in a 3-dimensional space. In particular, for each point on a smooth surface, we can define the principal curvatures $C_1 = 1/R_1$ and $C_2 = 1/R_2$ as the extremal values of the normal curvatures defined by the intersection of the normal planes (planes containing the surface normal vector at a given point) with the considered sur-

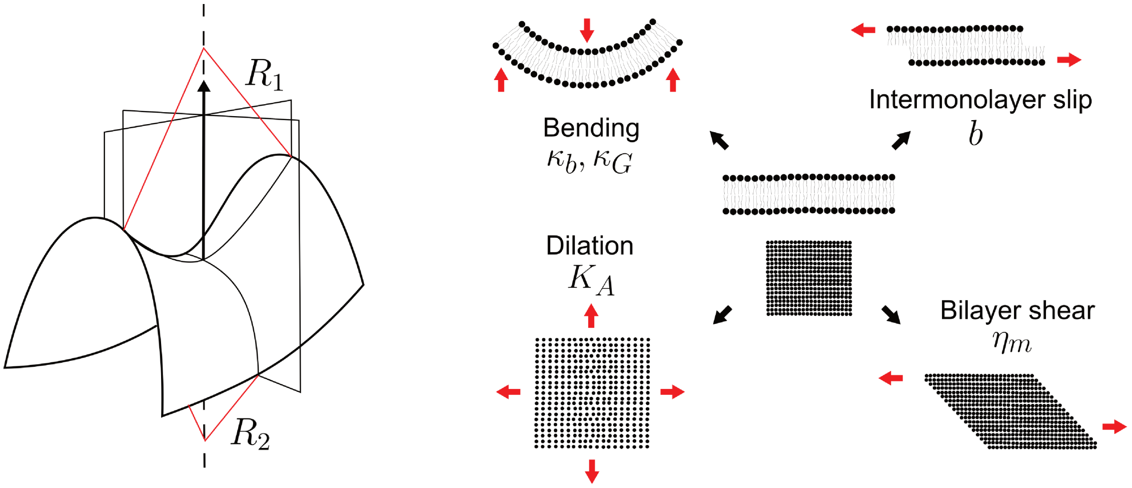

Figure 1.3: *(left)* Saddle surface with normal planes of principal curvature containing the normal vector of the considered point. *(right)* Standard modes of deformation of a lipid bilayer with associated modulii and viscosities. Note that for lipid membranes in the fluid phase, the shear elastic modulus vanishes and only dissipative quantities such as shear viscosity η_m and intermonolayer friction coefficient b are defined.

face, see Figure 1.3 *(left)*. Two key quantities can be defined from these principal curvatures, the mean curvature:

$$M \equiv \frac{1}{2}(C_1 + C_2), \tag{1.1}$$

and Gaussian curvature:

$$\bar{K} \equiv C_1 C_2. \tag{1.2}$$

Note that the principal curvatures can be positive or negative, and it is usually defined for surfaces enclosing an interior medium (such as vesicles) that curvatures bulging away from the interior are by convention positive and those bulging towards the interior of the vesicle are negative. Following this convention, a perfect sphere with radius R_s has a positive mean curvature $M = 1/R_s$.

This formalism allows to quantify the energetic cost associated to the deviation of local membrane curvature from a preferred value m, known as the membrane *spontaneous curvature*. This energy cost over a whole surface is given by the so-called Helfrich energy [11]:

$$E_b = \int \left[2\kappa_b(M-m)^2 + \kappa_G \bar{K}\right] \mathrm{d}A \tag{1.3}$$

with κ_b and κ_G the bending rigidity and Gaussian bending rigidity, respectively (Figure 1.3). These modules have units of energy and are material properties expected to depend on the membrane lipid composition and phase. The membrane spontaneous curvature m however, which describes the preferred curvature of an unconstrained piece of membrane, can originate from any asymmetry across the membrane. It was shown that lipid composition asymmetry between the two leaflets, asymmetric polymer adsorption or asymmetric sugar species across the bilayer induce an effective spontaneous curvature [12]. Note also that in the absence of topological changes, the Gauss-Bonnet theorem states that the integral over a closed surface of the Gaussian curvature is a constant. The term associated to the Gaussian curvature in Eq. 7.1 is therefore essentially constant and is usually disregarded.

Area expansion elasticity and membrane tension

In the last decades, the literature seemed to utilize the same terminology of *membrane tension*, usually denoted σ (or Σ), to describe different material properties. Here, we will try to clarify and figure what is the relevant interpretation for floppy giant unilammellar vesicles.

For an isolated lipid membrane, the number of lipids constituting it is fixed. In thermal equilibrium, there should exist an equilibrium distance between each lipid set by molecular interactions which would lead to a tensionless membrane with optimal area A_0 [13]. If the vesicle is dilated or compressed from A_0 to a value A, thereby imposing a change in the preferred inter-lipid distance such as sketched in Figure 1.3 *(right)*, the change in elastic stretching energy is given by the Hookean-like contribution [13]:

$$E_s = \frac{1}{2} K_A \frac{(A-A_0)^2}{A_0} \tag{1.4}$$

where K_A is an area compressibility modulus, and one can define a mechanical tension:

$$\Sigma_s = \frac{dE_s}{dA} = K_A \frac{A-A_0}{A_0} \tag{1.5}$$

Note that the mechanical tension derived here depends on the initial resting state and is not a constant, in opposition to the interfacial tension of liquid interfaces. In practice for lipid membranes, K_A is of the order of $\sim$ 100 mN m^{-1} [14], which is at least one order of magnitude above the lysis tension of the same membranes (tension at which the membrane ruptures ~ 5 mN m^{-1}). It means that very large stresses as compared to the scale set by the bending rigidity are needed to induce small area dilation and the membrane area can only increase by a few percents before it ruptures. For this reason, lipid vesicles are often assumed to have a constant area A_0.

However, micromanipulation experiments with increasing precision on lipid vesicles evidenced the existence of a *soft* area compliance regime which accounts for an entropy-driven tension [15, 16]. Indeed, the lateral restriction of conformations reduces the configurational entropy of the system and an effective tension therefore emerges even at constant membrane area $A = A_0$ [17]. In fact, under a microscope, for a tensionless membrane, one can only resolve a projected or apparent area and not the real membrane area A, as significant amount of the membrane area is ”hidden” in the thermal undulations that can not be resolved optically. When applying very tiny stresses ($\sim 10^{-6}$ N m^{-1}) to a presumably tensionless membrane, one can in fact measure a big apparent area increase $\Delta A/A$ due to the suppression of the thermal undulations of the membrane at finite temperature. This introduces a logarithmic dependence of the projected or *apparent* membrane area increase on the membrane tension increase with a prefactor that accounts for the competition between thermal energy and bending energy $8\pi\kappa_b/k_BT$. The existence of such a tension was suggested by the equilibrium theory of bending elastic thermal excitations, where a membrane tension characterizing the free energy increase associated to a projected area increase such that $\Delta E_\sigma = \sigma\Delta A$ was introduced [11, 18].

In many experimental contexts since then, such a tension parameter σ is attributed to the membrane and considered to account for the entropy related effects discussed in the previous paragraph. As we saw however, it is not a material parameter as it should depend on the constraints on the membrane (e.g. the volume of fluid enclosed in the case of vesicles). Still, it is often used as a constant, analogously to the interfacial tension of liquid droplets, suggesting that it acts as a chemical potential for membrane area. We showed previously that due to the finite number of lipids in a membrane, this assumption can not hold upon large membrane deformations. There is a framework in which this interpretation holds rigorously, which is when accounting for the contributions of a *spontaneous tension* $\tilde{\sigma}$ [19, 20].

Indeed, by rewriting the Helfrich energy of Eq. 7.1 without the Gaussian curvature term (for the reason discussed previously) as:

$$E_b = 2\kappa_b m^2 A - 4\kappa_b m \int M \mathrm{d}A + 2\kappa_b \int M^2 \mathrm{d}A, \tag{1.6}$$

it appears that a large membrane segment with area $\Delta A_{\tilde{\sigma}}$ frustrated to adopt a mean curvature $M \neq m$ contributes to the bending energy as [19]:

$$E_b \approx 2\kappa_b m^2 \Delta A_{\tilde{\sigma}} \tag{1.7}$$

Therefore, large membrane segments with $|M| \ll |m|$ experience a spontaneous tension:

$$\tilde{\sigma} = 2\kappa_b m^2 \tag{1.8}$$

which only depends on the property m and is therefore a priori constant.

In this thesis, we will therefore assume that the membrane tension σ is the sum of two components [13, 20, 21]:

$$\sigma = \Sigma + 2\kappa_b m^2 = \Sigma + \tilde{\sigma}, \tag{1.9}$$

where the so-called mechanical tension Σ accounts for the entropic effects discussed in the first part of this section and depends on the size, shape and constraints on the membrane [21], and a spontaneous tension arising from bilayer asymmetry. Note that while it is usually implicitly assumed that σ is a constant characterizing the energetic cost for extracting membrane area from a reservoir, it is in general not the case and the experiments reported in the following will bring evidences of that.

Finally, in the case of vesicles which enclose fluid, a difference in osmotic pressure exerted by osmotically active species in the interior and exterior compartments can be defined. This pressure dictates the prescribed fluid volume enclosed in a vesicle as solvent fluxes across the membrane over time allows to adjust the concentration inside the vesicle to reach a vanishing osmotic pressure difference. Considering the energy associated to the deviation of the volume from this prescribed volume set by osmotic conditions, the separation of energy scales with κ_b again allows to consider that the volume is essentially conserved.

Membrane shear viscosity and intermonolayer friction

Fluid lipid membranes are usually described as two-dimensional viscous fluids. The shear elastic modulus is therefore zero and in-plane shear deformations are only resisted by viscous forces characterized by a two-dimensional viscosity η_m, as depicted in Figure 1.3 *(right).* This 2D viscosity has the units of a 3D viscosity times a length, which is the membrane thickness h. To describe the competition between the membrane viscosity and the viscosity of the bulk fluid, one defines a dimensionless quantity $B = \eta_m/\eta l$, known as Boussinesq's number, where η is the 3D viscosity of the surrounding fluid and l is a typical lengthscale of the probing system. This quantity captures the relative importance of surface and bulk viscous contributions for a probing object with a typical size l.

In the absence of external constraints, microscopic objects embedded in a lipid bilayer undergo Brownian motion within this two-dimensional sheet with a modified friction force accounting for the 2D viscosity of the membrane. Available models describing the mobility of inclusions within lipid membranes are therefore considering the hydrodynamical problem of a disc embedded in a membrane. Models consider the disc to have the same thickness h as the membrane and to be surrounded by a 3D fluid with a viscosity η [22, 23, 24]. Such continuous approaches allowed to derive an expression for the translational friction coefficient for a disc inclusion of radius a known as the Saffman-Delbrück formula [22]:

$$\zeta_{SD} = 4\pi\eta_m \left[\log\left(\frac{\eta_m}{\eta a}\right) - \gamma\right]^{-1}, \tag{1.10}$$

where $\gamma = 0.5772$ is Euler's constant. Note that the drag experienced by the inclusion only weakly depends on its radius a. This model allowed to interpret experimental data on the diffusion of lipid domains and proteins within membranes [25, 26, 27]. Typical experimental values of the membrane viscosity for lipid bilayers are in between 7 and 80 nPa s m [28].

A signature from the non purely two-dimensional nature of the lipid bilayers can be evidenced in particular situations involving a relative motion between the two leaflets (monolayers) constituting the membrane [29, 30, 31, 32] (see Figure 1.3 *(right)*). Indeed, the dissipation associated to intermonolayer slip can become significant when suddenly changing the shape of lipid membranes, i.e. for example when rapidly pulling a nanotube from a spherical vesicle [33, 34]. An intermonolayer friction coefficient b can therefore be defined as the ratio between the force per unit area and the slip velocity [35]. Typical values of b are in between 10^6 and 10^8 Pa s m^{-1} [36].

1.2 Particle-membrane encounters

1.2.1 Microparticles, microswimmers, Janus colloids

Many micrometric sized objects of different nature interact with biological membranes. Physical models generally involve inert particles made of amorphous materials as a generic particle to probe the membrane response. Such systems are valuable tools to investigate the role of particle shape, size and surface properties on mechanisms such as cellular uptake. They fail however at reproducing one fundamental aspect characterizing biological components: their out of equilibrium nature. Indeed, many entities such as micro-organisms consume energy at the local level to produce work and perform autonomous locomotion in biological environments [37]. Examples include spermatozoa, bacteria or algae such as *Chlamydomonas reinhardtii*, which are able to exploit their flagella to perform autonomous locomotion, as described in Figure 1.4. This class of motile particles is known under the name of active particles, or microswimmers. The nonequilibrium nature of systems involving such active particles can lead to very different dynamics as compared to their passive counterpart [38].

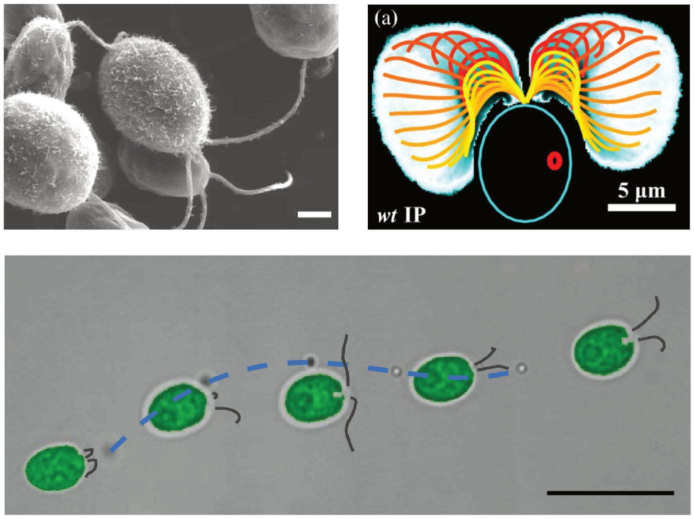

Figure 1.4: *(top left)* Scanning electron microscope image of *Chlamydomonas reinhardtii*, image from [39] (Dartmouth College electron microscope facility). The scale bar is 2 µm. *(top right)* Discrete waveforms of a beating flagella of chlamydomonas reinhardtii within one cycle ("breakstroke"), color coded in time, and overlaid on a spatial map of average flagellar residence time. [40] *(bottom)* Swimming chlamydomonas entraining a microparticle as the cell swims from the left to the right of the panel. The image here is a superposition of several snapshots at different times of a movie with a single algae swimming. The scale bar 20 µm, adapted from [41].

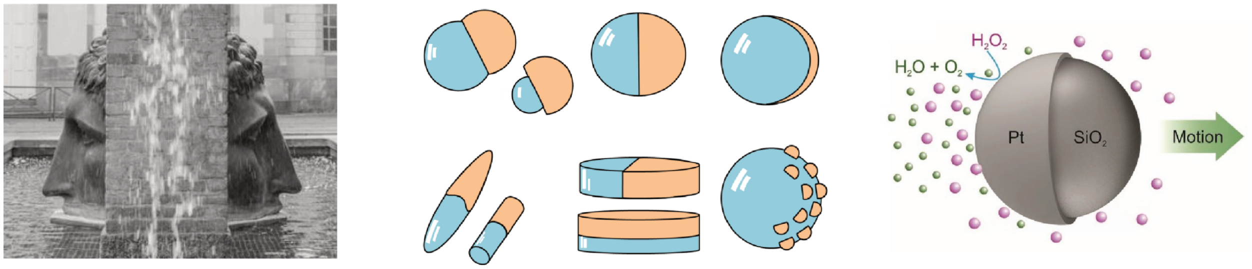

Figure 1.5: *(left)* The Janus fountain in Strasbourg illustrates the ”two-faced” nature of the class of particles that derive their name from this concept. *(middle)* Examples of possible Janus geometries (snowman/mushroom, spheres, patchy particles, ellipsoids/rods, discs, raspberry). Figure reproduced from Ref. [55]. *(right)* Example of self-propulsion mechanisms for a spherical Pt@SiO$_2$ Janus in hydrogen peroxide achieving autonomous motion through self-diffusiophoresis. Figure adapted from [56].

Apart from their utility as model systems for studying out-of-equilibrium statistical physics, artificial microswimmers are highly valued for their potential to perform various tasks in both technical and medical fields [42, 43, 44, 45]. One notable class of artificial swimmers that has attracted significant interest is the Janus particles. Named after the two-faced Roman god Janus, these colloids typically have two ”faces” with differing surface compositions, as illustrated in Figure 1.5. The strong spatial symmetry breaking, essential to observe persistent directed motion, makes Janus particles easily activated through various mechanisms. One such mechanism leading to self-propulsion is self-electrophoresis, where the motion of the colloid is driven by an electric field generated by the colloid itself [46, 47]. Another mechanism is self-thermophoresis, where Janus colloids become active and exhibit self-propulsion by absorbing light on their metal-coated side [48, 49, 50]. This absorption creates a local temperature gradient around the particle, driving its motion, as corroborated by observing the thermal slip flow field around the Janus colloid [49]. Additionally, Janus colloids can achieve autonomous propulsion through self-diffusiophoresis, which involves creating concentration gradients via chemical reactions on one face of the particle [51, 52, 53]. For example, the decomposition of H_2O_2 on the platinum-coated side of polystyrene colloids producing asymmetric distribution of O_2 around the particle generates phoretic forces, as depicted in Figure 1.5 *(right)* [54].

1.2.2 Swimmers and obstacles

For passive particles in the absence of external fields, the approach dynamics close to solid or fluid interfaces is dictated by the randomness of thermal Brownian motion. For microswimmers, however, while their dynamics is far from being deterministic, the fluid flows they

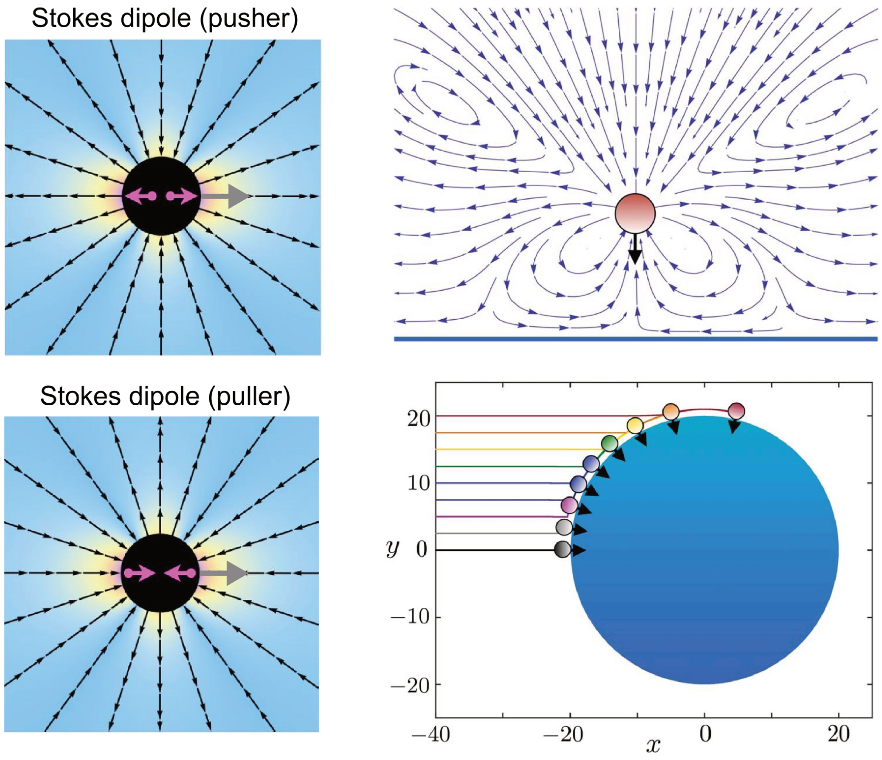

Figure 1.6: *(left)* Flow fields from force (Stokes) dipoles pusher and puller particles. Pink arrows represent the forces and grey arrow the direction of motion. Adapted from [57]. *(right)* Top panel shows the flow field around a puller swimmer close to a no-slip boundary. Bottom panel shows the final captured position on a spherical obstacle as a function of initial position of the swimmer varied along the y axis. Figures from [58].

generate through their swimming mechanisms lead to long-range hydrodynamic interactions with obstacles. Depending on the swimming mechanism of the considered system, the fluid flow pattern can be very complex [59]. However, it has been shown that the far-field hydrodynamics (at distances from the swimmer larger than the swimmer body size) can be accurately described by modeling the swimmers as force dipoles [60, 61, 62]. Two types of dipoles are usually distinguished depending on the sign of the dipole strength $p > 0$ or $p < 0$. If the surrounding fluid is pushed away along the direction of motion and pulled towards the sides (ensuring mass conservation), the swimmer is called a *pusher* ($p > 0$), see Figure 1.6. This is the case for some flagellated bacteria such as *E. coli* [62] or for Pt@SiO$_2$ Janus particles in H$_2$O$_2$ [63]. On the contrary, if the fluid is pulled towards the front and back and pushed away at the sides, the swimmer is said to be a *puller* ($p < 0$), see Figure 1.6. This is the case for the algae *Chlamydomonas reinhardtii*, described earlier in Figure 1.4, although it has been experimentally demonstrated that the flow pattern differs from that of a simple dipole [64]. Examples of artificial puller swimmers are more rare, but Cu@SiO$_2$ (half

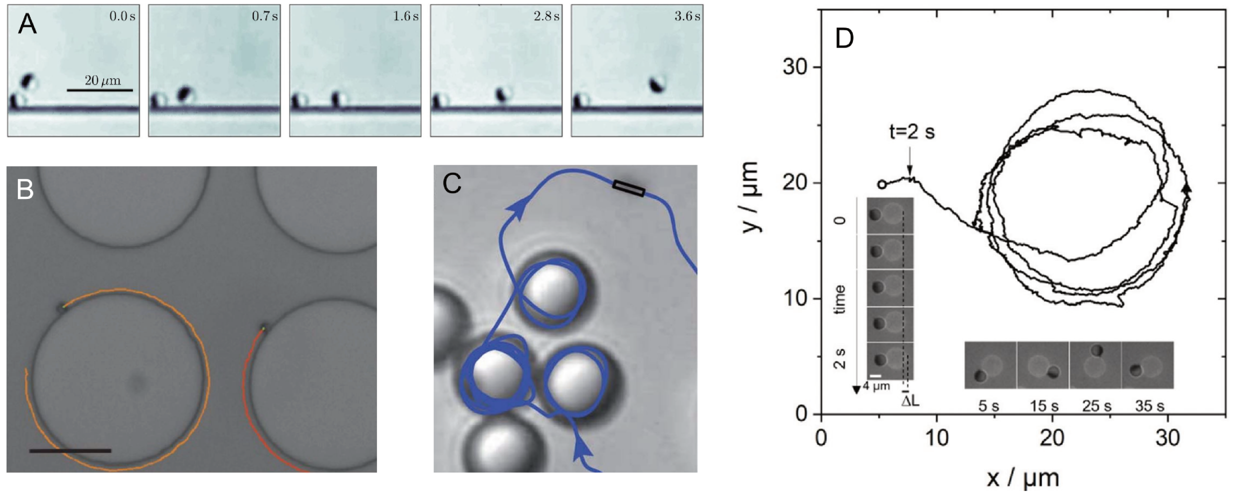

Figure 1.7: Pusher type swimmers interacting with solid obstacles for various systems and geometries. (A) Au-Si Janus, propelled by the local asymmetric demixing of a critical mixture upon illumination, close to a solid boundary showing a trapping event, from [68]. (B) Catalytic Pt@SiO_2 Janus colloid in H_2O_2 performing orbital motion around a circular post, from [69]. (C) Self-propelled Au–Pt rods captured at the periphery of inert SiO_2 spheres, from [70]. The rod is 2 μm long. (D) Pusher Pt@SiO_2 Janus colloid in H_2O_2 performing orbital motion around a POPC giant vesicle [71].

Copper-coated Silica particles) Janus colloids in aqueous solutions containing few percents of H_2O_2 exhibit puller-like behaviors [65, 66]. In particular, the fact that they swim with the catalyst face pointing in the direction of motion (i.e., Cu cap forward) implies that the slip is strongest on this leading face [67], which has been shown to lead to puller-type flows [65].

The properties of these self-generated flows, and therefore the puller or pusher type nature of the swimmer, dictate the interactions of swimmers with interfaces and other swimmers [60, 72, 58, 73, 74, 69]. Using the multipole representation of swimmers to solve Stokes equation, the hydrodynamic interactions of pusher and puller type swimmers with solid walls could be predicted [60]. In particular, it was predicted that pusher particles swimming parallel to a bounding wall would experience an attractive interaction with the wall while puller particles with the same orientation would be repelled. Considering the geometry of a large spherical solid obstacle, a similar modelling approach combining singular solutions to the Stokes equations and hard core repulsion predicted that pusher particle could be trapped in orbital motion around a critical obstacle size [58]. For pullers however, the model predicted a trapping at the obstacle periphery that would result in a motionless equilibrium state, the particle ending up "adsorbed" on the obstacle. The calculated fluid velocity field of a puller near a solid obstacle is shown in Figure 1.6 *(right)* together with the final captured position on a spherical obstacle as a function of initial position. The predicted behaviors were validated experimentally and appeared to be very robust for many pusher systems, along walls [68, 69, 74], circular posts [69, 75] or spherical giant colloids [76], as shown in Figure 1.7 (A,B,C). In fact, the same orbital trapping effect was reported also for soft obstacles, namely giant lipid vesicles, as shown in Figure 1.7 (D). For puller swimmers however, much less data are available to bring experimental confirmations to the predictions. Furthermore, it can be expected that soft boundaries, such as lipid membranes, may be deformed by the microswimmer, potentially triggering membrane shape transitions.

1.2.3 Adhesion-driven particle wrapping

In the previous section, we introduced the concept of passive and active particles. In this section, we will focus on the membrane deformations and shape transitions that can be induced by passive particles.

In order to observe shape remodelling, membranes must undergo continuous deformation to transition between states. As previously introduced (Section 1.1.2), deforming a lipid membrane incurs an energy cost primarily due to membrane bending rigidity and lateral tension. For the case of deformations induced by a particle, these energetic costs can be compensated by a decrease in the system's energy upon membrane-particle surface contact, if both surfaces show affinity. In biology, this affinity can arise from specific biological receptors. However, nonspecific physical forces can also lead to adhesion.

Pioneering experimental work by Dietrich *et al.* [78] reports on the spontaneous interaction between polystyrene microspheres and DOPC or SOPC lipid vesicles. Complete wrapping of the particle was observed and the equilibrium configurations were explained using a simple model accounting for the interplay between membrane elastic energy and particle-membrane adhesion energy (the bending contributions were neglected). The adhesion energy is characterized by an adhesion energy density w which can be written in terms of interfacial tensions, in analogy to wetting, and characterizes the adhesion energy $E_w = wA$ (A is the membrane area in contact with the particle surface and $w < 0$ if the contact is favorable). Note that the analogy with wetting holds for some limiting cases, but not in general as it assumes the membrane tension σ is constant, which is generally not the case upon deformation as discussed in Section 1.1.2. Still, the idea of using an adhesion energy density w instead of considering the full distance-dependent interaction potential between the membrane and particle surface was widely reused in subsequent works (w is in fact the value of the energy density at the global minimum of the distance-dependent interaction potential).

To gain more control over the adhesion strength in the system, recent approaches utilize depletion forces by adding a non-adsorbing polymer to the solution [77, 79, 80]. This method

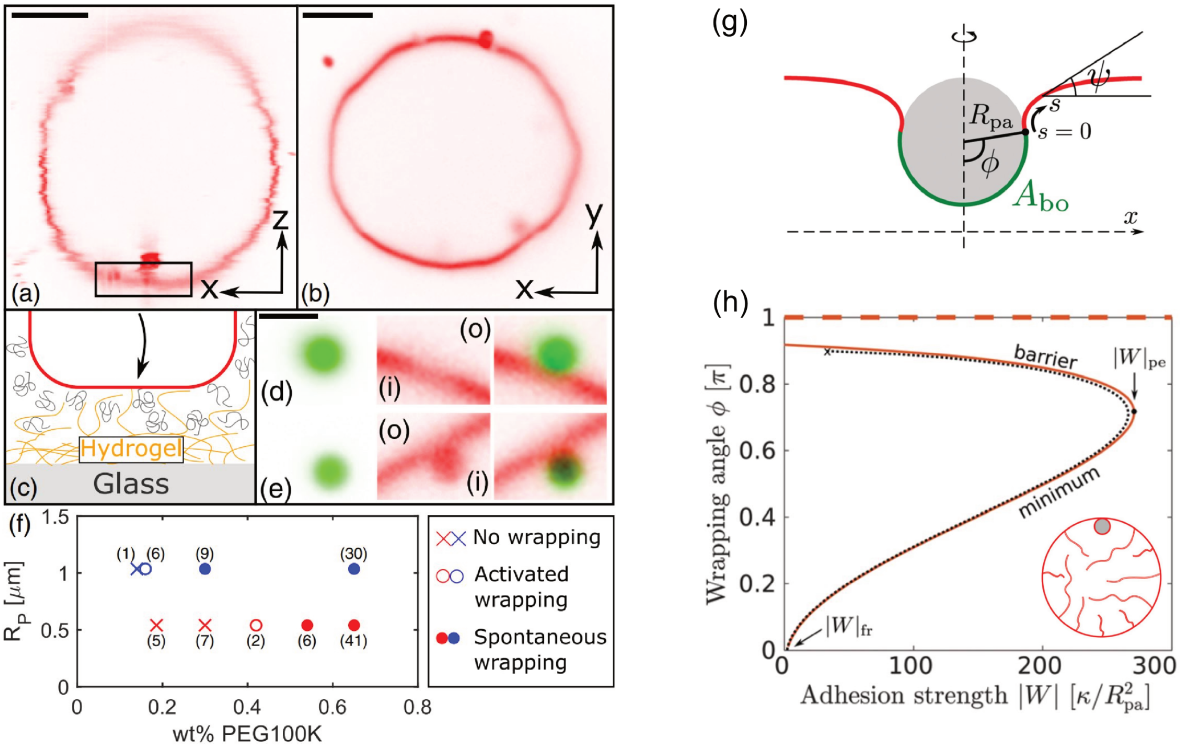

Figure 1.8: *(left)* Figure reproduced from [77]. (a,b) Cross-section sections of confocal image stacks of a GUV sedimented on a PEG-DA hydrogel. The scale bar is 10 µm. (c) Schematic diagram of the experimental system, and hypothesized mechanism for reduced depletion interactions against a hydrogel. (d,e) Confocal images of $R_P = 1.1\,\mu\mathrm{m}$ PS particles (green) and POPC membranes (red). The inside and outside of the GUV are indicated by i and o, respectively. The particle in (d) with 0.24 wt % PEG100K does not deform the membrane. The membrane wraps the particle in (e) at 0.53 wt % PEG100K. The scale bar is 2 µm in length. (f) Phase diagram based on the particle radius and amount of PEG depletant in the system. Numbers next to each data point indicate the number of membrane-particle pairs that were probed in each condition. *(right)* Figures from Ref. [20] showing (g) a schematic diagram with definition of the relevant parameters. (h) Graph of the wrapping angles ϕ corresponding to the maxima of the total energy landscapes $dE_{tot}/d\phi = 0$ (unbound and bound membrane segments, in red and green on the top diagram, respectively) as a function of the adhesive strength $|w|$, for negative spontaneous curvature $mR_P = -10$. Note the existence of two minima for $0 < |W| < |W|_{\mathrm{pe}}$, one for $0 < \phi < 0.7$ and one at $\phi = 1$ (dashed line).

allows for tunable, nonspecific and reversible adhesive interactions between the particle and the lipid membrane. Notably, Spanke *et al.* used polyethylene glycol (PEG) as a depletant to tune the adhesion strength between $R_P \sim 0.5 - 1\,\mu\mathrm{m}$ polystyrene colloids and POPC GUVs, see Figure 1.8. In the absence of external forces and for low tension membranes ($\sigma < 10^{-8}$ N.m^{-1}), they observed spontaneous complete wrapping of the particles above a given PEG concentration threshold, depending on the particle size. The experimental phase diagram is depicted in Figure 1.8 *(left)*. For low adhesion strength, no wrapping occurred, even when membrane deformation was induced using optical tweezers. For intermediate adhesion strengths, particles could be wrapped by applying an external force with optical tweezers, though this force was not quantified. The existence of this *activated regime* is predicted only for finite membrane tensions [81]. However, in this study, the tension was disregarded, and the *activated regime* was attributed to curvature effects. Numerical and theoretical works have predicted a stable complete wrapping state, possibly requiring overcoming an energy barrier, when the membrane curves away from the particle at the initial contact point [82, 83].

In a different regime characterized by large membrane spontaneous curvature $|m|R_P \gg 1$ and, consequently, large associated spontaneous tension $\tilde{\sigma} = 2\kappa_b m^2$ (see Section 1.1.2), recent theoretical works provide predictions for the stability of engulfment states of adhesive uniform particles [20]. In particular, these predictions suggest that even for vanishing adhesion strength, there exists a bistable coexistence of free/partial wrapping states ($\phi \approx 0$ as defined in Figure 1.8 *(right)*) and fully wrapped states ($\phi = \pi$) for negative spontaneous curvatures $m < 0$. This can be seen in Figure 1.8 *(right)* which reproduces results from Ref. [20], and shows the two equilibrium states coexisting over a wide range of adhesion strengths. Note that for positive m, the energy landscape is very different, and such bistability is not expected. An intuitive explanation is that for $m < 0$, the unbound membrane segment (represented in red in Figure 1.8 *(right)*) is energetically costly for intermediate wrapping angles, while the energy of this segment decreases with increasing wrapping angle for $m > 0$ [20].

For passive spherical Janus particles, if one hemisphere is strongly adhesive and the other is not, it was predicted theoretically and reported experimentally that partial wrapping of the particles is the most favorable configuration [84, 85, 86, 87]. This allowed to trigger active transportation of the vesicle partially adhered to the catalyst hemisphere [85, 86], but in those cases the activity was triggered only after the stable equilibrium partial engulfment state was reached. In the next section, I will summarize some important results in the recent literature focusing on the deformation of lipid membranes and vesicles induced by the motive force of active particles.

1.2.4 Activity-induced membrane deformations

In the previous section, some physical principles governing particle-membrane interactions were studied based on energetic considerations and interactions in equilibrium states. The applicability of these principles can therefore be questioned when dealing with active particles which are fundamentally out-of-equilibrium systems. The first consequence of this activity is the existence of nonequilibrium driving forces arising from the propulsion mechanism. Close to a lipid membrane, these forces can still be effective and impart localized forces on the membrane, if the particle has the proper orientation. The temporal evolution of the force direction is directly related to the particle orientation, whose dynamics is dictated by a Langevin equation that contains a stochastic component and eventually an interaction

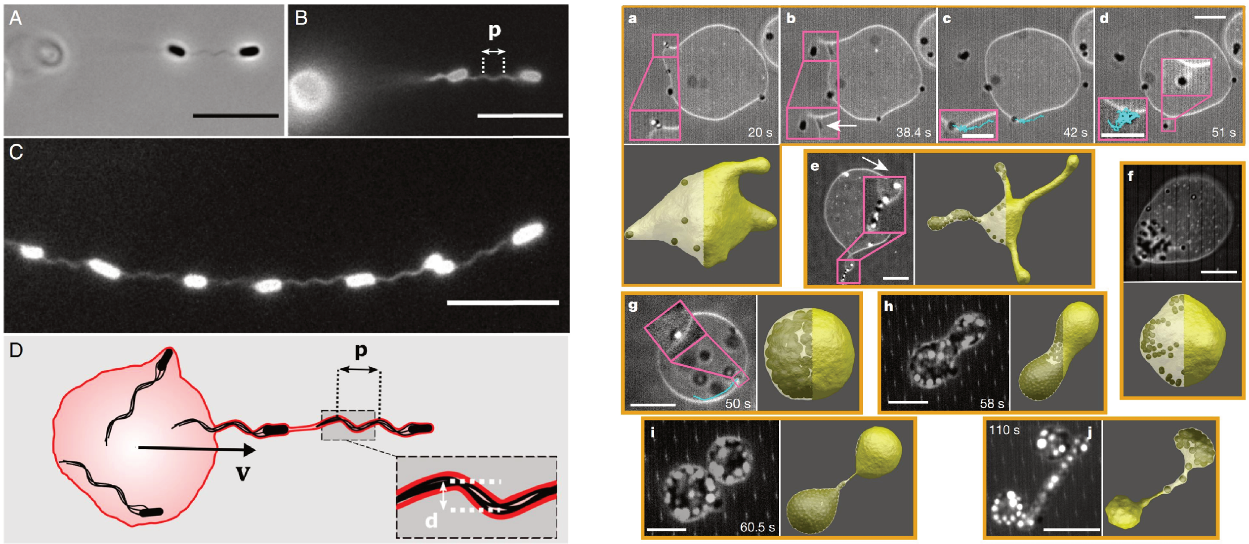

Figure 1.9: *(left)* Membrane tubes can propel GUVs by tightly coupling with the flagella bundles of the enclosed swimmer. (A) Phase contrast image of two cells in a tube. (B) Fluorescence image of the lipid tube displayed in A. (C) Fluorescence image of a tube containing multiple bacteria, showing the coupling with the flagella bundles behind each cell. (D) Schematic of the system (not to scale) describing the mechanism of GUV propulsion. The membrane (red contour) of the tube wraps the bacteria and adopts the shape of their helical flagella (pitch p, helical diameter. Scale bars are 10 µm. Figure reproduced from [88]. *(right)* Shapes adopted by vesicles encapsulating active Pt@SiO$_2$ (in H_2O_2, 0.5-6% vol. concentration) at different volume fractions, Figure from Ref. [89]. The top row (a-d) shows a sequence of time-lapse microscopy images showing various membrane deformations, notably partial and full wrapping to tethering. Below (e-j) are the different shapes that were observed together with simulation snapshots corroborating the experimental observations.

potential lading to a torque due to e.g. hydrodynamic coupling with the membrane. This is very different from the case when an external force is applied for example using optical tweezers [90], where the force acts in a prescribed direction.

Recently, experimental efforts to encapsulate active particles in lipid vesicles were reported [88, 89], and it was shown that they can induce large shape deformations. Encapsulated bacteria were shown to strongly deform the bounding vesicle in tubular structures, and that the whole structure could be propelled due to the coupling of the membrane shape to the flagellar bundles inside the vesicle [88], see Figure 1.9 *(left)*. Encapsulated artificial Pt@PS Janus microswimmers fueled by H_2O_2 in floppy vesicles on the other hand were shown to lead to a large variety of nonequilibrium vesicle shapes [89], as reported in Figure 1.9 *(right)*. Simulation studies allowed to establish a state diagram for the shapes adopted by the vesicles as a function of activity strength and volume fraction of particles in the vesicle. Although some activity-induced budding events were reported at the single particle level, Ref. [89] focuses more generally on the collective phenomena such as the active membrane shape fluctuations emerging in such systems.

When active particles are not enclosed in the vesicular lumen, observing active particle-

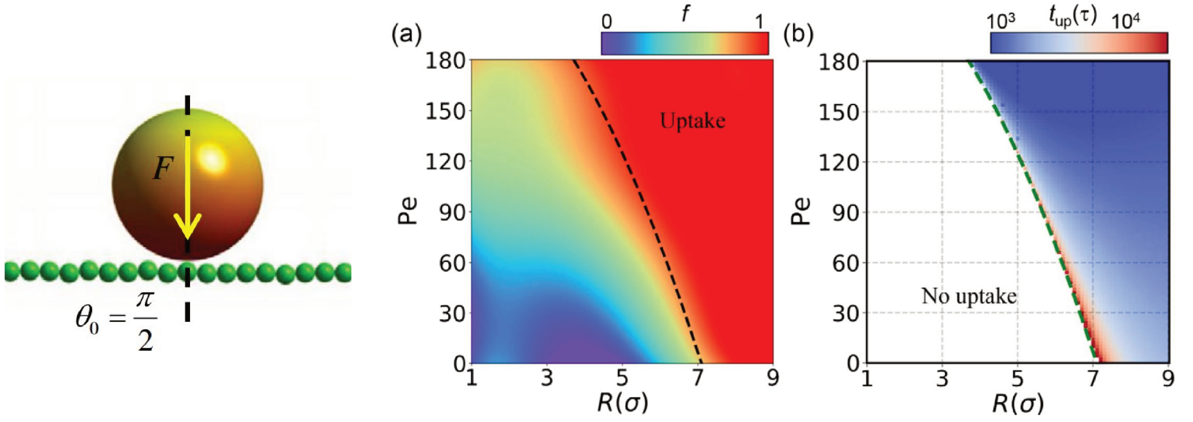

Figure 1.10: Figures reproduced from Ref. [91]. *(left)* Initial configuration an active particle oriented normal to the membrane. The force F is related to the active velocity v_0 as $F = \zeta_t v_0$. *(middle)* Final wrapping degree f ($f = 0$ for no wrapping, $f = 1$ for full wrapping) as a function of Péclet number $Pe = v_0 2R_P/D_t$ and particle size R_P in simulation lipid unit length σ for an active particle with initial orientation depicted on the left diagram. *(right)* Uptake time (in units of simulation time step τ) as a function of the same parameters. The dashed line in both graphs is a critical Pe for endocytosis prediction derived from a theory considering the free energy of the system as a sum of the bending, adhesion, and activity.

vesicle interactions in dilute solutions becomes much more complicated. Long-range hydrodynamic interactions and stochastic reorientation of the particles may prevent orthogonal orientation of the particles with respect to the membrane. This usually leads to either scattering of the particles by the vesicle or orbital motion [71]. To date, experimental investigations of deformations induced by artificial active particles from the exterior of the vesicle in dilute conditions have not been reported. Systematic investigations at the single-particle level on the uptake of spherical active particles have thus far only been conducted using theoretical and numerical tools [91, 92]. Chen *et al.* [91] reported results where the deformation of a planar membrane by an active particle is simulated by allowing the particle position and orientation to evolve according to coupled Langevin equations for rotational and translational motion. The membrane is modeled using a coarse-grained lipid agent model. The effects of initial particle orientation, particle size, and activity strength on the uptake dynamics were investigated.

In Figure 1.10, we present some of the results from Ref. [91] for an active particle with the self-propulsion force initially pointing towards the membrane. Color maps of the final wrapping degree and uptake time illustrate the effect of particle size and activity in this scenario. Notably, activity enables complete wrapping for smaller particle radii, and a higher activity strength accelerates the uptake dynamics. Additionally, interesting effects were reported, such as the non-monotonic dependence of uptake efficiency on activity strength for particles with initially tilted orientations. These findings suggest that rich and complex dynamics of the coupled membrane shape and particle motion may emerge from single active particle-membrane interactions, providing strong motivation for experimental exploration.

1.3 Confined Brownian motion

Microparticles, whether active or passive, undergo perpetual erratic motion due to collisions with the molecules of the surrounding fluid. This phenomenon, known as Brownian motion, was first observed by botanist Robert Brown in 1827 and later theoretically described by Albert Einstein in 1905 [93]. When particles are subjected to an external potential, such as an optical trap or due to interactions with surfaces and interfaces, their random motion due to thermal agitation is spatially constrained but still present. Furthermore, this random motion, which can be quantified by measuring the particle's position, contains valuable information about the particle's environment. The framework of statistical physics allows us to link the observables of particle trajectories to the properties of the surrounding fluid and the interactions confining the particles. In the following sections, we describe the theoretical framework of free and confined Brownian motion, which enables us to gather information on the dissipation and interactions experienced by microparticles throughout this work.

1.3.1 Unconstrained Brownian motion

The Langevin approach to Brownian motion does not consider every collisions of the lighter solvent particles colliding the considered object, but rather approximates those collisions to result in a stochastic force $F_{\mathrm{th}}(t)$. This force is not known exactly, and the whole point of this approach is to circumvent the need to know the exact behavior of this force, by describing its statistical properties only. This can be done by considering the evolution of the system on timescales much larger than the solvent molecules velocity relaxation time $\tau_m \sim 10^{-12}$ s (linked to the mean free path of the molecules divided by the mean thermal velocity). This timescales separation allows to approximate the thermal force $F_{\mathrm{th}}(t)$, in 1-dimension, as

$$F_{\mathrm{th}} = \sqrt{2k_{\mathrm{B}}T\zeta_t}\,\Gamma(t), \tag{1.11}$$

with $\Gamma(t)$ the Gaussian white noise, defined as :

$$\begin{aligned} \langle \Gamma(t) \rangle &= 0, \\ \langle \Gamma(t)\Gamma(t') \rangle &= \delta(t-t'). \end{aligned} \tag{1.12}$$

Where $|t-t'| \neq 0$ suggests $|t-t'| > \tau_m$. The other force experienced by a particle in a viscous fluid is the viscous drag force which is opposed to the movement of the object. Stokes showed that at small particle velocity, this drag force F_d is proportional to the particle velocity v such that:

$$F_d = -\zeta_t v, \tag{1.13}$$

where ζ_t is called the translational friction (or drag) coefficient. For a spherical particle of radius R_P immersed in a fluid of viscosity η far from boundaries, this coefficient of friction is given by Stokes' law and reads:

$$\zeta_t = 6\pi\eta R_P. \tag{1.14}$$

Now that we defined the friction force and defined the statistical properties of the stochastic force $F_{\mathrm{th}}(t)$, we can write the equation of motion for a particle of mass m, which in 1-dimension reads:

$$m\ddot{x}(t) = -\zeta_t \dot{x}(t) + \sqrt{2k_{\mathrm{B}}T\zeta_t}\,\Gamma(t). \tag{1.15}$$

Note that for small particle mass and large fluid viscosity (i.e. for low Reynolds number), the inertial term of Eq. 1.15 (left hand side) is vanishingly small as compared to other terms and can be disregarded. However, by solving Eq. 1.15 for $v(t) = \dot{x}(t)$, the time correlation of the particle velocity can be derived and has the form [94]:

$$\langle v(t)v(t')\rangle = \frac{k_B T}{m} e^{-|t-t'|/\tau_v}, \tag{1.16}$$

where $\tau_v = m/\zeta_t$ is a velocity relaxation timescale. From the velocity autocorrelation function, we can derive an important quantity, the mean squared displacement (MSD) $\langle (x(t) - x(0))^2 \rangle$. This quantity will be extensively used when studying the Brownian dynamics of particles as it can easily be calculated from experimental trajectories. It is related to the velocity autocorrelation through [94]:

$$\left\langle (x(t) - x(0))^2 \right\rangle = 2\int_0^t \int_0^{t_1} \langle v(t_2)v(0)\rangle \, \mathrm{d}t_2 \, \mathrm{d}t_1. \tag{1.17}$$

Provided that the timescales considered are much larger than the velocity relaxation time τ_v (it is usually the case in experiments, as $\tau_v < 10^{-6}$ s), the inner integral of the right hand side of Eq. 1.17 is a constant, which we call D_t:

$$\int_0^{t_1} \langle v(t_2)v(0)\rangle \, \mathrm{d}t_2 \approx \int_0^{\infty} \langle v(t_2)v(0)\rangle \, \mathrm{d}t_2 = D_t. \tag{1.18}$$

From Eqs. 1.17 and and 1.18, provided that $t \gg \tau_v$, we have:

$$\mathrm{MSD}(t) = \left\langle (x(t) - x(0))^2 \right\rangle = 2D_t t. \tag{1.19}$$

Note that this results holds in one dimension an can be generalised to two and three dimensions by replacing the factor 2 in the right hand side of Eq. 1.19 by 4 and 6, respectively. From Eqs. 1.16 and 1.18, it follows:

$$D_t = \frac{k_B T}{\zeta_t} \tag{1.20}$$

This equation, known as the Einstein relation, was used by Jean Perrin in 1908 to determine the Avogadro number by experimentally tracking diffusing colloids, and thereby definitively validated the discontinuous nature of matter. This relation is still widely used today to extract information from the dynamics of a colloid immersed in a Newtonian fluid. Note that this coefficient which we call D_t here is in fact a self-diffusion constant, and is in general different from the diffusion constant found in the diffusion equation. However, both are equal in the case of dilute solutions, which can be shown by looking at the particle positions distribution in a dilute solution resulting from the equilibrium between en external force and diffusion [94].

For the rotational motion about a single axis defined by an angle θ, a relation analogous to Eq. 1.19 can similarly be derived [95]. The mean squared angular displacement (MSAD) of a freely diffusing particle then reads:

$$\mathrm{MSAD}(t) = \left\langle (\theta(t) - \theta(0))^2 \right\rangle = 2D_r t, \tag{1.21}$$

with

$$D_r = \frac{k_B T}{\zeta_r}, \tag{1.22}$$

where ζ_r is the rotational friction constant relating the frictional torque $\bar{\tau}$ acting on a rotating sphere to the angular velocity Ω of the particle. Analogously to Eq. 1.13, we have:

$$\bar{\tau} = -\zeta_r \Omega. \tag{1.23}$$

In a bulk viscous fluid, Stokes calculated for a spherical particle with radius R_P:

$$\zeta_r = 8\pi\eta R_P^3. \tag{1.24}$$

1.3.2 Brownian motion in a harmonic potential

If the particle is placed in a potential $U(x,t)$, that could for example arise from the interaction with the laser beam of the optical tweezers, or from any other interaction, the Langevin equation along one dimension x becomes

$$m\ddot{x}(t) = -\zeta_t\dot{x}(t) - \frac{\partial U}{\partial x} + \sqrt{2k_\mathrm{B}T\zeta_t}\Gamma(t). \tag{1.25}$$

In the the overdamped limit (defined when $t \gg m/\zeta_t$), we can drop the inertial terms and the equation reduces to

$$\dot{x}(t) = -\frac{1}{\zeta_t}\frac{\partial U}{\partial x} + \sqrt{2k_BT/\zeta_t}\Gamma(t). \tag{1.26}$$

If the potential is modelled as harmonic with a stiffness κ such that $U = \frac{1}{2}\kappa x^2$, a relaxation time $\tau_t = \zeta_t/\kappa$ associated to the restoring force deriving from the potential emerges, and Eq. 1.26 can be written as:

$$\dot{x}(t) = -\frac{x(t)}{\tau_t} + \sqrt{2D_t}\Gamma(t). \tag{1.27}$$

By introducing the Wiener process $\mathrm{d}W(t) = \Gamma(t)\mathrm{d}t$, we can rewrite Eq. 1.27 into the following stochastic differential equation:

$$dx(t) = -\frac{x(t)}{\tau_t}dt + \sqrt{2D_t}\mathrm{d}W(t). \tag{1.28}$$

This equation which describes the instantaneous position of the microsphere in the harmonic well defines a so-called Ornstein-Uhlenbeck process. A solution can be derived and reads:

$$x(t) = x_0e^{-\frac{t}{\tau_t}} + \sqrt{2D_t}\int_0^t e^{-\frac{t-s}{\tau_t}}\,\Gamma(s)\,\mathrm{d}s, \tag{1.29}$$

where $x_0 = x(t=0)$.

In order to derive an expression for the MSD in the case of a Brownian particle in a harmonic trap, we can use Eq. 1.29 to derive the position autocorrelation function in a stationary state $\langle x(t)x(t')\rangle = \langle x(t+\Delta t)x(t)\rangle$. The equilibrium variance can be obtained from the equipartition theorem, and yields $\langle x(t)^2\rangle = k_BT/\kappa$, and it can be shown that the position autocorrelation function reads

$$\langle x(t+\Delta t)x(t)\rangle = \frac{k_BT}{\kappa}e^{-\frac{\kappa}{\zeta_t}\Delta t}. \tag{1.30}$$

From there, it follows:

$$\left\langle (x(t+\Delta t) - x(t))^2 \right\rangle = \left\langle x(t+\Delta t)^2 \right\rangle - 2\left\langle x(t+\Delta t)x(t)\right\rangle + \left\langle x(t)^2 \right\rangle, \tag{1.31}$$

and using the fact that $\langle x(t)^2\rangle = \langle x(t+\Delta t)^2\rangle = k_BT/\kappa$ from equipartition theorem for a stationary process and Eq. 1.30, we finally obatin:

$$\left\langle (x(t+\Delta t) - x(t))^2 \right\rangle = \frac{k_BT}{\kappa} - 2\frac{k_BT}{\kappa}e^{-\frac{\kappa}{\zeta}\Delta t} + \frac{k_BT}{\kappa} = \frac{2k_BT}{\kappa}\left[1 - e^{\frac{-\kappa}{\zeta_t}\Delta t}\right]. \tag{1.32}$$

Considering the expression of the MSD for a Brownian particle in a harmonic trap, it can easily be seen that at short timescales ($\Delta t \ll \tau_t$), the MSD grows linearly with Δt just like in the absence of a restoring force. Expanding the exponential term at first order for $\Delta t \ll \tau_t$ indeed directly yields

$$\left\langle (x(t+\Delta t) - x(t))^2 \right\rangle_{\Delta t \ll \tau_t} \approx 2\frac{k_BT}{\kappa}\left[1 - (1 - \frac{\kappa}{\zeta_t}\Delta t)\right] = 2D_t\Delta t. \tag{1.33}$$

The MSD then relaxes to the equilibrium variance value on the timescale $\tau_t = \zeta_t/\kappa$, and the process is then governed by the elastic response due to the harmonic trapping of the object.

To conclude, the MSD of a particle can provide two types of information on the environment of a particle, depending on the timescales at which the motion is studied. Looking at short timescales, the dissipations experienced by a particle can be accessed as the rate of change of the MSD is inversely proportional to the drag ζ_t felt by the particle. At larger timescales, the saturation of the particle translational motion variance can directly be linked to the stiffness of the harmonic potential in which the particle is trapped. This harmonic potential can arise from an optical trap, in which case the MSD can be used to calibrate the optical tweezers setup. But it can also arise from any interaction of the particle with its surrounding leading to an elastic response in the system. Those principles will extensively be used in this work.

Again, note that the same applies to rotational motion, and any restoring torque acting on a rotating particle $\bar{\tau} = -K/R_P(\theta - \theta_0)$, where K is a stiffness and has units of an energy, can be seen from the MSAD of a Brownian particle relaxing to a plateau value. A relation analogous to Eq. 1.32 holds for the MASD $\langle(\theta(t+\Delta t) - \theta(t))^2\rangle$ for an angle θ describing the orientation about a given axis, such that:

$$\left\langle(\theta(t+\Delta t) - \theta(t))^2\right\rangle = 2\frac{k_B T}{K}(1 - e^{\frac{K}{\zeta_r}\Delta t}). \tag{1.34}$$

1.3.3 Power spectral density

The spectral content of Brownian trajectories also provides information on the nature of the process at stake and the properties of the system. The quantity we will use to study the Brownian motion of particles in frequency space is the position power spectral density (PSD), which is the squared norm of $\hat{x}(\omega)$, the Fourier transform of the particle instantaneous position $x(t)$. Performing a Fourier transform of the Langevin equation of a Brownian particle in a harmonic potential Eq. 1.27, one obtains

$$-i\omega\hat{x}(\omega) = -\omega_t\hat{x}(\omega) + \sqrt{2D_t}\hat{\Gamma}(\omega), \tag{1.35}$$

where the position relaxation frequency $\omega_t = 1/\tau_t = \kappa/\zeta_t$ was introduced. It follows immediately:

$$\hat{x}(\omega) = \frac{\sqrt{2D_t}\hat{\Gamma}(\omega)}{\omega_t - i\omega}. \tag{1.36}$$

Taking the squared norm to obtain the power spectrum yields:

$$PSD(\omega) = |\hat{x}(\omega)\hat{x}^*(\omega)| = \frac{2D_t}{\omega_t^2 + \omega^2}, \tag{1.37}$$

or in terms of frequency $f = \omega/2\pi$:

$$PSD(f) = \frac{D_t}{2\pi^2(f_t^2 + f^2)}, \tag{1.38}$$

with $f_t = \kappa/2\pi\zeta_t$ the so-called corner frequency (sometimes *roll-off* frequency). We therefore have a Lorentzian shape, which in the low frequency limit tends to the value $PSD_{f \ll f_t} = k_B T\zeta_t/\pi^2\kappa^2$.

1.4 Content of the Thesis

In this thesis, I employ and combine various experimental techniques to investigate the deformations and shape transitions induced by externally driven or self-motile spherical particles on model membranes. The structure of the manuscript and the content of each chapter are described below.

Chapter 2 describes the main instruments and experimental methods I used in this work. I will describe the optical tweezers setup that I built and upgraded and explain how I combined it with a micropipette suction pressure experiment. The theoretical framework of membrane excess area is also introduced. The fabrication method of GUVs is presented, along with the sample preparation and deflation process to obtain floppy vesicles. The commercial and Janus microparticles used are detailed, together with the fabrication protocol of GUVs. Tracking methods and image analysis for extracting quantitative data from microscopy acquisitions are also described.

Experimental results for the entry of microparticles into giant unilamellar vesicles driven by optical tweezers are reported in **Chapter 3**. I provide a qualitative description of the phenomenon's dynamics using fluorescence microscopy and report quantitative measurements with engulfment force profiles. By varying physical parameters of the system (particle size, membrane tension), I investigate their influence on the energetics and dynamics of the process. I then examine the reversibility of the process using micropipette aspiration to increase the membrane tension and observe the expulsion of the engulfed particle back into the extravesicular fluid. Using an analogy with pore opening and associated line energy, I provide lower bounds for the energy required to open the neck nucleated upon wrapping and compare these with available predictions.

In **Chapter 4**, I present a system of active Cu@SiO_2 Janus particles fueled by glucose in physiological concentrations and visible light. I observe interactions between these active particles and GUVs, reporting on wrapping events that occur autonomously. I investigate the wrapping mechanism by analyzing the particle dynamics during various phases of the process, highlighting the role of hydrodynamic interactions that provide the necessary prolonged contact time for wrapping to occur. Additionally, I emphasize the crucial role of adhesion in our system by performing complementary experiments and using existing models to rationalize the uptake of the active Janus particle, showing the contribution of the unbound membrane segment to the outcome.

Chapter 5 discusses experimental investigations into the dynamics of fully wrapped particles, either after optically driven or autonomous engulfment. I show that the connection of the wrapped particle to the mother vesicle introduces additional dissipations that depend on the particle size. I explore the origin of this additional drag by comparing it with existing models and show that this drag increase is dependent on the tension of the membrane, with higher tension leading to higher drag experienced by the wrapped particle. Finally, I report on experiments involving an optically trapped spherical particle in close contact with a vesicle manipulated with a micropipette, collecting information on the dynamics and interaction energy of the particle upon interaction.

Chapter 6 discusses current challenges and ongoing projects following the main results of this work and provides a general conclusion to this thesis.

Chapter 2

Experimental methods, materials and theoretical framework for analysis

In this chapter, I will present the experimental tools and techniques implemented throughout my thesis, alongside the theoretical framework associated to the concepts involved. Furthermore, I will detail the fabrication procedures of all the materials and objects of study pertinent to this research. In a first part, manipulation and measurement techniques such as optical tweezers and micropipette suction technique are introduced. Then, the method for forming giant unilamellar vesicles and make them floppy will be described, followed by a detailed description of the microscopy and manipulation techniques utilized. Finally, the image analysis and tracking methods are described.

2.1 Optical tweezers

The ability of light to exert forces has been hypothesized since Kepler (1619), who proposed that the Sun's rays caused the deflection of comet tails. A few centuries later, Maxwell's theory of electromagnetism suggested that light's momentum could be transferred to objects. In 1986, Arthur Ashkin and his team developed a method to trap small objects, such as dielectric or metallic beads, using a tightly focused laser beam to confine particles in a high-intensity region of space [96, 97]. This section will provide a detailed description of the optical elements used to construct such an optical trap, followed by an explanation of the optimization and calibration procedures developed in the framework of this thesis.

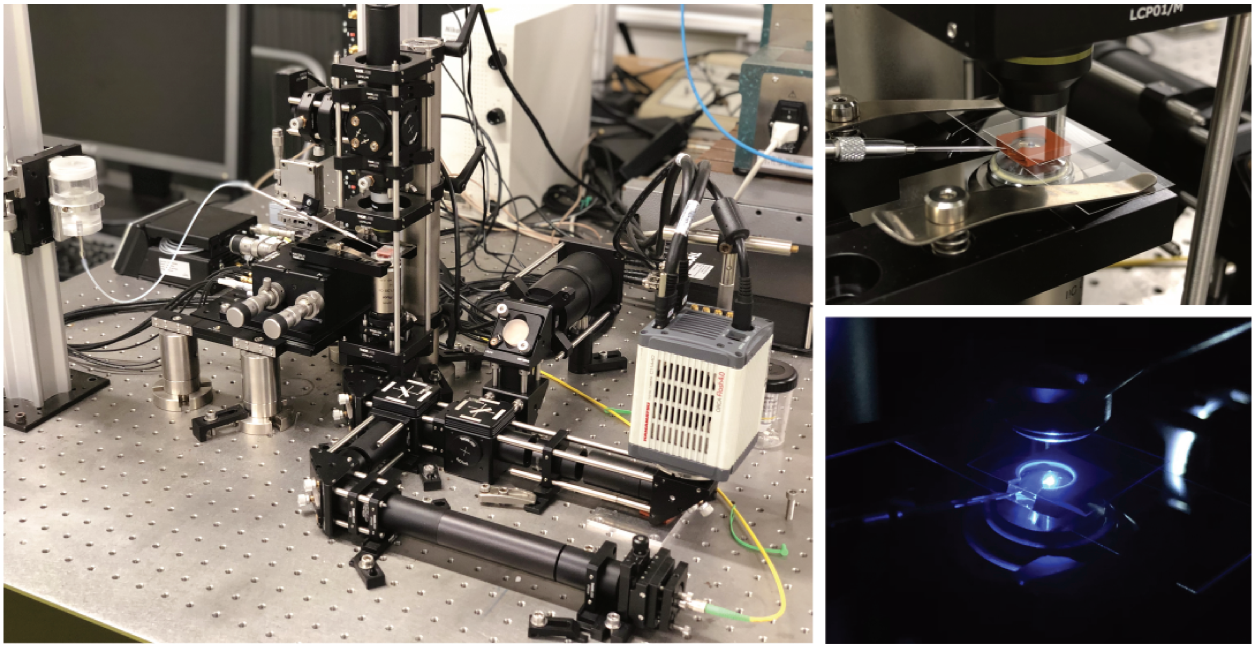

Figure 2.1: *(left)* Picture of the experimental setup combining optical tweezers, micropipette and fluorescence microscopy mounted on a vibration isolating optical table. *(top right)* Focus on the sample cell, which consists of two glass coverslips separated by a customized silicon spacer. This spacer contains the fluid sample and allows for the insertion of a micropipette through a small slit. *(bottom right)* Picture of the sample cell during fluorescence microscopy experiment.

2.1.1 Optical setup

The setup that was mounted for this work is a modified OTKB Modular Optical tweezers (Thorlabs Inc.) which furnishes the basic components needed to build an optical trap. A schematic diagram is provided in Figure 2.2. The laser source is a 976 nm single mode laser diode whose temperature is precisely controlled by a TEC controller and thermistor to ensure a stable power output of the laser, guaranteeing a constant trapping force. The laser power is adjustable and can reach 350 mW. The laser light generated is delivered via a single mode fiber (SM980-5.8-125) to a triplet collimator (TC06APC-980) of focal length 6.11 mm and numerical aperture NA=0.28, resulting in an output beam of 1.7 mm diameter. This beam is then expanded by a gallilean beam expander composed of achromatic doublets of -50 mm and + 250 mm focal lengths (ACN254-050-B and AC254-250-B, respectively). This step is crucial in order to obtain an efficient trap. The overfilling of the back aperture of the objective is compulsory to focus the entering beam, and this will occur only if the beam is properly expanded by the beam expander segment.

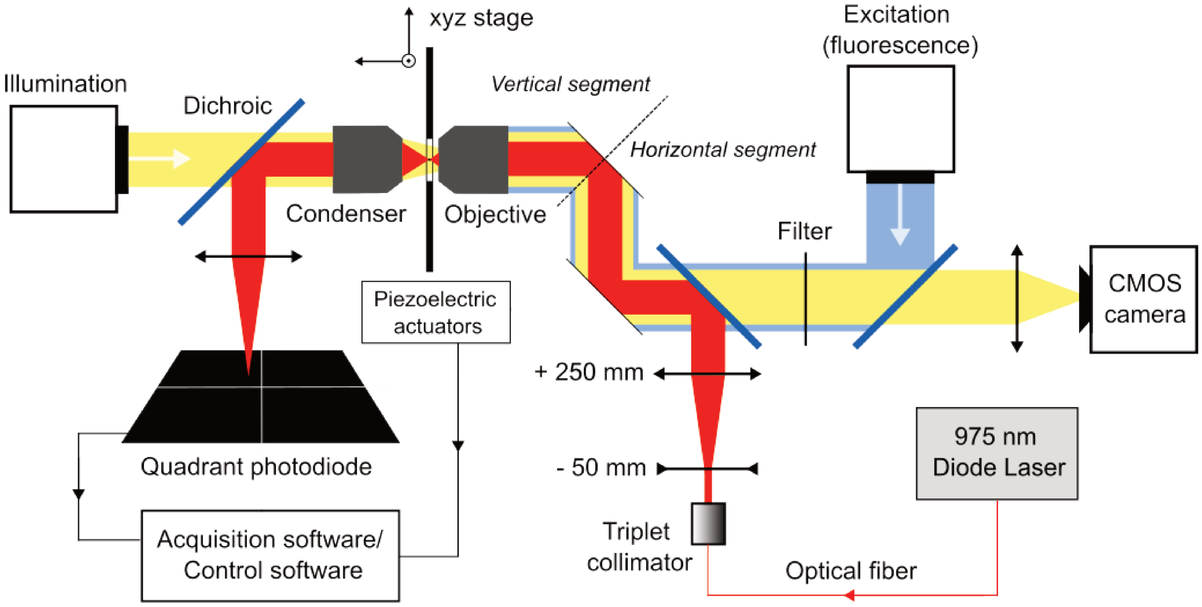

Figure 2.2: Schematics of the optical setup. The 975 nm wavelength trapping laser (in red) is expanded by a telescope (-50 mm/ +250 mm set of lenses). It is subsequently focused by the 100x objective to generate the optical trap in the sample. The light can then be collected by the condenser and focused on the quadrant photodiode thanks to a dichroic mirror and a converging lens.

The beam is then directed towards the back aperture of the objective with a dichroic mirror (DMSP805R, which will allow the visible illumination light to reach the camera) and a set of simple plane mirrors. The beam is then focused by an objective (100X Nikon Plan Fluorite Oil Immersion Objective, 1.3 NA, 0.16 mm working distance WD), which is used both to trap the particles and image the sample using a camera. In the direction opposite to the laser direction of propagation travels an illumination light generated by a LED emitting white light. This light passes through a condenser (Nikon 10X air condenser with a numerical aperture of 0.25) that shines the condensed light on the sample, which is collected by the objective. This light passes through the dichroic mirror and a shortpass filter (preventing laser light to reach the camera sensor) before being focused by a 200 mm focal length tube lens (AC254-200-A) on the camera sensor plane. The camera used is a Hamamatsu Orca Flash-4 CMOS with maximum pixel resolution 2048(H)×2048(V) which permits high temporal resolution (up to 1000 fps at a pixel resolution of 200x2048).

Finally, a mercury light source (Nikon C-HGFI Intensilight) is used as an excitation source for the fluorescent probes in the samples. The light from the mercury source is collimated and directed towards the back aperture of the objective (following the same path in the same direction as the trapping laser beam) thanks to a dichroic mirror. A blue filter is placed just after the light exit from the source which corresponds to the excitation wavelength for the fluorescent probes used in our experiments (nitrobenzodiazole, as we shall see in Section 2.7).

2.1.2 Alignment and optimization

As for any experimental setup involving optics, the efficiency of optical trapping depends on the quality of the alignement of the optical components on the breadboard. Even small misalignment of components on the optical path of the trapping laser may lead to optical aberrations and parasite reflections that could affect the trap efficiency. It is therefore an important step in the implementation of the optical tweezers.

The alignment of the optical components on the path of the trapping laser is done using standard optics alignment procedures (involving irises, diaphragms, screens, etc.). One of the encountered difficulties lays in the fact that the laser wavelength used is not in the visible range. Hence, special viewing cards to see the beam spot were used. One powerful tool in order to have a good idea on how well the laser light is focused by the objective consists in removing the shortpass filter after the dichroic mirror, allowing the laser light to reach the camera. By placing a coverslip after the objective, the reflection of the focused infrared laser beam on this coverslip can be imaged by the camera sensor, which is somewhat sensitive to infrared light. The interference pattern on the camera gives a good idea of how well focused and isotropic the trapping laser beam waist is.

After realigning the whole setup using this technique, the setup was able to trap 5 µm diameter polystyrene. Still, smaller (1 or 2 µm radius) polystyrene colloids could not be trapped. When approaching 1 polystyrene colloid close to the trap, a repulsion by the laser in the direction of propagation was observed. This behaviour is known to occur for not tightly enough focused laser beam, resulting in too weak restoring forces along the direction of laser propagation which are not able to balance radiation pressure. The key parameter for optimizing laser focusing is the size of the expanded beam before it enters the objective. This led us to investigate the beam expander segment. Our hypothesis was confirmed when we completely removed the converging lens from the expander segment, resulting in a diverging but larger beam at the entrance of the objective, which allowed us to trap smaller polystyrene colloids. Adjusting the distance between the two achromatic doublets in the beam expander had minimal impact on the beam size and introduced optical aberrations. To resolve this issue, we replaced the original converging lens supplied with the setup with a lens of larger focal length and increased the distance between the two lenses accordingly to obtain a larger beam spot. Specifically, a new lens with a focal length of +250 mm was used to replace the original +150 mm lens.

2.1.3 Back focal plane detection module

The laser beam transmitted through the trapped particle can be redirected and focused onto a detection module consisting of a quadrant photodiode (QPD) thanks to a dichroic mirror and a converging lens (see Figure 2.2). The interference of this transmitted beam with the remainder of the laser light leads to an interference pattern at the back focal plane of the condenser which depends on the particle position. This quadrant photodiode can therefore be used as a high acquisition frequency particle position detector, with an acquisition rate 2×10^5 Hz which is two orders of magnitude larger than the maximum rate reachable using the CMOS camera.

The QPD outputs data in volts. In order to perform quantitative position measurements, calibration of the detector responsivity factor is needed. To do so, a stuck particle on a substrate should be moved across the location of the optical trap by moving the sample stage with a fine control of the position, provided by computer-controlled actuation of the piezo-electric cells of the sample stage. Close to the trap center, there should be a linear relation between the QPD output voltage and the sample stage position. Within this linear range, one can therefore fit a conversion factor allowing to link the voltage along one direction to a position along this same direction.

The main disadvantage of this detection technique lies in the fact that the interference pattern in the back focal plane is not only sensitive to the particle position, but also on the position of any object on the path of the laser beam. For example, when a lipid vesicle is brought close to the optical trap, the signal detected on the QPD will be modified leading to inaccurate particle position determination. The back focal plane detection should therefore only be used when tracking the motion of a trapped particle far from any other object or interfaces, which makes it mostly suitable for calibration.

2.1.4 Calibration procedures and friction measurements

Calibrating optical tweezers transforms this powerful micromanipulation tool into a precise microforce measurement instrument capable of probing forces as small as a fraction of a picoNewton. In the harmonic approximation, the restoring force resulting from the particle interaction with the focused light beam is assumed to derive from the harmonic potential which, in one dimension, reads:

$$V_i(x_i) = \frac{1}{2}\kappa_i(x_i - x_{i,eq})^2 \tag{2.1}$$

where κ_i is the trapping stiffness along a dimension x_i and $x_{i,eq}$ the equilibrium position. Note that κ_i is not necessarily the same along x, y and z, and independent calibration should therefore be performed. This stiffness depends on parameters of the system such as the trapping laser output power, particle radius or particle material and it should be determined a priori in order to relate the force acting on the particle to its displacement from equilibrium position through $F = -\frac{dV(x_i)}{dx_i} = -\kappa_i(x_i - x_{i,eq})$. The accuracy of the measured force deduced from its displacement from equilibrium position therefore highly depends on the accuracy of the determination of the trapping stiffness κ_i. In the following, we will describe and compare three methods relying on different quantities to extract the trapping stiffness from an experimental trajectory.

Reconstruction of the energy potential from the trajectory

The first method consists in computing the equilibrium particle position probability density in the trap and assume it follows a Boltzmann distribution to recover the potential energy of the particle as a function of its distance from equilibrium position. Indeed, at thermal equilibrium and fixed temperature T, the particle position probability density $P_{eq}(x)$ is expected to follow:

$$\frac{P_{eq}(x)}{P_{eq}(x_0)} = \exp\left(-\frac{\Delta U(x)}{k_B T}\right) \tag{2.2}$$

where x_0 is the equilibrium position (position with minimum corresponding energy) in the well and $\Delta U(x) = U(x) - U(x_0)$. In Figure 2.3, we plot the one-dimensional temporal evolution of the particle relative position $\Delta x(t) = x(t) - \langle x(t) \rangle$ *(top)* and associated probability density *(bottom left)*. We can show that this equilibrium probability density is Gaussian and that its variance is related to trapping stiffness such that $\sigma_{eq}^2 = \langle x^2 \rangle_{eq} = k_B T/\kappa$. In order to have a direct visualization of the potential, we can use this distribution and note

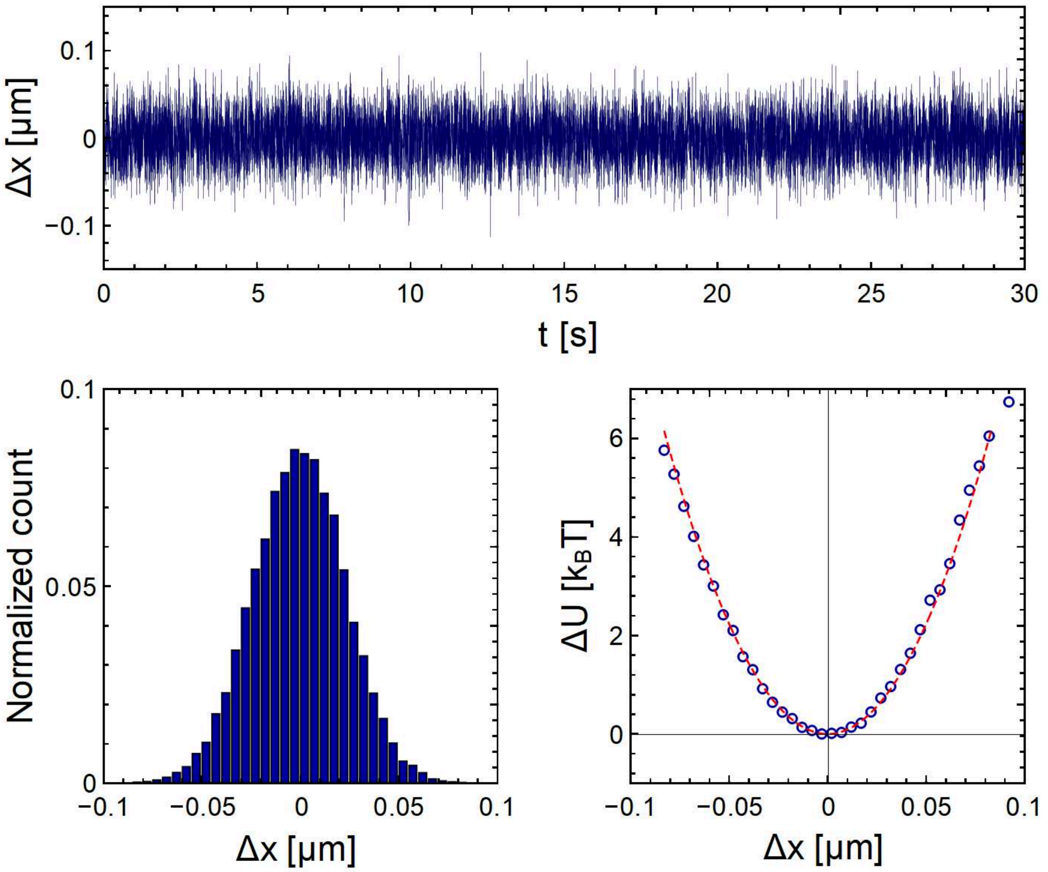

Figure 2.3: *(top)* One-dimensional trajectory for a $\mathrm{SiO_2}$ particle with $R_P = 1.93\,\mu\mathrm{m}$ optically trapped in pure MilliQ water at 80 mW trapping laser power output. *(bottom left)* Experimental position probability histogram calculated from the trajectory on top. *(bottom right)* Experimental effective relative potential energy as a function of relative position $\Delta x(t) = x(t) - \langle x(t) \rangle$ calculated using Boltzmann distribution. The red dashed line is a quadratic fit $\Delta U(x) = 1/2\kappa\Delta x^2$ yielding $\kappa = 7.31 \pm 0.08\,\mu\mathrm{N\,m^{-1}}$.

that $\lim_{N_{tot}\to\infty} N_{eq}(x)/N_{eq}(x_0) = P_{eq}(x)/P_{eq}(x_0)$, where N is the normalized count. Thus, the experimental effective potential $\Delta U(\Delta x)$ can be plotted by taking the log of Eq. 2.2. The bottom right plot in Figure 2.3 shows the potential obtained from such a calculation and evidences the expected harmonicity of the trapping potential in a 200 nm wide region centered on $\Delta x = 0$. Fitting the this experimental potential with $\Delta U(x) = 1/2\kappa\Delta x^2$ and κ the single fitting parameter yields $\kappa = 7.31 \pm 0.08\,\mu\mathrm{N\,m^{-1}}$, where the uncertainty accounts for the fit mean squared error.

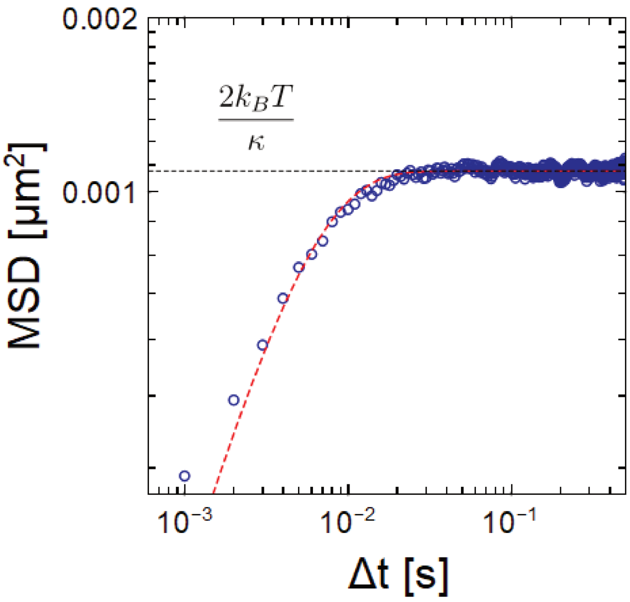

Figure 2.4: Log-log plot of the MSD along one axis as a function of lag time Δt for a $N = 30000$ points long trajectory at an acquisition rate of 1000 Hz. Red dashed line is a fit over the whole lag time range of Eq. 1.32 with κ and ζ_t as free parameters. The fit yields $\kappa = 7.56 \pm 0.08\,\mathrm{\mu N\,m^{-1}}$ and $\zeta_t = 3.49 \pm 0.06\,10^{-8}$ Pa s m.

Equipartition method

Another way to compute the trap stiffness from a particle trajectory is to use the equipartition theorem. The equipartition theorem states that the energy associated to any degree of freedom contributing quadratically to the energy has an average of $\frac{1}{2}k_BT$ at thermal equilibrium. In the case of a particle in a harmonic potential, along one dimension, we have:

$$\frac{1}{2}k_BT = \frac{1}{2}\kappa_i \left\langle x^2 \right\rangle_{eq} \tag{2.3}$$

where $\langle x^2 \rangle$ is the equilibrium statistical variance of the particle position. By measuring the equilibrium variance of a particle position from experimental trajectories at known temperature, the trap stiffness can directly be calculated from $\langle x^2 \rangle_{eq} = k_BT/\kappa_i$.

It can be easily seen from Eq. 1.31 and 1.32 that for time lags larger that the position relaxation timescale $\Delta t \gg \tau_t$, the mean squared displacement of a particle in a harmonic trap is simply twice the equilibrium position variance such that $\mathrm{MSD}(\Delta t)_{\Delta t \gg \tau_t} = 2\left\langle x^2 \right\rangle_{eq} = 2k_BT/\kappa_i$. The plateau value of the experimental MSD therefore directly yields the trapping stiffness. We show in Figure 2.4 a typical log-log one-dimensional MSD plot. The black dashed line stands for the plateau value used for calibration and the red dashed curve is the fit with Eq. 1.32 showing good agreement. The slight mismatch between the fit and experimental data at very short times is a signature of error on the position determination of the particle and will be discussed in greater details in Section 2.5.2. Still, both the plateau value and the full MSD fit yield the same value for the trapping stiffness $\kappa = 7.56 \pm 0.08\,\mu\mathrm{N\,m^{-1}}$, but the full fit with Eq. 1.32 provides dynamical information on the system before relaxation to the equilibrium distribution, and in particular on the translational friction ζ_t.

Power spectral density method

The third method used in this work to calibrate the optical tweezers relies on the computation of the power spectral density (PSD), defined and derived in Section 1.3.3. Analyzing the particle position fluctuations in frequency space was shown to allow the most precise calibration of optical traps [98] (less than 1% for weak trapping forces). The comparatively more accurate estimation of the trapping stiffness using the PSD is especially pronounced when the acquisition and amplification devices or tracking procedures (e.g. photodiode, camera) introduce artefacts such as electrical noise or pixel noise. Such contributions are usually present at high frequencies and can be ignored in the case of a frequency measurement such as the PSD, whereas they will artificially increase the variance of the measured signal. This increased variance will lead to artificially lower values of the trapping stiffness calculated by simple computation of the variance of the particle position time series.

In Figure 2.5, we plot the PSD for the same trajectory as in Figures 2.3 and 2.4 together with the fit using Eq. 1.38 with kappa and ζ_t as fitting parameters. The fit yields $\kappa = 7.36 \pm 0.04\,\mu\mathrm{N\,m^{-1}}$.

To conclude, we showed that the three methods relying on different principles yield very close values for κ ($7.31 \pm 0.08\,\mu\mathrm{N\,m^{-1}}$, $7.56 \pm 0.08\,\mu\mathrm{N\,m^{-1}}$ and $7.36 \pm 0.04\,\mu\mathrm{N\,m^{-1}}$) for a representative trajectory, which makes them all three suitable for calibration of the optical trap. The model-free reconstruction of the potential allows to check the harmonicity of the trap and to visualize its spatial extension, and the subsequent quadratic fit allows a robust time-independent measurement of κ as a unique fit parameter. Computing the MSD allows to extract the equilibrium variance from the plateau value, or using a model (Eq. 1.32), to fit the whole curve. The PSD allows interpretation in frequency space and to get rid of potential artifacts at precise frequencies. Note that for both PSD and MSD fits, the translational friction coefficient ζ_t was left as a free parameter, providing a direct measurement of ζ_t. In order to achieve the most precise quantification of κ, ζ_t could be fixed using Stokes relation

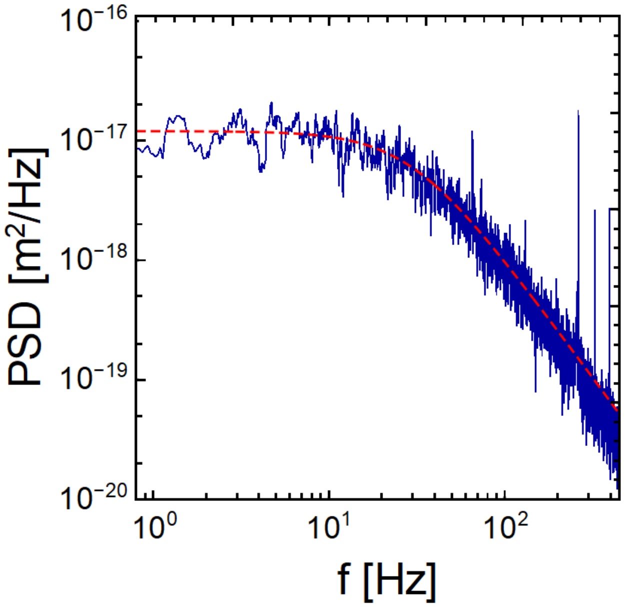

Figure 2.5: Power spectral density calculated from the same trajectory as the one in Figures 2.3 and 2.4. The fit yields $\kappa = 7.36 \pm 0.04\,\mu\mathrm{N\,m^{-1}}$ and $\zeta_t = 3.96 \pm 0.05\,10^{-8}$ Pa s m.

and knowing the particle R_P and surrounding fluid viscosity η. However, the friction is also dependent on the proximity of other interfaces (e.g. the sample cell subsrtate), and to allow the calibration to be independent on the position where it was performed in the sample, we let ζ_t as a free parameter.

For force measurements, these calibration methods are therefore complementary and unless otherwise stated, the trap stiffnesses used for each force measurement reported in the following chapters were calculated by averaging the κ extracted from the three methods. For the trajectory reported here, this leads to an average value $\kappa = 7.42 \pm 0.14\,\mu\mathrm{N\,m^{-1}}$ where the uncertainty accounts for the standard deviation.

Measurement of the friction coefficient ζ_t

We previously discussed the procedure allowing to extract the trapping stiffness κ from experimental trajectories. We showed that fitting the dynamical observables MSD and PSD provides a direct measurement of translational friction ζ_t, if it is left as a fitting parameter. For the case reported above, we measured ζ_t=3.49±0.06 10^{-8} Pa s m and ζ_t=3.96±0.05 10^{-8} Pa s m for the MSD and PSD method, respectively. As the measurements were performed in pure water with a $R_P = 1.93\,\mu\mathrm{m}$ SiO_2 particle far from any interface, we expect the measured translational friction to be close to the one predicted by Stokes' law $\zeta_{t,b} = 6\pi\eta R_P$ $= 3.64\ 10^{-8}$ Pa s m, which is the case.

Note that upon interaction with an interface or any other object, not only the friction felt by the particle but also the trapping stiffness might vary. One should then relax the constraint on κ to have an accurate measurement of ζ_t, while checking that the obtained value for κ agrees with the value obtained with the static approach (quadratic potential fitting procedure).

2.2 Micropipette aspiration technique

A micropipette is a powerful tool allowing to apply a suction pressure at the microscopic scale. Some of the first mechanical measurements on cell membranes and lipid bilayers were made using this technique. Applying aspiration pressures to a giant unilamellar vesicle involves several physical mechanisms, which allows to probe intrinsic membrane properties and access quantities such as the bending modulus κ_b and the stretching (or compressibility) modulus K_A (see Section 1.1.2). In this thesis, the micropipette will mostly be used in combination with optical tweezers in order to apply a mechanical stress on the giant vesicles. In this section, we will first briefly describe the material used, the fabrication procedures and the implementation of the hydrostatic pressure. In a second part, we will introduce the theoretical framework necessary to relate the micropipette aspiration pressure to properties of the system. Finally, we present an example of bending modulus measurement on a POPC vesicle.

2.2.1 Micropipette fabrication process

The fabrication of a micropipette involves the pulling of a heated glass capillary followed by a so-called *microforging* process in order to obtain a cylindrical and clean micropipette, with the desired inner diameter. In the following, the fabrication steps will be briefly described (details on the procedure can be found in Appendix 8.1).

Micropipette pulling

The capillaries used are borosilicate glass capillaries of inner diameter 0.78 or 0.58 mm and 1 mm outer diameter (Ref. GC100-10 Harvard Apparatus). The machine used to heat the capillary locally by means of a heating filament and subsequently pulling both ends of the capillary is the Sutter Instruments Co. P-97 Pipette Puller. This machine has many parameters the user can modify in order to obtain the desired micropipette shape. These are described in details in Appendix 8.1 For manipulation and mechanical characterization of GUVs, the aim is to end up with a cylindrical tip with around 5 microns inner diameter. Note that both thick and thin-walled capillaries can be used but they will need different parameters on the pulling machine to obtain the desired shape. The thick-walled capillaries (0.58 mm inner and 1 mm outer diameter) are however expected to be more robust regarding the microforging step and will less likely break in an unexpected way. They will therefore be used in all the experiments in this work.

If the pipette puller was not used for a long time, a RAMP test has to be performed in order to determine the HEAT value of the machine at which the glass capillary starts to melt locally (turn on the machine, choose any program, press clear an choose “NO” to access function, then press 1 to start a ramp test, of course a glass capillary must be in place when launching). This RAMP test heat value will be the basis to then tune the HEAT parameter.

Once the capillary was pulled, one ends up with two raw micropipettes (each one being one half of the initial capillary). These micropipettes have to undergo microforge manipulation in order to make sure the inner diameter is the good one, that the micropipette is cut perfectly straight, and that the tip is cylindrical (the fact that the pipette is nicely cylindrical is determined by the pulling step and cannot be adjusted in the microforge step).

Microforging

In order to cut the pulled pipettes, we use a homemade microforge designed by A. Schroder. The setup consists in a tungsten filament on which we deposit some powder of Sodium Tetraborate Decahydrate, with a micropipette holder allowing to hold the previously pulled raw micropipette. Micrometric screws allow to move the pipette around and bring it in contact with the filament. This setup is associated with a protected microscope objective Nikon 40x with large working distance and a BW Sony camera allowing to image the manipulation on a screen. The filament is plugged to a tuneable current delivering source, and one can heat it and melt the Sodium Tetraborate Decahydrate. The objective should be protected in order to avoid any damage on it arising from heating of the filament nearby.

When bringing the pipette in contact with the heated filament, one can shorten the pipette down to the desired inner diameter by melting the pipette glass on the filament, provided that the filament is hot enough. If the temperature of the filament is decreased (by lowering the current applied), when bringing the pipette in contact, the melted powder will capillarily rise in the micropipette. If the current source is suddenly switched off at a certain point, the system will cool down which will lead to the spontaneous straight breaking of the pipette at the level where the melted powder rose (at the meniscus). This procedure should result in the clean cutting of the micropipette edge at the desired inner diameter suitable for GUVs manipulation. Note that the pipette should be as cylindrical as possible.

2.2.2 Theory of fluctuations excess area and aspiration experiment

Lipid bilayers in a fluid phase possess low bending modulii typically of the order of 10-30 k_BT [9]. GUVs made of such a fluid bilayer in the absence of stress are therefore easily deformable objects which can exhibit large fluctuations. While the large wavelength fluctuations modes are observable by optical imaging, fluctuations with wavelengths comparable or smaller than the optical resolution can not be resolved. Hence, the projection of the observed apparent area A_{app} is smaller than the real area A. With constant vesicle volume, a reasonable assumption given that the suction pressures applied are typically several orders of magnitude below the osmotic pressures needed for water to cross the membrane within the experimental timescale, it was shown that aspiration experiments can be conducted in two distinct regimes. In the first regime, for small suction pressures, the volume as well as membrane real area A are constant and the observed apparent area increase is imputed to the work necessary to suppress the membrane thermally excited undulations. The apparent area increase associated to an increase in applied tension in this regime is therefore dictated by a competition between the entropic cost to suppress thermal fluctuations and bending energy. For higher suction pressures, one enters in a regime where all of the membrane excess area hidden in the fluctuations were suppressed, and the apparent area increase is imputed to a proper in-plane stretching of the vesicle membrane with a mean inter-lipid distance larger than the equilibrium one. In this regime, one directly probes the membrane stretching modulus K_A (compressibility modulus).

In the classical representation of Monge (valid for small fluctuations amplitudes), where $u(x, y)$ is the membrane position compared to a reference plane, it was shown that the average fluctuations amplitude $\langle|u(q)|^2\rangle$ of a Fourier mode q reads [17]:

$$\langle|u(q)|^2\rangle = \frac{k_B T}{\sigma q^2 + \kappa_b q^4} \tag{2.4}$$

For each fluctuation mode q there exists an associated surface excess $\alpha_q = \Delta A / A_q$. The total surface excess due to fluctuations can therefore be obtained by integrating Equation 2.4. This integral simplifies to [17]:

$$\alpha = \frac{A - A_P}{A_P} = \frac{k_B T}{8\pi\kappa_b} \ln\frac{\sigma_{max}}{\sigma}, \tag{2.5}$$

where A_P is the projected or *apparent* area, and under the assumption that $\sigma_{min} \ll \sigma \ll \sigma_{max}$, where $\sigma_{min} = \kappa_b \pi^2 / L^2$ is a lower bound with L the lengthscale associated to the vesicle size and $\sigma_{max} = \kappa_b \pi^2 / a^2$ where a is a microscopic cut-off. This condition is respected in most relevant cases with $\kappa_b = 10 - 30\ k_B T$, $L \sim 10\,\mu\text{m}$ and $a \approx 5 - 10$ nm.

Since the real area A of the vesicle membrane is not accessible experimentally, Evans *et.*

al. [14] expressed the relative increment of apparent area $\Delta\alpha$ as a function of the suction pressure, and in turn tension, compared to a reference state. This reference state is usually chosen at the minimal pressure at which a tongue of length L_0 can be aspirated in the micropipette and has a tension σ_0. It can be easily shown that $\Delta\alpha$ is related to the tension increase from a reference state as follows:

$$\Delta\alpha = \frac{k_B T}{8\pi\kappa_b} \ln \frac{\sigma}{\sigma_{L_0}} + \frac{\sigma - \sigma_{L_0}}{K_A}. \tag{2.6}$$

Typical experiments performed on giant vesicles consist in measuring the apparent area increase with respect to a reference state $\Delta\alpha$ (thanks to image analysis of optical microscopy acquisitions) corresponding to different membrane tensions induced by varying the aspiration suction pressure $\Delta P = P_o - P_i$, with P_o the pressure outside the vesicle and P_i the pressure in the micropipette. Then, one can fit the experimental σ versus $\Delta\alpha$ data using 2.6 and extract κ_b and K_A for a given vesicle.

2.2.3 Experimental procedure and bending rigidity measurement on a POPC bilayer

In our experimental setup, the suction pressure P_i inside the pipette is applied using an hydrostatic device. The latter consists in a water tank connected to the micropipette. The height relatively to the sample in which the micropipette is immersed Δh can be adjusted with a precision of the order of tens of microns by a micrometric screw. A picture of the setup that was mounted in combination with the optical tweezers setup is shown in Figure 2.1. The pressure difference ΔP induced by the device therefore simply reads $\Delta P = \rho g \Delta h$. The pressure difference $\Delta P = P_o - P_i$ is in turn related to the membrane tension σ by the applying the Laplace law twice such that:

$$\begin{aligned} P - P_o &= \frac{2\sigma}{R_{ve}}, \\ P - P_i &= \frac{2\sigma}{R_{pip}}, \\ \sigma &= \frac{\Delta P R_{pip}}{2\left(1 - \frac{R_{pip}}{R_{ve}}\right)}, \end{aligned} \tag{2.7}$$

where P is the pressure inside the vesicle, R_{pip} the radius of the spherical cap membrane segment in the micropipette and R_{ve} the vesicle radius. Experimentally, we therefore control the membrane tension simply by varying the water tank height. In a typical experiment, one varies the tank height stepwise and waits for at least 5 min at each step for equilibrium to be reached. Simultaneous bright field microscopy acquisition allows to monitor the vesicle apparent shape changes $\Delta\alpha$, fully characterized by R_{ve}, R_{pip} and $\Delta L = L - L_0$ (defined in Figure 2.6) as:

$$\Delta\alpha = \frac{\Delta L}{2R_{pip}} \left(\left(\frac{R_{pip}}{R_{ve}} \right)^2 - \left(\frac{R_{pip}}{R_{ve}} \right)^3 \right). \tag{2.8}$$

In Figure 2.6, we show results of an experiment performed in the low tension regime ($\sigma < 10^4$ N.m^{-1}) yielding the bending modulus κ_b of a POPC vesicle. By choosing a reference state with tension σ_0 and apparent area A_0, we plot $\ln(\sigma)$ as a function of the relative apparent area increase $\Delta\alpha$, and a linear fit yields $\kappa_b = 11.6 \pm 0.9\ k_BT$ following the logarithmic term (first term) in Equation 2.8 (the linear term is dropped in this low tension regime).

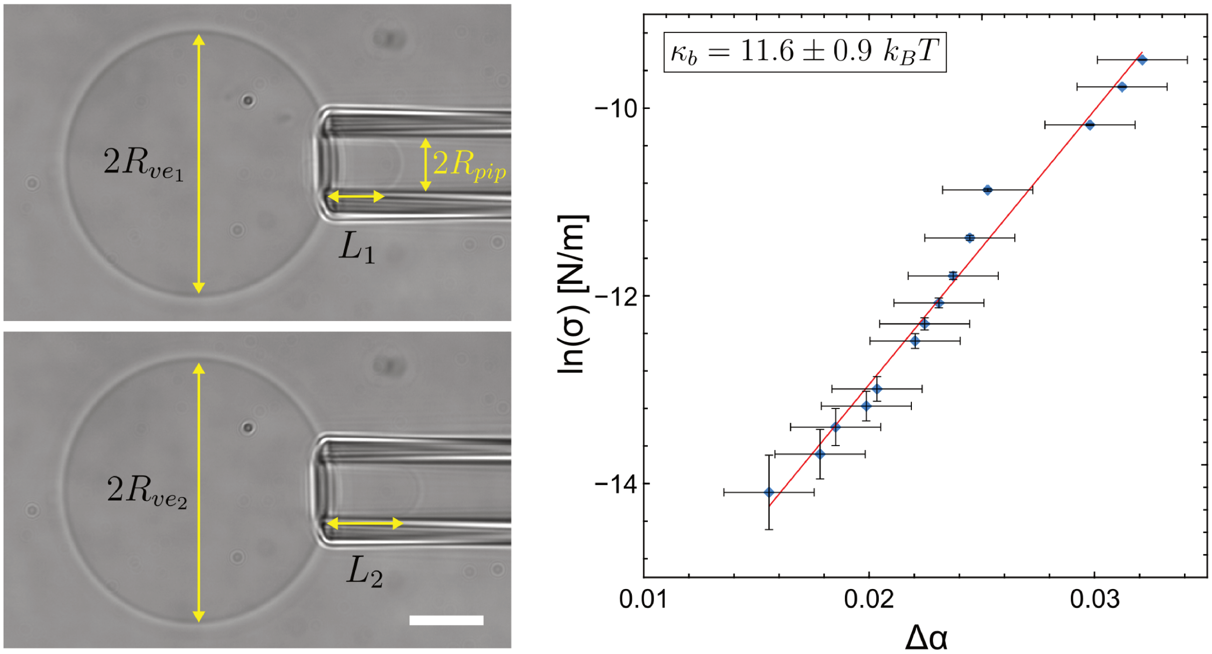

Figure 2.6: Aspiration experiment on a POPC giant vesicle for bending modulus κ_b measurement. Left panel shows bright field microscopy images at two different suction pressures ΔP, with definition of R_{ve}, R_{pip} and L. Scale bar is 5 µm. Right panel shows the associated $\ln(\sigma)$ as a function of $\Delta\alpha$ plot. The slope of a linear fit directly yields $\kappa_b = 11.6 \pm 0.9\ k_BT$.

The bending rigidity κ_b measured is in accordance with the literature for POPC vesicles in sugar solutions, which are known to reduce the value measured with a micropipette aspiration technique [28].

2.3 Lipids and giant unilamellar vesicles formation

Dried lipid stacks, once hydrated, spontaneously form structures in water, including giant vesicles. However, the large variety of structures formed upon simple hydration of a solid substrate on which lipids were previously dried makes it an inefficient method to fabricate giant unilamellar vesicles with high yield and low size polydispersity. Several methods have therefore been developed during the last decades to optimize the yield, typically involving electric fields or microfluidic devices [99, 100, 101]. The technique mostly used in this work is called gel-assisted swelling method and will described below.

2.3.1 Lipids

Two main phospholipids are used in this work which are POPC (1-palmitoyl-2-oleoyl-sn-glycero-3-phosphocholine) and DOPC (1,2-dioleoyl-sn-glycero-3-phosphocholine). Their main properties are described in the Table below.

Lipid	Complete name	Mw (g/mol)	T$_m$ (°C)
POPC (16:0-18:1)	1-palmitoyl-2-oleoyl-sn-glycero-3-phosphocholine	759.6	-3.5
DOPC (18:1)	1,2-dioleoyl-sn-glycero-3-phosphocholine	785.6	-17

Both POPC and DOPC have a melting temperature below 0°C, meaning that the lipids are in a fluid state for any experiment carried out at room temperature. This represents an important criterion both for the successful GUV formation and regarding the role of fluidity in remodelling processes which will be investigated in this thesis. As seen from their chemical structure shown in Figure 2.7, both these lipids share the same polar headgroup (phosphatidylcholine), while they differ in fatty acid chains length and unsaturations.

All the lipids used in this thesis were purchased from Avanti Polar Lipids and were received dissolved in chloroform at a concentration of 10 mg/mL. Such stock solutions were stored at -25°C and used during up to six months for experiments. Note that unless otherwise stated, all of the lipid preparations contain 1% of modified lipids with a fluorescent molecule (nitrobenzodiazole, or NBD) attached to the head in order to obtain fluorescent

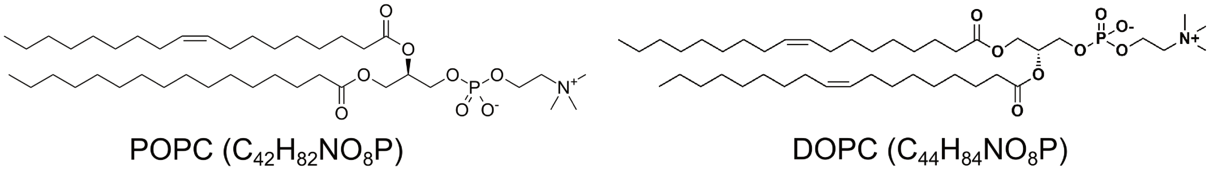

Figure 2.7: Chemical formulae of the POPC *(left)* and DOPC *(right)* lipids used in this work.

vesicles. The full name of the molecule is 1,2-dioleoyl-sn-glycero-3-phosphoethanolamine-N-(7-nitro-2-1,3-benzoxadiazol-4-yl) or (NBD-PE) and has the same fatty acid chains as DOPC (18:1).

2.3.2 Gel swelling fabrication method

The Giant unilamellar vesicles (GUVs) used in this work were prepared using a PVA (Polyvinyl alcohol) gel-assisted formation method [102], schematically depicted in Figure 2.8. First, a PVA gel is prepared by dissolving PVA in pure water (MilliQ water) at 5 % w/v concentration. A polytetrafluoroethylene (PTFE) plate machined to incorporate cylindrical wells, designed in the Mcube team, was used as a robust and chemically inert substrate for gel-

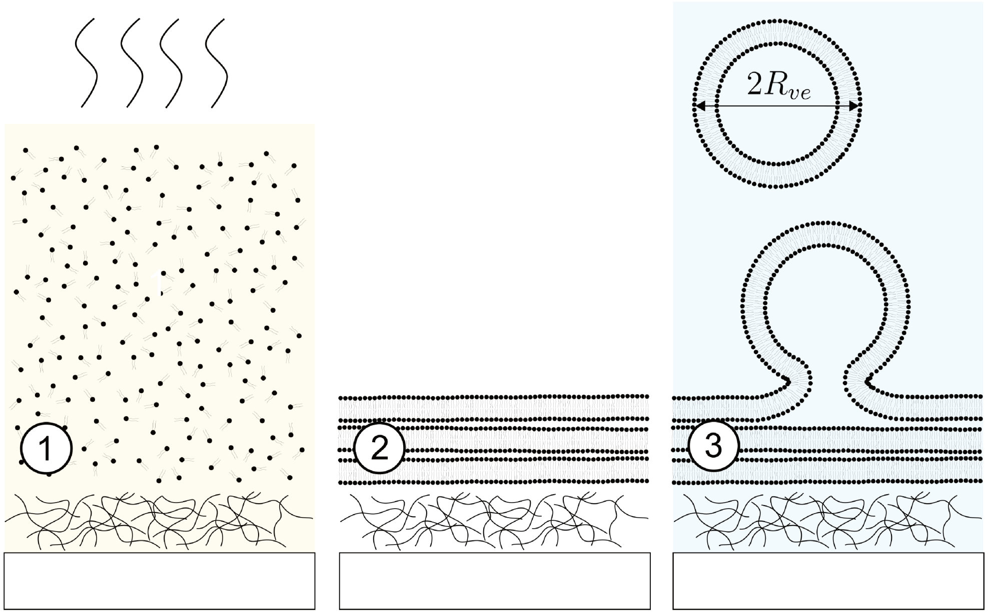

Figure 2.8: Sketch depicting the different steps involved in the fabrication of GUVs using the gel-assisted formation method adapted from [102].

assisted GUV formation. A volume of 200 µL of the prepared PVA gel is uniformly spread at the bottom of a cylindrical well of the PTFE plate and dried for 45 minutes at 80°C in an oven. In the case of POPC/POPC-NBD vesicles, 5 μL of a 99:1 (molar) mixture of POPC (1-Palmitoyl-2-oleoylphosphatidylcholine) and POPC-NBD (POPC fluorescently labelled with Nitrobenzoxadiazole) lipids in chloroform (1 g/L) are spread on the PVA gel and vacuum dried in a desiccator for 15 minutes. This first solvent evaporation stage is represented in (1) (Figure 2.8). The lipids under solvent evaporation spontaneously form stacks of lipid layers supported by the dried PVA gel film as sketched in (2).

This lipid system obtained is then hydrated with 200 μL of sucrose (150 mM) and left undisturbed and sealed (in order to limit water evaporation leading to sucrose concentration increase) for 2-3 hours. During this time, vesicles are allowed to grow as shown in (3), with the PVA acting as a water sink enhancing the hydration rate of the lipid stacks and therefore optimizing the vesicle growth rate and size distribution. The vesicle suspension is then collected and sedimented in 1 mL of glucose (150 mM) solution. The slight density mismatch between the sucrose solution inside the vesicle and the sucrose/glucose solution in the aqueous medium allows the vesicles to sediment both in the collecting tube and at the bottom of the observation cell without strongly deforming the vesicle.

In Figure 2.9 we show a typical epifluorescence microscopy image of a GUV prepared with

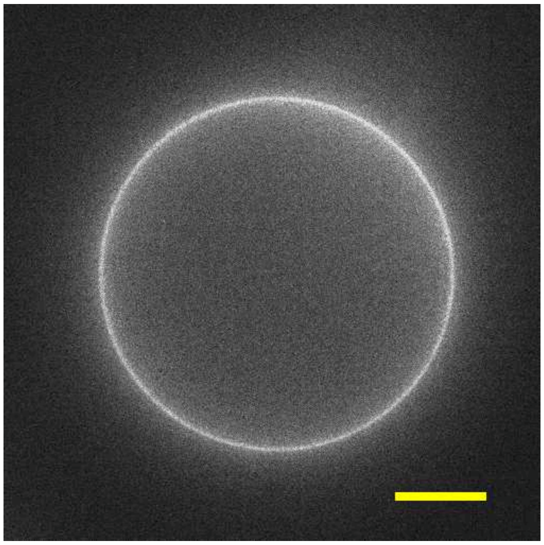

Figure 2.9: Representative epifluorescence microscopy image of a POPC GUV containing 1% NBD-labelled POPC lipids prepared with the PVA gel swelling method in isotonic conditions. The scale bar is 5 µm.

the protocol described right after preparation. Note that the gel swelling method produces vesicles with a rather broad distribution of sizes, with a maximum which depends on the time the vesicles were allowed to grow in the hydration step [102]. Since experiments are performed at the single vesicle level however, the vesicles with desired radius ($10\,\mu\text{m} < R_{ve} < 20\,\mu\text{m}$) can be picked in the sample and size distribution statistics is not of great importance in our case. Note that systematic studies have shown that the PVA gel swelling method allows to obtain vesicles with very similar membrane bending rigidity, capacitance and viscosity as compared to other standard techniques (e.g. electroformation) [103].

2.3.3 Osmotic deflation of initially tense vesicles

Glucose and sucrose molecules are not able to diffuse across the lipid membrane on timescales relevant for our experiments. They therefore act as osmotically active solutes. The outer solution concentration (containing mostly glucose and a few percents of sucrose molecules) relative to the inner sucrose concentration can therefore be tuned to create a slight hypertonicity that will lead to outward solvent (water) fluxes across the membrane over the course of time. The volume of fluid enclosed by the vesicles therefore diminishes as the vesicle ”deflates” with its area remaining constant. This leads to less constraints on the membrane, and therefore lower membrane tension, as the long wavelengths thermal undulations of the membranes become visible under the microscope, as seen on the confocal microscopy images in Figure 2.10.

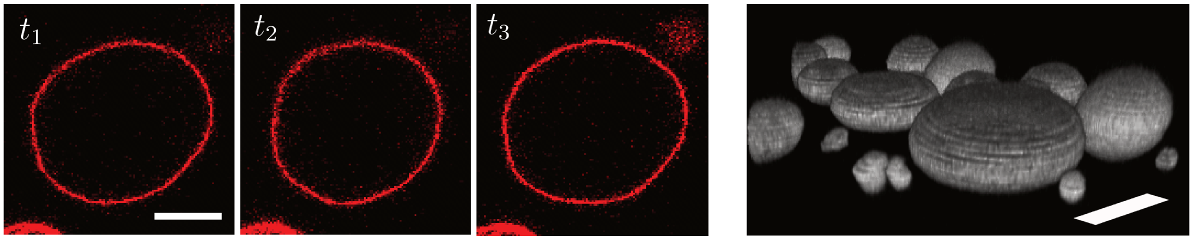

Figure 2.10: *(left)* Confocal microscopy of a deflated GUV in the equatorial plane with low tension showing large thermal undulations. 2 seconds are elapsed between t_1 and t_3. *(right)* 3D reconstruction of a confocal fluorescence microscopy scan of osmotically deflated POPC GUVs sedimented on a glass substrate. The non-spherical shape of the vesicles can be attributed to the deformations induced by gravitational forces acting on the vesicle due to the density mismatch between the inner and outer aqueous solutions.

In order to obtain deflated vesicles, one disperses a volume $V_{GUV} \approx 1 - 2\,\mu\text{L}$ of concentrated vesicle solution in an observation cell containing a volume $V_{sol} = 180\,\mu\text{L}$ of matching concentration glucose solution and let the sample open for the solvent to evaporate. Over the course of time, the evaporation of water will drive the osmotic imbalance and slowly deflate the vesicles. This method gives the opportunity to visually follow under the microscope the evolution of the vesicle and the appearence of large thermal fluctuations as a signature of low tension vesicles. After ~ 1 hour, the sample is sealed to stop the evaporation and experiments can be performed. One can calculate that given the geometry of our sample, and considering reasonable values for the relative humidity, air and sample temperature, etc. the evaporation rate of water is of the order of $\sim 5\,\mu\mathrm{L\,h^{-1}}$. This corresponds for a 5% concentration increase per hour for a sample with initial volume $V \approx 180\,\mu\mathrm{L}$.

2.3.4 Internal structures in floppy vesicles

We showed previously that osmotic deflation induces an increase of the surface-to-volume ratio and excess membrane area that can lead to larger amplitude fluctuations of the large wavelength membrane fluctuation modes. However, when looking closely at the vesicles in fluorescence microscopy, it appears immediately that in fact only a small proportion of vesicles behave as shown in Figure 2.10 *(left)*. Indeed, most vesicles show a large variety of structures such as buds, tubes of various sizes and shapes, as shown in the epifluorescence microscopy image in Figure 2.11 *(left)*. Note that most of these structures are inward structures. On the right (Figure 2.11 *(right)*), we show the variability in the apparent curvature of the structures, going from no structure (top) to highly curved tubular structures with curvature radii close to the resolution limit of the optical microscope ($R_t < 1\,\mu\mathrm{m}$ bottom).

These observations can be put in perspective with recent works which consider that these structures are a direct consequence of the existence of a membrane spontaneous curvature $m \neq 0$ [12, 19, 21]. Indeed, it may seem intuitive that when reducing the volume enclosed by the vesicle, the tension of the membrane becomes small enough that the membrane would preferentially form structures with mean curvature M closer to m to reduce the bending energy of the system. Following this reasoning, assuming the spontaneous curvature is homogeneous, a vesicle with $m > 0$ would form outward-pointing structures, while vesicles with $m < 0$ would form inward pointing structures with $M < 0$. In our system, the vast majority of structures pointing inwards with $M < 0$ can then be interpreted as the signature of a negative spontaneous curvature $m < 0$. Furthermore, the curvature of the formed structures in a same batch of deflated lipids show a large variability, going from no structures (top in Figure 2.11 (right)), to strongly curved inward tubes with curvature radii $< 1\,\mu\mathrm{m}$ (bottom), with all the intermediate structures with radii of the order of few microns (middle). In

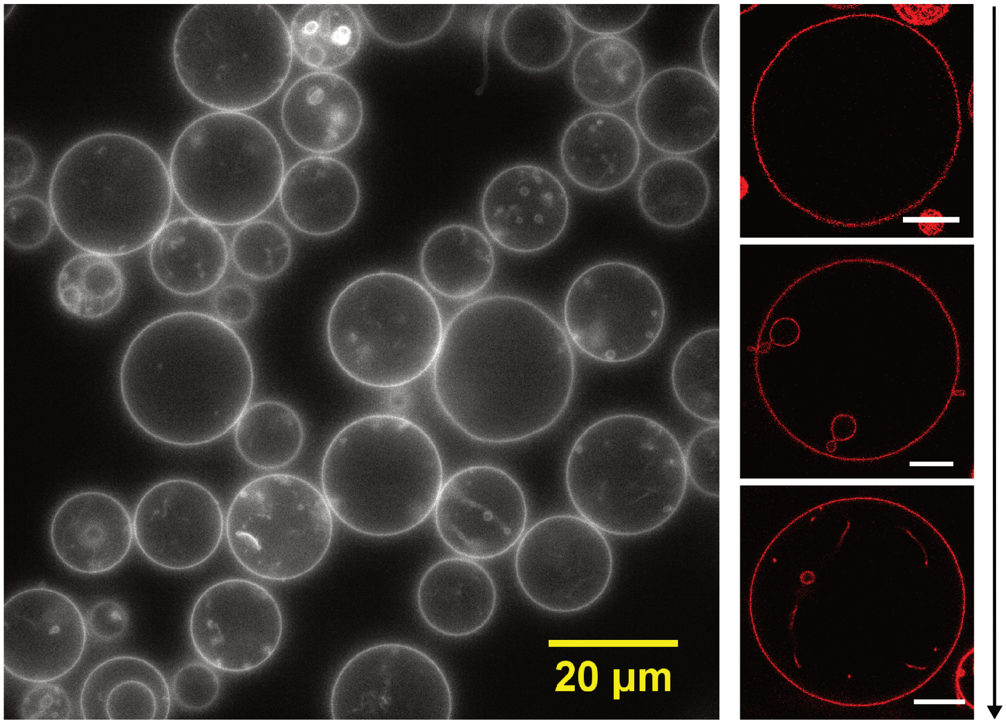

Figure 2.11: *(left)* Epifluorescence microscopy image of concentrated POPC giant unilamellar vesicles after osmotic deflation upon evaporation of the sample during 30 minutes. The vesicles show many internal structures of various sizes and shapes. *(right)* Representative confocal microscopy snapshots in the equatorial plane of deflated GUVs showing the variability of curvature of the internal structures in a same batch. The top image shows a GUV with no apparent structure, while below we see spherical bud-like structures with radii of curvature of the order of few microns. The bottom picture shows a GUV with tubular structures with radii $< 1\,\mu\text{m}$. Scale bars on the right are $5\,\mu\text{m}$

terms of membrane spontaneous curvature, this means that vesicles in a same sample do not possess all the same spontaneous curvature.

The existence of a membrane spontaneous curvature in a system with an asymmetry of sugar species across the bilayer was already reported and described [104, 19, 9]. However, Bhatia et al. [104] reported outward-bulging (suggesting $m > 0$) structures for a similar system with GUVs enclosing 200 mM sucrose aqueous solution and a 200 mM outer glucose concentration. In this work, the lipid composition was slightly different as the GUVs contained 10% cholesterol. Our observation are therefore in strong contradiction with the conclusions drawn in Ref. [104]. These differences can be attributed to the absence of cholesterol in our system, or to the different fabrication method employed. The gel-assisted swelling fabrication method we employ (in contrast with the electroformation used in Ref. [104]) involves a gel of polymer with high molecular weight (PVA Mw 145 000, Sigma-Aldrich). Such long chained polymer is used to avoid the transfer of polymers on the fabricated GUVs upon swelling, and no trace of polymers can be effectively seen by fluorescent labelling of the gel [102]. However, it could be suspected that a very tiny fraction of polymer are adsorbed on the bottom leaflet of the supported lipid stacks during swelling or in solution which results in PVA enclosed in the vesicles. The coupling between an adsorbed polymer and membrane configurations is not trivial and depending on the flexibility and degree of adsorption of the polymer might lead to a local spontaneous curvature of both signs [105, 106].

2.4 Colloidal particles

2.4.1 Isotropic particles

The particles used in this work are spherical non-porous Silica (SiO_2), Melamine formaldehyde (MF) and Polystyrene (PS) particles, all purchased from microParticles GmbH. Partcles with different radii for each material with $0.49\,\mu\text{m} < R_P < 2.5\,\mu\text{m}$ were used throughout the thesis. The manufacturer guarantees high size monodispersity (coefficient of variation $CV < 5\%$) and provides the following informations:

Material	Density [g.cm^{-3}]	Refractive index	Hydrophilicity
Silica	1.85	1.42	Hydrophilic
MF	1.51	1.68	Hydrophilic
PS	1.05	1.48	Hydrophobic

Zeta potential of the Silica and Melamine formaldehyde particles was measured using Malvern Zetasizer Nano ZS. The zeta potential of Silica particles was measured to be $Z_{\text{Si}} = -75 \pm 5$ mV while the one for MF reads $Z_{\text{MF}} = 25 \pm 6$ mV. Measurements of Zeta potential for Polystyrene particles in water in the literature agree on $-60 < Z_{\text{PS}} < -40$ mV [107, 108, 109].

Diluted particle solutions were prepared from the highly concentrated mother dispersion (5% (w/v) aqueous suspension) by performing a tenfold dilution in a 0.5 mL Eppendorf tube. The particles were subsequently thoroughly cleaned by performing cycles of centrifugation, removal of the supernatant, and redispersion in fresh MilliQ water. This cleaning procedure ensured the removal of potential stabilizing agents. The clean colloidal aqueous dispersions were then stored at 4°C until use. The cleaning procedure was repeated if the storage time exceeded 3 days.

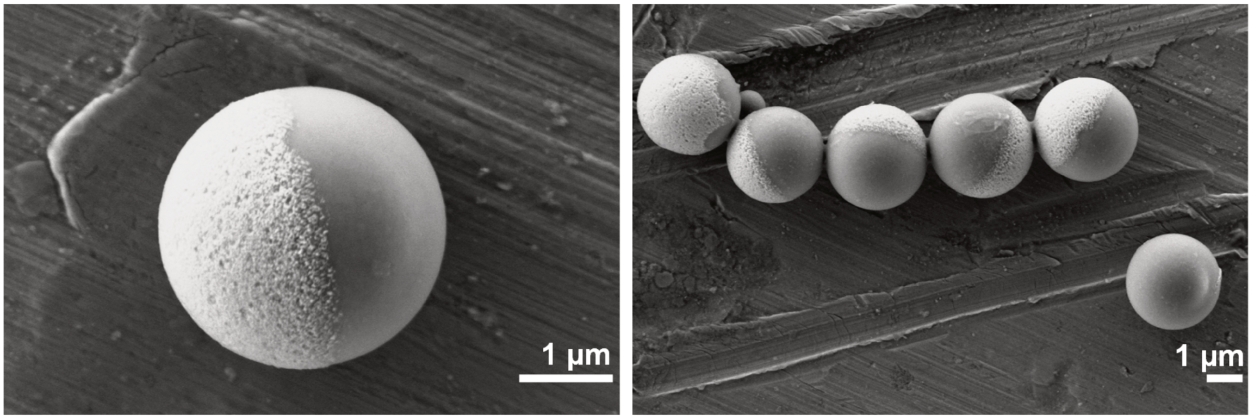

Figure 2.12: Scanning electron microscopy images of the $R_P = 1.5\,\mu\mathrm{m}$ Cu@SiO$_2$ used in this work. The acquisitions were performed by Sharan *et al.* (Simmchen Group TU Dresden). The Figure was reproduced from Ref.[65].

2.4.2 Janus particles

The Janus particles used in this work consist of commercial silica particles with a metallic cap (in our case, made of copper) deposited on them. This fabrication process is widely employed in the active Janus colloids community [110]. The particular Janus particles used in our experiments were fabricated by our collaborators from the group of Juliane Simmchen at Technische Universität Dresden [65, 66].

Briefly, the fabrication process consists in drop casting a diluted solution of commercial SiO$_2$ microspheres of radius $R_P = 1.5\,\mu\mathrm{m}$ (Sigma Aldrich) on a plasma clean glass slide. After evaporation of the solvent (ethanol), a nanometric (30 nm) Cu layer was subsequently thermally deposited on the microspheres monolayer. The half Cu-coated microspheres attached to the glass slide were then immersed in an Eppendorf tube and released in MilliQ water thanks to short ultrasonic pulses to avoid damage of the Cu cap and limit the detachment of Cu from the glass slide. The particles were then cleaned following the cleaning procedure described in Sec. 2.4.1 and stored at 4°C until use.

In bright field microscopy, the Cu@SiO$_2$ Janus particles show a darker hemisphere which stands for the Cu coated hemisphere and a brighter hemisphere standing for the bare SiO$_2$, as shown in Figure 2.13. This is expected due to the difference in refractive index between the two materials. However, signature of this Janus aspect can only be perceived when the plane defined by the Janus boundary is orthogonal to the imaging plane. When the out-of plane orientation is such that the cap points downwards (or upwards), the particles' projection in the imaging plane is just a dark disk, from which no information on the in-plane orientation can be deduced.

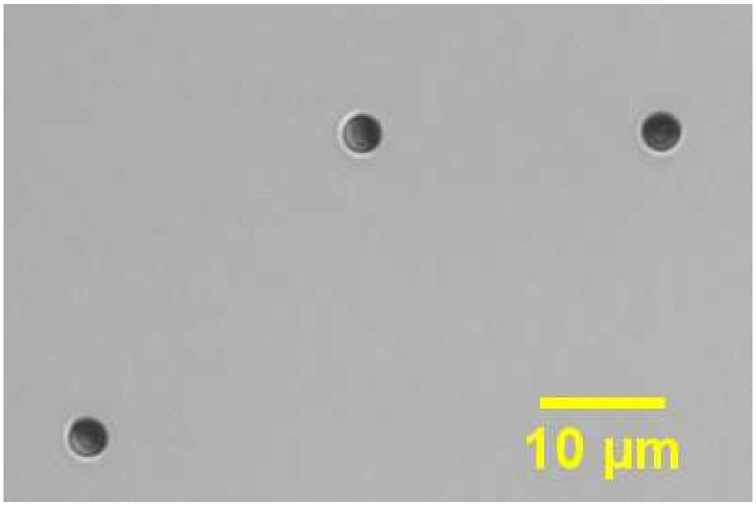

Figure 2.13: Bright field microscopy image of three Cu@SiO$_2$ Janus particles with $R_P = 1.5\,\mu\text{m}$ in 100 mM glucose aqueous solution under 2 mW blue light irradiation before image processing.

2.5 Tracking algorithms

The accuracy of physical quantities extracted from the dynamics of microparticles largely depends on the precision of the position and orientation measurements. Various methods exist for accurately tracking the 3D motion of colloids, such as interferometry [111, 112] or total internal reflection microscopy [113]. However, these methods are often highly sensitive to nearby objects, and therefore inappropriate to study the motion upon interaction with another object, and do not provide direct visualization of the sample. In contrast, optical bright field microscopy acquisitions enable direct visualization of particle positions and interacting objects, making it a powerful tool. Recent advancements in camera resolution and acquisition rates have allowed the observation of phenomena occurring at very short timescales, which was previously unachievable and led to the preference for other techniques in particle tracking. With these acquisition issues resolved, the accuracy of measurements depends on post-acquisition image processing, particularly the tracking.

All the image processing and tracking routines were performed on optical microscopy (bright field if not otherwise stated) acquisitions collected by a Hamamatsu Orca Flash-4 CMOS camera with a x100 Nikon Oil objective mounted on the optical tweezers setup, or

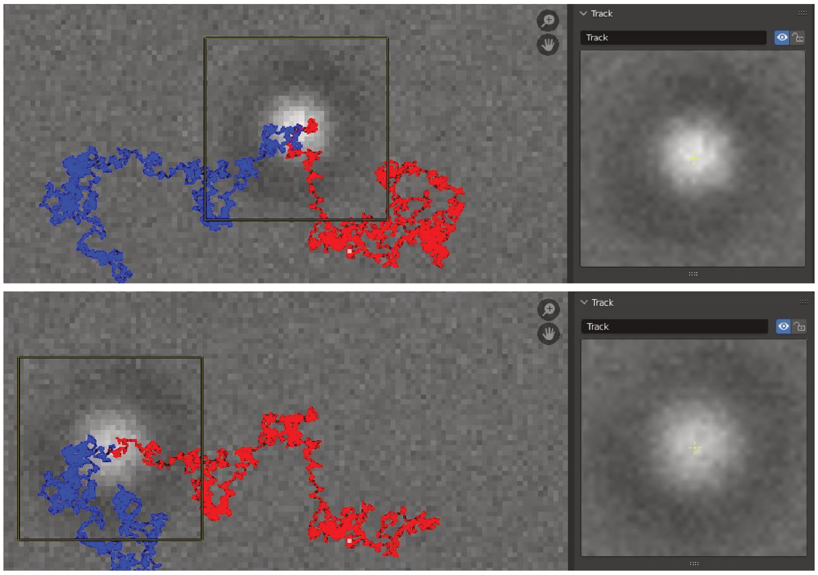

Figure 2.14: Screenshots of the blender feature tracking interface during tracking of a freely diffusing $R_P = 0.49\,\mu\mathrm{m}$ SiO_2 particle acquired a 995 Hz at two different times t_1 (top) and t_2 (bottom) of a trajectory, with $t_1 < t_2$. On the left is the movie with the current tracking frame, with the position of the 2500 previously tracked positions (red) and the 2500 next positions (blue) of the tracked particle. The right box allows to visualize the evolution of the tracked frame centered on the center of mass of the tracked object, and should therefore be the frame of the particle. For accurate tracking, the particle should appear motionless in this box which guarantees that the marker tracks the center of mass of the particle correctly. This is the case for the tracking shown here as the tracking frame remains locked to the particle projected COM over the course of the entire acquisition, and a fortiori for the two times shown here.

with x60 (x40) Nikon water immersion (air) objective for the experiments performed on the commercial Nikon Eclipse TE2000 inverted microscope. In the following the tracking routines used to extract translational and rotational trajectories of isotropic and Janus particles will be described.

2.5.1 Center of mass translational motion tracking

The center of mass (COM) tracking of both isotropic and Janus particles was performed using two complementary techniques, depending on the acquisition content and magnification. The first technique utilizes the motion tracking feature of the open-source software *Blender* (https://www.blender.org/). Blender includes a correlation-based Kanade-Lucas-Tomasi (KLT) feature tracking algorithm that enables controlled and accurate 2D tracking of objects in a video. These algorithms are powerful tools for estimating the optical flow field from sequences with many features and are widely used in fields such as computer vision and robotics. The algorithm comprises two main components: feature detection and feature tracking. For our system, the feature detection algorithm struggles with detecting particles in our bright field microscopy acquisitions. In such cases, the user can manually input the center of mass coordinates of the object to be tracked. Subsequent frames are then analyzed using a combination of a Kalman Filter [114] and optical flow techniques, specifically the Lucas-Kanade method, which calculates the motion of the tracked feature based on the spatial intensity gradient of the image. Briefly, the Lucas-Kanade method determines the optical flow vectors by solving the optical flow equations using a least squares approach [115]. The feature tracking interface in Blender allows to visualize the evolution of the tracking in real time and includes a refinement tool, where features are reassessed and adjusted to minimize drift over long sequences. This ensures control, precision and reliability in tracking particles in microscopy acquisitions, even for particles with changing aspect (e.g. due to oscillations around focus) over the course of time.

2.5.2 Tracking error

There might be an error on the tracked position arising from the tracker, especially for noisy acquisitions due to fast acquisition rate. As a result, the particle position (in one dimension) extracted from tracking $x(t_n)$ at time t_n differs from the real position $x_r(t_n)$ such that [116, 117, 118]

$$x(t_n) = x_r(t_n) + \delta(t_n), \tag{2.9}$$

where $\delta(t_n)$ is a tracking error, which can be as a first approximation modelled as an uncorrelated (white) noise, such that $\langle \delta(t) \rangle = 0$ and $\langle \delta(t_i)\delta(t_j) \rangle = \delta_{ij}\sigma_0^2$, where brackets stand for time average. It follows that if we propagate the position error, we have for the MSD:

$$\begin{aligned}
\left\langle (x(t+\Delta t) - x(t))^2 \right\rangle &= \left\langle (x(t+\Delta t) + \delta(t+\Delta t) - x(t) - \delta(t))^2 \right\rangle && (2.10)\\
&= \left\langle (x_r(t+\Delta t) - x_r(t) + \delta(t+\Delta t) - \delta(t))^2 \right\rangle && (2.11)\\
&= \left\langle (x_r(t+\Delta t) - x_r(t))^2 \right\rangle + \left\langle \delta(t+\Delta t) - \delta(t))^2 \right\rangle && (2.12)\\
&= \left\langle (x_r(t+\Delta t) - x_r(t))^2 \right\rangle + 2\sigma_0^2. && (2.13)
\end{aligned}$$

This means that tracking errors (or any uncorrelated error on the position determination) leads to an overestimation of the mean squared displacement, which is however only relevant on very short timescales, when $\langle (x_r(t+\Delta t) - x_r(t))^2 \rangle \approx 2\sigma_0^2$. Similarly, position power spectral density might also carry the signature of tracking errors and noise at high frequency. In many cases throughout this work, e.g. for calibration of the optical trap, such small deviations are of no concern because other sources of error are dominant. However, for precise friction measurements, the fact that MSD fitting is done on short timescales where tracking errors could play a role makes the PSD a preferable observable, as the fit is done over the whole spectrum.

2.5.3 Rotational motion tracking of Janus particles

The anisotropic surface composition of Janus particles causes orientation-dependent attenuation of transmitted light to the camera, resulting in a varying appearance of the particle based on its orientation. This characteristic enables the monitoring of particle orientation over time in some situations.

In-plane orientation

Tracking of the in-plane orientation (characterized by the angle φ) was performed using a method adapted from previously elaborated methods for fluorescent Platinum coated par-

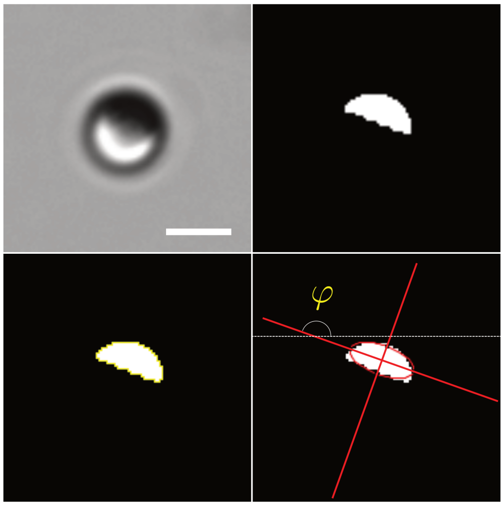

Figure 2.15: Extraction of the in-plane orientation of a Janus particle from a bright field microscopy image *(top left)*. The scale bar is 2 µm. *(top right)* shows the result of the binarization, inversion and filtering of the bright field image. *(bottom left)* In yellow appears the detected contour by the ”Wand” ImageJ tool. *(bottom right)* Ellipse fitting on the detected contour and definition of the in-plane orientation angle φ as the angle between the ellipse long axis and a fixed axis in the lab frame.

ticles [71, 86, 119]. An example for the extraction of φ of Janus particle (Cu@SiO$_2$) from bright field microscopy acquisitions is depicted in Figure 2.15 and will be exposed in the following. Using the image analysis open source software ImageJ (https://imagej.net/), one can threshold the grey scale bright field microscopy image in order to have a binary image with only the copper cap visible (which has lower pixel intensity than the background and the bare hemisphere of the Cu-SiO$_2$ Janus). Doing so, the projection of the copper cap in the imaging plane is isolated and its geometrical parameters can be extracted. In particular, fitting an ellipse to the half-moon shaped cap projection allows to determine the angle between the long axis of the ellipse and a fixed axis on the image. An ImageJ routine allows to repeat this for each frame of a movie, providing an orientation trajectory. The full ImageJ macro code allowing to perform the described operations is given in Appendix 8.2. The associated tracking error is low provided that the particle out-of-plane orientation does not significantly deviates from $\theta = \pi/2$, where θ is the angle between the substrate normal and the normal of the plane containing the Janus boundaries [119].

Out-of-plane orientation

The out-of-plane orientation of the particle can also be estimated from the darker area corresponding to the projection of the Cu metallic cap of Janus particles. Indeed, the projected area of the Cu cap A_{cu} should be related to the out-of-plane orientation of the particle θ as

$$A_{\mathrm{Cu}} = \frac{1}{2}\pi(1 + \cos\theta)R_P^2, \tag{2.14}$$

such that A_{Cu} is maximal for $\theta = 0$ with $A_{\mathrm{Cu}} = \pi R_P^2$, when the particle points downwards and the measured projected area is the disk corresponding to the particle projection. $A_{\mathrm{Cu}} = \pi R_P^2/2$ (half moon) when $\theta = \pi/2$. $A_{\mathrm{Cu}} = 0$ when $\theta = \pi$. Note however that this method is valid for fluorescence microscopy experiments. In transmission bright field experiments, it is not possible to discriminate if the particle is pointing upward or downward, since the projected area appears to be the same if the particle has an out-of-plane orientation θ or $\pi - \theta$.

Chapter 3

Optically driven microparticle interaction with lipid vesicles

3.1 Introduction

Recent approaches using generic physical forces to trigger the wrapping of a passive particle by a giant vesicle rely on depletants to generate effective entropic attractive forces between the membrane and particle surface [77, 79, 80]. In the limit of negligible membrane tensions, Spanke *et al.* have shown that spontaneous particle wrapping by a lipid vesicle can occur above a given depletant concentration (i.e. adhesion) [77]. In the same work, optical tweezers were used as an external energy input to overcome the energy barrier separating a non wrapping and a stable full wrapping state when the adhesion was insufficient for spontaneous adhesion-driven wrapping to occur. The existence of this unexpectedly robust so-called *activated wrapping* regime [77] for vanishing membrane tensions was attributed to the membrane finite mean curvature initially bulging towards the particle [83, 82]. However, while both experimental and theoretical efforts allowed to establish laws for the wrapping/non-wrapping phase diagram boundaries as a function of various physical parameters [82, 20], experimental investigations on the magnitude of the energy barrier height separating two stable wrapping states are very limited. Other energy barriers, such as contributions associated to the shape energy of the unbound (not in contact with the particle) membrane surface area during the wrapping process may exist, preventing spontaneous particle wrapping by the membrane [81, 120, 20].

Two important lengthscales allow to describe the system, namely the bendocapillary length $\lambda_\sigma = \sqrt{\kappa_b/\sigma}$ capturing the competition between membrane bending and tension, and the adhesion length $\lambda_w = \sqrt{2\kappa_b/w}$ describing the competition between bending and adhesion. Experiments reported in Ref. [77] were carried out in a regime governed by the membrane bending, where the particle radius $R_P < \lambda_\sigma$. The energies associated to the membrane tension σ were therefore disregarded and it was concluded that it plays no role in the wrapping behavior. In a regime governed by the membrane tension, $R_P > \lambda_\sigma$ with $\sigma \sim 1\,\mu\mathrm{N\,m^{-1}}$ (negligible bending), fully reversible wrapping of particles by pushing them across a free-standing membrane using optical forces was also observed [121]. Alternatively, optical tweezers were used to force the uptake of a particle [90, 122]. However, the poor optical imaging resolution did not allow to image the local membrane deformations. Here, we investigate a regime where vesicles possess low membrane tensions with $\sigma \sim 10\,\mathrm{nN\,m^{-1}}$ and a typical bending rigidity $\kappa_b \approx 10^{-19}$ J, yielding a bendocapillary length in the range $1\,\mu\mathrm{m} < \lambda_\sigma < 3\,\mu\mathrm{m}$. Hence, membrane deformations induced by particles with radii R_P of the order of a micron lay in a crossover regime, where both tension and bending may significantly contribute to the total energy. In this regime, signature of membrane properties such as spontaneous curvature, can be evidenced and play a crucial role in the forced uptake process, in particular due to its coupling to the membrane tension through the spontaneous tension $\tilde{\sigma} = 2\kappa m^2$.

In the following, I report on experimental investigations on the ability for membranes with low tension to stably wrap a spherical particle in the limit of vanishing particle-membrane adhesion if an external force is provided. We combine force measurements with fluorescence and bright field microscopy to relate the measured forces to the deformation and shape transitions of the membrane induced by the particle. In a first part, we achieve optically driven particle engulfment of non-adhesive particles and describe the influence of relevant physical parameters on the outcome and the measured force profiles. The existence of a stable full wrapping state even for non-adhesive particles owing to the stability of the membrane neck nucleated upon engulfment will be investigated in a second part by coupling the optical tweezers to a micropipette suction experiment. Finally, other phenomena occurring upon deformation of a lipid membrane by an optically trapped particle will be investigated thereby providing additional qualitative insights on the particle-membrane interactions.

3.2 Optically driven particle endocytosis

The encounter between the trapped particle and the vesicle is achieved by imposing a relative motion between the two objects. While the trapped particle position in space is determined by the focused laser beam waist position which remains motionless, the position of the surrounding sample can be adjusted by moving the sample stage. Fine control of the stage displacement and displacement velocity can be achieved thanks to piezoelectric controllers.

3.2.1 Typical deformations and associated force profiles

Imaging the membrane deformations during particle engulfment

In a sample containing a diluted solution of spherical particles and osmotically deflated POPC lipid vesicles one can trap a particle and bring it close to a floppy vesicle using the xyz micrometric screws of the sample stage such that the equators of both objects are contained in a same plane. Then, relative motion at constant speed is imposed using the piezoelectric drivers. The particle comes in contact with the vesicle and starts to deform it as shown by fluorescence microscopy in Figure 3.1 for a relative velocity $v_{rel} = 0.30 \pm 0.02\,\mu\mathrm{m\,s^{-1}}$. Before contact, the vesicle has a small positive mean curvature $M = 1/R_v$ with R_v the initial vesicle radius. Upon contact with the particle, the vesicle deforms and locally adopts a curvature of opposite sign $M = -1/R_P$ with R_P the particle radius. Note that in the early stages of

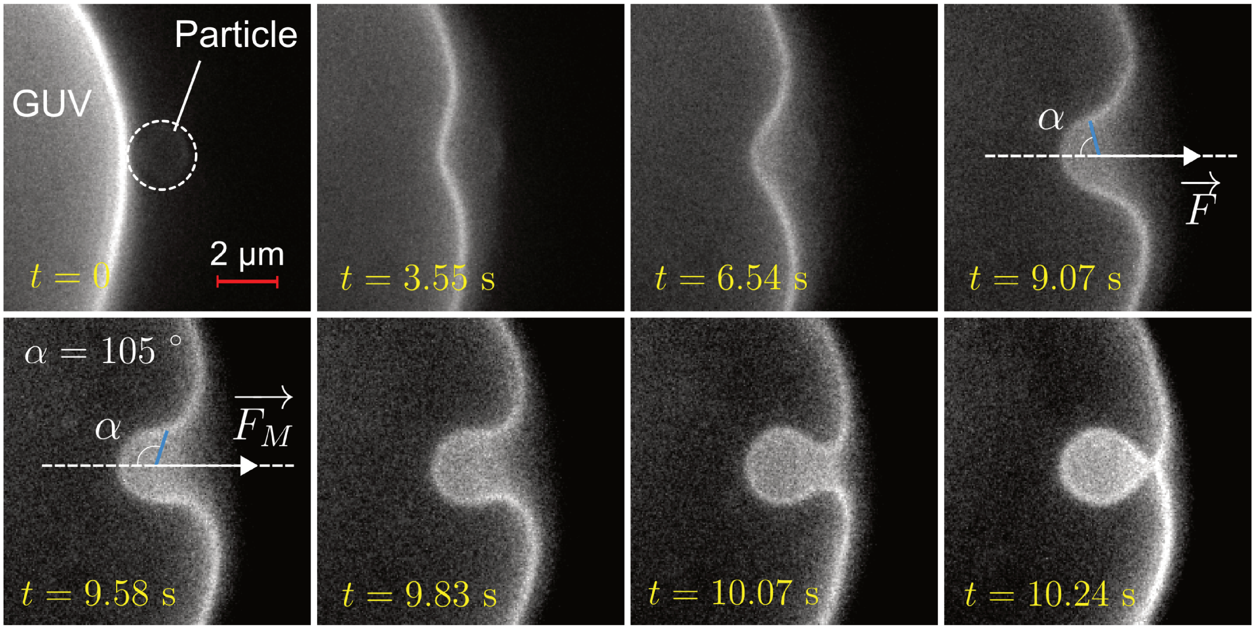

Figure 3.1: Snapshots of a fluorescence microscopy acquisition during which an optically trapped $R_P = 1.15\,\mu\mathrm{m}$ SiO_2 particle deforms and becomes engulfed by a POPC GUV containing 1% NBD fluorescent probes. The relative displacement between the stage and the optical trap is done at velocity $v_{rel} = 0.30 \pm 0.02\,\mu\mathrm{m\,s^{-1}}$. The time stamps allow to notice that the neck closure dynamics happens on a much smaller timescale that the induced deformation, which is a signature of an instability.

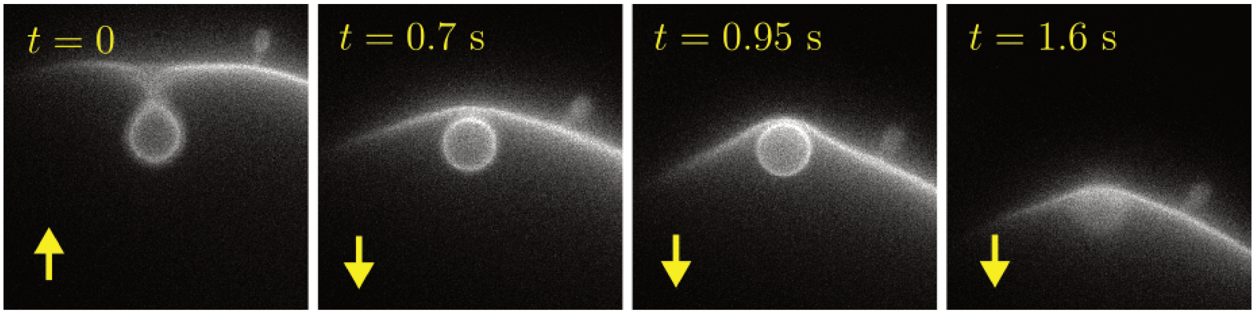

Figure 3.2: Snapshots of a fluorescence microscopy acquisition during which the motion direction of the sample stage (i.e. of the vesicle) relatively to the particle is reversed (starting from the 2^{nd} frame). The yellow arrows show the direction of motion of the sample while the particle remains steady in the trap, except for the last snapshot where the particle is pulled out from the trap by the force exerted by the membrane.

the deformation (corresponding to the top row in Figure 3.1), turning off the optical trap results in the particle being expelled and the vesicle recovering its initial shape. This first reversible process is referred to as the *elastic* deformation.

At some time t_c corresponding to a critical penetration depth d (with corresponding critical wrapping angle $\alpha_c = 105°$ here), the unbound (free) membrane area collapse to form a membrane neck behind the particle. It is important to note the timescales separation between the elastic deformation (top row in Figure 3.1) whose dynamics is dictated by v_{rel}, and the neck closure dynamics (bottom row in Figure 3.1) taking place in a few hundreds of milliseconds, suggesting that it arises from an instability of the free membrane segment with intrinsic dynamics. Once the nucleation of the neck took place, the particle remains wrapped indefinitely when the optical trap is switched off. Additionally, it is impossible to take the particle back out and unwrap it using the same optical force in the opposite direction. This is illustrated in Figure 3.2 where fluorescence microscopy snapshots of an acquisition during which the sample stage motion direction is changed after the neck was formed, resulting in the particle being pulled out from the optical trap due to the force exerted by the membrane. If the trapping force is increased by increasing the laser optical power output, the same experiment results in the whole membrane being dragged by the particle, and re-opening of the neck was never observed.

The pear-like shape of the membrane bud enclosing the particle suggests that the membrane is not adhered to the particle and that some fluid was enclosed together with the particle upon neck closure. This can be interpreted as an additional signature of the instability-driven neck closure dynamics, which also implies that the latter is independent of the particle-membrane interaction and solely dictated by the shape energy of the free membrane segment. Such instability is analogous to first order shape transitions reported in tube pulling assays [123, 124] and reminiscent of shape instabilities reported for deflated vesicles in elongational flows [125, 126, 127]. The geometry can also be seen as a lipid membrane spanning between two parallel axisymmetric rings. Just like for soap films, the shape energy of the membrane leads to two different stable shapes in this case: a catenoid-like shape (for short distances between the two rings) and a small radius cylindrical nanotube (for large distances) [128]. However, it was shown for a suspended membrane between two axisymmetric rings that the transition between these two stable shapes take place in less than a millisecond and is fully reversible [128]. This is not what we observe in the vast majority of cases (see e.g. 3.2) where reversing the motion direction does not lead to reopening of the membrane and release of the particle.

Typical force profiles upon engulfment

Figure 3.3 shows a force profile associated to the forced penetration performed at constant speed. The force is plotted as a function of the time of the experiment, which can be converted into a length (proportional to the penetration depth d) as the experiments are performed at constant speed. The profiles can be decomposed in distinct steps. First, the force oscillates around zero when the particle approaches the GUV. Indeed, the Stokes friction before contact $F_v = 6\pi\eta R_P v_{rel} \approx 0.01$ pN can not be resolved and is therefore negligible in our experiments [121]. The influence of the v_{rel} on the force profiles acquired is discussed in Appendix 8.3. Around $t = 3$ s, the particle touches the GUV and the force grows linearly in time reaching a maximum value F_M corresponding to the end of the *elastic* membrane deformation regime. The sharp drop of the force after the maximum corresponds to the formation of the neck and complete wrapping of the particle. If the optical trap is released when the force drops down to zero, the particle remains stably wrapped by the membrane.

In our experiments, continuing the particle entry inside the GUV leads to the formation of a membrane tube with associated plateau force [129, 130]:

$$F_{tube} = f_{in} = 2\pi\sqrt{2\kappa_b\sigma} + 4\pi\kappa_b m \tag{3.1}$$

(from $t \approx 6$ s to the end), where f_{in} stands for the force needed to pull an inward tube and m a membrane spontaneous curvature. Note that m can be positive or negative, which dictates the contribution of the second term of the right hand side in Eq. 3.1. We focus

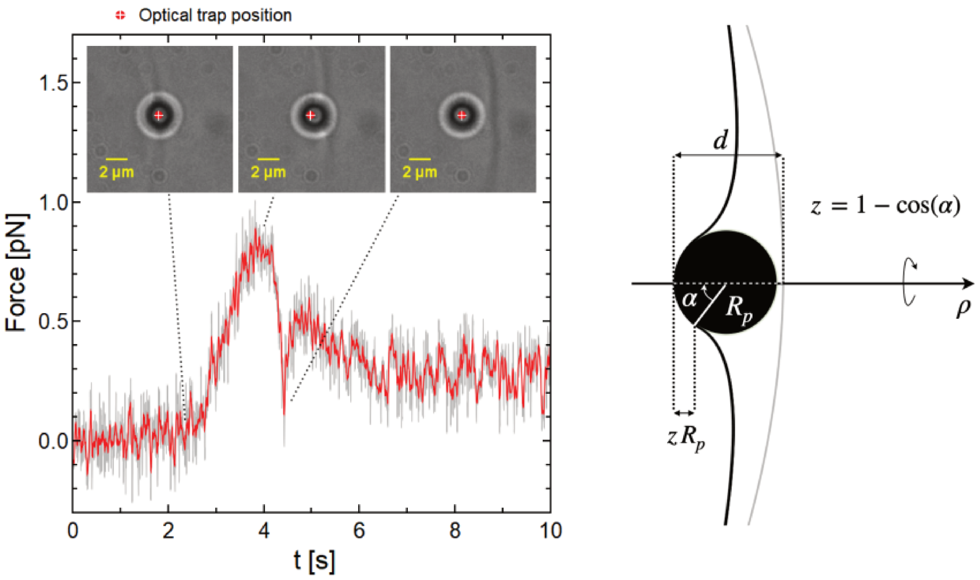

Figure 3.3: *(left)* Typical force profile for an optically trapped $R_P = 1.15\,\mu\mathrm{m}$ particle upon forced wrapping by a POPC GUV at relative motion speed $v_{rel} = 1.88 \pm 0.02\,\mu\mathrm{m\,s^{-1}}$. Bright field microscopy snapshots at key moments are also represented. *(right)* Schematic representation of a spherical particle deforming a vesicle membrane and definition of the wrapping angle α, penetration depth d and penetration degree z.

on the tube force for small penetration depths d. For larger d, the connection of the tube to the mother vesicle might diffuse out of the observation plane. This leads to inaccurate measurement of the tube force as it might have a component along the direction normal to the observation plane. Also, for large d, rich dynamics of the tube can be observed and shape instabilities such as pearling can occur. The force rebound measured after the sharp force drop associated to the wrapping of the particle in Fig 3.3 accounts for the force barrier to go from the stable engulfed state with an ideal neck where membrane and particle are in contact [77] to a state where the fully wrapped particle is connected to the GUV with a tube. This is reminiscent of the situation where a point force is applied to a GUV to form outward tubes in which a force overshoot is measured just before the catenoid-like pulled membrane segment collapses into a tube [123, 131, 132, 133].

3.2.2 Successive entry of particles in a same vesicle and the role of membrane area reservoirs

The maximum force provided by optical trapping during penetration F_M contains information on the energy barrier that has to be overcome to wrap a particle in absence of strong binding [134] and spontaneous wrapping. We start by analyzing how F_M relates to F_{tube} and, in turn, to the membrane properties. To do so, we perform an experiment depicted in Figure 3.4 which consists in successive penetration of $R_P = 1.15\,\mu\text{m}$ SiO_2 particles in the same GUV, thereby conserving all the properties of the system except the membrane area that is consumed by each particle remaining stably wrapped after penetration. Results in Fig 3.5 show two representative force profiles for this experiment and shows the correlated increase of F_M and F_{tube} as well as an increase of the time t_c between contact and neck closure. In this experiment the optical spring constant was fixed, and we were able to engulf up to 6 particles while the 7$^{\text{th}}$ did not enter with the optical forces reachable at this fixed optical power. As explained in the following, these differences reveal the impact of the membrane area reservoir and membrane tension on the energy barrier for wrapping. We postulate that the plateau force F_{tube} depends only on the properties of the membrane and is independent on the particle interaction with the membrane. For the first 3 penetrating particles F_{tube} does not vary, which according to Eq. 3.1 points to a constant tension σ. However, the area consumed by the first 3 penetrating particles does not translate into a measurable decrease of the external spherical area of the vesicle, meaning that the forced wrapping process induces a change of apparent membrane area. In the low tension regime, it is expected that a change of membrane apparent area $\Delta A/A$ induces a membrane tension change $\Delta(\ln \Sigma)$ due to unfolding of the membrane thermal undulations such that [14]:

$$\ln(\Sigma/\Sigma_0) \approx (8\pi\kappa_b/k_BT) \times \Delta A/A. \tag{3.2}$$

Assuming $\Sigma_0 = 10^{-9} - 10^{-10}$ N.m^{-1}, it would lead to $\Delta A/A \approx 10^{-3}$, which is one order of magnitude lower than the expected area change $R_P^2/R_v^2 \approx 10^{-2}$ in our experimental system. This picture of an apparent area increase leading to a tension increase according to Eq. 3.2 therefore fails to interpret our experimental results for the tube force for all the penetrated particles. Indeed, low tension vesicles always show some membrane area reservoirs, stored

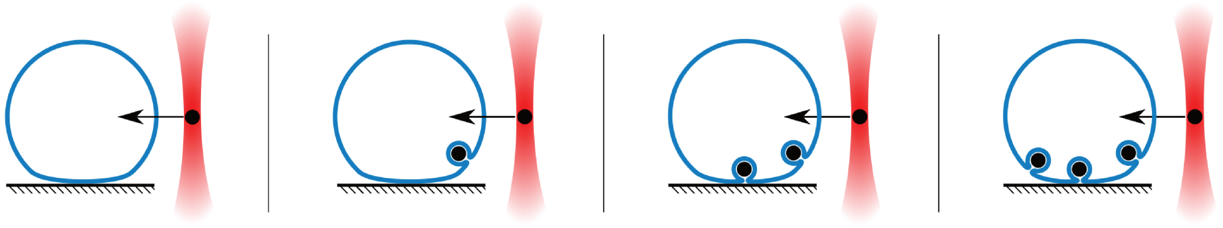

Figure 3.4: Schematic representation of the experiment performed consisting in successive engulfment by optical tweezers of several particles in a same vesicle. Once engulfed with the optical tweezers and released in the intravesicular space, the wrapped particles sediment at the bottom of the vesicle while remaining wrapped and connected to the vesicle with a membrane neck or tube.

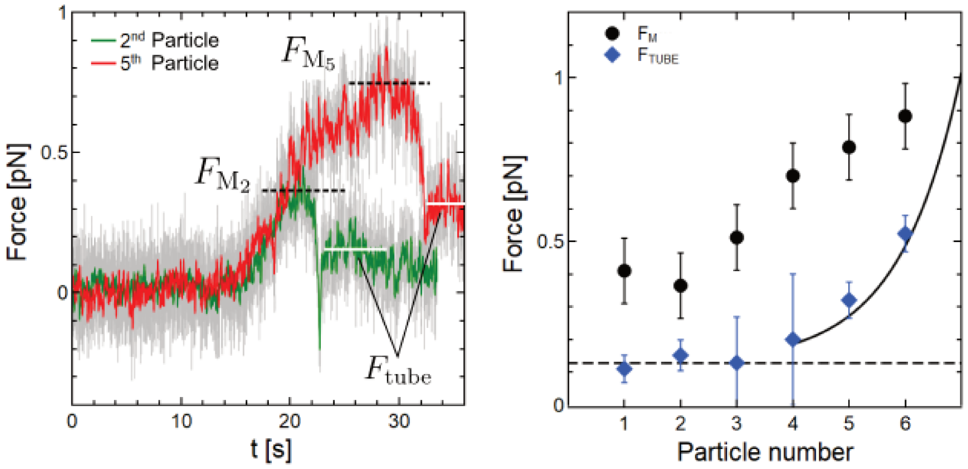

Figure 3.5: *(left)* Representative force profiles F versus time of the 2nd and 5th penetrated $R_P = 1.15\,\mu\mathrm{m}$ $\mathrm{SiO_2}$ particles performed at $v_{rel} = 0.30 \pm 0.02\,\mu\mathrm{m\,s^{-1}}$. *(right)* Measured maximum force F_M and tube force for each successive particle extracted from the force profiles. The dashed black line is f_{in} with constant $\Sigma = 5\,\mathrm{nN\,m^{-1}}$ and $m = -0.1\,\mu\mathrm{m^{-1}}$. Plain black line is f_{in} with Σ following Eq. 3.2 with $\Delta A/A$ and $\Sigma_0 = 5\,\mathrm{nN\,m^{-1}}$.

as internal structures presumably stabilised by (negative) spontaneous membrane curvature m as described for bilayers exposed to asymmetric sugar solutions [19]. These structures might not be visible in bright field microscopy but can be seen using fluorescence microscopy and are always present in our system, see Section 2.3. Note that not all of these structures constitute accessible area reservoirs and significant force might be needed to pull the material constituting some of these tubes or buds. This will be discussed in the following section 3.3. If one accounts for the existence of a spontaneous curvature m and its contribution to tension, the force needed to pull a tube f_{in} discussed earlier for the plateau force reads $f_{in} = 2\pi\sqrt{2\kappa_b\left(\Sigma + 2\kappa_b m^2\right)} + 4\pi\kappa_b m$. We can then interpret $F_{tube} = f_{in}$ data in two regimes. The first one for the first three particles where the measured F_{tube} remains constant and where only the membrane area from the reservoirs is consumed, which corresponds to the dashed line in Figure 3.5 for $|m| = 0.1\,\mu\mathrm{m^{-1}}$. The tension here therefore really acts as a chemical potential for the membrane area reservoirs and remains constant. The second regime starts instead when the membrane area stored in the reservoirs is not accessible anymore and the mechanical membrane tension Σ starts to increase as expected from Equation (3.2), see Figure 3.5 *(right)*. The existence of large area reservoirs leading to distinct regimes when submitting floppy vesicles to strains was also recently evidenced in the case of flow-induced elongation [135, 127, 125].

In order to further evidence the role of tension, we performed the same experiment with

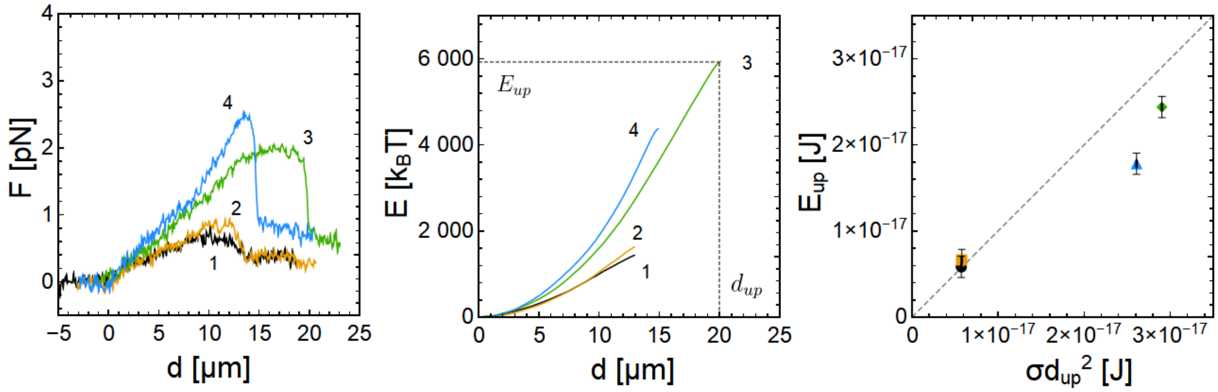

Figure 3.6: *(left)* Force profiles for 4 successively engulfed $R_P = 2.13\,\mu\text{m}$ in a floppy POPC vesicle. First, second , third and fourth particle corresponds to the black, orange, green and blue curves, respectively. (middle) Energy profiles evaluated from the integration of the force profiles, which define the uptake energy E_{up} and penetration depth d_{up}. *(right)* E_{up} vs σd_{up}^2 for the four successively penetrated particles. σ is evaluated from the plateau force F_{tube} of the force profiles while d_{up} and E_{up} can both be extracted from the associated energy curves. The dashed line stands for $E_{up} = \sigma d_{up}^2$.

bigger particles with $R_P = 2.13\,\mu\text{m}$. Doing so, each particle being successively engulfed consumes more membrane area, and the smaller curvature radii of the particle minimizes the bending contribution. Figure 3.6 shows the experimental force profiles acquired upon successive optically forced engulfment of particles. Again, the results show that F_M grows for each successively engulfed particles. Also, the plateau force is constant for the two first penetrated particles and then grows with successive engulfment, which confirms our previous observations and supports the hypothesis of membrane area reservoirs being consumed leading to the absence of tension increase. An additional feature we can clearly see here is the fact that the more tense the vesicles, the sharper the force drop is. This indicates that the dynamics of the instability of the unbound membrane segment depends on the membrane tension.

This time, we plot the force as a function of displacement, which directly translates into penetration depth (by taking initial contact point to be $d = 0$). This allows to extract from the force profiles the energy E_{up} provided by the optical trap to induce full wrapping of the particle by the membrane. Indeed, we have:

$$E_{up} = \int_0^{d_{up}} F(d)\,\mathrm{d}d, \tag{3.3}$$

with the critical penetration depth at which neck closure occurs d_{up}. Integrating the force profiles $F(d)$ therefore directly yield E_{up} which lays in the range 1000-6000 k_BT for this set of experiments, see Figure 3.6 *(middle)*, and agrees with previous measurements [90, 136]. Surprisingly, the magnitude of E_{up} is not monotonic for successive particles, as the 3^{rd} penetrated particle required more energy than the 4^{th}. F_M however remains monotonic as previously shown for smaller particles. We can plot E_{up} as a function of σd_{up} (Figure 3.6 *(right)*, where σ is the tension extracted from F_{tube}), which corresponds to the energy associated to the tension on the typical lengthscale d_{up} over which the membrane is deformed before the neck formation, therefore also accounting for the deformation of the unbound membrane segment. The plot shows that for each penetration the results lay close to the line $E_{up} = \sigma d_{up}^2$, meaning that the tension represents the main contribution to describe the energy of uptake E_{up}.

3.2.3 Modelling of the force and energy profiles

We showed that even for low tension vesicles, membrane area consumption (and associated vesicle volume increase) upon successive entry can lead to large tension increase which translates in higher force needed to trigger engulfment. In order to evidence other contributions to the experimental force profiles obtained, we have to consider the energy landscape models composed of bending, tension and adhesion contributions, in the limit $R_v \gg R_P$ [81]. In these models only the membrane area bound to the particle contributes to the energy landscape, under the assumption that the unbound membrane close to the particle can adopt vanishing energy shapes (we already have evidences that it might not be the case in our system). The energies expressed with the parameters of our system are [81]:

$$E_b = 4\pi\kappa_b\,(1 + mR_P)\,(1 - \cos\alpha), \tag{3.4}$$

$$E_\sigma = \sigma\pi R_P^2(1 - \cos\alpha)^2\ , \tag{3.5}$$

$$E_w = w2\pi R_P^2(1 - \cos\alpha)\ . \tag{3.6}$$

We calculate the force contribution from the energy by taking the derivative of the energy with respect to displacement of the contact line along the particle $s = R_P\alpha$. Hence, the force is $F = -dE/\left(R_P d\alpha\right)$. The modulii of the force contributions acting on the contact line between the bound and unbound membrane regions then take the form :

$$F_b = \frac{\kappa_b 4\pi \sin\alpha}{R_P} + 4\pi\kappa_b m, \tag{3.7}$$

$$F_\sigma = 2\pi R_P \sigma \sin\alpha(1-\cos\alpha)\ , \tag{3.8}$$

$$F_w = 2\pi R_P w \sin\alpha\ . \tag{3.9}$$

We can postulate that the maximum force recorded can be found by summing of the contributions in Equation (3.4 - 3.6) at their maximum (around $\pi/2$).

3.2.4 Particle size dependence

To investigate the bending contribution to the force profile, we performed similar wrapping experiments on multiple vesicles with a distribution of tensions around $\sigma = 10\,\mathrm{nN\,m^{-1}}$ (inferred from tube plateau force) using three different Silica particle sizes $R_P = 0.75\,\mathrm{\mu m}$, $R_P = 1.15\,\mathrm{\mu m}$ and $R_P = 2.13\,\mathrm{\mu m}$. The results are shown in Figure 3.7. As seen from Equation (3.7), the bending contribution to the force acting on the entering particle is inversely proportional to the particle radius R_P, and was plot for $\alpha = \pi/2$ in Figure 3.7 for vanishing spontaneous curvature (solid black line) and for $m = -0.1\,\mathrm{\mu m^{-1}}$ and $m = -0.5\,\mathrm{\mu m^{-1}}$ (from top to bottom line). As the vertical dispersion of F_M for individual measurements in Fig 3.7 stands for the dispersion in the membrane tensions of the penetrated GUVs, it appears that the averages as well as lowest measured values for the two smallest sizes follow a $\propto 1/R_P$ dependency. Here we have an additional signature of a negative spontaneous curvature in the fact that F_M is systematically smaller than the bending contribution with $m = 0$ (solid black line in Figure 3.7*(left)*). For the largest particle radius $R_P = 2.15\ \mu$m however, the results do not seem to follow the trend if we only take into account the bending cost. Indeed, considering that the membrane area needed to wrap the particle scales with $\propto R_P^2$, the tension contribution ($F_\sigma \propto R_P$) when using large particles can no longer be disregarded. Hence, tension contributions ultimately play a role during the penetration of the particle resulting in higher F_M.

In Figure 3.7 *(right)*, we plot our results and the ones reported by Dols-Perez et al. [121] operated in a tension-dominated regime, $R_P > \lambda_\sigma$ where F_M scales linearly with R_P, $F_M \propto R_P$ (Equation 3.5). The dashed red lines in both panels of Figure 3.7 correspond to the tension contribution to the maximum force (Equation 3.5) for $\sigma = 30\,\mathrm{nN\,m^{-1}}$, while the plain red line corresponds to a higher tension reported by Dols-Perez et al [121]. For vanishing adhesion, F_M is the sum of a bending contribution inversely proportional to R_P

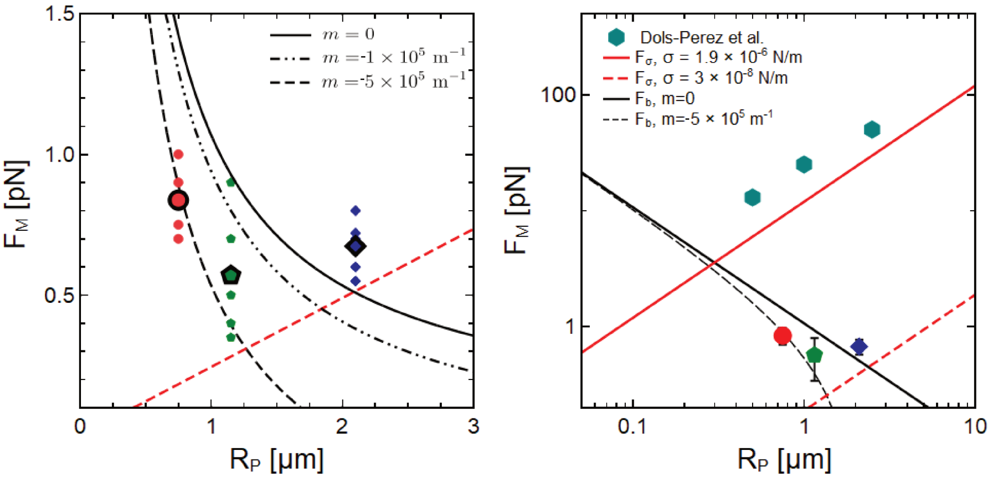

Figure 3.7: *(left)* Maximum force recorded upon penetration of Silica particles with radii $R_P = 0.7, 1.1$ and $2.13\,\mu\mathrm{m}$. Smaller dots correspond to individual measurements while bigger ones are averages. Black solid curve is the maximum of $F_b(R_P)$ (Equation 3.4) for $m = 0$ while the dashed lines correspond to $m = -0.1\,\mu\mathrm{m}^{-1}$ and $m = -0.5\,\mu\mathrm{m}^{-1}$ respectively. Red dashed curve is the maximum of $F_\sigma(R_P)$ for $\sigma = 30\,\mathrm{nN\,m}^{-1}$ (Equation 3.8 which is a representative value of the measured tension in our system. *(right)* F_M vs R_P in log-log scale. Solid red line is the maximum of $F_\sigma(R_P)$ for $\sigma = 1.9\,\mu\mathrm{N\,m}^{-1}$ measured in [121] together with experimental F_M.

and a tension contribution linear with R_P. Hence, F_M shows a minimum at $R_P \approx \lambda_\sigma$ in a cross-over regime between the bending and the tension dominated regimes, see Figure 3.7. In other terms, for vanishing adhesion, the properties of the membrane set a lengthscale $\lambda_\sigma = \sqrt{\kappa_b/\sigma}$ for which the magnitude of the external force needed to drive the wrapping of a spherical colloid is minimal.

3.2.5 Particle-membrane surface interactions influence

In order to study the influence of the particle-membrane affinity on the shape transitions, we performed optically forced engulfment experiments with particles made of different materials, namely Polystyrene, Melamine formaldehyde and Silica. These particles show different physico-chemical properties (e.g. Zeta Potential measurements, see Section 2.4) which we expect to translate into different affinity w with the membrane [77, 86]. For floppy vesicles, we were able to enter and stably wrap both MF and PS particles using the same range of trapping forces as used for Silica particles. Examples of force profiles for the three different particle materials are shown in Figure 3.8 together with the energy as a function of penetration depth (obtained by integration of the force profile) in inset. Note that in all cases a force of the order a picoNewton is required to trigger the instability leading to stable wrapping of

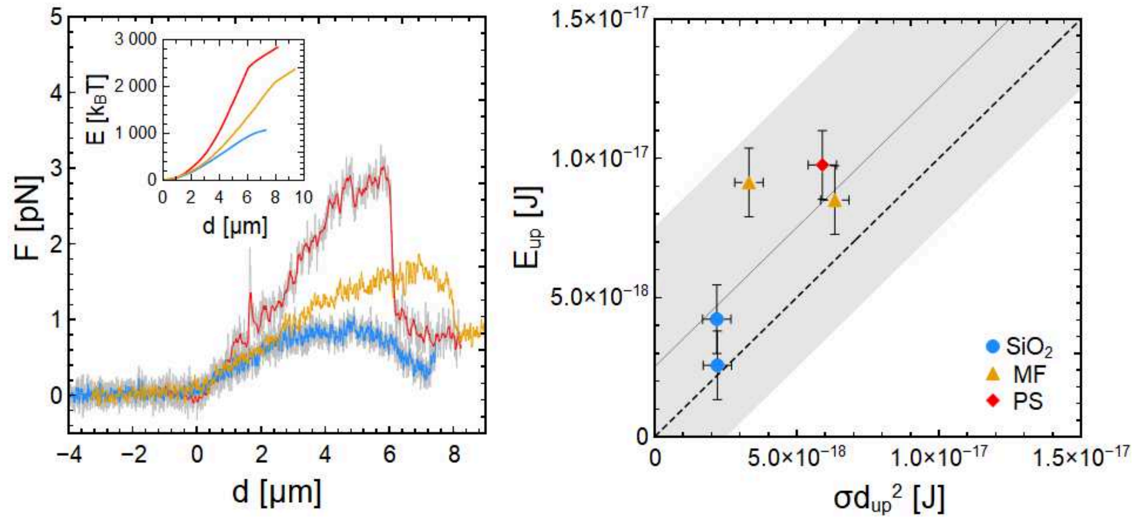

Figure 3.8: *(left)* Example of force profiles F vs d upon optically forced wrapping of $R_P = 1.2\ \mu$m Polystyrene (red), $R_P = 1.2\ \mu$m Melamine Formaldehyde (orange) and $R_P = 1.15\ \mu$m Silica (blue) *(right)* E_{up} vs σd_{up}^2. Each point corresponds to an experiment in which E_{up} and d_{up} was extracted from the experimental E vs d curve and σ from the plateau force of the associated force profile. The black dashed line corresponds to $E_{up} = \sigma d_{up}^2$. The grey line accounts for the bending contribution and stands for $E_{up} = \sigma d_{up}^2 + 8\pi\kappa_b$, while the grey shaded area $E_{up} = \sigma d_{up}^2 + 8\pi\kappa_b \pm w4\pi R_P^2$ where $R_P = 1.2\ \mu$m and $w = 2 \times 10^{-7}$ N.m^{-1}.

the particle, which points to a similar ultra-weak particle-membrane affinity for all particle types.

In Figure 3.8 *(right)* we show that the uptake energy E_{up} for different materials are all close to the line $E_{up} = \sigma d_{up}^2 + 8\pi\kappa_b$ meaning that considering only bending and tension is enough to interpret the data (spontaneous curvature here would bring a small additional offset to this line). The fact that a point is above $E_{up} = \sigma d_{up}^2 + 8\pi\kappa_b$ could be interpreted as a small additional cost due to unfavorable particle-membrane surface interactions ($w > 0$) while points below could indicate favorable particle-membrane surface interaction ($w < 0$). Following this reasoning, Figure 3.8*(right)* suggests that $w < 0$ for Silica, while we tend to have $w > 0$ for PS and MF, while the grey area containing all the points indicate that $|w| < 2 \times 10^{-7}$ N.m^{-1} in all cases.

Reasoning in terms of force knowing that $F_M = F_{b,max} + F_{\sigma,max} + F_{w,max}$, we can evaluate w to be $(F_M - F_b - F_\sigma)/2\pi R_P$, which is plotted as a function of σ for the different particle types in Figure 3.9. As expected, w remains weak ($< 3 \times 10^{-7}$ N.m^{-1}) showing again both signs, and that there is no clear correlation between the membrane tension and evaluated particle adhesion w. Surprisingly here, a same material can show both positive or negative values of w. While trends might emerge from averages, additional contributions ignored in our simplified model considering only the local contributions F_σ, F_b and F_w have an influence on the maximum force F_M. In particular, the presence of accessible area reservoirs and variability in the membrane spontaneous curvature m for each vesicle as seen in Section 3.2.2. Similarly, a size dependent contribution associated to the unbound membrane segment could explain the apparent size dependence of the inferred w for SiO_2 particles in Figure 3.9.

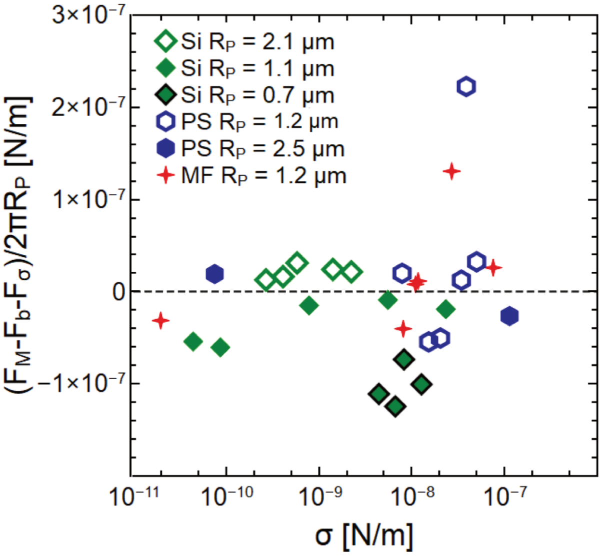

Figure 3.9: $(F_M - F_b - F_\sigma)/2\pi R_P$ as a function of tension σ extracted from F_{tube} for a set of experiments performed with multiple particle materials (PS, MF and SiO_2). In the absence of other contributions, we should have $(F_M - F_b - F_\sigma)/2\pi R_P = F_w/2\pi R_P = w$.

These results agree with the picture of a weak and non specific adhesion where the interaction between the particle and the membrane is mediated by a water film of h = 10-100 nm thickness [137]. The value of w being in reality an approximation from distance-dependent particle-membrane interaction potential (which can result from the contributions of electrostatic double layer [85], steric [77], hydrophobic and Van der Waals interactions [138]) might be sensitive to dynamical effects such as vesicle and particle fluctuations or drainage of the water film between the two surfaces.

In conclusion, applying an external pN force leads to the stable membrane wrapping of even non adhesive particles. Indeed, we expect that even particles with unfavorable (repulsive) particle-membrane surface interactions could be stably fully wrapped as the wrapping is triggered by an instability of the free membrane segment collapsing into a neck. The repulsive particle membrane interaction would in fact only increase the particle-membrane distance during the forced deformation and the particle would remain stably wrapped as long as the energy costs of bending, tension and repulsive particle-membrane interaction in the fully wrapped state is lower than the energy needed to open the neck. We conclude that this stability arises from the high energy cost associated to the opening of the neck formed upon wrapping. The next section will be dedicated to evaluating the energy associated to the neck opening.

3.3 Membrane neck stability

In the optically driven microparticle engulfment experiments, we bring the particle from a non-wrapping state to a stable full-wrapping state in the absence of favorable particle-membrane interactions. If a very weakly favorable or unfavorable particle-membrane affinity can exist, it is negligible compared to the energetic costs needed to bend and work against the tension σ such that $\mid wA_b \mid \ll \sigma A_b + 8\pi\kappa_b(1 + mR_P)$, where $A_b = 4\pi R_P^2$ for the bound membrane segment at full engulfment ($\alpha = \pi$ for Equations 3.4 - 3.6).

The stability of the full wrapping state can therefore not be explained by the interplay between favorable particle-membrane interactions and energetic costs to deform the bound membrane segment, as it is usually the case for adhesion-driven engulfment [77, 79]. The stability should therefore be provided by the shape transitions experienced by the unbound membrane segments. We showed in Section 3.2 that the collapsing of the unbound membrane segment into a neck dramatically changes the energy landscape, as the energy barrier to re-open the neck in order to bring the particle from the fully wrapped state to the non wrapping state is much higher than when doing the opposite. This leads to an irreversibility of the process, or at least introduces a hysteresis. In the following, we report on experiments taking advantage of a micropipette to put under tension a vesicle in which a particle was previously engulfed. Doing so, we probe the reversibility of the process and quantify the energy required to open the neck formed upon particle wrapping. We then confront our results to existing models of membrane necks stability.

3.3.1 Neck opening by applying stress with a micropipette

A micropipette can serve as a potent micromanipulation instrument for exerting precise stress on individual vesicles, unlike the indiscriminate nature of osmotic stresses. The fabrication and operation principles are described in Section 2.2. Here, we apply a suction pressure ΔP on floppy vesicles in which a $R_P = 1.15$ μm Silica particle was previously optically engulfed. We recall that the pressure difference applied ΔP translates into membrane tension through Laplace's law following Equation 2.7. Fluorescence microscopy images of a typical experiment are shown in Figure 3.10, with the engulfed particle optically trapped with a weak trapping stiffness, only to maintain it at the vesicle equator allowing to have it in the same plane as the micropipette. When no pressure is applied ($\Delta P = 0$, left panel) the vesicles show the usual large thermal undulations observable for floppy (deflated) vesicles. By applying a suction pressure $\Delta P < 0$, a tongue gets sucked into the micropipette and an increase in sphericity can be observed. In the case here, we can see that the particle is slightly displaced from its equilibrium position in the optical trapped, meaning that the membrane neck is pulling it towards the membrane of the mother vesicle. Still, the particle remains stably wrapped and no opening of the neck is observed in this experiment.

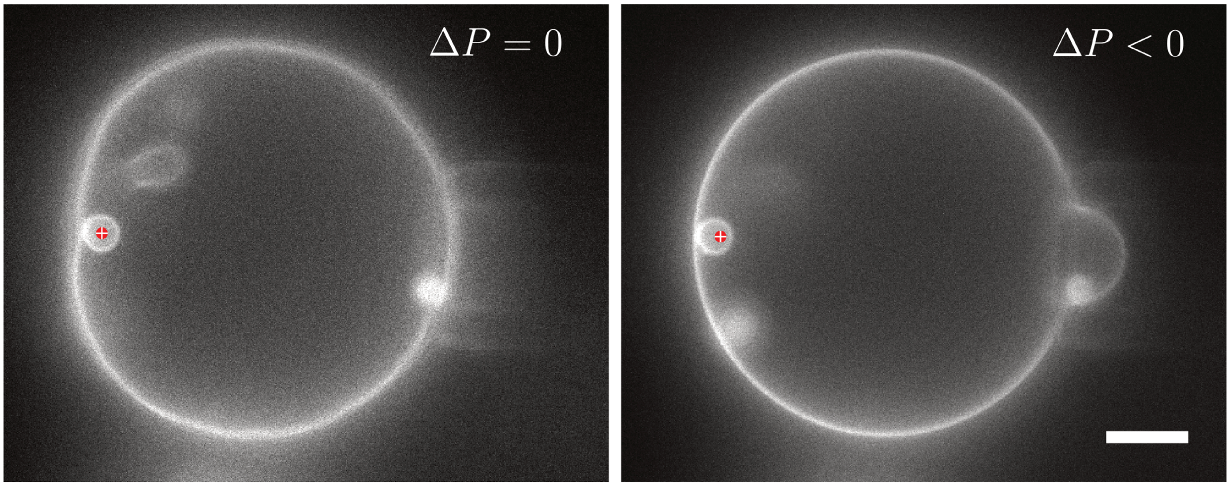

Figure 3.10: Fluorescence microscopy snapshots of an experiment consisting in applying suction pressure to an initially floppy giant vesicle in which a $R_P = 1.15$ μm SiO_2 was engulfed thanks to optical forces. The particle is held in an optical trap (center of the laser beam waist shown as a red dot) with weak trapping stiffness ($\kappa = 2\,\mu\mathrm{N\,m^{-1}}$) in order to keep the particle at the vesicle equator to have both the wrapped particle and the membrane segment aspirated in the micropipette in the imaging plane.

In a typical experimental protocol, we increase ΔP step wise (and conversely, σ), and wait 1 minute between each pressure step, while maintaining the particle at the vesicle equator with a weak optical trap. There can be two outcomes for such experiments. The first one is the one depicted in Figure 3.11, where the neck opens at a critical tension σ_c which translates in a brutal radial displacement of the particle from the intravesicular space towards the exterior in less than 100 milliseconds. Simultaneously, an apparent area increase

ΔA_{app} can be observed from the increase of the cylindrical portion length $\Delta L = L_f - L_i$ of the tongue. This apparent area increase corresponds to the surface area that was wrapping the engulfed particle, confirming the opening of the membrane neck and release of the particle. We can check that $\Delta A_{app} = 2\pi R_{pip} \Delta L \approx 4\pi R_P^2$. Note that an additional experimental evidence of the irrelevance of adhesion in the stability of the wrapping can be observed from examples where the bud containing the wrapped particle also contains a large volume of exterior aqueous solutions, see Appendix 8.4. In this case, similar critical tensions σ_c were measured. The other outcome in our experiments is that the particle remains wrapped and no neck opening occurs in the range of pressure our setup allows to explore $\Delta P < 40$ Pa, i.e. $\sigma < 0.1\,\mathrm{mN\,m^{-1}}$. Data on the neck opening statistics for $N = 18$ experiments are shown in Figure 3.12, showing that in more than half of the cases (≈ 60 %), we could not observe an opening of the neck for the range of tensions accessible, meaning that the critical tension for neck opening $\sigma_c > 0.1\,\mathrm{mN\,m^{-1}}$. In ≈ 40 % of the cases, the neck was opening as described above and a critical tension σ_c could be measured, and the mean value is reported in Figure 3.12 and is $\sigma_c = 34\,\mathrm{\mu N\,m^{-1}}$.

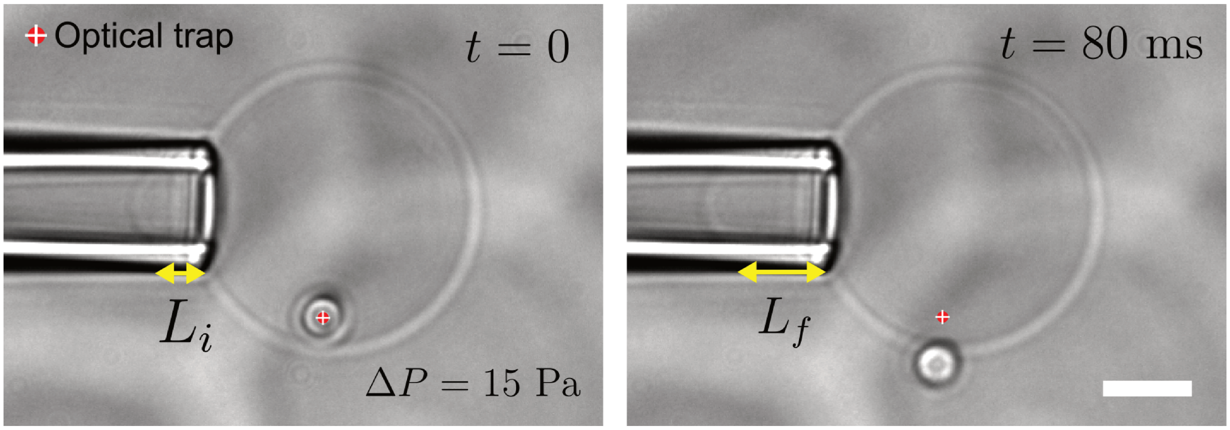

Figure 3.11: Bright field microscopy snapshots of an experiment consisting in applying suction pressure to an initially floppy giant vesicle in which a $R_P = 1.15\mu$m SiO_2 was engulfed thanks to optical forces. *(left)* The wrapped particle is held in an optical trap (center of the laser beam waist shown as a red dot) with weak stiffness ($\kappa = 2\,\mathrm{\mu N\,m^{-1}}$) in order to keep the particle at the vesicle equator and to have both the wrapped particle and the aspirated membrane segment in the imaging plane. *(right)* The particle was unwrapped (due to neck opening) and the particle escaped from the optical trap and was expelled from the intravesicular space.

It appears that there is a large variability on the tension σ_c at which neck opening is triggered, as it may vary over several orders of magnitude. This dispersion can be related to the physical mechanism which stabilizes this narrow neck shape of the membrane. We know from geometrical considerations that narrow necks in the absence of spontaneous curvature, although being highly curved along the profile, are not penalized by large bending energy costs as the mean curvature is reduced to vanishing values due to the opposite sign curvature along the parallels [81, 139, 13].

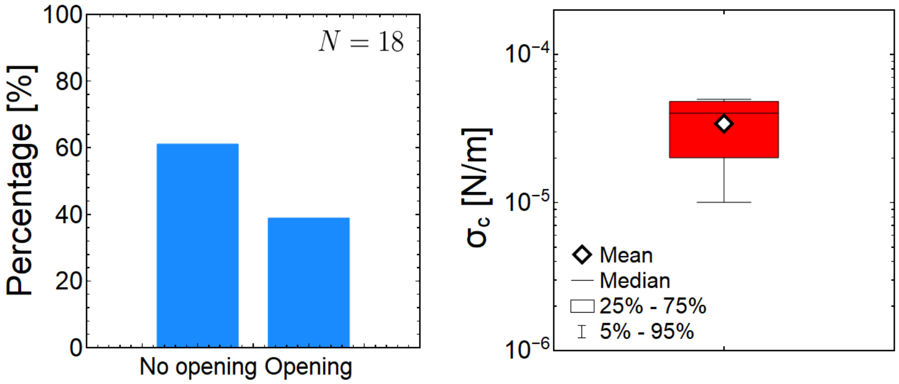

Figure 3.12: *(left)* Neck opening statistics upon putting POPC vesicles with an engulfed $R_P = 1.15$ μm Silica particle under tension over $N = 18$. *No opening* stands for the cases when no opening of the neck was observed in the tension range accessible ($\sigma < 10^{-4}$ N/m), while *Opening* accounts for the cases where an opening was reported. *(right)* Average value of the critical tension σ_c at which neck opening occurred (for $N = 5$ experiments).

Finally, if the neck shape has principal curvatures radii of the order of the bilayer thickness, one could expect rearrangements of the lipid bilayer at the points of highest curvature. For example, hemifusion of the membrane could be expected. However, such rearrangements do not happen spontaneously and energy should be provided for them to take place. It was often proposed that the particle-membrane adhesion can drive the fusion processes and even lead to fission between the bud containing the particle and the mother vesicle. Despite the absence of strong adhesion or constriction forces provided by proteins such as dynamin in our system, it was shown that constriction forces arising from spontaneous curvature alone be large enough to induce neck fission [13].

While the mechanisms underlying the stability of the fully wrapped state for optically forced wrapping (in absence of strong adhesion) were never investigated experimentally, we will try in the next section to link the critical tension for opening σ_c to an energy barrier for neck opening.

3.3.2 Analogy with pore opening and energy quantification

As a first approximation, we will model the membrane neck as if it was a pore. Indeed, if we forget about the membrane bud and consider that the energetic cost associated to neck opening is proportional to the radius of the neck as seen from the top (see Figure 3.13), one gets an expression for the neck energy:

$$E_{neck} = \gamma_l 2\pi r, \tag{3.10}$$

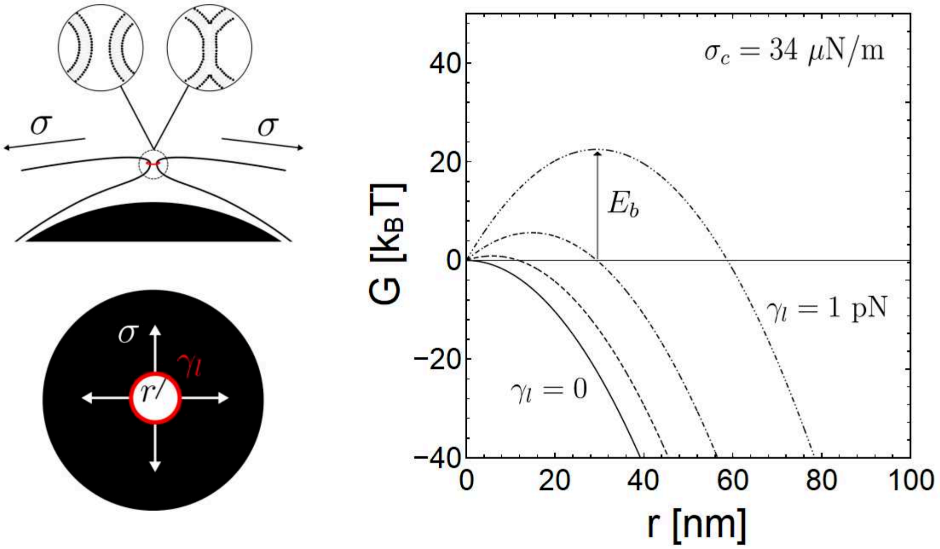

Figure 3.13: *(left)* Schematics of neck opening mechanism and analogy with pore opening. The top panel shows a side view of the neck profile with eventual membrane topologies at the neck. The bottom panel shows a top view of the system and illustrates the analogy with a pore where the membrane neck has a radius r and a line tension γ_l associated. *(right)* Graph of the energy G versus neck radius r in analogy with a pore. The tension contribution $-\sigma 4\pi r^2$ is kept constant with $\sigma_c = 34\ \mu$N/m the mean value of the experimentally measured critical tension.

where r is the neck opening radius. $\gamma_l = E_{neck}/2\pi r$ therefore captures all the energy contributions resisting the opening of the neck under the assumption that the latter are linear with r. Note that this is a strong assumption as the energy of the neck most probably depends on its full shape with associated mean (and eventually Gaussian) curvatures and eventually other contributions arising from membrane partial fusion which might result nonlinear energy dependence on r. The neck energy competes with the membrane tension energy, for which an opening of the neck to a radius r would provide a negative contribution to the overall energy as it reduces the membrane area by πr^2. The associated energy $G(r)$ of the system therefore reads:

$$G(r) = -\sigma \pi r^2 + \gamma_l 2\pi r \tag{3.11}$$

with σ the membrane tension. In the low tension regime, the first term in Equation 3.13 is negligible and G is linear with r. The only stable state is $r = 0$. However, when we apply a suction pressure with the micropipette and induce an increase of membrane tension, the first term starts to dominate for large r due to its $\propto r^2$ dependency. For a membrane neck initially close to $r = 0$ (after forced wrapping), there is now an energy barrier separating the stable state $r = 0$ and $r = \infty$, as seen in Figure 3.13.

When the critical tension σ_c is reached, this barrier should be comparable to thermal energy as the barrier crossing happens without additional energy input. By fixing σ_c to the experimentally measured values, we can have an idea of the line tension γ_l characterizing the neck leading to an energy barrier E_b that can be overcome by thermal energy. Doing so, we can estimate $\gamma_l \sim 1\,\mathrm{pN}$ (Figure 3.13). In the next section, we will focus on confronting these results to the currently established theory of membrane necks stability.

3.3.3 Comparison with theory of membrane necks stability

In the framework of spontaneous curvature elasticity theory developed in the past decades, stability relations of membrane neck in presence or absence of an adhesive particle in the membrane bud were derived [13, 82, 140]. The simplest stability criterion, derived considering solely bending energy contributions, for an exterior neck (corresponding to an inward-pointing bud, as in our case) in absence of adhesive particle in the bud reads [13]:

$$m \leq M_{ne} = \frac{1}{2}\left(\frac{1}{R_l} - \frac{1}{R_s}\right) \tag{3.12}$$

where m is the membrane spontaneous curvature and M_{ne} the neck mean curvature which only depends on the curvature radii of the adjacent membrane segments R_l of the mother vesicle and R_s of the opposite curvature membrane bud. Considering the case where $R_s = R_P = 1.15$ μm and the size dispersion of our vesicles 7 μm $< R_l <$ 20 μm yields -3.6×10^5 m^{-1} $> M_{ne} > -4.1 \times 10^5$ m^{-1}, which in turn implies $|m| > 3.6 \times 10^5$ m^{-1} as a lower bound for the spontaneous curvature absolute value in our system for it to be able to stabilize the formed neck. These values are consistent with spontaneous curvature values obtained previously in Section 3.2.

In fact, these stability relations can be derived by parameterizing the shape of the vesicle-bud complex as two hemispheres connected by two unduloid-shaped segments forming a neck of radius r. It was shown that the bending energy of such a shape has the form [13]:

$$G_{be} = G_{be}(0) - 8\pi\kappa_b\,(m - M_{ne})\,r, \tag{3.13}$$

where $G_{be}(0)$ is the energy associated to the shape far from the neck. The stability relations are simply obtained from the fact that G_{be} must increase with increasing r, imposing $M_{ne} \geq m$ (i.e. Equation 3.12). Furthermore, the linearity of the bending contributions to the neck energy G_{be} with the neck radius r legitimates our approach of treating E_{neck} as a line tension energy. In the absence of other contributions than bending, by identification of Equation 3.10 with Equation 3.13, we have:

$$\gamma_l = 4\kappa_b(M_{ne} - m) \tag{3.14}$$

Following this model, in order to have $\gamma_l \sim 1$ pN as estimated from the pore analogy, $(M_{ne} - m)$ should be of the order of 10^{-6} m^{-1}. Using the experimental bound $M_{ne} = -3.6 \times 10^5$ m^{-1}, this yields $m \approx 6 \times 10^{-5}$ m^{-1}, which is in the expected range of m. The neck opening tension measured σ_c therefore suggest that a stabilization by spontaneous curvature is possible as it agrees with values of m inferred from force measurements and from the structures observed optical microscopy. However, for the cases when a tension of $\sigma \sim 0.1\,\mathrm{mN\,m^{-1}}$ was not sufficient to trigger the opening of the neck, it either means that the membranes in those cases possessed much larger spontaneous curvature absolute values, or that other mechanisms than spontaneous curvature-induced constriction forces were at play. In particular, additional costs for opening are to be expected if a rearrangement of the lipids occurred at the neck, and a stalk or partial fusion of the lipids was initiated [141].

3.4 Particle induced budding

When performing optically induced engulfment experiments in fluorescence microscopy, we noticed, in some rare cases, that deformation of the membrane by the particle would cause the nucleation of membrane buds inside the vesicle. The snapshots in Figure 3.14 shows an example of such dynamics where an optically trapped $R_P = 2.13\,\mu\mathrm{m}$ Silica colloid is brought in contact with a floppy GUV. In a few seconds, a necklace of ≈ 10 membrane buds is formed.

One striking feature in this process is the very low size variability of the nucleated buds

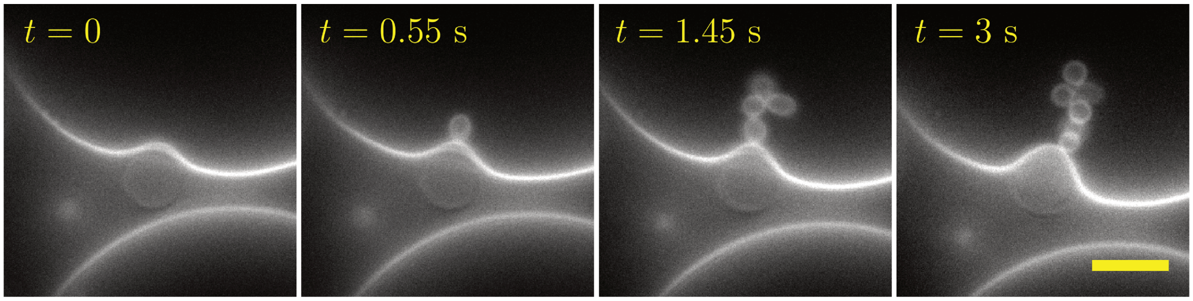

Figure 3.14: Fluorescence microscopy snapshots of particle-induced budding with a $R_P = 2.13\,\mu\text{m}$ Silica particle and a POPC vesicle with 1% fluorescently labelled lipids (NBD). Scale bar is $5\,\mu\text{m}$.

forming the necklace. The existence and stability of these structures is well described in the frame of spontaneous curvature theory [19, 13], and the radius of the mean curvature of these spherical buds (with radius R_{bud}) should correspond to the spontaneous curvature $|m| = 1/R_{bud}$ of the membrane. We observe different sizes for the structures nucleated, as shown for example in Figure 3.15 where tubes are nucleated with radii no bigger than few hundreds of nanometers upon contact with a $R_P = 1.15\,\mu\text{m}$. This could be an additional evidence of a variability of membrane spontaneous curvatures in our sample, which we already discussed in Section 2.11. It might also be that a spontaneous curvature is induced by the presence of the particle, as the latter further increases the asymmetry between the interior and exterior membrane leaflets.

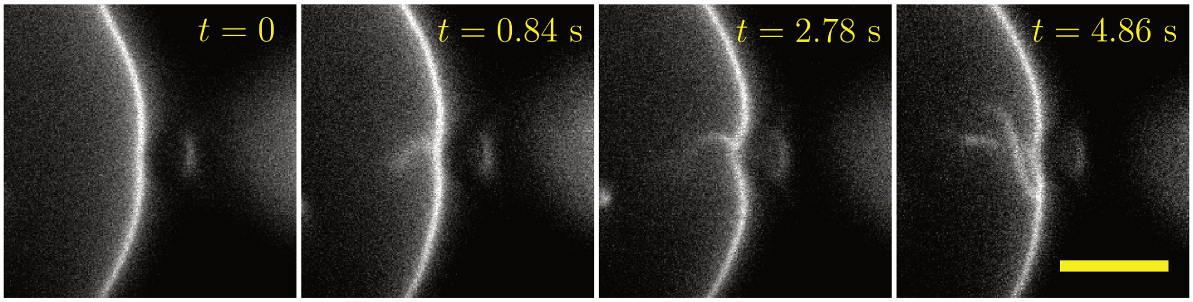

Figure 3.15: Fluorescence microscopy snapshots of particle-induced budding with a $R_P = 1.15\,\mu\text{m}$ Silica particle and a POPC vesicle with 1% fluorescently labelled lipids (NBD). Scale bar is $5\,\mu\text{m}$.

While it is rather clear why these structures are thermodynamically favorable, the formation dynamics of these structures is however less characterized. Since an energy barrier might exist to nucleate those buds, it is not surprising that it might take time for deflated vesicles to remodel their shape to thermally reach global energy minima. Here, the optically trapped particle in proximity provides energy in two ways, reducing the barrier height and thereby accelerating the nucleation dynamics. Firstly, the fact that the optically trapped particle locally heats the surrounding fluid and the membrane. A temperature increase $\Delta T \approx 10^{\circ}$ C was measured in the vicinity of Polystyrene microparticles in water for a 980 nm trapping wavelength laser at 100 mW power output [142]. Such temperature increase will only have a little impact on magnitude of thermal energy, but might help overcoming small energy barriers. Secondly, and most importantly, the fact that the optical force pushes the particle against the membrane, locally bending the membrane such that the local mean curvature adopts $M = -1/R_P$. Doing so, the optical force provides part of the energy necessary for the buds to be nucleated. Note that the fact that fluid is able to move from the exterior solution towards the buds is again a signature of a large water gap between the particle surface and the lipid membrane.

3.5 Conclusion

In this chapter, we have performed force-driven entry of spherical microparticles of various compositions into giant unilamellar vesicles by means of optical tweezers in a regime of weak adhesion where the particle size compares to the bendocapillary length of the membrane. Investigations on the driven wrapping dynamics using fluorescence microscopy and force measurements upon wrapping allowed to evidence the existence of an instability in the shape of the unbound membrane segment leading to stable wrapping. Our experiments point to the role of membrane excess area stored in the vesicle area reservoirs stabilized by spontaneous membrane curvature. These structures appear to contribute as a shape-independent term to the membrane tension, analogously to the interfacial tension of liquid interfaces and in agreement with recent theoretical predictions [20], until all of the accessible area reservoir is consumed. Varying the particle size, we show that a force minimum should exist for a particle size comparable to the lengthscale emerging from properties of the membrane, namely the bendocapillary length. By means of a micropipette, we could probe the degree of reversibility of the wrapping process in the case of optically driven wrapping and quantify the membrane tension necessary for the neck to re-open. We showed that there is a large variability in the degree of reversibility in our system. This can be imputed to variability in spontaneous curvature or to other energy barriers due to lipids reorganization at the membrane neck.

Chapter 4

Active Janus colloid autonomous interaction with floppy vesicles

4.1 Introduction

Catalytic microswimmers are micron-sized objects, that can self-propel and perform a variety of tasks on the micro-scale including drug delivery and environmental remediation. They can achieve self-propulsion through chemical reactions that create concentration gradients that induce fluid flows in the surrounding solution. Efficient propulsion of the microswimmer requires a high reaction rate, which is usually achieved by the addition of highly reactive compounds such as hydrogen peroxide (H_2O_2) [143] or hydrazine (N_2H_4) [144], which are decomposed by the microswimmer. However, these toxic compounds limit potential applications e.g. in biological systems. Therefore, several works have focused on extending the range of propulsion reactions for catalytic microswimmers, including galvanic exchange reactions [145], photodeposition [146], the degradation of organic pollutants [147, 148] or the oxidation of amines to imines [149]. One very promising approach for powering of catalytic microswimmers in biological media is the use of a fuel that is also used by nature - glucose. Wang *et al.* have shown, that Cu_2O microspheres can move in aqueous solutions of glucose under irradiation with visible light. The persistent motion of the microparticles is due to the photocatalytic oxidation of glucose to formic acid and the corresponding shorter monosaccharides arabinose, erythrose and glyceraldehyde [150]. In their work, Wang *et al.* used symmetrical spherical particles, and the symmetry breaking necessary for propulsion was introduced by shining light on one side of the particle. Due to self-shadowing effects, asymmetric reaction rates would indeed result in a directed motion away from the light source.

Here, we introduce $Cu@SiO_2$ Janus particles that can move in an aqueous glucose solution under visible light irradiation. The Cu is converted to photocatalytic copper oxides, when the particles are dispersed in water. Due to their asymmetric Janus structure, these particles have an intrinsic ability to move in any direction, and they are not biased by the direction of the light source. Hence, they can perform autonomous active motion and can show complex interactions in confinement or when close to interfaces. In particular, interactions with soft interfaces such as phospholipid membranes of cells represent a situation of confinement encountered in many processes. It was found that Janus swimmers are able to deform giant lipid vesicles when enclosed inside them [89], a response that has also been confirmed for biological active matter [151] and by theoretical considerations [152, 153]. Freely swimming Janus particles however, showed interactions that resemble the generic interactions of active matter with obstacles [154, 69, 155]. For pusher type swimmers, persistent orbital motion of Janus swimmers around giant vesicles was reported [71], and active transportation of the vesicles by a single particle could be achieved after applying strong forces [86]. To the best of our knowledge, no other behavior was reported upon interaction of freely swimming active Janus particles with cell-like compartments. While in previous experiments the Janus particles were usually made from $Pt@SiO_2$, which swim away from the metal cap and generally are considered to be pushers [63], we use a new combination of $Cu@SiO_2$ particles with glucose fuel. As other copper Janus particles [92, 65, 66], these microswimmers move towards the catalyst cap. This different swimming mode enables different types of interactions with vesicles, and may allow to observe endocytic-like behaviors.

4.2 Glucose fuelled $Cu@SiO_2$ Janus colloid self-propulsion

$Cu@SiO_2$ Janus particles were fabricated by thermal deposition of a 30 nm metallic Cu layer on a monolayer of commercial SiO_2 particles of radius $R_P \approx 1.5\,\mu m$, covering one hemisphere. These particles can self-propel catalytically when immersed in H_2O_2 and swim towards the metal cap [65], which can be interpreted as a puller type swimming mode because of the strongest slip of the velocity being on the front face [156] (see Section 1.2.2). Here, we observe self-propelled motion in a fuel different from H_2O_2. When immersed in a glucose aqueous solution at physiological concentration (25-100 mM), under homogeneous light irradiation provided by standard microscope illumination conditions, these particles show active propulsion as shown in Figure 4.2. The sedimented particles navigate in a two dimensional plane close to the glass substrate, which allows to image them with bright field microscopy and track their center of mass with image treatment techniques (see 2.5.1). During some

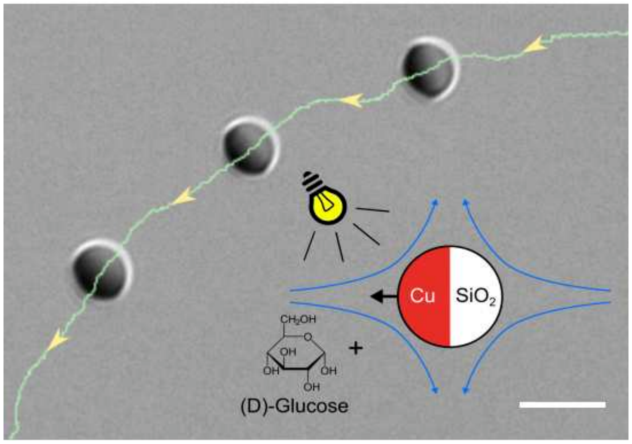

Figure 4.1: Bright field microscopy snapshot and trajectory (green) of a Cu@SiO$_2$ Janus swimmer in a 100 mM glucose solution. Inset sketches the active motion mechanism and most probable fluid flow in the swimmer frame (puller). The scale bar is 5 µm.

segments of the trajectory, the plane defined by the Janus boundary is orthogonal to the imaging plane. The hemisphere of the particle coated with the Cu layer appears darker than the bare hemisphere and allows to track the in-plane orientation of the particle (see 2.15). The dynamics of these swimmers, which appear very different from the Pt@SiO$_2$ pusher particles, will be studied in greater details in Section 6.1. Here, in order to evidence the out-of-equilibrium nature of Cu@SiO$_2$ particle dynamics in glucose and quantify the projected active velocity, we plot the center of mass 2-dimensional mean squared displacement (MSD $= \langle(x(t+\Delta t)-x(t))^2\rangle + \langle(y(t+\Delta t)-y(t))^2\rangle$) for single particles. The most standard model of the MSD of an active Brownian particle with persistent velocity, on timescales shorter than the rotational diffusion time ($\tau_{ro,b} = 1/D_{ro,b} = 8\pi\eta R_P^3/k_\mathrm{B}T = 21$ s), reads [143]:

$$\mathrm{MSD}\,(\Delta t) = 4D_t\Delta t + V^2\Delta t^2, \tag{4.1}$$

where Δt is the time lag, D_t the transnational diffusion coefficient of the spherical particle (in the bulk $D_{t,b} = k_BT/6\pi\eta R_P$) and V an average projected speed on the plane of observation. The MSD of Cu@SiO$_2$ particles in glucose, shown for representative cases in Figure 4.2 *(left)*, clearly displays a linear (diffusive) regime followed by a quadratic (ballistic) regime at longer times. The crossover between those two regimes occurs at a characteristic timescale $\tau_c = 4D_t/V^2$ where the passive and active contributions are comparable. Fitting MSD data with Equation (4.1) allows to extract both the translational diffusion coefficient and the projected active velocity for single trajectories (fits are plain white lines in the inset of Figure 4.2 *(left)*). We can show that an increase of the glucose concentration results in an increase of the average projected velocity, see Figure 4.2 *(right)*. Similarly, illuminating

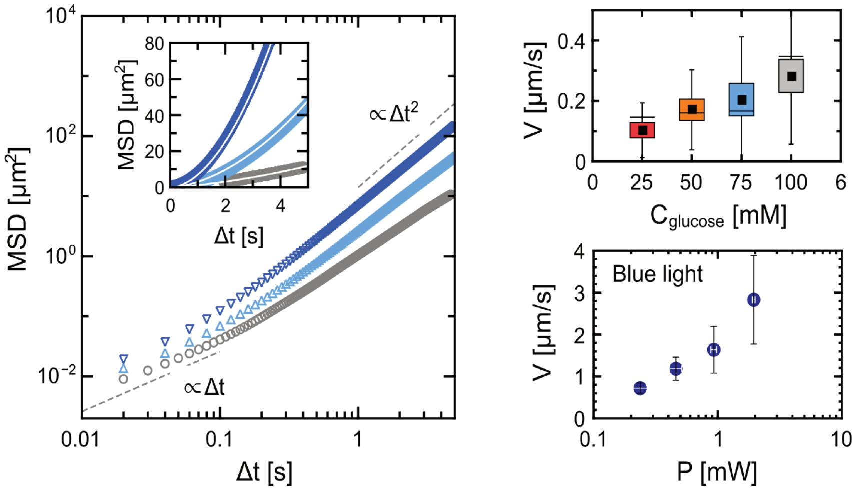

Figure 4.2: *(left)* Mean squared displacement as a function of lag time in log-log scale for three representative trajectories of particles immersed in 100 mM glucose with only white light (grey circles), white light and 0.46 mW blue light radiation (light blue up-pointing triangles) and white light and 1.96 mW blue light radiation (dark blue down-pointing triangles). Inset shows a linear scale representation with fits (white plain lines) allowing to extract projected velocity using equation 1. For these three cases, fit yields $V = 0.48\ \mu\text{m.s}^{-1}$, $V = 1.23\ \mu\text{m.s}^{-1}$ and $V = 2.33\ \mu\text{m.s}^{-1}$ (bottom to top). *(right)* Projected active velocity V extracted from MSD fits for particles immersed in glucose solutions of increasing concentration in normal illumination conditions. Black squares stand for averages on 10 trajectories. Projected active velocity measured for particles immersed in a 100 mM glucose solution under different blue light illumination powers.

the sample with blue light of increasing power will also enhance the measured projected velocities as shown in Figure 4.2 *(right)*. We have also evaluated the effect of the white light illumination on the active speed (Appendix 8.5). Values of D_t extracted from MSD fits for lower glucose concentrations (i.e. low activity) agree with the diffusion of particles close to a solid wall for a gap distance $d \approx 300$ nm (Appendix 8.7). For higher glucose concentrations, D_t increases and becomes comparable to the bulk prediction. Either an increase of the gap distance between the particle and the substrate or additional noise, both induced by the active propulsion mechanism can explain this increase of the the measured D_t. For pusher swimmers however, it was reported that the gap distance to the substrate remains constant for increasing degrees of activity [157]. Note also that we rely here on a model which might not apply to particles showing puller dynamics and that this measured increase of the diffusion constant might be the signature of other effects. This will be discussed in Section 6.1.

4.3 Particle-vesicle encounter and engulfment phenomenon

In this section, we describe the phenomenon observed when an active Cu@SiO_2 particle in a glucose solution spontaneously interacts with a giant unilamellar vesicle (GUV). This phenomenon can be described as composed of two steps: (i) the hydrodynamic capture, and (ii) the particle being wrapped by the vesicle membrane. Note that the particle activity depends on exposure to visible light and physiological glucose concentrations. Hence, we got rid of the limitations of using H_2O_2 as a fuel, which is not biocompatible and generally harmful for cells [158, 159]. In all experiments, we used GUVs made of phospholipids in the low-tension membrane regime ($\sigma \sim 10^{-8}$ N.m^{-1}), which are pertinent systems to study endocytic-like phenomena [160, 161] in the absence of receptor-mediated interaction or large external forces [90, 77, 162]. Figure 4.3 *(left)* illustrates a typical result obtained few minutes after the spontaneous interaction between active particles and GUVs. Some active particles are already engulfed by GUVs and for one isolated particle we could track its active trajectory before and after encountering a GUV. The impact of the activity on the encounter rate is evident as it allows the particles to explore larger areas in a given time with respect to passive Brownian particles. The impact of far-field hydrodynamic interactions on the encounter rate is hard to evidence, because directional changes can be due either to hydrodynamic interaction or Brownian rotational diffusion. Still, even in diluted situations this kind of event happens at a high rate and after few minutes, most of the active particles in the

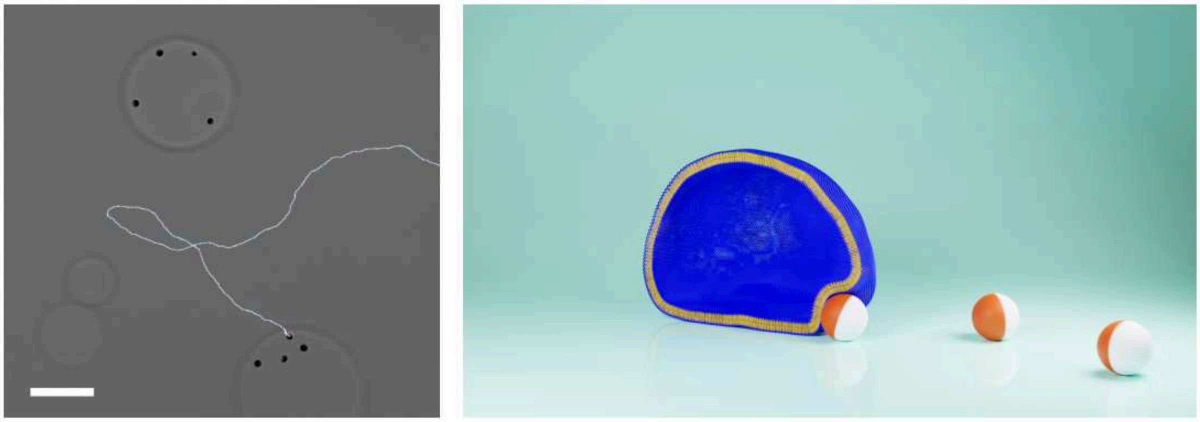

Figure 4.3: *(left)* Bright field microscopy snapshot with the backward in time trajectory of a particle in contact with a POPC GUV. The particles at the periphery or inside GUVs were already in contact with the GUV before the start of the acquisition. The scale bar is 20 µm. *(right)* 3D visualization of the configuration during hydrodynamic docking.

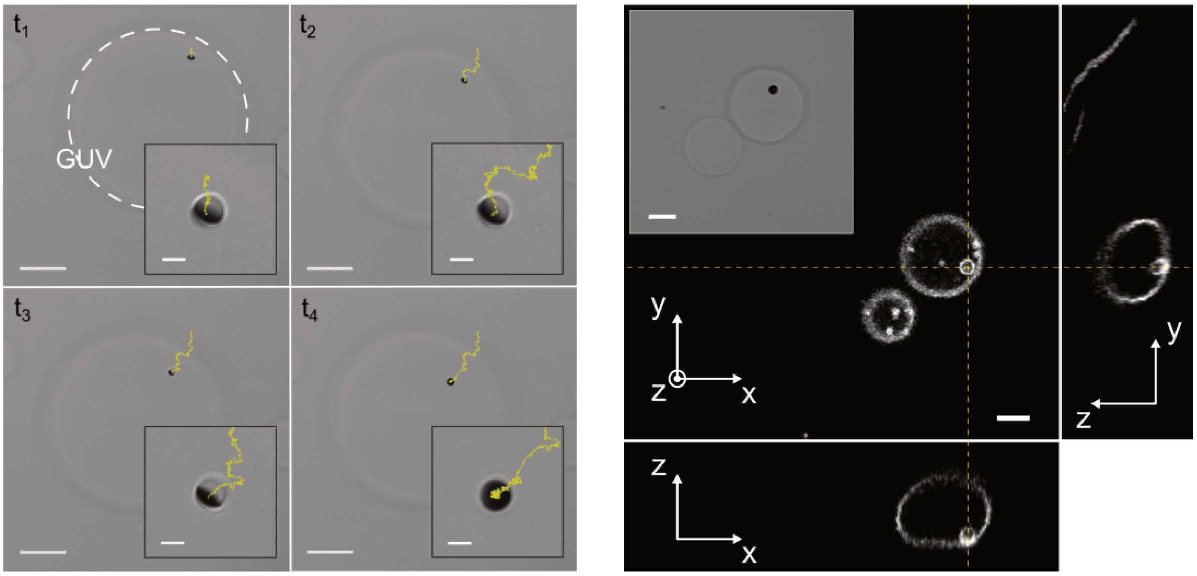

Figure 4.4: *(left)* Snapshots of a bright field microscopy acquisition showing wrapping of a Janus Cu@SiO_2 particle by a POPC GUV. Backward in time trajectory is shown in yellow. Scale bars are 15 µm. In insets, scale bars are 2 µm. *(right)* Confocal microscopy images showing the xy, zy and zx planes allowing to show the fluorescence signal from the lipids corresponding to the GUV and the wrapped particle. Inset shows the corresponding bright field image. Scale bars are 5 µm and 7 µm in confocal and bright field acquisitions, respectively.

sample are engulfed by GUVs (Figure 4.3). In the first step of the interaction, the particle moves in the wedge defined by the bottom wall and the GUV membrane, which is slightly deformed by the particle, as sketched in Figure 4.3 *(right)*. The first two snapshots at times t_1 and t_2 in Figure 4.4 *(left)* correspond to bright field microscopy images of the *capture*.

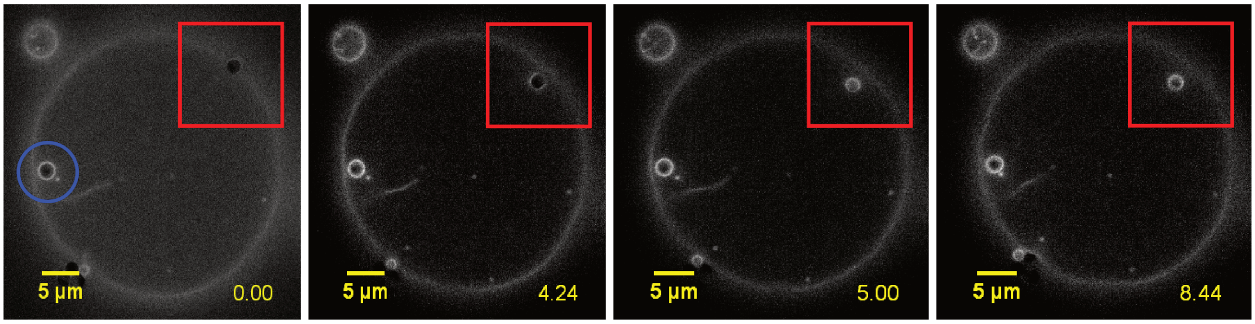

Figure 4.5: Fluorescence microscopy snapshots of an acquisition which shows the engulfment dynamics of a particle (occurring in the region delimited by the red rectangle). The blue circle designates a Cu@SiO_2 particle that is already fully wrapped by the vesicle at the start of the acquisition. Stamps account for the time in seconds elapsed since the acquisition start.

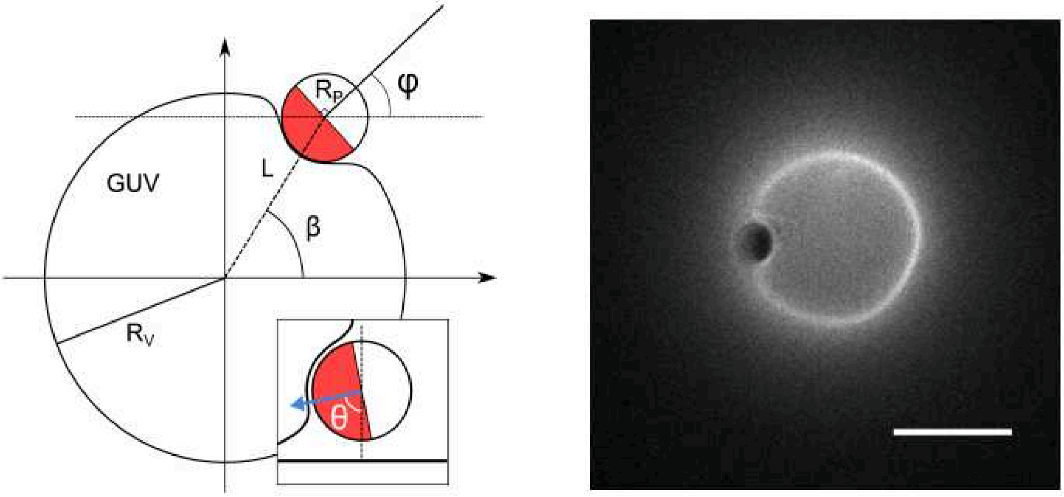

Figure 4.6: *(left)* Sketch defining the angles φ, β the distance L and the out-of-plane angle θ. *(right)* Fluorescence microscopy image of a particle in the capture phase, deforming the GUV. Scale bar is 10 µm.

After the hydrodynamic capture, which can last several tens of seconds, a transition occurs and a sudden radial displacement of the particle towards the projected GUV center of mass is observed at the time t_3 in Figure 4.4 *(left)*. At time t_4, the particle appears completely dark, evidencing a change of orientation and the trajectory shows a more confined diffusion than previously. Using confocal microscopy, we can show that at this final stage, the particle is inside the GUV volume while being fully wrapped by the lipid membrane (Figure 4.4 *(right)*), and remains in this stable state indefinitely. Figure 4.5 shows the wrapping process dynamics in fluorescence microscopy with the particle becoming fluorescent as a result of full wrapping by the fluorescently labelled lipid membrane. Note that in our experimental conditions, the wrapped particle is connected to the mother vesicle with a small neck or tube, as demonstrated in Section 3.2. Particle engulfment occurs only for floppy GUVs showing low tensions ($\sigma < 10^{-7}$ N.m^{-1}) and as shown in Figure 4.4, it occurs at the GUV periphery in the wedge defined by the bottom wall and the lipid membrane. In the next sections, we will describe quantitatively the two different steps of the phenomenon introduced here.

4.4 Active particle hydrodynamic docking at the vesicle periphery

In order to elucidate on the mechanism responsible for capture of the particle at the GUV periphery, we quantify here the particle motion focusing our attention on the rotational dynamics. During the *capture* phase, the Cu cap of the particle is indeed systematically facing the GUV membrane. A top view of the situation is sketched in Figure 4.6 *(left)*, together with the definition of the particle orientation angle φ in the observation plane. The azimuthal angle of the particle radial position β and the distance between the particle and GUV projected centers L are also defined. An additional particle angle θ for the out-of-plane orientation can be defined as sketched in the inset of Figure 3A ($\theta = 0$ when the Janus boundary is parallel to the observation plane and the Cu hemisphere points towards the substrate). A component of the active propulsion force is oriented towards the lipid membrane and promotes the deformation of the latter. This orientation can be observed in bright field microscopy as in Figure 4.4 *(left)* and deformation of the vesicle can be confirmed using fluorescence microscopy as shown in Figure 4.6 *(right)*.

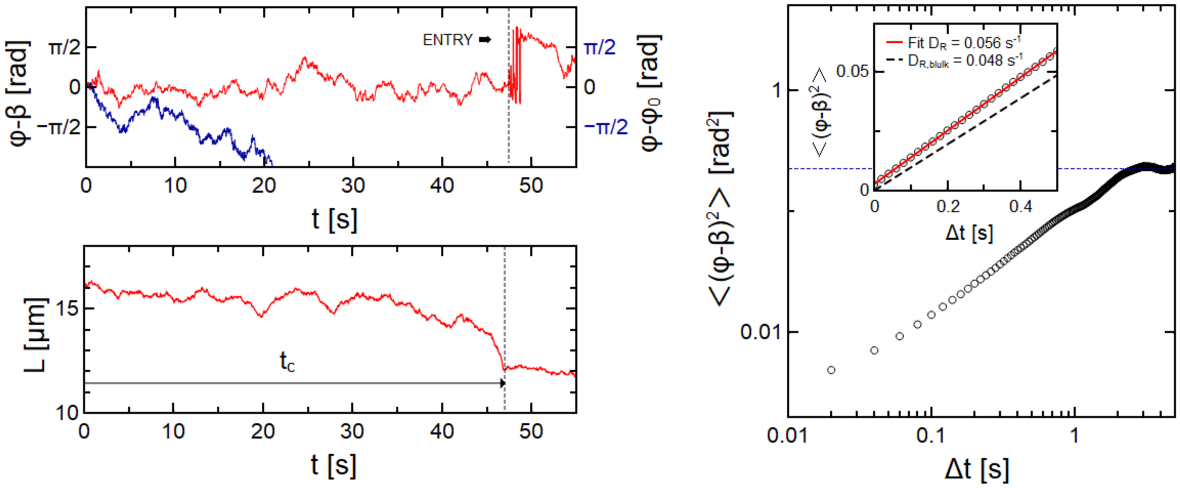

Figure 4.7: *(top left)* Red curve shows the temporal evolution of the angular difference $\varphi - \beta$ for a particle in contact with a GUV before being wrapped. The blue curve shows the evolution of the angle φ with respect to $\varphi_0 = \varphi(t = 0)$ for a particle far from a GUV. *(bottom left)* Evolution of the distance L over time for a particle in contact with the GUV at $t = 0$. (*right*) Log-log graph of the mean squared angular displacement for φ during the capture phase, before the full wrapping transition. At short times (inset), we can fit the diffusion coefficient D_r while the plateau at long times evidences the angular confinement of the particle during this phase.

The time evolution of the angular difference $\varphi - \beta$, plotted in Figure 4.7 *(top left)*, shows a zero mean value $\langle \varphi - \beta \rangle \approx 0$, and a clear orientational confinement of the particle with the Cu cap facing towards the GUV projected center. The confinement effect is apparent when comparing $\varphi - \beta$ to the time evolution of the orientation $\varphi - \varphi_0$ (where $\varphi_0 = \varphi(t = 0)$ is a reference angle) of an active particle far from the GUV, also shown in Figure 4.7 *(top left)*. Here, the in-plane particle orientation during capture $\langle \varphi - \beta \rangle \approx 0$ is very different from the one observed for pusher type swimmers, which align as $\langle \varphi - \beta \rangle \approx \pi/2$ performing orbital motion around GUVs, as seen in Figure 4.8, or solid spherical obstacles [71, 69, 74, 58]. These results point to a self-propulsion mechanism of Cu@SiO_2colloids in glucose generating puller-type swimmer flow-fields, as it is in H_2O_2 with the Cu cap forward [65]. Far-field hydrodynamics models indeed predict that puller type swimmers encountering a spherical obstacle should be trapped by the interface and remain motionless even for reasonably low dipole strengths and small obstacles [73]. Hence, the *capture* observed in our experiments can be attributed to the far-field hydrodynamic attraction expected for puller active particles close to obstacles. The additional complexity arising from the softness and fluidity of the GUV membrane does not seem to modify the attractive nature of those interactions.

The particle orientation is however not frozen and $\varphi - \beta$ show significant fluctuations, which indicates rotational diffusion at short times while experiencing an effective restoring torque at long times. Hence, we calculated the mean squared angular displacement (MSAD) of $\varphi - \beta$, which we plot in Figure 4.7 *(right)*. At short times, the slope of the MSAD allows to extract the in-plane rotational friction ζ_φ experienced by the particle during the capture phase. The fit yields $\zeta_\varphi = 7.3 \times 10^{-20}$ N.s.m (plain red line in the inset) which is close to the theoretical value expected for the rotational friction experienced by a spherical $R_P = 1.5$ µmm particle in the bulk $\zeta_{ro,b} = 8\pi\eta R_P^3 = 8.5 \times 10^{-20}$ N.s.m. Hence, no additional dissipations due to the GUV membrane are experienced by the particle during the *capture*, that points to a large water gap (> 100 nm) between the membrane and the particle surface, [119] which does not permit adhesive surface interactions to play a role and agrees with a far-field hydrodynamic interaction.

The magnitude of the MSAD($\varphi - \beta$) plateau at long times, plotted in Figure 4.7 *(right)*, provides an angular range $\varphi^* = \sqrt{\langle (\varphi - \beta)^2 \rangle_{sat}} \approx 0.47$ rad, which describes the competition between the Brownian diffusion that tends to randomize the particle orientation and an effective restoring torque tending to align the particle towards $\varphi - \beta = 0$. As described before, the origin of this restoring torque can be purely hydrodynamic. In this first stage of the interaction between the active colloid and the GUV characterized by far-field hydrodynamic effects, the adhesion energies between the two particle faces (Cu and SiO_2) and the GUV membrane, quantified by an adhesive energy per unit area w, are not expected to play a significant role for the particle orientational confinement. In Appendix 8.8, we calculate the adhesion energy density difference between the Cu and SiO_2 hemisphere which would correspond to the angular range measured here.

Note that our ability to unequivocally determine the in-plane orientation φ during capture relies on the out-of-plane orientation $\theta \approx \pi/2$ (see inset in Figure 4.6 *(left)*), which makes the Janus boundary visible under the microscope in bright field. While $\theta \approx \pi/2$ is a signature of an hydrodynamic interaction with the lipid vesicle membrane, the bright field acquisitions do not allow to univocally determine if the Cu hemisphere is pointing upwards or downwards (see Section 2.5.3). In bright-field microscopy, particles show the same aspect for $\theta - \Delta\theta$ and $\theta + \Delta\theta$. Hence, we cannot determine whether the particle is slightly oriented towards the lipid membrane as shown in Figure 4.3B, or towards the glass substrate. Still, in our experiments $\langle \varphi - \beta \rangle \approx 0$ shows that the interaction with the lipid membrane dictates the engulfment behavior of the active particle by the GUV.

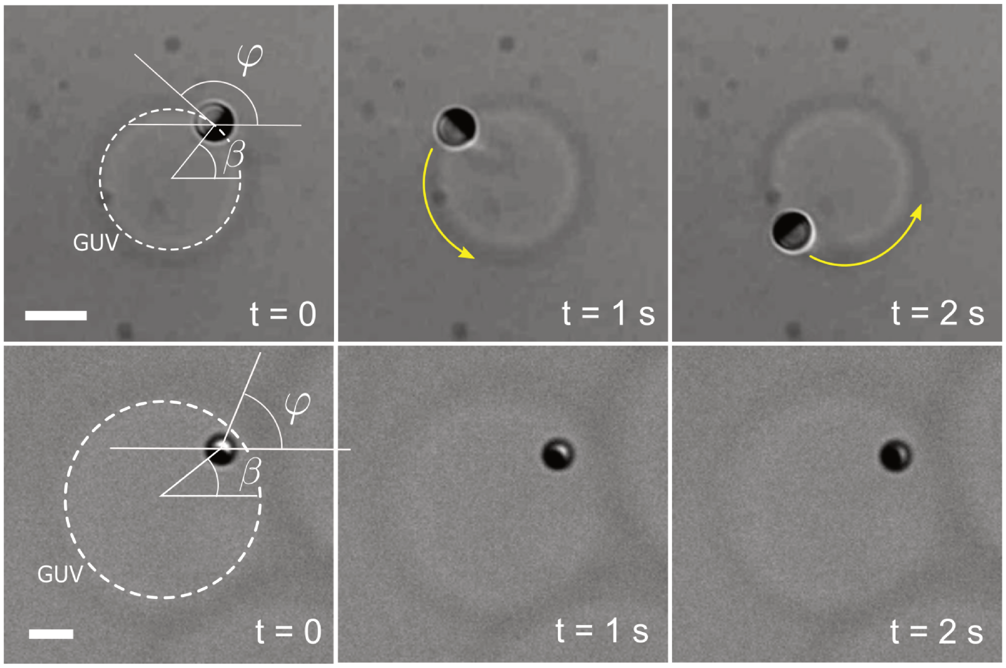

Figure 4.8: Comparison between the behavior of swimming $Pt@SiO_2$ Janus colloids in H_2O_2 and $Cu@SiO_2$ in glucose, evidencing the difference in hydrodynamic interactions. *(Top row)* Snapshots of a Pt-Si Janus puller swimmer in H_2O_2 at the periphery of a GUV for three times spaced of 1 second. *(Bottom row)* Snapshots of a $Cu@SiO_2$ Janus in glucose during the capture phase at the periphery of a GUV at three different times. Scale bars are 5 µm.

The transition to full wrapping is evidenced by an abrupt variation of the distance L in Figure 4.7 *(bottom left)* at the end of the capture phase. The approaching of the particle is however not always a direct effect of the transition to full wrapping. It happens that the particle first moves towards the GUV projected center of mass and remains confined between the GUV and the substrate before undergoing the full wrapping transition. It can also be seen in Figure 4.7 *(top left)* that after the transition (represented by the vertical dashed line), the in-plane orientation φ can not be precisely measured and show large variations as a result of the out-of-plane reorientation of the particle, which does not allow to image the Janus boundary. During the capture step, there is a dynamics associated with the drainage of the water film such that the particle-membrane distance is not the equilibrium one. Indeed, the particle-membrane surface interaction potential, in the case of non-specific adhesion, is minimal at separation distances in the range 20-100 nm [163, 164] while the basin of attraction associated to the hydrodynamic capture is of the order of the swimmer body size (few micrometers here) [73]. The characteristic time τ_d associated to the drainage of the water film can be estimated from Reynolds law [165] and yields $\tau_d \approx 10^1$ s with the active propulsion as driving force. To investigate the dynamics towards the wrapping transition, measurements on the membrane profile upon wrapping and the driving forces of the process will be discussed in the following section.

4.5 Wrapping transition dynamics

The dynamics of the GUV wrapping the active particle can be followed using fluorescence microscopy. In most cases, the transition to full wrapping takes place at the periphery of the vesicle in Figure 4.4. In some rare cases for GUVs of small sizes (7-10 µm radii), the particle can slowly crawl underneath the vesicle and reach the GUV projected center, as depicted in Figure 4.9. In this case, one can take advantage of the geometry to monitor the evolution of the projected GUV area and particle fluorescence during the wrapping dynamics. In Figure 4.9 *(left)*, one can see fluorescence microscopy snapshots of an active particle that came in contact with a relatively small GUV, and during the capture phase reaches the center of the circular projected GUV area. At time $\tau_1 = 19.72$ s after the start of the acquisition, the particle is not wrapped yet and the situation corresponds to the one depicted on the top panel of Figure 4.9 *(right)*. At time $\tau_4 = 22.08$ s, the particle is fully wrapped and the situation corresponds to the situation of the lower panel in Figure 4.9 *(right)*, while intermediate times correspond to the dynamics of full wrapping transition ($\tau_2 = 21.12$ s and $\tau_3 = 21.16$ s). In Figure 4.10 *(left)*, we show representative intensity profiles passing through the projected GUV center of fluorescence microscopy images from Figure 4.9 *(left)*. The two external peaks correspond to the bright circle coming from the GUV projection in the imaging plane. Such profiles allow to follow the evolution of an apparent projected radius $R_{v,app}(t)$ during the full wrapping transition from the distance between these two peaks.

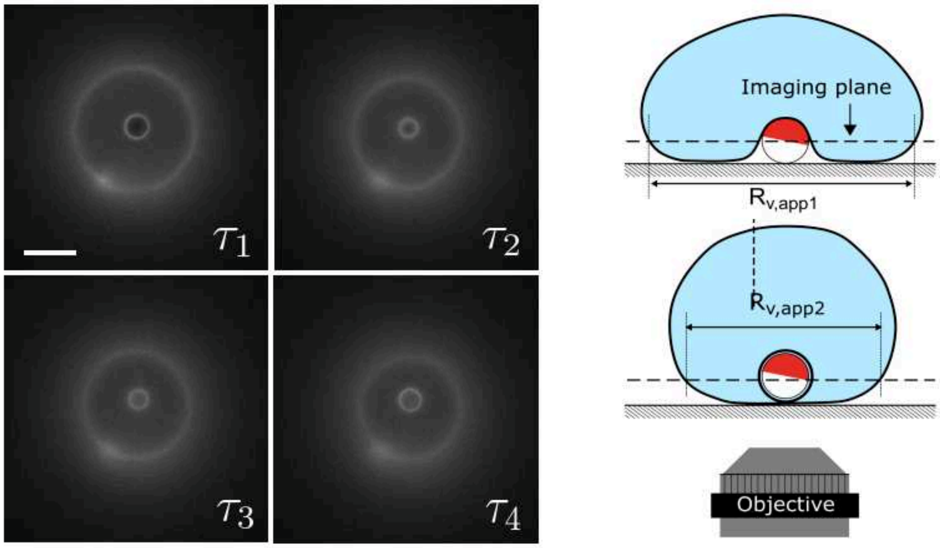

Figure 4.9: *(left)* Snapshots of a fluorescence microscopy acquisition showing the partial wrapping to full wrapping transition in the case of a GUV sitting on top of the particle (see schematics on the right). The outer ring is the membrane and the inside smaller ring becoming a disk is the partially wrapped particle becoming fully wrapped as seen from below. 1. 44 seconds separate τ_1 and τ_2. Scale bar is 5 µm in length. *(right)* Sketch illustrating the situation on the left.

Plotting the evolution of $R_{v,app}$ during the transition (from τ_1 to τ_4) in Figure 4.10 *(right)* shows a decrease of more than a micron, which is a signature of the full wrapping transition. Indeed, fully enveloping the particle with membrane requires pulling more membrane surface area to the wrapping site resulting in a decrease of the apparent vesicle projected radius (as depicted on the sketch in Figure 4.9 *(right)*) as the GUV sphericity increases. Conversely, the fluorescence signal measured from the region corresponding to the particle projected area (quantified by the so-called pixel integrated density in Figure 4.10 *(right)*) increases following the same dynamics, confirming the full wrapping of the particle. During this transition, the contact line advances from the equator of particle (the Janus boundary) to its pole. We show here that this transition occurs in a time $t_{in} \approx 2$ s, resulting in a contact line velocity $v_c = \pi R_P / 2t_{in} = 1.17\ \mu\text{m.s}^{-1}$. This is comparable to contact line velocities measured in the system of Spanke et al. [166], where wrapping was triggered by depletion attraction with

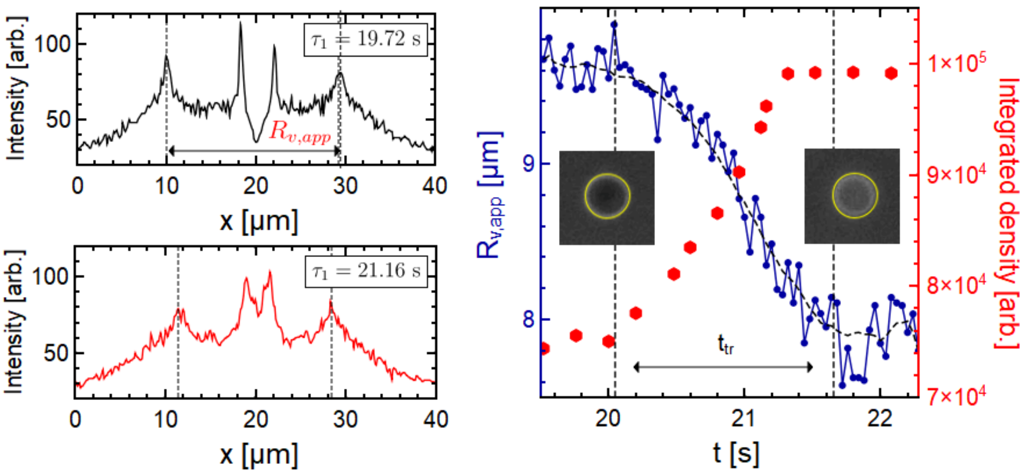

Figure 4.10: *(left)* Intensity profiles along a line passing through the projected GUV center and corresponding to the times τ_1 and τ_4 showing how $R_{v,app}$ is extracted. *(right)* Temporal evolution during the wrapping transition of $R_{v,app}$ and the integrated pixel density in the region of the acquisition bounded by the particle contour. This reflects the increase of fluorescence signal collected from this region corresponding to the presence of lipids due to full wrapping.

adhesion energy densities of the order of 10^{-6} N.m^{-1} for similar particle size ($R_P = 1$ μm).

In order to evaluate the adhesion energy densities in our system, we performed adhesion experiments of GUVs on planar SiO$_2$ and Cu surfaces [167, 168, 165]. We are able to thermally deposit a nanometric Cu layer on glass slides over several cm^2 surface area using the same technique employed to deposit the cap on the SiO$_2$ particles. Figure 4.11 *(left)* illustrates the performed experiment to determine w and defines the contact radius of cur-

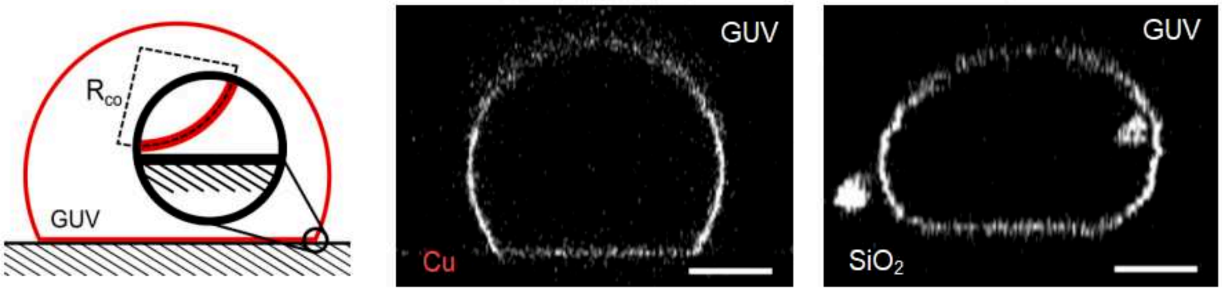

Figure 4.11: *(left)* Sketch of the experiment and definition of the contact curvature radius R_{co}. *(middle)* Representative transverse views (xz plane) from a confocal microscopy acquisitions of osmotically deflated POPC GUVs sedimented on a Copper coated glass substrate and *(right)* on a bare glass substrate. Scale bars are 10 µm in length.

vature R_{co} which will be of interest here. Using a confocal microscope, we can extract the full 3-dimensional shape of the adhesive vesicles. If we compare typical side view profiles (x-z plane) acquired with confocal microscopy of an initially floppy vesicle on Cu (Figure 4.11 *(middle)*) or on SiO_2 glass (Figure 4.11 *(right)*), it is clear that the interaction with the bottom substrate is very different leading to different vesicle shapes. The shape of the unbound part of the membrane is very close to a spherical cap (expected in the limit of high adhesion [165]) in the case of Cu substrate, while the shape is more elongated and the membrane appears more fluctuating for SiO_2. Indeed, the bending energy that tends to maximize the membrane curvature radius over the whole surface area is in competition with the adhesion energy that tends to maximize the membrane area in contact with the surface. The curvature radius at contact therefore reads [167]:

$$R_{co} = \sqrt{\frac{\kappa_b}{2w}}, \tag{4.2}$$

with κ_b the bending modulus of the membrane. For a deflated GUV on a Cu covered glass slide, the resolution of the profile acquired with confocal microscopy does not allow to fit a circle to extract a curvature. The fact that the curvature is beyond the limit set by our resolution allows however to set a lower bound for the curvature which yields a lower bound for the adhesion energy density w. If one takes $R_{co,\mathrm{Cu}} \leq 0.5\,\mu\mathrm{m}$ as the resolution-limited higher bound of measurable curvature radius, we get $w_{\mathrm{Cu}} \geq 2 \times 10^{-7}$ N.m^{-1} as a bounding value for the adhesion energy density. For the case of the bare glass substrate, however, the situation is different and one can always define a radius of contact curvature using confocal images and ImageJ analysis techniques [169]. The average fitted radius on $N = 5$ different GUVS is $\langle R_{co,\mathrm{SiO_2}} \rangle = 7.5 \pm 0.6\,\mu\mathrm{m}$ yielding $w_{\mathrm{SiO_2}} = 8.8 \pm 1.3 \ \times 10^{-10}$ N.m^{-1}.

Hence, the associated adhesion energy density w_{Cu} is several orders of magnitude larger than $w_{\mathrm{SiO_2}}$ in this geometry. This attractive interaction potential between a POPC lipid bilayer and a Cu surface results from many contributions including electrostatic double-layer, van der Waals, hydration, hydrophobic and steric repulsion [170]. Electrostatic attraction alone between the slightly positively charged Cu (zeta potential $Z_{\mathrm{Cu}} \approx +14$ mV [65, 66]) and the zwitterionic POPC (reported to show slightly negative zeta potential $Z_{\mathrm{POPC}} \approx -7$ mV [171]) could hardly explain the measured adhesion. Other short range chemical interactions could play a role. For example, it was shown that Cu^{2+} ions can bind to PC and PE lipid headgroups [172, 173] and induce structural changes on the membrane. It is not obvious however how to quantify these effects in terms of an effective adhesion.

4.6 Theoretical modelling of the wrapping energy landscape

In the previous sections, we showed that active Cu@SiO$_2$ Janus particles are able to deform GUV membranes until reaching a stable complete engulfment. We also measured the equilibrium adhesion energy densities and the characteristic capture time. By using these experimental values, in this section, we model the driving energies and costs associated to the particle engulfment, in order to understand its stability. We will also try to gain insights on the dynamics of the phenomenon, in particular the duration of the capture time t_c before the wrapping transition.

The system considered in this model is composed of a particle and a fluid membrane with bending rigidity κ_b, tension σ and particle-membrane adhesive energy per unit area w. If one assumes a flat membrane and negligible volume conservation constraints, the free energy of the system can be described with the following Helfrich-Canham Hamiltonian [174]:

$$E_{\mathrm{tot}} = \int_{A_{tot}} \frac{\kappa_b}{2}(2M - m)^2 \,\mathrm{d}A - \int_{A_b} w \,\mathrm{d}A + \sigma\Delta A - fh, \tag{4.3}$$

with M the membrane mean curvature, m a spontaneous membrane curvature, ΔA the membrane excess area pulled to the wrapping site, A_b the membrane area bound to the particle, f the propulsion force and h penetration depth. Note that the Helfrich Hamiltonian usually contains a Gaussian curvature term, which will be ignored in the following due to the absence of topology change [81]. The energetic cost associated to the membrane area detached from the glass substrate upon wrapping is disregarded, as it is expected to be small compared to other contributions ($< w_{\mathrm{SiO_2}}\Delta A \approx 10^{-9} \times 10^{-10} \approx 20\ k_{\mathrm{B}}T$ for $w_{\mathrm{SiO_2}} = 8.8 \pm 1.3 \times 10^{-10}$ N.m^{-1} as measured in the previous section and assuming the largest possible area difference $\Delta A \sim 100\,\mu\mathrm{m}^2$ in Figure 4.9).

4.6.1 Local membrane deformations

Let us first consider that the adhesion, bending and tension contributions of the membrane segment *bound* to the particle dictate the wrapping angle α defined in the inset of Figure 4.12 *(left)*. Thus, we ignore at the moment the contribution of the free segment (the vesicle area that is not bound to the particle). This simplification is expected to apply to infinite planar membranes with vanishing spontaneous curvature [81, 138], and has been used to explain the experimental wrapping phase diagram of isotropic particles adhering to floppy vesicles with small spontaneous curvature $|m| \leq 4 \times 10^4$ m^{-1} [77]. In the case of a spherical particle with radius R_P, the energies associated with tension and bending for the bound membrane area $A_b = 2\pi R_P^2(1-\cos\alpha)$ are: $E_\sigma = \pi\sigma R_P^2(1-\cos\alpha)^2$ and $E_b = 4\pi\kappa_b(1+mR_P)(1-\cos\alpha)$ respectively, where m is a membrane spontaneous curvature. These two contributions can be calculated in our system using a standard value of the bending rigidity $\kappa_b = 27.3 \pm 5.1\ k_\mathrm{B}T \approx 10^{-19}$ J for POPC vesicles in glucose/sucrose solutions [103] and a tension $\sigma = 10^{-8}$ N/m as a representative value accounting for the tension distribution from previous the force measurements on floppy vesicles prepared with the same protocol, see Section 3.2. The two negative (energetically favorable) contributions to the free energy of the system can also be estimated. The work done by the propulsion force f can be expressed as a function of α as $E_f = -fR_P(1-\cos\alpha)$. Here, an upper bound of the active force f in our system can be calculated by taking it to be equal to the translational friction force when the particle is far from a GUV at the highest measured projected velocity V. We then have $f = \zeta_{tr,b}V = 6\pi\eta R_P V \approx 0.1$ pN. Considering the Janus geometry of the particle, the

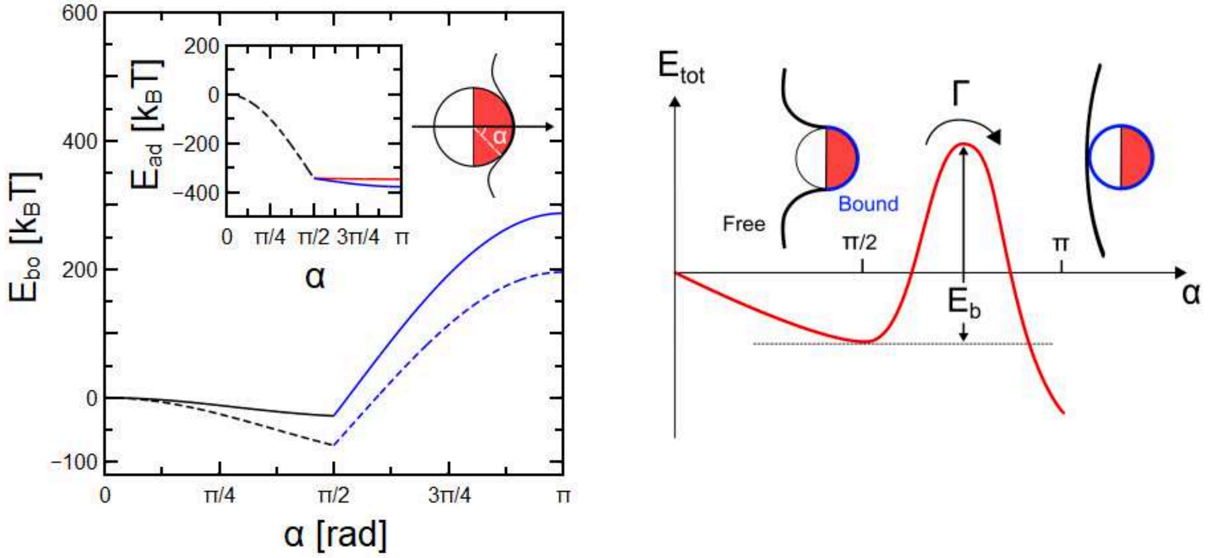

Figure 4.12: *(left)* Energy associated to the membrane segment bound to the particle E_{bo} as a function of wrapping angle. Plain line stands for spontaneous curvature $m = 0$ and dashed line to $m = -10^5\ \mu$m^{-1}. Insets show the adhesion energy between the membrane and the particle as a function of wrapping angle considering the particle is wrapped with the copper facing towards the membrane. Definition of the wrapping angle α is also recalled on the inset sketch. *(right)* Illustration of the expected shape of the total energy ($E_{bo} + E_{free}$) as a function of wrapping angle α and definition of the energy barrier E_b between the partial and full wrapping states with associated hopping rate Γ.

adhesion energy density w is not constant throughout the wrapping process. Indeed, the adhesion energy density of Cu w_{Cu} and SiO$_2$ w_{SiO_2} with the membrane are very different, as shown in the previous section. The adhesion energy then reads:

$$E_{ad} = \begin{cases} 2\pi R_P^2 \left(1 - \cos\alpha\right) w_{Cu} & \alpha < \pi/2 \\ 2\pi R_P^2 w_{Cu} + 2R_P^2 \left(\sin\left(\alpha - \frac{\pi}{2}\right)\right) w_{Si} & \alpha \geq \pi/2 \end{cases} \tag{4.4}$$

if one considers that the wrapping occurs with the Cu cap facing the membrane first, as in experiments. Taking $w_{\text{Cu}} = 0.2\,\mu\text{N}\,\text{m}^{-1}$ the lower bound inferred from confocal microscopy acquisitions and $w_{\text{SiO}_2} = 0.88$ nN.m^{-1} allows to have a full description of the wrapping energy landscape for the bound membrane segment. In Figure 4.12 *(left)* we plot the sum of the contributions for the bound membrane segment together with the active force and adhesion contributions $E_{bo} = E_b + E_\sigma + E_f + E_{ad}$ as a function of wrapping angle α defined in the sketch. Inset shows the evolution of E_{ad} alone when taking into account the Janus geometry (Equation (8.3)). It appears clearly that using values of w_{Cu} inferred from experiments, the adhesion is what drives the wrapping and not the active force as it is much weaker, $|E_{ad}| > |E_f|$. However, due to the Janus geometry and the difference in the Cu and SiO$_2$ affinities with the membrane, the only minimum is predicted at $\alpha = \pi/2$ as shown by the E_{bo} vs α curves in Figure 4.12 *(left)*. Note that the evolution of $E_{bo}(\alpha)$ is qualitatively the same in the presence of a negative spontaneous curvature $m = -10^5$ m^{-1} expected in our system due to the inner sucrose/outer glucose solution asymmetry across the membrane [162, 175]. In other terms, when considering only the bound membrane segment, a stable partial wrapping up to the equator is predicted due to the anisotropy in particle adhesive properties ($w_{\text{Cu}} \gg w_{\text{SiO}_2}$), and the full wrapping state $\alpha = \pi$ appears highly unstable and energetically costly. This is not consistent with our observations at long times, showing that particles can undergo a transition to full wrapping ($\alpha = \pi$, see Figure 4.4 and 4.9). The minimum at $\alpha = \pi/2$ may however describe the transitory state observed experimentally in Figure 4.6. Hence, the assumption that the energy associated to the shape of the free membrane segment E_{free} is negligible does not hold for our system.

In Figure 4.12 *(right)*, we sketch the shape of the total energy profile for a Janus particle $E_{tot}(\alpha) = E_{bo}(\alpha) + E_{free}(\alpha)$ which would be consistent with our experimental observations, with a global minimum at $\alpha = \pi$. The shapes adopted by the unbound (free) membrane segment for $0 < \alpha < \pi$ might be costly in regards to both tension and bending in the presence of a spontaneous curvature[81]. However, when $\alpha = \pi$ (full wrapping), a narrow neck is formed behind the particle and the rest of the vesicle adopts a shape with $M \approx 1/R_v$.

Narrow necks are highly curved shapes, but the principal curvatures being of opposite signs lead to vanishing mean curvatures and in turn low bending energies, which could explain the lower energy for the state $\alpha = \pi$ from the unbound membrane segment standpoint [81, 176]. This is however only rigorously true if $m = 0$, but we showed in Section 3.3 that the neck structure formed upon wrapping is very stable. This gives rise to an energy barrier E_b that separates the metastable partial wrapping state and the stable full wrapping state. Theoretical and numerical works considering isotropic adhesive particles and the full vesicle shape already reported the existence of bistable regimes, where an energy barrier separates the free/partially engulfed and the completely engulfed states which are therefore (meta)stable [82, 177, 20]. Taking into account the presence of a negative spontaneous curvature, the calculations performed in Ref. [82] indeed predict a bistable regime in our range of particle and vesicle sizes, and considering the particle to be isotropic with $w = w_{\mathrm{Cu}} \sim 10^{-7}$ N.m^{-1}. Furthermore, more recent results carefully considering contributions from a constant-tension reservoir or spontaneous tension predict bistability for negative spontaneous curvatures for a broad range of adhesion strength [20]. Even if these models consider vesicle shapes simpler than the ones observed in our systems and do not account for the Janus particle geometry, they allow to rationalize the stability of the fully wrapped state from contributions of the unbound membrane segment.

4.6.2 Energy barrier calculation

While calculation of the full energy associated to both the particle-membrane interaction and the full membrane shape is impossible with our experimental data (the full membrane shape can not be determined), we could try estimate the energy barrier E_b separating the partial wrapping state and the full wrapping state. Indeed, for cases when the capture time is large compared to the fast local relaxation processes in the potential well (~ 1 s) around $\alpha = \pi/2$ (such as for the cases in Figure 4.12C), we can use the Kramers theory of escape over an energy barrier. The latter links a hopping rate Γ, i.e. the inverse average time spent by the particle in the metastable state before hopping $\langle t_{hop} \rangle$, to E_b such as [178, 76]:

$$\Gamma = \frac{1}{\langle t_{hop} \rangle} = \frac{k D_\alpha}{2\pi k_B T} \exp\left(-\frac{E_b}{k_B T}\right) \tag{4.5}$$

where D_α characterizes the dynamics of the fluctuations of the wrapping angle α in the potential well of stiffness k (in the harmonic approximation) around the minimum $\alpha = \pi/2$. Note that D_α has the dimension of a rotational diffusion coefficient (without being one) and k is an energy. Extracting k and D_α in our system would imply being able to resolve the

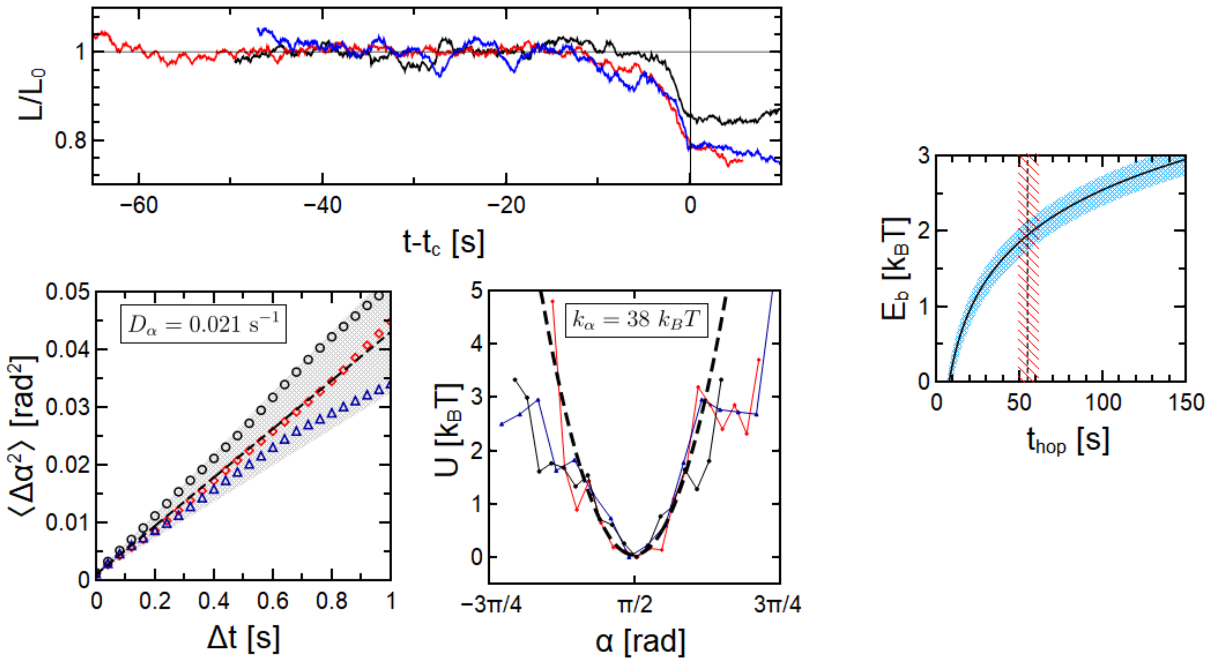

Figure 4.13: *(top left)* Temporal evolution of $L(t)/L_0$ extracted from image analysis (where L_0 is the average distance during the capture step) for three wrapping experiments with $t - t_c = 0$ taken as the moment the full wrapping transition occurred. *(bottom left)* Diffusivity D_α and stiffness k_α extraction by converting position fluctuations into degree of wrapping fluctuations through Eq. 4.7. *(right)* Height of the energy barrier E_b as a function of the inverse hopping rate $1/\Gamma = t_{hop}$ using the Kramers theory [178, 76] of escape over an energy barrier using stiffness and diffusivity deduced from the two bottom left panels. Vertical dashed line stands for average t_c from *(top left)*.

fluctuations of α in the partial wrapping state, which is not possible with our setup. One quantity that we can measure however is the distance L between the particle and the GUV projected center of mass, see Figure 4.13. We can impute the fluctuations of L to fluctuations of α as:

$$\Delta L = R_P \left(\sin\left(\frac{\pi}{2} - \alpha\right) - \sin\left(\frac{\pi}{2} - (\alpha + \Delta\alpha)\right)\right) \tag{4.6}$$

Which in the small angle approximation $\sin(x) \approx x$ (as $\alpha \approx \pi/2$ in the half wrapped state and $\Delta\alpha \ll 1$), yields:

$$\Delta L = -R_P \Delta\alpha \tag{4.7}$$

Hence, we can plot the distribution of α (see Figure 4.13 *(bottom left)*) inferred from L and translate it in an effective potential $\Delta U(\alpha)$, which we can fit assuming it is quadratic around

$\alpha = \pi/2$ to extract the stiffness k. The average stiffness of the quadratic trapping potential using our data is $k = 38 \pm 4\ k_\mathrm{B}T$. Diffusivity D_α can be inferred from a linear fit at short times of the mean squared angular displacement curves of α as a function of lag time (see Figure 4.13 *(bottom left)*) . The mean diffusivity D_α measured here is $D_\alpha = 0.021 \pm 0.002$ rad^2.s^{-1} (Supplementary Information). We can plot E_b as a function of t_{hop} (Figure 4.12 *(right)*) by reversing Equation 4.5 and by plugging in the calculated k and D_α. This allows to visualize the expected magnitude of E_b for hopping times few tens of seconds long which is what we observe in experiments as a lower bound. Note that t_c can be larger than t_{hop} as it might take some time for the water gap between the particle and the membrane to drain and the adhesion measured in equilibrium to be effective. Still, t_c provides an upper bound for t_{hop} and this reasoning allows to estimate that the full energy profile considering the full (bound and free) membrane shape leads to an energy barrier $E_b \approx 2\ k_\mathrm{B}T$, see Figure 4.13 *(right)*.

4.7 Conclusion

To conclude, we designed a system that autonomously reproduces endocytosis and the wrapping of artificial active swimmers by giant vesicles, only by providing visible light and physiological glucose concentrations. We showed that the velocity of the active particle is not the quantity to maximize in order to observe engulfment by cell-like compartments. In fact, our results evidence the key role of long contact times between the swimmer and the wrapping host. Long contact times during which an active propulsion force component of the particle is directed towards the membrane indeed allow the liquid film between the two objects to drain and physicochemical interactions to be triggered leading to adhesion between the two surfaces. Additionally, time is needed for the system to overcome energy barriers separating two wrapping states. It is therefore crucial that far-field interactions, such as the long-range hydrodynamic attraction between the puller swimmer and the soft obstacle here, prevent the particle to swim away from the vesicle membrane. To generalize, for future investigations we can predict that bigger particles sizes would facilitate the hydrodynamic docking of the particle at the vesicle periphery, due to reduced magnitude of the orientational and translational Brownian noise. However, the associated increase in tension cost will lead to a higher energy barrier [179] and therefore increase the average hopping time over the barrier. This leads to a more effective but slower overall process. For tenser membranes, this energy barrier could be lowered by increasing the adhesion of the particle via designing Janus colloids with both faces showing $w \geq \sigma$. Increasing the membrane negative spontaneous curvature m could also facilitate the full wrapping transition. However, one must bare in mind that spontaneous curvature gives rise to a spontaneous tension $\tilde{\sigma} = 2\kappa_b m^2$, which might be significant for large values of m. For smaller particle sizes, the decrease of the tension energetic cost is followed by an increase of the bending energy cost, leading to a similar barrier height. The enhanced translational and rotational diffusion would however prevent the slow processes to occur as the particle is more likely to diffuse away or reorient before adhesion is triggered. Note that from Reynold's law of drainage, we expect the duration of the film drainage step to be larger for larger spherical particles. However, non-spherical particle shapes could minimize the drainage time to trigger adhesion faster.

Chapter 5

Translational and rotational diffusion of engulfed and confined particles

5.1 Introduction

In the previous chapters, I demonstrated that driven microparticles can induce shape remodelling of floppy vesicles until reaching stable particle wrapping by lipid membranes. Regardless of the engulfment pathway, no change of topology was observed, and the fully wrapped particles remained connected to the mother vesicle. In the first part of this chapter, I report on the diffusion of the microparticles in the fully engulfed state. Translational and rotational dynamics of optically and autonomously engulfed particles were studied in order to evaluate the dissipation in this particular situation. In a second part, I report on the role played by membrane tension on the particle translational diffusion to elucidate on the main dissipative mechanisms at stake. Finally, I describe how optical tweezers can be used to force the interaction of a particle with a tense vesicle membrane, allowing to infer membrane properties from the resulting particle energy landscape.

5.2 Thermal dynamics of free and engulfed particles

5.2.1 Isotropic particles

After a particle was stably engulfed by optical tweezers, as described in Chapter 3, the wrapped particle remains connected to the mother vesicle by a membrane segment which can be a neck or a tube. In order to gain insight on the properties of this structure by analyzing its effect on the particle dynamics, we performed a set of experiments in which we

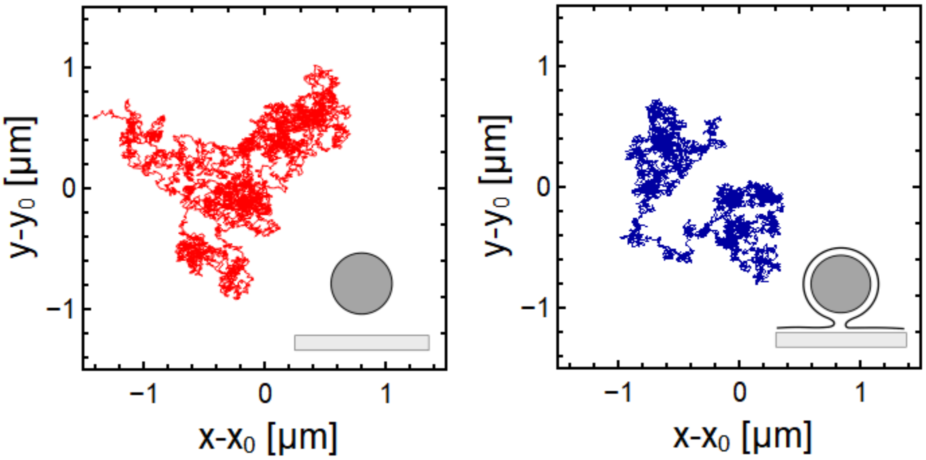

Figure 5.1: Representative trajectories in the xy plane of length $N = 10\,000$ points acquired at 996 frames per second for a *(left)* Free (not wrapped) and *(right)* Wrapped particle with radius $R_P = 1.15\,\mu\text{m}$. Both trajectories resemble standard free Brownian trajectories with no apparent spatial confinement.

track the motion of SiO_2 particles at acquisition frequency close to 1 kHz (996 fps) in the free and wrapped situation. The so-called *free* case refers to the situation where a particle diffuses close to the substrate in the absence of a lipid membrane in proximity, whereas the *wrapped* case refers to the situation where the particle was previously fully wrapped in a lipid vesicle with optical tweezers. Representative trajectories are shown in Figure 5.1, with a total duration of the trajectory of 10 s. Both free and wrapped particle trajectories resemble standard Brownian trajectories on the timescales at stake, and no clear sign of anomalous diffusion or elasticity in the system can be observed.

We plot the experimental two-dimensional mean squared displacement curves associated to several wrapped and free trajectories ($N > 5$ for each case) in Figure 5.2. It appears that for all particle sizes, the MSD shows a purely diffusive behavior for $\Delta t < 1$ s. This confirms that the presence of a neck or tube does not introduce any elasticity at the considered timescales and agrees with the picture of a neck diffusing in the fluid lipid bilayer which only contributes as an additional dissipation of the thermal energy. Indeed, the diffusion appears systematically slowed down for the wrapped particle cases comparatively to the free cases, for all particle sizes.

We quantify this slowing down of the diffusion by extracting the average translational diffusion coefficient $D_t(R_P)$ from linear fits of the MSDs and plot it as a function of par-

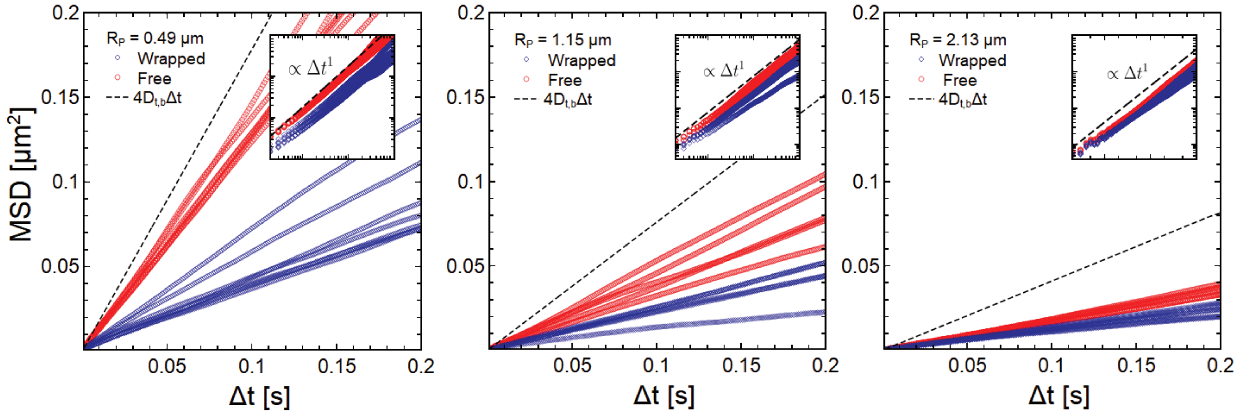

Figure 5.2: 2-dimensional mean squared displacement curves of Free (not wrapped) and Wrapped particles on short timescales for particles with radii $R_P = 0.49\,\mu$m *(left)* , $R_P = 1.15\,\mu$m *(middle)* and $R_P = 2.13\,\mu$m *(right)*. Inset shows a log-log representation up to $\Delta t = 1$ s and evidences the evolution $\propto \Delta t^a$ with $a = 1$. The dashed line stands for the predictions from Stokes-Einstein relation $\langle (x(t+\Delta t) - x(t))^2 \rangle + \langle (y(t+\Delta t) - y(t))^2 \rangle = 4D_{t,b}\Delta t$ with $D_{t,b} = k_B T/(6\pi\eta R_P)$.

ticle size in Figure 5.3 *(left)*. It appears that the experimental values of $D_t(R_P)$ both in the free and wrapped cases lay below the theoretical Stokes-Einstein prediction. This is expected due to the presence of the underlying substrate imposing no-slip boundary conditions, leading to a particle-wall distance dependent drag increase factor $f(h_P)$ such that $\zeta_t(h_P) = f(h_P)\zeta_{t,b} = f(h_P)6\pi\eta R_P$ with $f(h_P \gg R_P) = 1$ far from the interface. In this situation, an expression for $f(h_P)$ is given by the approximate solution to the Stokes equation derived by Fàxen [180, 181]. The dashed line in Figure 5.3 *(left)* stands for the drag correction for a wall-particle surface gap distance $h_P = 200$ nm and shows that the measured diffusion coefficients for the free case can be explained by a drag increase due to proximity of the wall at a reasonable average distance at low ionic strength. Predictions for the reduced drag $\zeta_t/\zeta_{t,b}$ for gap distances $h_P = 240, 360$ and 600 nm, together with experimental values calculated through $\zeta_t = k_B T/D_t$, are plotted in Figure 5.3 *(right)*. Those distances are in agreement with the equilibrium distance of the particle from the substrate considering the balance of electrostatic and gravitational forces, see Appendix 8.9. The increasing monotonic dependence of the reduced translational drag on the particle radius for free particles (red points) is therefore a result of the monotonic decrease of the particle-wall distance h_P with R_P.

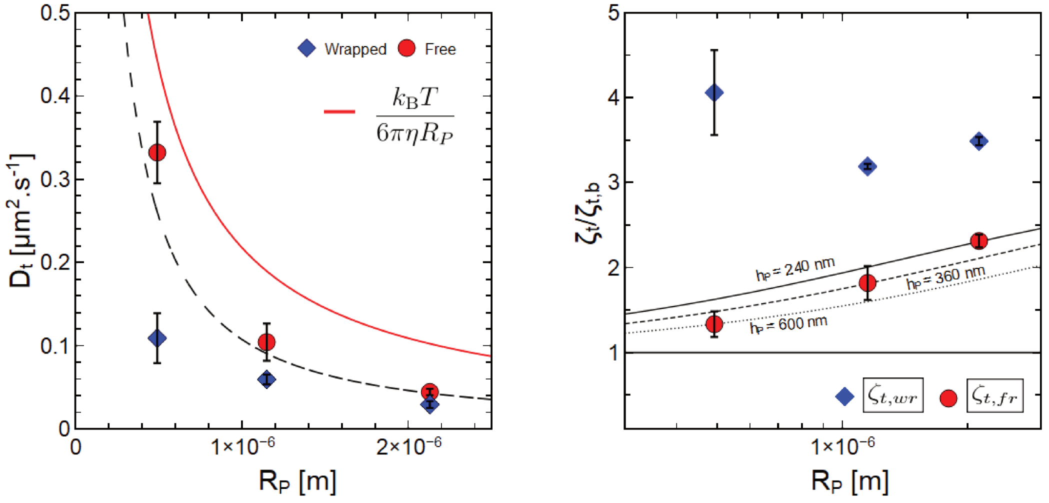

Figure 5.3: *(left)* Average experimental D_t versus particle size R_P calculated from $N \geq 5$ trajectories from different particles engulfed in different vesicles for each point. Error bars stand for the standard deviation. Red plain line represents the bulk prediction from Stokes-Einstein relation, and black dashed line stands for the modified drag resulting from the presence of a solid bounding wall (the substrate) at a gap distance h_P=200 nm as calculated by Fàxen equations [180] *(right)* Reduced experimental drag $\zeta_t/\zeta_{t,b}$ as a function of particle size for free (red discs) and wrapped (blue diamonds) cases with theoretical predictions from Faxén for three different gap distances.

Considering particle-wall distance h_P and hydrodynamic radius R_w variations

For the wrapped particles, we measure a 3 to 4-fold translational drag increase from the bulk prediction value, with a non-monotonic size-dependence as shown by the blue diamonds in Figure 5.3 *(right)*. If we do not consider other dissipative mechanisms than the ones in the simple picture we established by now for free particles, one could be tempted to impute this drag increase to an increase of the hydrodynamic radius $R_w > R_P$ of the wrapped particle or to a decrease of the particle-wall distance h_P (see Figure 5.4 for definition). In most cases, a small volume of fluid is enclosed in the membrane bud with the particle upon optically driven wrapping such that the radius of the membrane bud (that can be determined in fluorescence microscopy) is only few hundreds of nanometers at most bigger than the bare particle radius R_P, i.e. $1 < R_w/R_P < 1.2$ (except in very rare cases as reported in Appendix 8.4). The influence of the wrapping membrane on the equilibrium particle-wall distance h_P is however hard to determine, as the presence of membranes might change for example the electrostatic repulsion with the substrate. Still, the presence of two bilayers between the particle surface and the solid wall in this geometry allows to define a lower bound $h_P > 10$ nm thereby providing a higher bound value $f(h_P = 10\,\text{nm}) \approx 3$ according to Fàxen. We can explain our

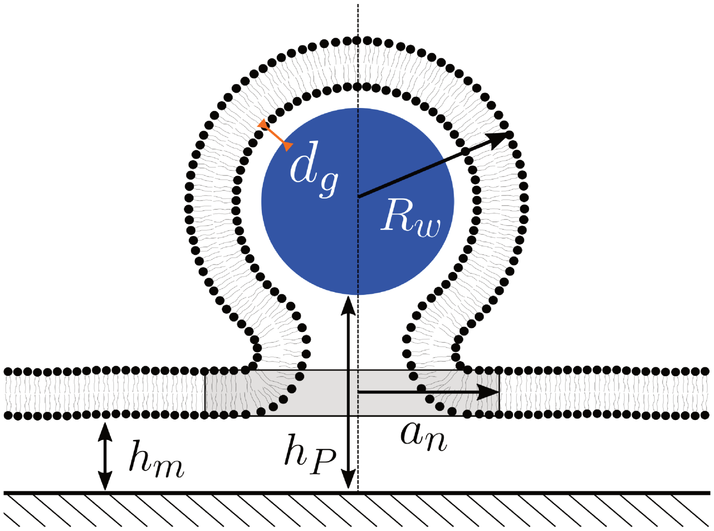

Figure 5.4: Schematic representation of the wrapped particle situation with definition of the effective radius R_w, equivalent disk radius a_n, and film thickness d_g, membrane and particle gap distance h_m and h_P, respectively.

measurements within this framework only considering the limit where both $R_w = 1.2R_P$ and $h_P = 10$ nm yields:

$$\frac{\zeta_{t,wr}}{\zeta_{t,b}} = \frac{f(h_P)6\pi\eta R_w}{6\pi\eta R_P} = f(h_P)\frac{R_w}{R_P} < 3 \times 1.2 = 3.6 \tag{5.1}$$

which could be one interpretation of the drag increase matching our measurements, but failing at capturing the non-monotonic size-dependence of $\zeta_t/\zeta_{t,b}$ with R_P. Indeed, we showed that for the free particles, the dependence of $f(h_P)$ on R_P was a result of the competition between gravitational and electrostatic forces and was monotonic.

Considering membrane viscosity contributions

The analysis of the previous section completely neglects the contribution of the lipid membrane viscosity. Dissipations on the vesicle membrane are indeed expected to occur in our system, which is composed of a particle being wrapped and connected to the mother vesicle with a neck/tube structure. The motion of the particle is now coupled to the motion of this structure within the lipid membrane, which experiences a drag depending on the membrane 2D viscosity η_m. While no model exists accounting for our complex geometry of a wrapped particle connected to a lipid membrane moving close to a wall, we can compare our results with some existing models describing ideal situations. In particular, we can model the neck structure connecting the wrapped particle to the lipid membrane as a solid cylindrical inclusion a_n and account for the dissipations associated to its translational motion in the fluid lipid bilayer.

The translational drag on a cylindrical inclusion of radius a in a lipid membrane with two dimensional viscosity η_m was modelled by Saffman and Delbrück [22] and was later modified by Evans and Sackmann [182] to account for the presence of a solid substrate closeby. This last model can be used in our case to estimate the additional contribution to the drag from a neck of radius a_n that has to diffuse with the wrapped particle in the plane of the mother vesicle membrane (see scheme Figure 5.4). In the case of a thin lubricating layer of thickness $h_m \ll \eta_m/\eta = 1\,\mu\text{m}$ between the membrane and the underlying solid substrate, the drag force exerted on the translating disk is proportional to its velocity with the drag coefficient [182]:

$$\zeta_{ES} = 4\pi\eta_m \left[\frac{1}{4}\epsilon^2 + \frac{\epsilon K_1(\epsilon)}{K_0(\epsilon)}\right] = 4\pi\eta_m\chi(\epsilon) \tag{5.2}$$

where $\epsilon = a_n\sqrt{\frac{\eta}{h_m\eta_m}}$ is the dimensionless radius in the lubrication approximation and

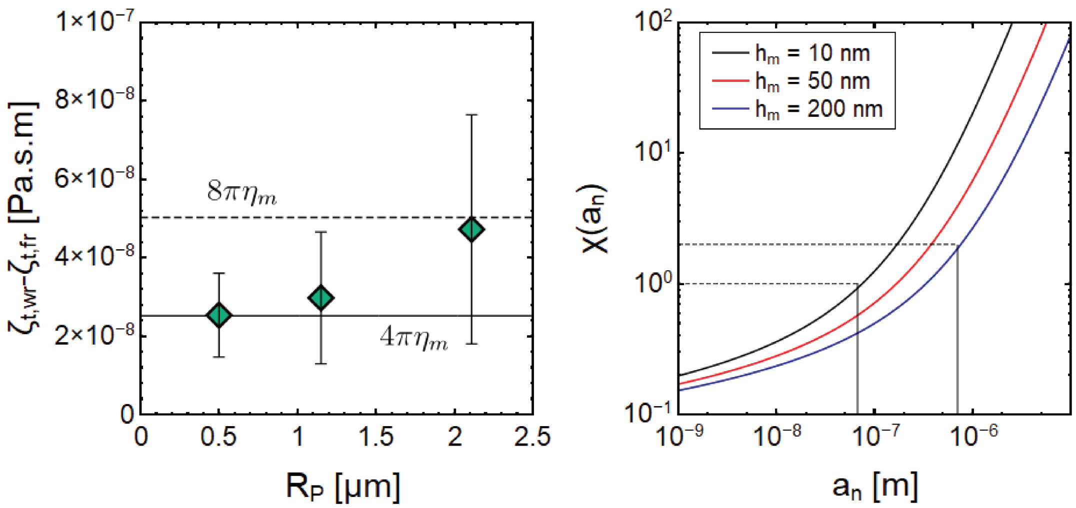

Figure 5.5: *(left)* Plot of the difference between the experimentally measured drags for wrapped and free particles $\zeta_{t,wr}(R_P) - \zeta_{t,fr}(R_P)$ as function of particle radius R_P. The plain and dashed lines are $4\pi\eta_m$ and $8\pi\eta_m$, respectively, which corresponds to ζ_{ES} as in Eq. 5.2 with $\chi(\epsilon) = 1$ and $\chi(\epsilon) = 2$. *(right)* Plot of the function $\chi(a_n, h_m)$ as defined in Eq. 5.2 where the dependence on $\epsilon = a_n\sqrt{\eta/h_m\eta_m}$ is replaced by a dependency in the equivalent disk radius a_n and membrane distance to the wall h_m, with $\eta = \eta_w = 0.001$ and $\eta_m = 2 \times 10^{-9}$ Pa.s.m. It appears that in order to have $1 < \chi(a_n, h_m) < 2$ as suggested from the left plot, it implies $70\,\text{nm} < a_n < 700\,\text{nm}$ for realistic values of h_m with $10\,\text{nm} < h_m < 200\,\text{nm}$.

K_1 and K_0 are first and zero order modified Bessel functions of the second kind. Assuming that the wrapped particle-neck complex diffuses as a single solid object, we can sum the drag exerted disk inclusion with the modified Stokes drag from Eq. 5.1, which yields:

$$\frac{\zeta_{t,wr}}{\zeta_{t,b}} = \frac{f(h_P)6\pi\eta R_w + \zeta_{ES}}{6\pi\eta R_P} = \frac{R_w}{R_P} f(h_P, R_P) + \frac{2}{3}\frac{\eta_m}{\eta R_P}\chi(\epsilon) \tag{5.3}$$

Here, the second term of the right hand side is proportional to the ratio of lengthscales $\eta_m/\eta R_P$ which is the Boussinesq number describing the relative importance of membrane viscosity contributions as compared to bulk, and introduces a $\propto 1/R_P$ dependency. This could explain the larger measured drag for the smallest particle radius and the non-monotonic dependence with R_P. Indeed, we showed that the first term on the right hand side increases monotonically with R_P due to the increase of $f(h, R_P)$ as the particle comes close to the substrate for larger particle size.

In Figure 5.5 *(left)*, we plot the difference $\zeta_{t,wr} - \zeta_{t,fr}$ of the experimentally measured drags as a function of R_P. Doing so, we expect to isolate the contribution associated to the diffusion of the equivalent inclusion in the membrane $\zeta_{t,wr} - \zeta_{t,fr} = \zeta_{ES}$, if one assumes that the height h_P is approximately the same in the wrapped and free cases. It appears that the difference is almost constant with a small increase with increasing radius, and $4\pi\eta_m < \zeta_{t,wr} - \zeta_{t,fr} < 8\pi\eta_m$ for our range of particles and using a typical value for the membrane viscosity $\eta_m = 2 \times 10^{-9}$ Pa.s.m. In other terms, our data seem to agree with an almost constant contribution of the prediction from Evans Sackmann given by Eq. 5.2, with $1 < \chi(\epsilon) < 2$. Note that in our system, while we do not know the radius of the equivalent disk that has to diffuse within the membrane a_n nor do we know the membrane distance h_m, we can easily estimate η and η_m as they are tabulated properties of the bulk fluid and membrane, respectively. Hence, we plot $\chi(a_n)$ for reasonable values of h_m in Figure 5.5 *(right)* and see that $1 < \chi(a_n) < 2$ implies $70\,\text{nm} < a_n < 700\,\text{nm}$.

To summarize, the experimental drag measurements on engulfed and free particles close to a solid substrate allowed to evidence that the coupling of the wrapped particle motion with the connecting structure translating within the membrane brings additional dissipation. This additional drag is of the order of $\sim 10^{-8}$ Pa.s.m and is almost constant for the range of particle radii probed (a small monotonic increase with R_P is measured but lays within the errorbars). The magnitude of this contribution is consistent with theoretical predictions of Evans and Sackmann [182] considering a typical membrane viscosity $\eta_m = 2 \times 10^{-9}$ Pa.s.m if the radius of the structure equivalent disk radius embedded in the 2D membrane is of the order $70\,\text{nm} < a_n < 700\,\text{nm}$. Such values for the equivalent disk radius are realistic, despite being larger than the expected radius of the membrane neck considered so far (e.g. in Section 3.3.3 where we had the neck radius $r \approx 10$ nm). In fact, other dissipative contributions could exist which could lead to the overestimation of the equivalent radius in this simple model of a particle coupled to a disk inclusion in a membrane, and we will investigate on these contributions in the following sections.

5.2.2 Janus particles

For isotropic particles engulfed by optical tweezers, the structure nucleated between the wrapped particle and the mother vesicle depends on the point at which the relative motion between the optically trapped particle and the vesicle is stopped, as shown in fluorescence micropscopy. It is however sure that in most cases, a tube is nucleated once the particle is further penetrated in the intravesicular space. How these structures behave once the trapping laser is switched off and the particle sediments at the bottom at the vesicle (before recording of the experiments started) is hard to determine. On the other hand, the autonomous engulfment of the active Cu@SiO$_2$ Janus particles being driven by a weak propulsion force comparatively to the force generated by the optical, it is highly unlikely that a tube is nucleated once the particle is fully wrapped by the membrane. Furthermore,

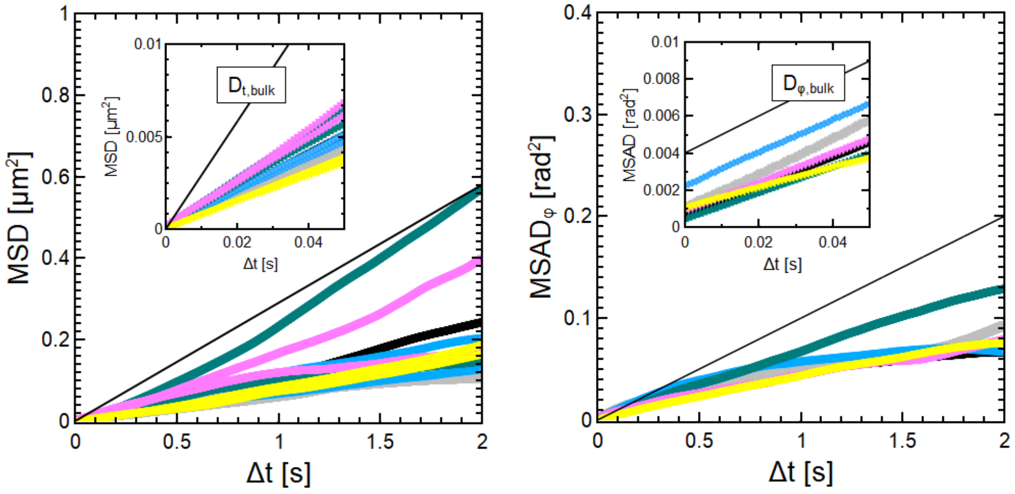

Figure 5.6: *(left)* Mean squared displacement curves (1D) for engulfed Janus Cu@SiO$_2$ particles computed from $N = 20000$ points long trajectories acquired at 980 fps ($\approx$ 20 s). Inset shows the behavior at short timescales at which the diffusion coefficient is fitted. The plain black line is the prediction from Stokes' law. *(right)* Corresponding in-plane mean squared angular displacement curves for the same trajectories as on the left. The plain black line is the prediction from Stokes' law. Inset shows the behavior at short timescales.

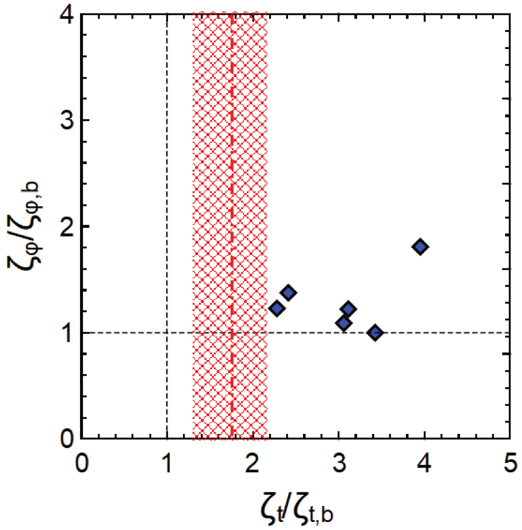

Figure 5.7: Reduced in-plane rotational friction $\zeta_\varphi/\zeta_{r,b}$ versus reduced translational friction $\zeta_t/\zeta_{t,b}$ for fully wrapped Janus Cu@SiO$_2$ particles, where $\zeta_{r,b} = 8\pi\eta R_P^3$ and $\zeta_{t,b} = 6\pi\eta R_P$. The red dashed line is the average reduced translational friction measured for free (not wrapped) Janus Cu@SiO$_2$, with the shaded area standing for the standard deviation.

the particle reorientation with the Cu cap towards the bottom points to the quenching of the active mechanisms leading to the active motion of the particles, which can be rationalized by the poor diffusion of glucose through the membrane neck leading to the absence of reactant triggering the photocatalytic reaction responsible for activity. One could also expect that the adhesion of the Cu cap to the membrane evidenced previously might lead to different final membrane-particle distances than in the optically driven process. Finally, the absence of forces driving the pulling of a tube once a neck is nucleated should guarantee that the structure connecting the particle to the mother vesicle is the same in all cases.

For Janus particles, in the cases where the Janus boundary is visible in bright field microscopy (i.e. when $\theta \approx \pi/2$), not only the translational dynamics but also the rotational dynamics of engulfed particles can be studied (see Section 2.5.3). As mentioned in Section 4.3, in a majority of cases, Cu@SiO$_2$ particles point show an orientation $\theta \approx 0$ once engulfed, which makes the acquisition of φ impossible. Here, we take advantage of the rare cases when this was not the case to also study the in-plane rotational dynamics of fully wrapped Janus particles. In Figure 5.6, we plot both the MSD and MSAD associated to the in-plane rotational motion about the z-axis characterized by the angle φ (see Figure 4.7) calculated from 20 s long trajectories acquired at 980 fps. For both translational and angular motion, no signature of a trapping effect (i.e. elasticity) is observed on the timescales under consideration (2 s and 0.05 s for the insets) as seen by the linearity of the MSD and MSAD with Δt. Just like for isotropic particles, the translational diffusion on short timescales is severely slowed down for all the cases. For the rotational degree of freedom, the reduction of the diffusion coefficient however is less pronounced.

We plot in Figure 5.7 (left) the reduced rotational drag $\zeta_\varphi/\zeta_{r,b}$ as a function of reduced translational drag $\zeta_t/\zeta_{t,b}$ extracted from data of Figure 5.6 for Janus particles with radius $R_P = 1.5\,\mu\text{m}$. This representation allows to visualize the absence of strong correlation between the rotational and translational drag increase for wrapped particles. For the translation, we recover the reduced drag $\zeta_t/\zeta_{t,b} \approx 1.8$ for free particles near the glass substrate and $\zeta_t/\zeta_{t,b} \approx 3$ on average for wrapped Janus particles. This is in accordance with the measurements for isotropic particles and therefore underlines the independence of the driving mechanism on the translational drag acting on the particle in the final wrapping state.

The measured in-plane rotational drag values are closer to the bulk predictions, with $1 \leq \zeta_\varphi/\zeta_{r,b} < 2$ (Figure 5.7). Indeed, the influence of the presence of a solid (or fluid) interface on this mode of motion about an axis normal to the interface is expected to be weak [183]. The other source of dissipation for the rotation would be the one associated to shear stresses that act on the membrane, the water gap between the particle and the membrane, and also on the bulk water on the other side of the membrane. To the best of our knowledge, no models exist in the literature describing the rotational drag experienced by a spherical particle in such a geometry.

For the sake of comparison, we could refer to limiting scenarios in order to determine where most of the dissipation occurs. First, we can consider that the membrane wrapping the particle is immobile and refer to the hydrodynamic result for a spherical Couette geometry. In such cases, the viscous dissipation is due to the slow motion of the fluid contained (in the small gap) between two concentric hard spheres by assuming that the inner sphere rotates while the outer sphere stays at rest. Hence, we assume the radius of the inner sphere is R_P and the radius of the outer sphere is $R_P + d_g$ where d_g is the thickness of the water gap (see Figure 5.4). Note that the lipid membrane acts as a solid–liquid interface in this picture, and no dissipation due to the membrane viscosity can be described within this assumption. In this case, the rotational drag felt by the inner sphere can be written as [184]:

$$\zeta_{\varphi,S} = \frac{8\pi\eta R_P^3}{\left[1 - \left(\frac{R_P}{R_P + d_g}\right)^3\right]} \tag{5.4}$$

Interpreting the variability of our data for ζ_φ as a variability of d_g implies $400\,\mathrm{nm} < d_g < \infty$. Fluorescence microscopy images of wrapped particles allow to measure the apparent diameter of the wrapped particle and the results are not in accordance with the existence of the such large water gaps between the particle and the membrane, except for rare cases (see Appendix 8.4). Now, assuming a mobile membrane in contact with the particle, we could consider the model describing the limiting scenario of a disc rotating while embedded in a planar membrane. Evans and Sackmann [182] calculated the rotational drag acting on such an embedded disk with radius a close to a solid wall to be $\zeta_{ES,disk} \approx 4\pi\eta_m a^2$. Considering that this contribution adds to the Stokes contribution for rotational drag in the bulk, and with the disc radius a as a fitting parameter for our results, we find $0 \leq a \leq 1.7\,\mu\mathrm{m}$. Such a large variability in the equivalent diffusing disk radius is hard to interpret when considering our geometry, which is why we would need a model considering the shear transmission and dissipation in the water gap and across of the wrapping lipid bilayer in this spherical geometry to interpret our data. A collaboration is currently ongoing with researchers to model and numerically simulate the drag experienced by wrapped (and also partially-wrapped) colloids close to a solid interface.

5.3 Tension-dependent diffusion of engulfed particles

In the previous section, the particle size was used as a parameter to investigate the dissipative processes occurring in the specific geometry of an engulfed colloid connected to a vesicle. In this section, we explore the influence of membrane properties on dissipation, with a particular focus on the membrane tension σ.

To do so, we use a micropipette (see Section 2.2) to apply stress and thereby control the tension of the vesicles, after a particle was engulfed with optical tweezers. The measurements were performed in the two geometries described in Figure 5.8 for the unconstrained *(left)* and optically trapped at the equator *(right)* cases. Note that the denomination *unconstrained* here refers to the case when the particle is engulfed, but is not optically trapped and therefore sediments at the bottom of the vesicle due to gravitational force, as shown in Figure 5.8.

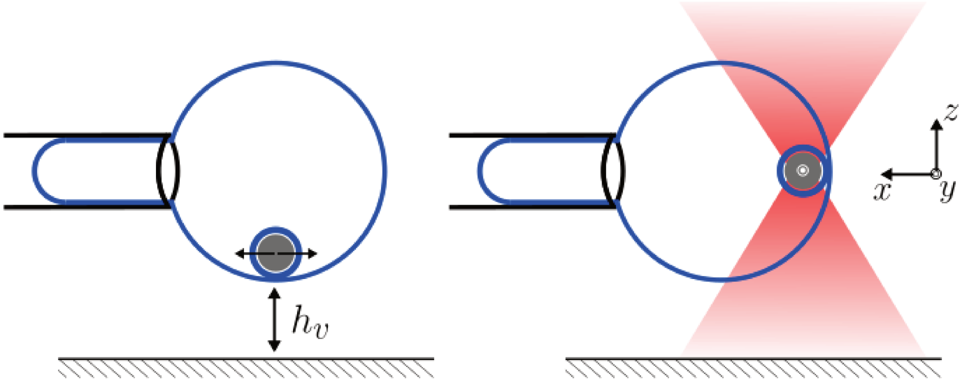

Figure 5.8: Sketch of the experiment for unconstrained *(left)* and optically trapped *(right)* engulfed particle translational diffusion measurements as a function of membrane tension.

5.3.1 Diffusion of unconstrained engulfed particles

First, I describe the experiment in the absence of optical trap. As discussed in Section 3.2, particles once wrapped by the membrane and penetrated in the intravesicular space sediment at the bottom of the vesicle once the optical trap is switched off. Despite the experimental difficulty to monitor the evolution of the structure connecting the wrapped particle to the vesicle during the sedimentation, we are sure that a structure is always present in this state as it can be evidenced by pulling on the particle with optical tweezers. The experiment then consists in aspirating the vesicle with the micropipette and lift it above the substrate in order to have $h_v > 10\,\mu\text{m}$ (see Figure 5.8) and minimize the contributions of the substrate proximity to the drag.

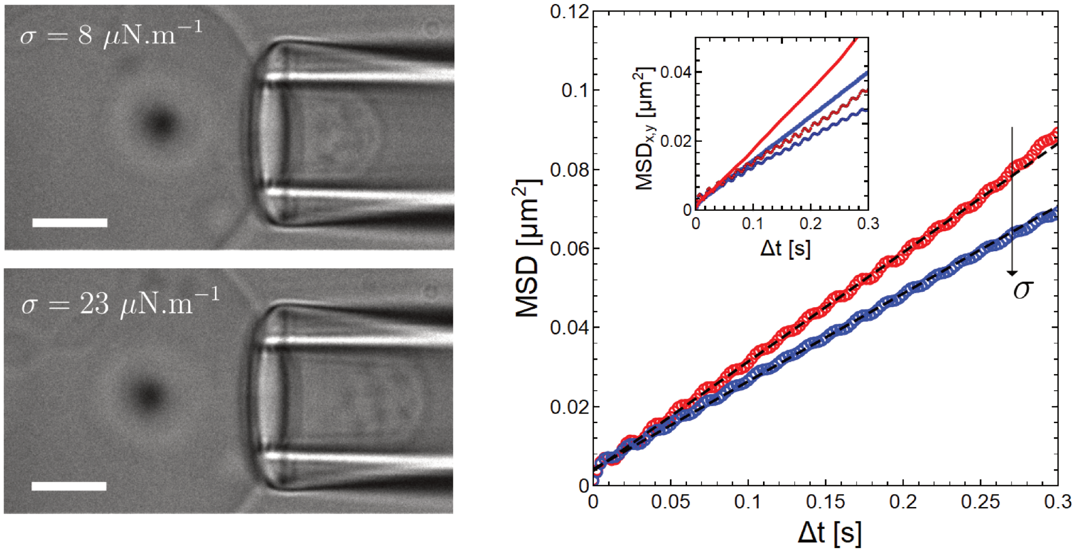

Figure 5.9: *(left)* Bright field microscopy images of a GUV aspirated by a micropipette, with an engulfed $R_P = 1.15\,\mu\text{m}$ particle (out-of-focus) appearing as a blurry dark point. The scale bar is 5 µm. *(right)* Two dimensional MSD $\langle(x(t+\Delta t) - x(t))^2\rangle + \langle(y(t+\Delta t) - y(t))^2\rangle$ for the engulfed particle at two different membrane tensions. The red curve (top) is the lower tension membrane while the more tense is the blue one (bottom). Dashed black lines are fits yielding $D_t = 0.068\,\mu\text{m}^2/\text{s}$ for the lower tension (red) and $D_t = 0.055\,\mu\text{m}^2/\text{s}$ (blue) for the tenser vesicle. Inset shows the two components of the motion separated and shows that the motion along the micropipette has a slower diffusion than the perpendicular one. Both components are however similarily impacted by the tension increase.

After pre-stressing the vesicle by applying a pressure $\sigma \approx 0.1\,\text{m}\,\text{N}\,\text{m}^{-1}$, we perform measurements by recording high acquisition rate movies with the field of view containing both the vesicle aspirated in the micropipette and the engulfed microparticle, as shown in Figure 5.9 *(left)*. Due to geometry, it is not possible to have both the particle and the aspirated vesicle segment in focus. We choose to keep the image focus on the aspirated membrane segment as it allows to make sure that the aspiration pressure is properly applied. The particle being out of focus can still be efficiently tracked with our tracking routine, and we do not expect it to introduce inaccuracies in our measurements of the particle position. Additionnally, geometrical corrections associated to the fact that the particle diffuses on a sphere (the vesicle, see Figure 5.8) and not in a plane can be disregarded as the particle only explores a small region of space close to the bottom of the vesicle, which has a radius much larger than the explored area.

In Figure 5.9 *(right)* we report the two-dimensional MSD of an engulfed particle upon increasing the the membrane tension. In a single acquisition of 30 000 images acquired at

419 fps, we increase the tension applied with the micropipette step-wise from $\sigma = 8\,\mu\mathrm{N\,m^{-1}}$ to $\sigma = 23\,\mu\mathrm{N\,m^{-1}}$ at 10 000 frames. The red curve shows the MSD for the particle motion during the first 10 000 frames and the blue curve for the last 10 000 frames. The motion is not analyzed during 10 000-20 000 frames as it corresponds to the time for the membrane to reach the higher equilibrium tension. It clearly appears that the slope of the MSD curve for lower tension is larger than for the higher tension case. Linear fits up to $\Delta t = 0.3$ s allow to extract $D_t = 0.068\,\mu\mathrm{m}^2/\mathrm{s}$ and $D_t = 0.055\,\mu\mathrm{m}^2/\mathrm{s}$ for the low and high membrane tension cases, respectively. Such an relative increase in drag coefficient with increasing tension was systematically measured when reproducing this experiment in this geometry. Before discussing the origin of this tension-dependent diffusion for engulfed particles, we will perform a similar experiment with the particle optically trapped at the equator. Doing so, we can maintain both the particle and the aspirated vesicle segment in the imaging plane and confirm that the effect is not an artefact arising from the geometry.

5.3.2 Engulfed particles optically trapped at the vesicle equator

In order to investigate on the robustness of the tension-dependent diffusion of engulfed particles, we perform the experiment described in Figure 5.8 *(right)*. By weakly trapping ($\kappa < 10^{-6}$ N.m^{-1}) the engulfed particle to maintain it in focus together with the micropipette, we can perform the same experiment as the one performed in Section 5.3.1. Again, during a single acquisition, we perform a sudden step-wise increase of the applied tension and subsequently track the motion of the particle in the optical trap. Figure 5.10 shows bright field images of the experiment and the plots of the two quantities used to extract the translational friction coefficient ζ_t and stiffness κ for the motion parallel to the mother vesicle membrane (along the axis y, as defined in Figure 5.8 *(right)*). Note that upon increasing the tension, the particle is slightly displaced from its equilibrium position in the trap along the direction perpendicular to the membrane. This results in a smaller effective trap stiffness along y and explains the difference in plateau height between the red MSD curve (low tension) and black one (high tension). When fitting the data, κ will therefore also be a fit parameter. Values extracted from fits of the MSD and PSD data with Eq. 1.32 and 1.38 are plot in Figure 5.10 *(right)*. The measured values for the translational friction ζ_t confirm the existence of a tension-dependent dissipative process, as ζ_t shows a roughly twofold increase for a threefold tension increase.

5.3.3 Diffusion measurements in a wide membrane tension range

We proved the robustness of the phenomenon by measuring a relative decrease of particle mobility associated to an increase of the membrane tension for both trapped and not trapped particles. In order to extend the range of tensions probed, we measured the diffusion coefficient from MSD curves for particles engulfed in non-stressed floppy vesicles ($\sigma < 10^{-7}$ N.m^{-1}). The corresponding tension then is not the one applied with the micropipette, but the one measured from the tube force, as described in Section 3.2. In Figure 5.11, we plot the measured diffusion and corresponding friction coefficient for these non-stressed low tension vesicles (triangles) together with values measured for the experiment described in Section 5.3.1 (hexagons), where the engulfed particle is not trapped and the vesicle tension is controlled with the micropipette. Note that in the low tension regime (triangles), the vesicle-substrate distance h_v (Figure 5.8) can not be controlled as the vesicle is not manipulated with the micropipette. A significant contribution of the paricle-wall proximity is expected, as already discussed in Section 5.2.1. However, despite this contribution which is

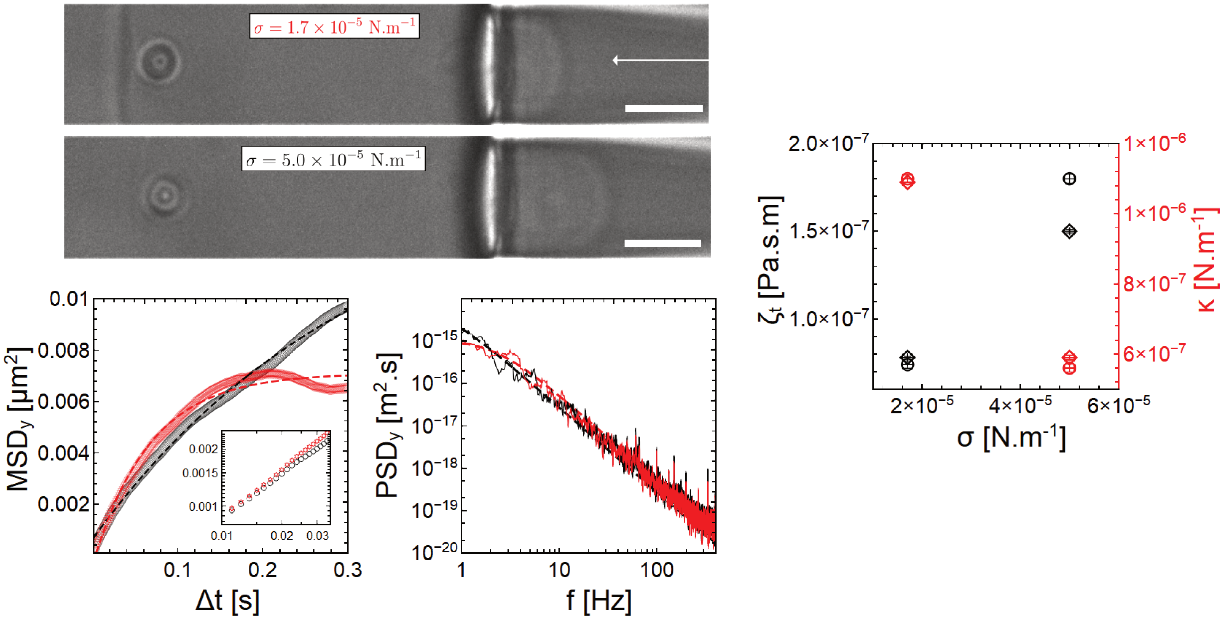

Figure 5.10: *(topleft)* Bright field microscopy images of the optically trapped engulfed particle at the equator of an aspirated vesicle for two applied tensions. *(bottom left)* 1-dimensional MSD and PSD for the motion along the tangent axis to the vesicle membrane. Red and black dashed lines stand for fits with Eq. 1.32 for the MSD and 1.38 for the PSD, with log-log scale representation of short time regime of the MSD in inset. *(right)* Parameters extracted from the MSD (diamonds) and PSD (circles) fits as a function of applied membrane tension σ. Errorbars account for the fit standard deviation values.

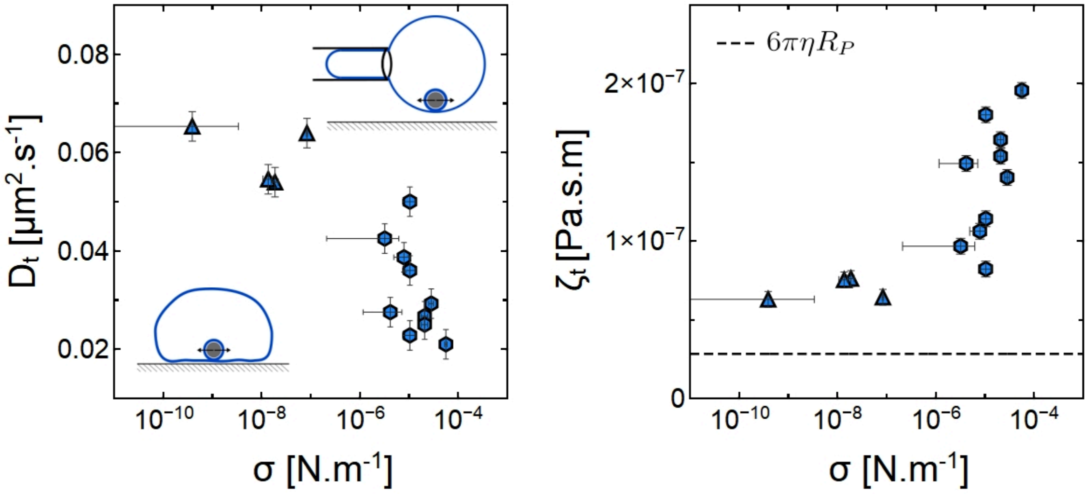

Figure 5.11: *(left)* Translational diffusion coefficient D_t and corresponding friction coefficient *(right)* experienced by engulfed particles. Triangles correspond to measurements where the vesicles were not under tension and the tension value was extracted from the force profile. Hexagons correspond to measurements with vesicles under tension by the micropipette suction pressure, without optical trap. The sketches represent each situation.

not present for higher tension as the vesicles are further away from the substrate in z, we can still observe a decrease in mobility for higher membrane tensions.

Quantitatively, the highest measured drag experienced by engulfed particles in the most tense vesicle is $\zeta_t = 0.2\,\mu\mathrm{Pa\,s\,m} \approx 10 \times 6\pi\eta R_P$. In other terms, the particle mobility is equivalent to a particle submitted to a drag coefficient given by Stokes law with an effective viscosity $\eta_{\mathrm{eff}} = 10\eta$, where η is the bulk fluid viscosity. In the following, we will investigate on the possible origins of the tension dependence of the dissipation in this system.

5.3.4 Potential mechanisms and existing models

We previously described the wrapped particle together with the structure connecting it to the mother vesicle (neck) as a particle coupled to a disk embedded in the mother vesicle membrane to account for the dissipation associated to the shear stresses within the lipid membrane. However, neither the Stokes drag nor the Evans-Sackmann model for a disk diffusing in a lipid membrane close to a solid substrate show explicit dependence on the membrane tension. Other long established continuous models describing the diffusion of inclusions within membranes such as the Saffman-Delbrück model, widely used to describe the diffusion of proteins in lipid membranes, also do not show explicit dependence on membrane tension [22, 185]. More recently, several experimental works reported deviations from the Saffman-Delbrück model [186, 187, 188]. In particular, the influence of membrane tension on the mobility of curvature-inducing proteins was evidenced and interpreted as an effect of local protein-induced membrane deformations, which are affected by membrane tension [188]. It was shown that the local deformations induced by proteins with an internal structure would induce additional contributions associated to i) membrane fluctuations, ii) the friction between the two lipid monolayers, iii) friction within monolayers, and iv) hydrodynamic friction in the bulk fluid. In the case of proteins reported in Ref. [188], the effective drag coefficient was shown to depend on a decreasing function of the tension $W(\sigma)$, such that

$$\zeta_t \propto \frac{\Theta^2 \eta W(\sigma)}{2a_b}, \tag{5.5}$$

where Θ captures the induced curvature by the inclusion and a_b is a cutoff length corresponding to the bilayer thickness ($\approx 5\,\mathrm{nm}$). With $\lim_{\sigma\to\infty} W(\sigma) = 0$, this model can not be used to interpret our data as it predicts an opposite behaviour, namely a decrease of the drag coefficient for increasing tension. However, the fact that the deformation is less localized for higher tension, expected from the fact that deformation of the membrane occurs

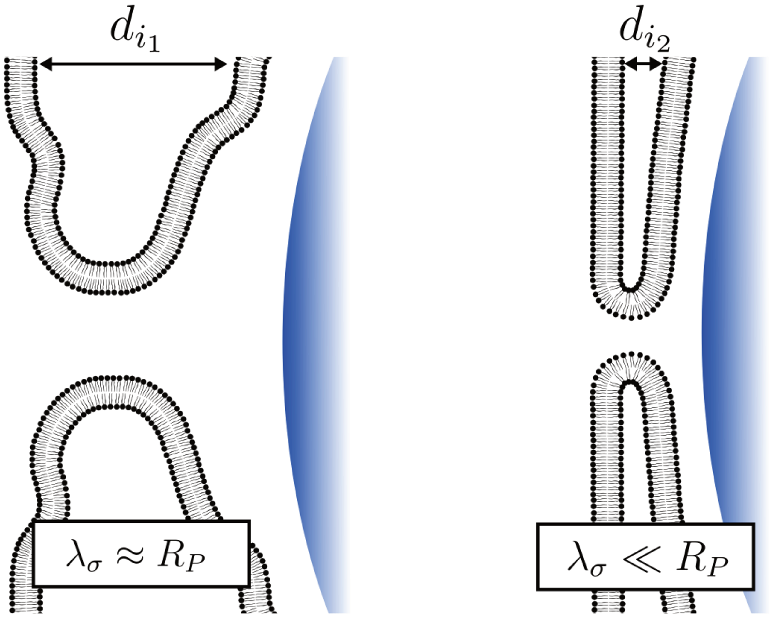

Figure 5.12: Sketch of the expected geometry and variation of the interbilayer distance d_i for low tension ($\lambda_\sigma \approx R_P$) on the *(left)* and high tension ($\lambda_\sigma \ll R_P$) on the *(right)*.

on lengthscales of the order of $\lambda_\sigma = \sqrt{\kappa_b/\sigma}$ (and confirmed by simulations [188]), can have other implications in our geometry.

First, the changes in the membrane shape in vicinity of the neck structure connecting the vesicle membrane to the wrapped particle can lead to more strongly curved membrane segments. While recent works suggest that there exists a correlation between the diffusion of proteins through constrictions and the mean and Gaussian curvature of these narrow structures [189], it could be that curvature has an influence on the diffusion of the whole membrane Ω-shaped bud (containing a particle in our case).

Secondly, reduction of the spatial extension of the membrane deformations due to a tension increase, considering our exact geometry, should translate to a decrease of the distance between the mother vesicle membrane and the lipid bilayer wrapping the membrane, which we call d_i. In Figure 5.12, we describe schematically the expected influence of a higher tension on the shape adopted by the membrane and in particular on the distance between the wrapping bilayer and the mother vesicle bilayer d_i.

Indeed, for the low membrane tension regime, the inter-bilayer distance is expected to be large due to large membrane fluctuations and associated steric repulsion. A reasonable lower bound approximation for the interbilayer distance d_i in this case would be the amplitude of the bilayer undulations at low tension $\xi_\perp \geq 200$ nm [165]. Higher membrane tension leads to suppression of these large thermal undulations, see 2.2.2. In the absence of other repulsive forces such as electrostatics (lipids are zwitterionic), the interbilayer distance for high membrane tension can reach values as small as a few nanometers, until the hydration force prevents further thinning of the water gap. When interbilayer distance becomes small, shearing of the water layer upon translational motion of the wrapped particle participates in increasing the drag experienced by the diffusing particle. In order to provide quantitative insights on the magnitude of this contribution, we perform in the following section experiments allowing to study the influence of the proximity of a fluid bilayer on the drag experienced by an optically trapped particle.

5.4 Confined particle close to a lipid membrane: dynamics and interactions

In this section, we report on experimental investigations on the interactions between a micrometric particle approached to a lipid membrane until contact. Displacement of the particle from its equilibrium position in the optical trap upon approach of the vesicle is interpreted as a result of the interaction with the membrane, assuming that the latter does not interfere with the trapping laser. Using the particle position data, we evidence the signature of the local membrane elastic response dominated by tension and investigate on the tangential dynamics parallel to the membrane upon close contact.

5.4.1 Particle-vesicle membrane at high tension

The experimental protocol consists in approaching a vesicle, whose tension and spatial position is controlled using a micropipette, close to a particle in an optical trap. Piezoelectric actuators allow for precise and remote control of the particle-membrane relative distance. Snapshots of a bright field microscopy acquisition of the experiment are shown in Figure 5.13, where the vesicle position is changed along the axis x over time. Note that the absolute distance between the particle surface and the membrane is hard to measure precisely in those conditions. We therefore perform the experiment scanning a wide range of particle-

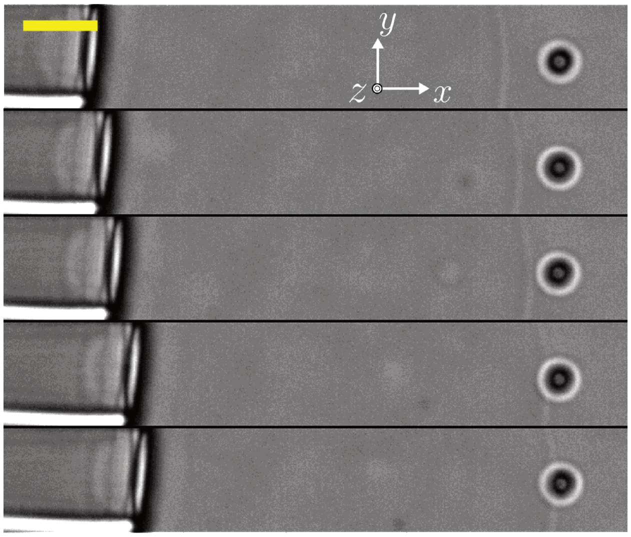

Figure 5.13: Sequence of bright field microscopy images of a vesicle under tension approached to an optically trapped $R_P = 1.15\,\mu\text{m}$ SiO$_2$ particle at 20 mW laser power ($\kappa = 3.1\,\mu\text{N}\,\text{m}^{-1}$). The aspirated vesicle is approached step-wise with $\approx 180\,\text{nm}$ steps thanks to interfaced piezoelectric actuators driving the sample stage. Scale bar is $5\,\mu\text{m}$.

membrane distances in a single acquisition, and track the particle motion in the xy plane (see Section 2.5.1). We plot the evolution of the particle center of mass position relatively to the equilibrium position in the optical trap $[x_0, y_0]$ along both directions (defined in Figure 5.13) $\Delta x(t) = x(t) - x_0$ and $\Delta y(t) = y(t) - y_0$ in Figure 5.14. We also provide the trajectory $(\Delta x(t), \Delta y(t))$ in the inset of Figure 5.14 *(left)*.

5.4.2 Potential stiffening and membrane elastic response

We focus first on the dynamics along x, describing the dynamics of the particle perpendicular to the lipid membrane, which we assume to be planar (Figure 5.14 *(left)*). For times $0 < t < 60$ s of the acquisition, the particle position fluctuates in the optical trap with a variance dictated by the optical trapping power. The presence of the vesicle membrane does not seem to have any noticeable effect on the particle position as no signature of the step-wise approach each ≈ 5 s can be observed. On the contrary, starting from $t = 60$ s, approach of the vesicle translates into a displacement of the particle from its equilibrium position far from any interface and the particle position oscillates around another value which depends on the vesicle position. The optical trap being calibrated, this displacement is linearly related to the force exerted on the particle with the proportionality constant $\kappa = 3.1\,\mu\mathrm{N\,m^{-1}}$,

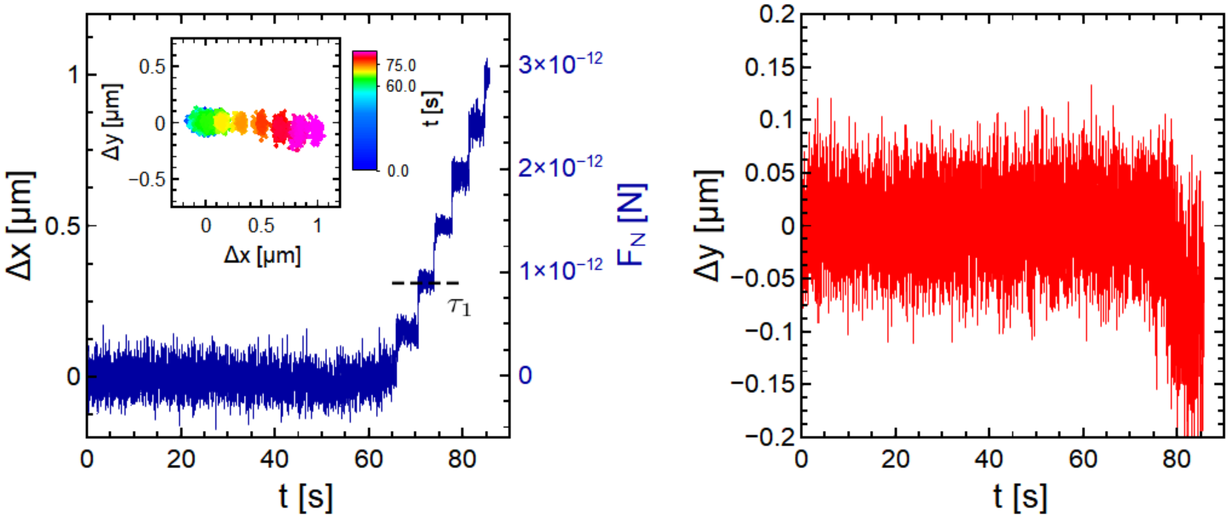

Figure 5.14: Trajectories extracted from the experiment in Figure 5.13 acquired at 200 fps. *(left)* Temporal evolution of the relative position $\Delta x(t) = x(t) - x_0$, where x_0 is the center of the optical trap, upon step-wise approach of an optically trapped $R_P = 1.15\,\mu\mathrm{m}$ SiO_2 particle as shown in Figure 5.13. Note that the axis x corresponds to the direction perpendicaular to the membrane. Inset shows the two dimensional trajectory with the color map allowing to visualize the time evolution. *(right)* Evolution of $\Delta y(t) = y(t) - y_0$.

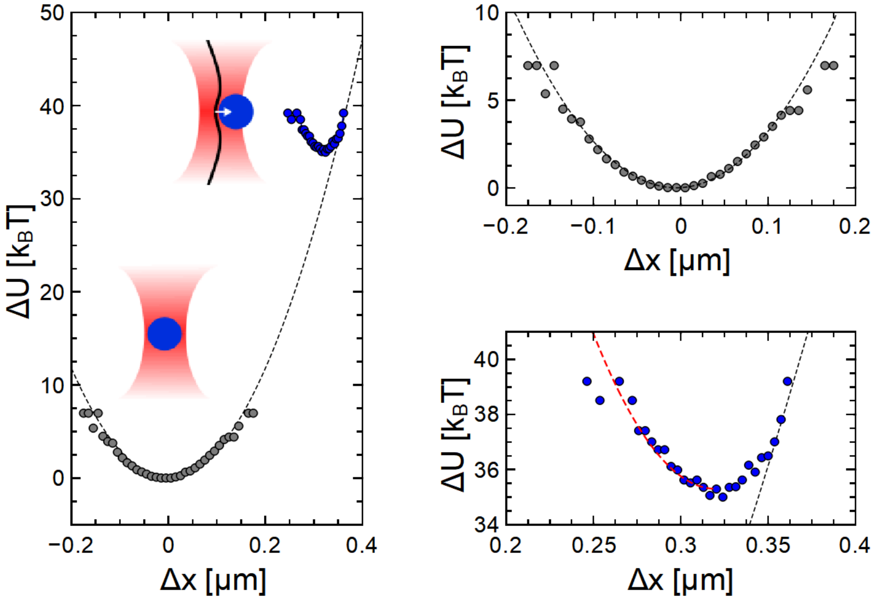

Figure 5.15: *(left)* Experimental potential energy as a function of center of mass position for the vesicle membrane being far from the particle ($t < 20$ s in Figure 5.14, grey circles) and for $70 < t < 74.5$ s with $F_N = 0.94 \pm 0.03\,\mathrm{pN}$ (blue circles). The black dashed line is the harmonic potential of the optical trap $\Delta U = \frac{1}{2}\kappa\Delta x^2$ with $\kappa = 3.1\,\mu\mathrm{N\,m^{-1}}$ obtained from MSD and PSD calibration. *(top right)* Focus on the equilibrium potential far from the membrane. *(bottom right)* Focus on the equilibrium potential with the membrane pushing the particle and evidence of the asymmetry in the potential. The black dashed line is the harmonic potential of the optical trap $\Delta U = \frac{1}{2}\kappa\Delta x^2$ with $\kappa = 3.1\,\mu\mathrm{N\,m^{-1}}$, and the red dashed line is $\Delta U = \Delta U_0 + \kappa_\sigma(\Delta x - \Delta x_m)^2$ with $\kappa_\sigma = 1150\ k_BT.\mu\mathrm{m}^{-2} = 4.7265 \times 10^{-6}$ $\mathrm{N.m^{-1}}$ and $\Delta x_m = 0.32\,\mu\mathrm{m}$.

and the force appears on the right axis in Figure 5.14 *(left)*. This new equilibrium position $\langle\Delta x\rangle_m \neq 0$ is therefore a direct measurement of the force exerted by the membrane on the particle, and reciprocally. In addition to a shift of the position around which the particle position fluctuates, we can also notice a decrease of the variance of these fluctuations.

This increase in particle confinement is a result of a change in the energy landscape in which the particle evolves. The effective position-dependent potential energy of the particle can be reconstructed from the trajectory using Boltzmann distribution at equilibrium (Section 2.1.4). We plot such experimental potentials for two extreme cases in Figure 5.15. The first case is for small times t since the start of the acquisition $t < 20$ s, i.e. large particle-membrane distances $> 1\,\mu\mathrm{m}$, where the only force acting on the particle is the one deriving from the optical trapping harmonic potential. It is plotted as grey circles in Figure 5.15 *(left)* and *(top right)*, together with the harmonic potential $\Delta U = \frac{1}{2}\kappa\Delta x^2$ with $\kappa = 3.1\,\mu\mathrm{N\,m^{-1}}$ associated to the optical trap (not a fit). The blue circles on Figure 5.15 *(left)* and *(bottom* *right)* represent the effective energy for the portion of the trajectory $70 < t < 74.5$ s with an equivalent normal force $F_N = 0.94 \pm 0.03\,\mathrm{pN}$. Note that an offset ΔU_0 was artificially added to the experimental values $\Delta U(\Delta x)$ for the case where the membrane is pushing the particle (blue circles) . Here, both the displacement of the equilibrium position (position of lowest energy) and the increase in potential stiffness comparatively to the case of the membrane being far can clearly be visualized. In fact, the potential to which the particle is submitted is now asymmetric due to the asymmetry of the situation and the different origin of the forces acting on the particle. Indeed, the restoring force acting on the particle for increasing Δx is the optical trapping force, while for decreasing Δx, the restoring force comes from the elasticity of the membrane.

In Figure 5.15 *(bottom right)*, we focus on the asymmetry in the potential. We postulate that in the direction of increasing Δx, the harmonic potential of the optical tweezers maintains the same stiffness, which seems reasonable graphically. In the opposite direction, the potential shows a qualitatively lower stiffness. In the case of a vesicle put under tension with $\sigma = 1\,\mathrm{\mu N\,m^{-1}}$, we expect the deformations to be primarily resisted by membrane tension, as $R_P \gg \sqrt{\kappa_b/\sigma}$. We know from Eq. 3.5 that the energy associated to tension is quadratic with the particle degree of penetration z. We can therefore try to relate the stiffness of the experimental potential to the tension-related deformation costs through $\Delta x - \Delta x_m = R_P \Delta z$. If we fit the left side of the potential with a quadratic function $\Delta U = \Delta U_0 + \kappa_\sigma(\Delta x - \Delta x_m)^2$ with ΔU_0 and κ_σ as fitting parameters and $\Delta x_m = 0.32\,\mathrm{\mu m}$.

$$\kappa_\sigma(\Delta x - \Delta x_m)^2 = \sigma\pi R_P^2 \Delta z^2 = \sigma\pi(\Delta x - \Delta x_m)^2 \tag{5.6}$$

Note that Δx_m should correspond to the particle position at which the membrane is not deformed and its value has an influence on the extracted stiffness κ_σ. However, optical microscopy acquisitions do not allow to precisely measure Δx_m but it should be equal or slightly greater than the particle displacement from its equilibrium position far from the membrane. We therefore choose the lower bound $\Delta x_m = 0.32\,\mathrm{\mu m}$. With these approximations, the fit (red dashed line in Figure 5.15 *(bottom right)*) yields $\sigma = \kappa_\sigma/\pi = 1.5 \times 10^{-6}$ N.m^{-1} which is accordance with the order of magnitude of the tension applied with the micropiette suction.

With more statistics (i.e. longer measurements) and a better estimation of Δx_m, this experimental protocol could allow to probe the elastic response of lipid membranes an infer some of its properties such as tension σ and bending modulus κ_b. Particularly, in a bending-dominated regime, the energy should scale linearly with z and the slope of the potential would therefore provide a direct local measurement of κ_b, according to Eq. 3.4.

5.4.3 Lateral particle dynamics and related dissipations

Focusing on the confined Brownian dynamics of the particle parallel to the fluid membrane, i.e. along y, a much weaker effect of the membrane proximity is observed. Indeed, the position fluctuates around $\Delta y = 0$ with no apparent variance change throughout the whole acquisition, except at very long times $t > 75$ s corresponding to the particle escaping the harmonic region of the optical trap. This is expected as the particle should not experience additional confinement. However, an increase in the drag force exerted on the particle translating at such distances of the membrane with 2D viscosity η_m could exist.

In order to probe the existence and magnitude of this membrane proximity-induced drag increase, we compute the position power spectrum along y in the two extreme cases already considered in the previous section, i.e. large particle membrane distance $d_m > 1\,\mu\text{m}$ (black curve) and membrane deformation with associated normal force $F_N = 0.94 \pm 0.03\,\text{pN}$ (red curve) in Figure 5.16. It appears that the curves almost perfectly overlap, pointing to no measurable change in the translational friction coefficient for the tangential motion of the

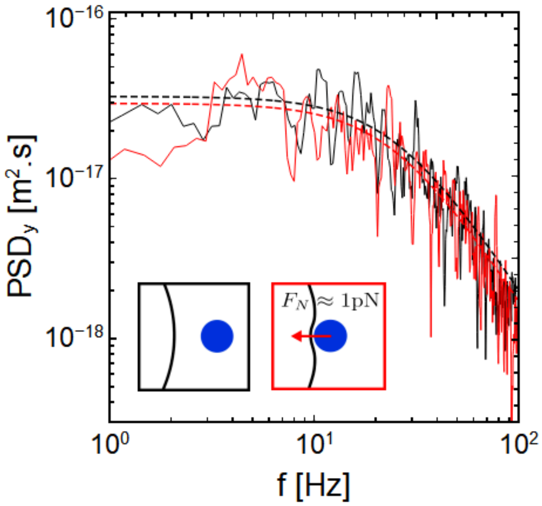

Figure 5.16: Position power spectral density in the two extreme cases of large particle-membrane distance (black plain line) and particle-membrane contact (red plain line). Dashed lines of the corresponding colors are fits following Eq. 1.38 yielding the stiffness κ and friction coefficient ζ_t. For the membrane being far (black), the fit yields $\kappa = 3.1 \pm 0.09\,\mu\text{N}\,\text{m}^{-1}$ and $\zeta_t = 19.5 \pm 1.2\,\text{nPa}\,\text{m}\,\text{s}$. For the particle deforming the membrane (black), the fit yields $\kappa = 3.56 \pm 0.12\,\mu\text{N}\,\text{m}^{-1}$ and $\zeta_t = 22.9 \pm 1.7\,\text{nPa}\,\text{m}\,\text{s}$.

particle. Fits with Eq. 1.38 (dashed lines) suggest an increase from $\zeta_t = 19.5 \pm 1.2\,\mathrm{nPa\,m\,s}$ for the membrane far to $\zeta_t = 22.9 \pm 1.7\,\mathrm{nPa\,m\,s}$ for the membrane deformed, but which is in the errorbars and therefore at the limit of precision of the measurement. This negligible friction coefficient increase is consistent with previous measurements reported in the literature for less tense membranes [190]. Jünger *et al.* indeed reported a maximum friction increase of 8% from the bulk value at smallest accessible distances from the membrane using photonic force microscopy.

5.5 Conclusion

In this Chapter, we used experimental trajectories of the microparticle in different situations to harvest information on the dissipation and interactions with a lipid bilayer. We first studied the diffusion of engulfed isotropic and Janus particles after their complete wrapping by floppy vesicles, either driven by optical tweezers or in active conditions. We showed that engulfed particles experience dissipations due to the coupling of their motion with the motion of the structure connecting them to the mother vesicle (the neck). Using different particle sizes and comparing our data with existing simple models indicated that the measured increase could be explained by the dissipative mechanisms associated to translation of the neck in the fluid membrane. The consistency of the measured reduced drag $\zeta_t/\zeta_{t,b} \approx 3$ for $R_P \approx 1\,\mu\mathrm{m}$ isotropic particles and Janus particles engulfed with different driving mechanisms suggest some universality in the diffusion properties of the final structure.

We evidenced a robust dependence of the engulfed particles' mobility on the tension of the hosting membrane in different configurations. No experimental work to the best of our knowledge reported such dependence of increasing drag coefficient with increasing friction (the opposite trend was measured for curvature-inducing proteins). Furthermore, no theoretical work reports on a tension-dependent dissipative mechanism that could occur in our system. In a last section, we checked using optical tweezers that this measured drag increase was not a result of the reduction of the particle-membrane distance. Indeed, our measurements for the friction parallel to a tense lipid membrane, in accordance with previous measurements from the literature [190], indicate that the increase of the friction along this direction can not exceed a few percents. To conclude, another dissipative mechanism has to be envisaged to explain our results which suggest that engulfed particles can experience a translational drag as large as 10 times the bulk prediction from Stokes' Law.

Chapter 6

Perspectives & general conclusion

In this chapter, I present selected preliminary results obtained during the course of this thesis, which represent some perspectives for future investigations. The two topics selcted are: the active dynamics of $Cu@SiO_2$ particles in glucose solutions, and the drag experienced by confined microparticles in close contact with solid walls and supported membranes. These studies build on the work detailed in the previous chapters, providing valuable insights and laying the groundwork for future research on these topics. The chapter will conclude with a general summary, synthesizing the key findings of the entire thesis and briefly discussing their broader implications.

6.1 On the dynamics of active $Cu@SiO_2$ particles

Active particles, besides undergoing thermal diffusion, possess a constant propulsion speed V_0 along a vector whose direction varies over time [191, 57]. For Janus particles undergoing self-diffusiophoresis, the propulsion force direction is set by the metallic cap orientation, which leads to a coupling between translational and rotational motion. To quantify the particle activity, the mean squared displacement (MSD) is often computed and fitted using models assuming the velocity vector lies in the plane of motion [143, 192, 57]. In Section 4.2, we used this model to measure the activity of $Cu@SiO_2$ Janus particles in glucose, showing its dependence on glucose concentration and illumination. The model extracts V, the average projected velocity in the observation plane, which may differ from V_0 based on the particle's out-of-plane orientation dynamics (angle θ, see Figure 6.1). The only scenario where the extracted V equals V_0 is when the particle's out-of-plane orientation is fixed at $\theta = \pi/2$ and the change of orientation occurs only because of the in-plane angle φ. This holds also for systems like $Pt@SiO_2$ Janus colloids in H_2O_2 [143], though some features of the dynamics

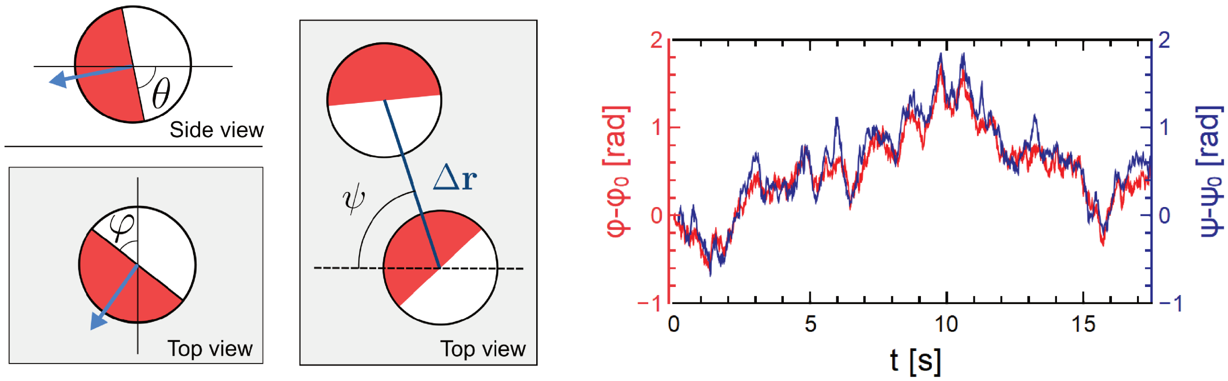

Figure 6.1: *(left)* Sketch defining the Euler angles θ and φ. The blue vector corresponds to the active propulsion velocity vector $\mathbf{V_0}$. ψ is the angle defined by the displacement vector $\Delta\mathbf{r}(\Delta t)$ and a reference axis in the lab frame. *(right)* Red curve shows the evolution of $\varphi(t) - \varphi_0$, where $\varphi_0 = \varphi(t = 0)$ by image analysis, during a persistent segment ($\theta \approx \pi/2$) of a Cu@SiO$_2$ particle trajectory in 100 mM glucose at $I = I_{\text{MAX}}$. The blue curve $\psi - \psi_0$ was obtained by $\psi(t) = \arctan\left(\frac{\bar{v_y}(t)}{\bar{v_x}(t)}\right)$ where $\bar{v_x}(t)$ and $\bar{v_y}(t)$ are the filtered instantaneous velocity components, and $\psi_0 = \psi(t = 0)$.

are overlooked, and the analysis mainly focuses on V.

Generally, the out-of-plane particle orientation confinement results from the interactions (hydrodynamics, electrostatics, etc.) between the faces of the particle and the underlying substrate [193, 60, 58]. Hence, active particles, generating different fluid flux through different swimming mechanisms (e.g. pushers or pullers), are expected to modify the hydrodynamic interactions with the substrate. In turn, they may exhibit more complex out-of-plane orientation dynamics. For example, the non-gaussianity of the particle displacement probability density due to particle orientation constrained in a plane and not freely diffusing on a unit sphere was studied [194]. A very recent study to characterize the intermittency in the motion of catalytic microswimmers was also reported [195]. In the following, we present preliminary results on the non-trivial rotational dynamics of Cu@SiO$_2$ Janus particles in glucose and the impact on the active translational dynamics.

6.1.1 Activity modulation by white light and velocity spectra

We evidenced in Section 4.2 the dependence of Cu@SiO$_2$ motion on glucose concentration of the solvent and exposure to blue light. In Figure 6.2, we plot the two-dimensional particle velocity power spectra together with trajectories of Cu@SiO$_2$ particles in 100 mM glucose aqueous solution upon varying only the white light illumination intensity of the microscope

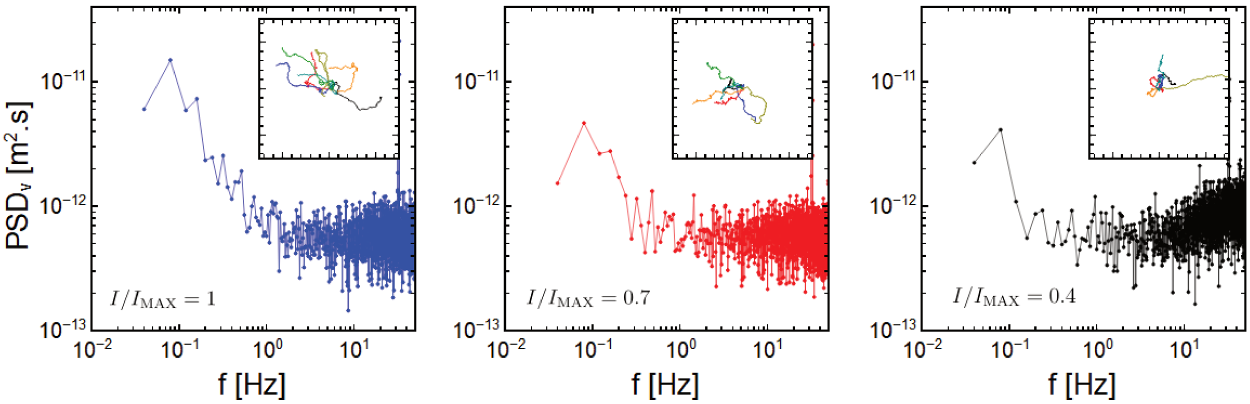

Figure 6.2: Velocity power spectral densities of Cu@SiO$_2$ particles in different white light illumination conditions. The spectra are obtained from average of the individual spectra associated to the trajectories in inset (25 s long at 100 fps acquisition frequency) for each sample illumination conditions, namely $I/I_{\mathrm{MAX}} = 1, 0.7$ and 0.4 from left to right, where I is the white light illumination intensity and I_{MAX} the maximum intensity that can be provided by the light source.

from its maximum intensity I_{MAX} to a fraction $I = 0.4 I_{\mathrm{MAX}}$. Particle velocity power spectra are calculated as $PSD_v(f) = \langle |\tilde{\mathbf{v}}(f)|^2 \rangle$, where $\tilde{\mathbf{v}}(f)$ is the Fourier transform of the (instantaneous) discrete experimental velocity $\mathbf{v}_i = (\mathbf{r}_i - \mathbf{r}_{i-1})/\Delta t$. We notice the illumination-dependent behavior of active particles with trajectories spanning a larger area for high light intensity as compared to the lower intensities. When having a closer look, the trajectories also seem to have *defects* where the particle either brutally reorients in the opposite direction or stops its persistent motion and seem to diffuse in a purely Brownian fashion for some time.

The velocity spectrum of a purely Brownian particle should be flat with $PSD_v(f) = 4D_t$. For our system, Figure 6.2 clearly shows a deviation from the flat spectrum at some frequency f_a whose value depends on the light intensity. For the high frequency region, the velocity spectrum in every conditions relax to the same plateau value $\langle PSD_v \rangle_{f \gg f_a} \approx 5 \times 10^{-13}$ m^2.s^{-1}, which is comparable to the value expected from Stokes-Einstein relation $4D_t = 4k_B T / 6\pi\eta R_P = 5.8 \times 10^{-13}$ m^2.s^{-1}. Note that the increase in magnitude of the plateau for high frequencies in the case of lowest light intensity (black curve, on the right in Figure 6.2) is due to the increase of pixel noise in the acquisition due to low light exposure. The information we would like to extract from these spectra is the cutoff frequency $f_a = 1/\tau_a$ which describes the timescale at which the data should be filtered in order to be left with only the persistent dynamics of the particle and neglect the Brownian noise-associated dynamics. This is in fact nothing more than a low pass filtering process. In practice, we perform a sliding average over a timescale τ_a separately on each component of the 2D experimental instantaneous velocity $\bar{v_x}$ and $\bar{v_y}$ and obtain a smoothed or *filtered* velocity $V_f = \bar{v_x} + \bar{v_y}$.

6.1.2 In-plane orientation during persistent segments

Now that we have this new filtered instantaneous velocity $V_f(t)$, we can start to look at the smooth dynamics (i.e. the dynamics purely associated to the propulsion force) of the particle during persistent segments of the trajectory. During these persistent segments, the particle out-of-plane orientation is confined close to $\theta = \pi/2$ which allows to track experimentally the in-plane orientation φ of the particle over time (see Section 2.5.3). If, as postulated, the active propulsion force dictates the smooth translational dynamics, the in-plane orientation should correspond to the displacement angle ψ as defined in Figure 6.1 *(left)*. If we compute $\psi(t)$ from the filtered velocity components such that $\psi(t) = \arctan\left(\frac{\bar{v_y}(t)}{\bar{v_x}(t)}\right)$, and plot it together with the experimentally measured $\varphi(t)$ in Figure 6.1 *(right)*, we obtain a good overlap. This proves that the filtering procedure introduced before allows to capture the smooth dynamics associated to the active propulsion force.

6.1.3 Out-of-plane orientation dynamics

Now that we gained confidence in the information contained in the filtered velocity V_f, we can look at its evolution along a whole trajectory. We plot in Figure 6.3 *(left)* such a two dimensional trajectory in the lab frame xy of a Cu@SiO$_2$ Janus particle in 100 mM glucose under maximum white light intensity illumination $I = I_{\mathrm{MAX}}$. We add a colormap accounting for the filtered velocity $V_f(t)$ along the trajectory resulting from a sliding average over $\tau_a = 2.1$ s for each velocity component. It appears that the particle alternates between persistent segments with relatively large filtered projected velocity and slow segments where the particle does not swim in a prescribed direction and with $V_f \approx 0$. We can also notice that when V_f drops to zero, a reorientation event seems to occur (the direction is randomized on a timescale much smaller than $1/D_r$). All of these observations suggest that the modulation of the projected velocity $V_f(t)$ along the trajectory originates from a change in out-of plane orientation θ.

In order to test this hypothesis, we plot the evolution of V_f together with the evolution of experimentally measured θ, in Figure 6.3 *(top right)*. The out-of-plane orientation angle θ can be inferred from image analysis through the projected Cu cap area $A_{Cu} = \pi/2(1 + \cos\theta)R_P^2$, see Section 2.5.3. Correlations in time between the increase of the smoothed projected velocity $V_f(t)$ and out-of-plane orientation angle $\theta(t)$ during particle motion in glucose can be clearly observed. In particular, one can see that sharp increases or sharp decreases of

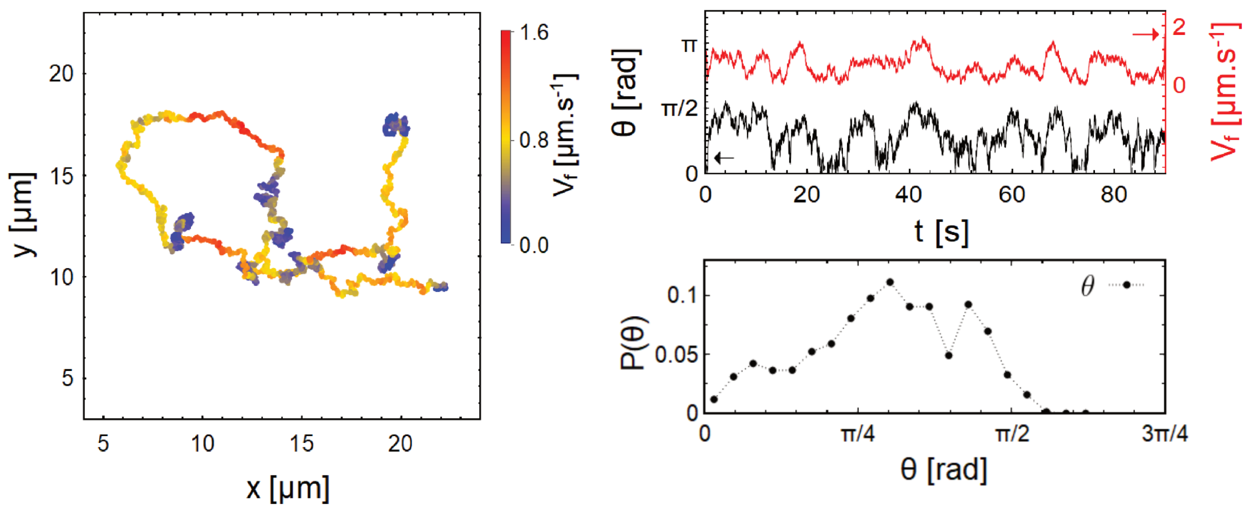

Figure 6.3: *(left)* Cu@SiO$_2$ Janus particle trajectory in 100 mM glucose aqueous solution of 9000 points acquired at 100 fps. Color map shows the filtered velocity $V_f(t)$ obtained from 2.1 s sliding average over the raw instantaneous velocity components. *(top right)* Black curve shows the temporal evolution of the out-of-plane oriantation angle $\theta(t)$ measured from image analysis following the method described in Section 2.5.3. The red curve is the filtered velocity V_f already shown as a color map on the left panel. *(bottom right)* Experimental out-of-plane orientation probability density $P(\theta)$ calculated for the same trajectory as the left and top right panels.

$V_f(t)$ are correlated with changes in θ and that the maximum values of V_f are systematically reached when $\theta \approx \pi/2$. Considering a constant propulsion speed V_0, there should be a simple relation between the projected smooth velocity V_f and θ such that:

$$V_f(t) = V_0 |\sin\theta(t)|. \tag{6.1}$$

Hence, comparing the evolution of $\theta(t)$ measured from image analysis to the evolution of $\theta_{V_f}(t) = \arcsin(V_f/V_{f,max})$ should in principle allow to confirm whether V_0 is constant or not. Our preliminary results in fact suggest that $\theta(t)$ and $\arcsin(V_f/V_{f,max})$ do not overlap perfectly, but more statistics and confidence in the angle and velocity extraction procedures from experimental acquisitions should be gained before drawing conclusions.

On the other hand, being able to measure the out-of plane orientation of swimming Cu@SiO$_2$ particles could provide information on the interactions (hydrodynamic, electrostatic, etc.) with the underlying substrate leading to an effective torque acting on the particle. For example, we plot in Figure 6.3 *(bottom right)* the probability density of the measured θ for the same trajectory, which seems to show several peaks. The multimodality of the probability density could be the signature of a complex orientation energy landscape of the particle resulting from interactions with the substrate. More statistics is needed in order to confirm the robustness of the multimodality and infer an orientation energy landscape from the existence and position of maxima.

Investigations are therefore currently ongoing to understand the dynamics of this system and the interactions from which it results. In particular, simulations and theoretical efforts in collaboration with Igor Kulić will hopefully allow to gain insights on the physics at stake.

6.2 On the mobility of optically confined microparticles against walls and supported membranes

In Section 5.4, we demonstrated that the close proximity of a vesicle membrane to a SiO_2 microparticle has a negligible impact on the drag experienced by the particle when moving parallel to the interface. In this section, we extend our investigation using a similar methodology but in a slightly different geometry, where the microparticle is brought near a solid-liquid interface with supported membranes. In this configuration, the non-deformable nature of the solid interface supporting the lipid membranes should in principle allow for the exploration of dissipation at smaller gap distances. This regime is particularly intriguing, as lipid membranes are known to act as effective boundary lubricants under macroscopic shear stress, but few experimental data exist for microscopic systems.

In order to probe the dissipations in these conditions, we rely on the geometry described

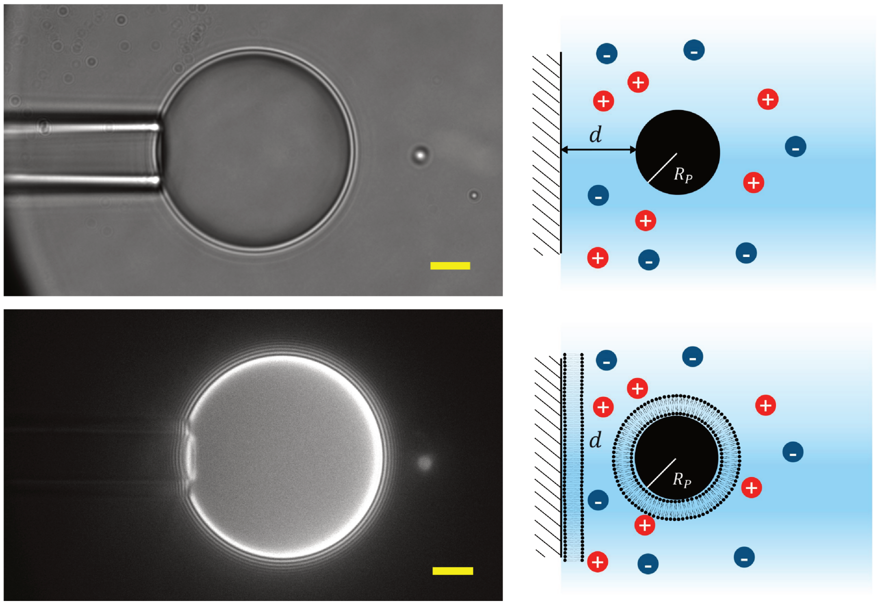

Figure 6.4: *(top)* Bright field microscopy image of a giant SiO_2 particle ($R_{P,G} \approx 12.5\,\mu m$) held in place spatially thanks to a micropipette. Nearby is an optically trapped $R_{P,s} = 0.76\,\mu m$ SiO_2 particle (appearing as a bright spot). The relative distance between the two objects can be precisely controlled thanks to piezoelectric actuation of the sample stage, but the absolute distance d is hard to access experimentally. The scale bar is $5\,\mu m$. *(bottom)* Fluorescence microscopy of a giant SiO_2 and an optically trapped $R_P = 0.76\,\mu m$ SiO_2 particle both coated with a DOPC lipid bilayer thanks to the SUV fusion method [170]. On the right is the corresponding scheme for each situation, in the presence of salt (NaCl) to screen the electrostatic repulsion.

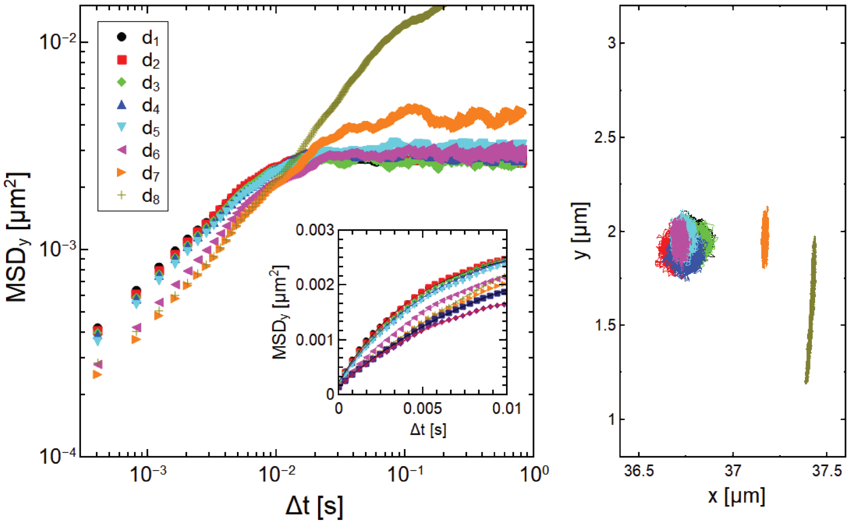

Figure 6.5: *(left)* Representative log-log plot of the mean squared displacement along y (parallel motion) for 8 different positions of the small bead with respect to the giant bead, corresponding to surface-to-surface distances d_i with $1 < i < 8$ and $d_1 > d_2 > ... > d_8$. Inset shows the short time regime in a linear scale, together with the fits (Eq. 1.32) allowing to extract the translational friction ζ_t. *(right)* Associated trajectories at each distance d_i. The shape of the trajectories evolve as a function of the proximity of the giant bead and the particle is pushed away from the center of the trap due to the interaction with the giant bead.

in Figure 6.4. A *giant* ($R_{P,G} = 12.5\,\mu\text{m}$) colloid is maintained stationary with the help of a micropipette by applying strong suction pressures. Similarly to what was described in 5.4, the whole sample can then be moved in order to modulate the position of the giant colloid relatively to an optically trapped $R_{P,s} = 0.76\,\mu\text{m}$ SiO_2 microparticle. The SiO_2 surfaces of both colloids can be covered with a lipid bilayer using the SUV fusion method, described in Ref. [196]. Reproducing this protocol, we could successfully coat with a bilayer both colloids as shown by the fluorescence microscopy images in Figure 6.4 *(bottom)*. In order to be able to probe small gap distances d, we add 8 mM NaCl in the aqueous solution to screen the electrostatic repulsion betwwen the negatively charged surfaces (the Debye length becomes of the order of a nanometer). By making sure the equatorial planes of the giant and small beads contained in the imaging plane, one can have an estimation of the surface-to-surface distance d which can be calculated from the inter-center of mass distance L_G extracted from image analysis as:

$$d = L_G - R_{P,G} - R_{P,s}. \tag{6.2}$$

By recording the particle motion at high acquisition rate (1000 fps) for several gap distances d, we can compute the MSD for each step and extract the translational friction coefficient experienced by the particle. In Figure 6.5, we plot the MSD curves and associated trajectories for a representative experiment where supported membranes were adsorbed on the two colloids' surfaces. d is decreased step-wise and a fast acquisition of the particle motion is performed at fixed d. It appears clearly in the log-log plot that the diffusion (at short times) is reduced upon approaching the giant colloid. The trapping stiffness is also changing for very small distances as the particle is displaced from its equilibrium position in the optical trap along x which results in a weaker trapping strength along y. By performing fits using Eq. 1.32 with κ and ζ_t as free parameters, we can extract ζ_t as a function of d which we plot in Figure 6.6 for the situation of bare SiO_2 (black points) interfaces and DOPC bilayer-coated SiO_2 (red points).

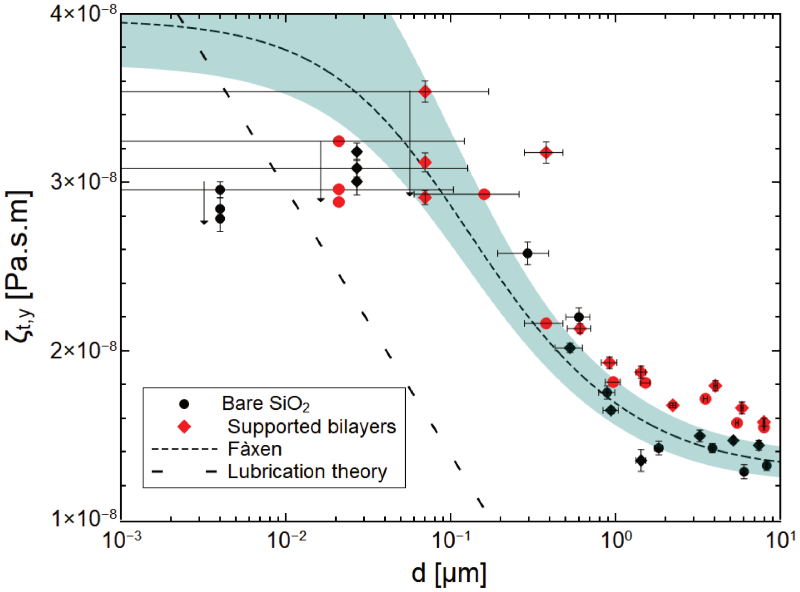

Figure 6.6: Measured translational drag coefficient ζ_t as a function of inferred surface-to-surface distance d. The red disks and diamonds stand for the surfaces coated with DOPC lipid bilayers, while the black disks and diamonds stand for bare SiO_2 surfaces. Disks and diamonds stand for different sets of experiments, performed with different samples. The black dashed line surrounded by the green shaded area account for Fàxen's formula for drag modification close to a wall with the area accounting for an uncertainty on the particle radius $R_P = 0.76 \pm 0.05\,\mu\text{m}$. The black arrows for the points laying on the same vertical line represent the decrease of measured drag upon increase of the trapping laser optical power (i.e. increasing κ) and thereby exerting more force in the direction normal to the interface.

Figure 6.6 shows that we measured an increase in the particle translational drag for decreasing d. For bare interfaces (the black points) and $d > 0.1$ μm , data are well described by the law of Faxén (see Appendix 8.6) for the drag modification due to a bounding solid wall. For the supported membranes (red data), the measured drag is systematically greater than for bare interfaces. The fact that additional dissipation arise from the presence of a bilayer is not surprising, as it can be interpreted as a larger hydrodynamic radius. Still, the magnitude here suggests that the equivalent radius would be more than 500 nm greater than the bare particle radius, which is much greater than the expected thickness of the bilayer and water gap [170, 196].

The most interesting feature here is the saturation of the measured drag upon decreasing d for both bare and bilayer-coated surfaces. Indeed, for the smallest distances, the particle is displaced from its equilibrium position in the optical trap, meaning that the restoring force acts normal to the solid wall, thereby pushing the particle against the giant colloid. In those conditions, when increasing the laser power output, which leads to increasing the stiffness and therefore the force, a lower translational drag is measured. This is shown by the descending arrows for experimental points on a same vertical line. We checked the robustness of the phenomenon by performing the same experiment several times in different samples, and checked that it was not a geometric effect due to a increase in d (or changes in focus) by using larger particle sizes for the optically trapped probe.

From the point of view of hydrodynamics, it is hard to envisage how the particle could experience less drag when brought closer to a solid boundary. Current investigations are therefore conducted in order to understand what leads to this reduction of the drag.

6.3 General conclusion

Cellular processes like endocytosis require continuous membrane deformation. The energy landscape and dynamics of such processes are influenced by particle-membrane interactions and the coupled dynamics of both entities. In this thesis, we employed experimental techniques to study driven particle wrapping using a model system. We used optical tweezers to probe the forces involved in particle wrapping under a directed external force, examining the influence of various physical parameters and the process's reversibility. We demonstrated that stable, complete wrapping of an active particle can occur autonomously, even in the absence of biological machinery.

In **Chapter 3**, we investigated force-driven entry of spherical microparticles into giant unilamellar vesicles using optical tweezers under vanishing adhesion conditions. Our studies revealed an instability in the shape of the unbound membrane segment, leading to stable wrapping. We highlighted the role of membrane excess area stored in vesicle area reservoirs, which contribute to membrane tension similarly to interfacial tension in liquid interfaces. By successively penetrating particles in a same vesicle, we showed that this regime of constant tension is limited by the availability of membrane area reservoir, and tension can significantly increase upon tiny membrane area consumption, as described by established theories. By varying particle size, we found a force minimum for particle sizes comparable to the membrane's bendocapillary length. Using micropipette aspiration, we probed the degree of reversibility of the wrapping process and quantified the membrane tension required for neck re-opening, showing variability in the degree of reversibility likely due to differences in spontaneous curvature.

In **Chapter 4** we report on a model a system that autonomously mimics the first stages of endocytosis, where active Janus particles can approach, deform and become wrapped by giant vesicles using visible light and physiological glucose concentrations. We investigated the physical interactions responsible for stable wrapping in this situation where the interaction dynamics, especially at large distances, is dictated by the stochastic dynamics of the active particle and long-range interactions with the host. Our results showed that long contact times, rather than maximizing particle velocity, are crucial for successful wrapping, especially in the presence of adhesion and negative spontaneous curvature. Long-range hydrodynamic interactions help maintain contact between the particle and membrane, allowing adhesion and overcoming energy barriers. Finally, we show that similarly to the case of particle wrapping driven by optical tweezers, the stability of the fully wrapped state is provided by the large energetic cost associated to the unbound membrane segment for intermediate wrapping states.

Chapter 5 was dedicated to analyze the dissipation and interactions of microparticles with lipid bilayers. We studied the diffusion of fully wrapped isotropic and Janus particles by floppy vesicles, showing that engulfed particles experience dissipation due to the coupling with the neck structure. Our data suggested a universal increase in drag, with a significant dependence on particle size and membrane tension. This contrasts with previous reports for curvature-inducing proteins and demands for new theoretical explanations. Indeed, our findings indicated that engulfed particles could experience a drag up to 10 times the bulk prediction from Stokes' Law for tense membranes and we showed that such increase in the translational drag can not be due proximity to the bilayer and solid substrate only. We conclude that another dissipation pathway exists in this particular geometry of a wrapped particle connected to a mother vesicle by a neck.

Overall, the results obtained over the course of this thesis provide valuable insights into the physical criteria required for stable wrapping of driven particles by lipid vesicles thanks to an external directional force, or in the context of autonomously navigating self-propelled particles. These findings are significant for understanding from a physical standpoint the biological processes resulting in uptake of inert particles or swimmers by biological units. Potential applications could be expected in domains ranging from drug delivery, nanomedicine, or microbial infection, to micromotor design in wastewater treatment contexts.

Chapter 7

Résumé de thèse en français

L'interaction d'un corps microscopique avec une membrane constitue une situation omniprésente à l'échelle cellulaire. Ces interactions jouent un rôle crucial dans divers contextes, notamment lors de la phagocytose des microbes par les cellules immunitaires [1, 2] et la propagation intercellulaire des pathogènes bactériens [3, 4]. Lors de tels processus, la membrane cellulaire se déforme au contact d'un corps étranger et subit des transitions de forme et de topologie pour permettre l'internalisation. Dans certains cas, le corps étranger est une microparticule inerte soumise à la diffusion Brownienne, comme dans le cas de l'exposition des cellules aux microplastiques [5]. Dans d'autres cas, la particule consomme de l'énergie de son environnement et la convertit en mouvement dirigé ou en forces mécaniques, se maintenant ainsi hors de l'équilibre thermique. Cette propriété est observée chez les micro-organismes tels que les bactéries, mais peut également être reproduite dans des systèmes artificiels. Dans ces systèmes, il peut être difficile de distinguer les contributions des mécanismes biologiques actifs de celles des interactions physiques menant à l'engloutissement. Reproduire les processus complexes de remodelage de la forme des membranes se produisant en biologie en l'absence de machinerie biologique constitue donc une approche prometteuse pour mettre en évidence et étudier le rôle des interactions physiques. Dans cette thèse, nous utilisons des systèmes modèles artificiels pour étudier expérimentalement les principes physiques régissant l'enveloppement de microparticules par en présence d'une force externe ou dans le cas de particules actives.

Introduction et motivations

Les membranes biologiques sont des structures dynamiques essentielles à la compartimentation cellulaire, caractérisées par leur fluidité et leur faible rigidité de courbure. L'unité structurale fondamentale de ces membranes est la bicouche lipidique, formée par l'auto-assemblage des phospholipides amphiphiles dans des environnements aqueux. En fonction de leur composition et des conditions, ces bicouches peuvent former diverses structures, y compris des vésicules telles que les petites vésicules unilamellaires (SUVs, taille $< 10\,\text{nm}$), les grandes vésicules unilamellaires (LUVs, taille comprise entre 10 nm et 1 µm), ainsi que les vésicules unilamellaires géantes (GUVs, taille 1-100 µm). Les vésicules unilamellaires géantes (ou GUVs) sont particulièrement utiles pour étudier les propriétés des membranes en raison de leur visibilité au microscope optique et constituent donc un système modèle idéal pour un compartiment cellulaire.

Les membranes lipidiques au coeur des membranes biologiques pouvant être décrites comme des fluides bidimensionnels, elles ne possèdent pas de module élastique de cisaillement dans le plan. Elles possèdent cependant une élasticité de courbure, dont l'énergie associée est décrite par le hamiltonien de Helfrich [11], impliquant des paramètres tels que le module de courbure κ_b ayant les unités d'une énergie, et la courbure spontanée m décrivant la courbure optimale de la membrane du fait de l'existence d'une asymétrie entre les deux feuillets constituant ou de leur exposition à différents environnements [13]:

$$E_b = \int \left[2\kappa_b(M-m)^2 + \kappa_G \bar{K}\right] \mathrm{d}A \tag{7.1}$$

avec M la courbure moyenne et $\bar{K}$ la courbure Gaussienne de la surface que constitue la membrane et κ_G le module Gaussien. En plus du coût énergétique associé à la courbure d'un segment de membrane, il existe une énergie associée à l'étirement d'un segment de membrane d'une quantité d'aire ΔA. La tension membranaire σ caractérisant ce coût énergétique ($E_\sigma = \sigma \Delta A$), est une propriété qui peut varier d'une membrane à l'autre selon les contraintes auxquelles elles sont soumises (par exemple du volume de fluide qu'elles contiennent dans le cas de vésicules). Selon le régime, pour les membranes lipidiques, cette tension peut résulter à la fois d'effets entropiques liés aux ondulations thermiques de la membrane ainsi que de la présence d'une courbure spontanée (et d'une tension spontanée associée), ou encore du changement de la distance d'équillibre intermonéculaire des lipides constituant la membrane. Enfin, les membranes lipidiques présentent une viscosité de cisaillement et une friction intermonocouche, affectant la dynamique des objets inclus dans la membrane et des changements de forme.

Lors de la déformation d'une membrane ou d'une vésicule lipidique par une microparticule, une source d'énergie est donc nécessaire pour surmonter les coûts énergétiques associés aux modes de déformation de la membrane introduits plus haut. Cette énergie peut être apportée par une adhésion entre l'objet et la membrane, ou une force extérieure. Cette dernière peut être apportée par un dispositif tel qu'une pince optique, ou résultant d'une activité de la particule convertissant à l'échelle locale de l'énergie chimique en mouvement persistant (particule active).

Le cas d'une particule active se déplacant de manière autonome s'avère être très différent du cas où la force est exrcée à l'aide d'un champ externe dans la mesure où la direction de la force n'est plus dictée par l'opérateur mais par la dynamique orientationelle de la particule active. Cette dynamique d'orientation en plus d'être stochastique peut être affectée par les interactions physiques avec son environnement, et en particulier avec la membrane. Observer l'interaction prolongée menant à l'enrobage d'une telle particule active par une membrane lipidique nécessite donc des interactions favorables, à longue autant qu'à courte portée. Or, dans ces systèmes, les interactions hydrodynamiques dominent souvent les phénomènes à longue et moyenne portée avec des obstacles solides [60, 72, 58, 73, 74, 69]. Comprendre et exploiter ces interactions entre une particule active et un objet déformable comme une membrane lipidique permettrait donc de donner lieu à des transitions de forme semblables à celles à l'oeuvre dans une grande variété de processus biologiques.

Le travail mené au cours de ma thèse se focalise sur l'étude des principes physiques à l'oeuvre lors de l'engloutissement d'une particule micrométrique par une compartiment biologique modèle (une GUV) en présence d'une force éxtérieure et peut être scindé en trois axes distincts:

- L'utilisation d'une pince optique pour obtenir des mesures quantitatives des forces à l'oeuvre au cours de l'engloutissement forcé de particules et établir le paysage énergétique associé à l'engloutissement de la particule sur un système contrôlé.
- Le développement d'un système de particules actives artificielles permettant de reproduire l'endocytose dans le cas où les particules sont libres, et où par conséquent, la force exercée n'est plus dictée par la position relative du piège optique mais par l'orientation de la particule.
- L'étude de la dynamique translationnelle ou rotationnelle de particules, piégées optiquement ou non, dans différentes situations, à savoir une fois complètement englouties par une vésicule lipidique ou confinées proche d'une membrane supportée.

Dans la suite, les approches expérimentales développées et mises en oeuvre dans le cadre de mes travaux seront décrites et les principaux résultats exposés.

Résultats

Les débuts de ma thèse ont été consacrés à la mise en place et l'optimisation des performances de piégage d'une pince optique. Le dispositif mis en place juste avant mon arrivée n'était en effet pas en mesure de piéger des particules micrométriques constitutées de matériaux à densité plus faible que la Silice. La focalisation du faisceau laser générant le piège optique n'étant pas de bonne qualité menait à un piégage selon l'axe de propagation du faisceau plus faible que la pression de radiation exercée par ce dernier sur la particule. Dans le cas de particules denses, la force de gravité était suffisante pour contrebalancer la pression de radiation s'exerçant sur la particule en direction opposée, ce qui n'était plus le cas pour les particules moins denses. Une fois l'optimisation effectuée, le montage était en mesure de piéger des particules composées de matériaux polymériques peu denses tels que le Polystyrene ou la Melamine Formaldehyde. Enfin, la mise en place de protocoles de calibration de la pince optique (permettant les mesures quantitatives de force) ainsi que l'interfaçage des cellules piezoélectriques pilotant la platine porte-échantillon ont permis de passer à des investgations experimentales sur les systèmes d'intérêt.

Interaction forcée optiquement

Dans un premier temps, j'ai mené des investigations expérimentales combinant des mesures de force avec de l'imagerie optique en fluorescence ainsi qu'en champ clair au cours de l'engloutissement forcé de microparticules par des vésicules unilamellaires géantes constituées d'un seul type de lipide (1-palmitoyl-2-oleoyl-sn-glycero-3-phosphocholine ou POPC) en phase fluide à température ambiante. Ces éxperiences ont été menées dans un régime d'adhésion négligeable entre la particule et la membrane (densité d'énergie adhésive surfacique $|w| < 10^{-7}$ N.m^{-1}) et où la taille des particules (de rayon R_P) est comparable à la longueur bendocapillaire, $R_P \approx \lambda_\sigma$. La longueur bendocapillaire est une longueur caractéristique du système qui émerge des propriétés de la membrane resistant sa déformation, à savoir sa tension σ et son module de courbure κ_b, tel que $\lambda_\sigma = \sqrt{\kappa_b/\sigma}$. Pour se trouver dans ce régime, il est nécéssaire d'abaisser la tension membranaire de sorte à ce qu'elle atteigne des valeurs $\sigma < 10^{-7}$ N.m^{-1}. Pour ce faire, les vésicules géantes formées grâce à une méthode impliquant l'hydratation de films précurseurs déposés sur un substrat de gel de PVA (polyvinyl alcohol) sont *dégonflées* osmotiquement en modifiant la concentration en glucose

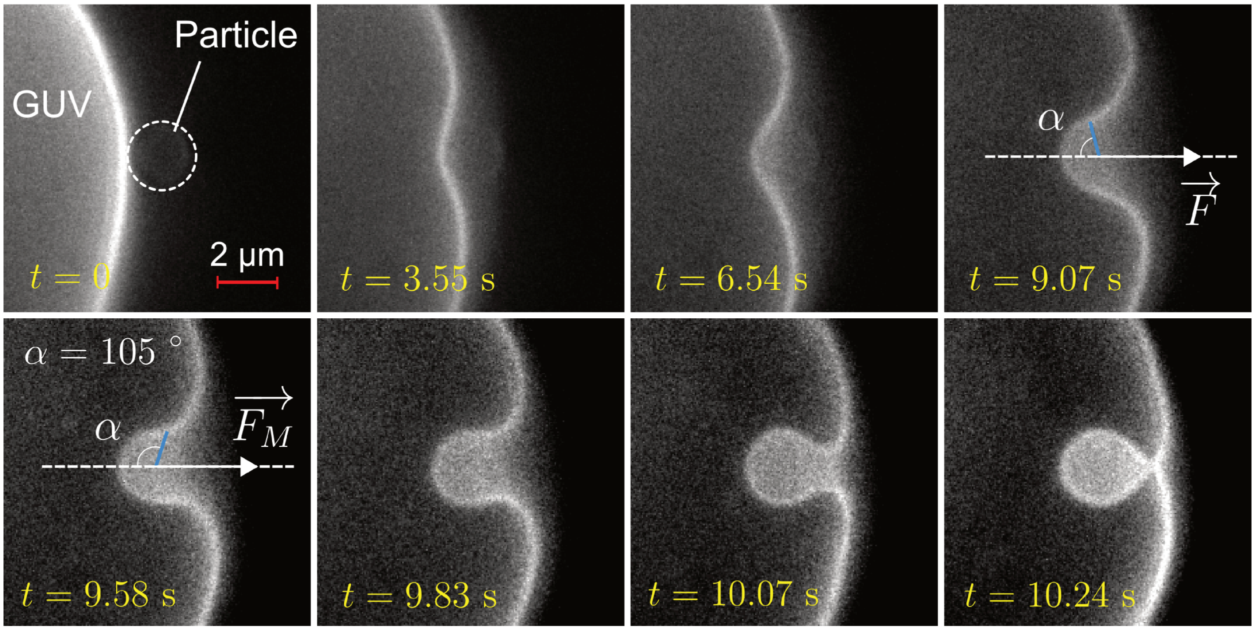

Figure 7.1: Instantanés d'une acquisition de microscopie en fluorescence durant laquelle une particule de $R_P = 1.15\,\mu\mathrm{m}$ en SiO_2, piégée optiquement, se déforme et est engloutie par une GUV de POPC contenant 1% de sondes fluorescentes NBD. Le déplacement relatif entre la platine et le piège optique est effectué à une vitesse $v_{rel} = 0.30 \pm 0.02\,\mu\mathrm{m\,s^{-1}}$. Les horodatages permettent de remarquer que la dynamique de fermeture du col se produit sur une échelle de temps beaucoup plus courte que la déformation induite, ce qui est une signature d'une instabilité.

de la solution dans laquelle les vésicules sont immergées. En effet, si la concentration en glucose à l'extérieur augmente, un flux de solvent (de l'eau) du compartiment intérieur vers l'exterieur de la vésicule mène à la réduction du volume de fluide emprisonné, et par suite à un abaissement de la tension de la membrane.

Nos expériences ont permis de résoudre les déformations de la membrane autour de la particule au cours de l'engloutissement (voir Figure 7.1) et de mesurer la force nécéssaire à la pénétration par enrobage de la particule dans une GUV. Un graphe représentant la forme typique du profil de force associé à l'engloutissement d'une particule de silice est montré sur la Figure 7.2, ainsi que la définition des quantités déterminant le degré d'enrobage et de déformation de la membrane. Nous avons étudié les effets des contributions de la courbure et de la tension de la membrane en utilisant différentes tailles de particules, ainsi que l'effet de l'adhésion des particules en utilisant des particules fabriquées à partir de différents matériaux. Afin de ne pas altérer les propriétés de la membrane, aucun déplétant, sel ou autre espèce chimique n'a été ajoutée. Les interactions entre la particule et la membrane sont

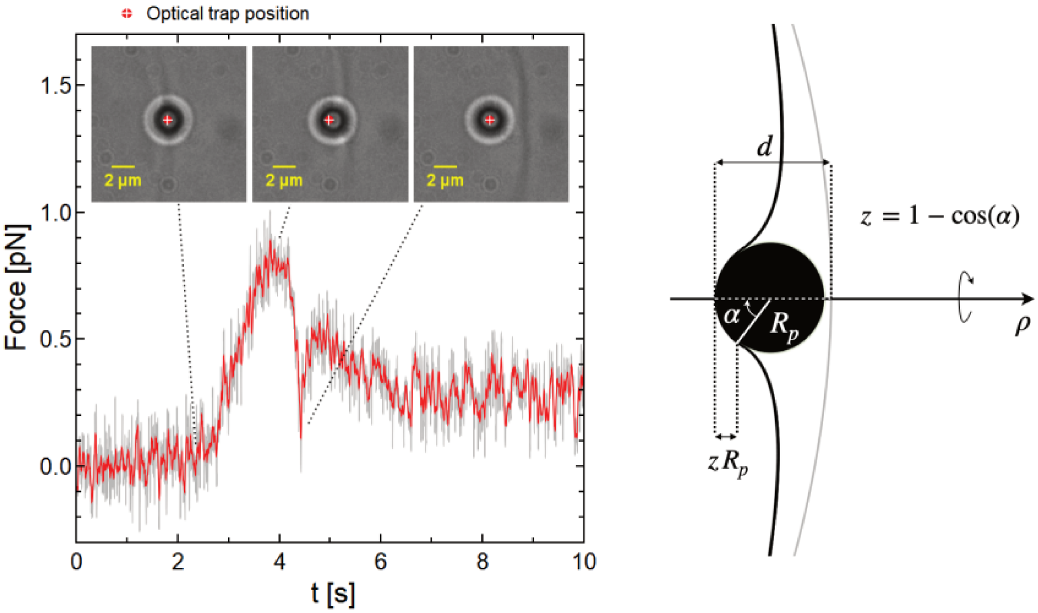

Figure 7.2: *(gauche)* Profil de force typique pour une particule de $R_P = 1.15\,\mu\text{m}$ piégée optiquement lors de l'enveloppement forcé par une GUV de POPC à une vitesse de mouvement relatif $v_{rel} = 1.88 \pm 0.02\,\mu\text{m}\,\text{s}^{-1}$. Des instantanés de microscopie en champ clair à des moments clés sont également représentés. *(droite)* Représentation schématique d'une particule sphérique déformant une membrane vésiculaire et définition de l'angle d'enveloppement α, de la profondeur de pénétration d et du degré de pénétration z.

donc faiblement favorables ou défavorables et non spécifiques [168, 197]. Nous avons exploré un régime encore inexploré dans lequel l'adhésion a un impact mineur sur les transitions de forme induites sur la membrane, qui dépendent crucialement de l'énergie et de la dynamique associée au cou (ou col) de la membrane formé lorsqu'une particule est entièrement enveloppée [81, 123, 124, 131, 128].

Une particule une fois engloutie à l'aide de la pince optique reste connectée à la vésicule géante par ce cou adoptant une forme proche d'une caténoïde très stable, ce qui rend le processus sinon irreversible, au moins asymétrique. Ceci a pu être mis en évidence dans un premier temps en utilisant la force optique pour essayer d'extraire la particule enrobée de l'espace intravesiculaire, ce qui s'est avéré impossible avec les forces optiques atteingnables (<10 pN). En l'absence d'adhésion entre la particule et la membrane, c'est la stabilité de cette portion de membrane qui confère la stabilité à l'état d'enrobage complet. Il est donc intéressant de chercher à mesurer l'énergie nécessaire pour que ce cou (ou col) se réouvre et laisse la particule à nouveau libre. Pour ce faire, j'ai consacré du temps à la mise en place d'un montage combinant la pince optique et un montage de micropipette, permettant de

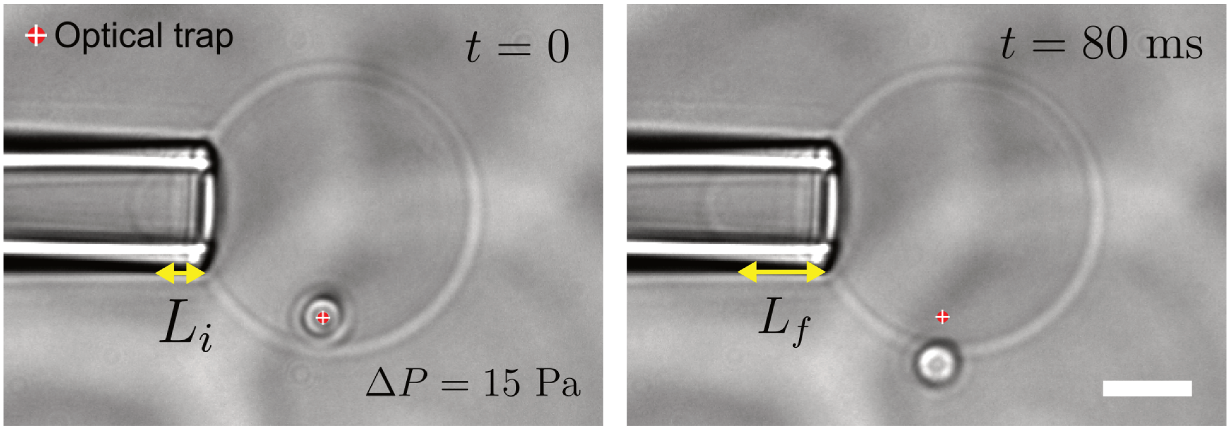

Figure 7.3: Instantanés de microscopie en champ clair d'une expérience consistant à appliquer une pression d'aspiration sur une vésicule géante initialement flasque dans laquelle une particule de $R_P = 1.15\mu$m de SiO_2 a été engloutie grâce à des forces optiques. *(gauche)* La particule enveloppée est maintenue dans un piège optique (centre du faisceau laser représenté par un point rouge) avec une faible raideur ($\kappa = 2\,\mu N\,m^{-1}$) afin de garder la particule à l'équateur de la vésicule et d'avoir à la fois la particule enveloppée et le segment de membrane aspirée dans le plan d'imagerie. *(droite)* La particule a été désenveloppée (en raison de l'ouverture du col) et la particule a échappé au piège optique et a été expulsée de l'espace intravésiculaire.

controller la tension d'une vesicule en lui appliquant une pression de suction. Un montage de micropipette ayant existé au sein de l'équipe Mcube avant mon arrivée, le travail a consisté à adapter des éléments du montage de sorte à former un nouveau montage combinant à la fois pince optique et aspiration par micropipette (et microscopie de fluorescence). Ce montage a par la suite permis d'évaluer l'énergie nécéssaire pour l'ouverture du cou en augmentant par pallier la tension induite par la micropipette sur une vésicule dans laquelle une particule a été préalablement engloutie, puis maitenue à l'équateur de la vésicule à l'aide de la pince optique. Des images en microscopie optique champ clair d'une telle expérience sont montrées en Figure 7.3, où une particule engloutie est expulsée une fois un seuil de tension appliquée sur la vesicule atteint. Cette expulsion de la particule se traduit également par l'augmentation de la portion d'aire de la membrane aspirée dans la micropipette, correspondant à la surface de membrane enrobant la particule avant son expulsion. Par comparaison avec des modèles existants considérant la stabilité des cols de membrane, nos mesures suggèrent que la présence d'une courbure spontanée négative (favorisant les structures courbant vers l'interieur de la vésicule) soit responsable de la stabilité de cette strcture, et a fortiori de l'état d'enrobage complet de particules non-adhésives. Il s'avère effectivement que les mesures de force, ainsi que les observations en microscopie optique suggèrent l'existence d'une courbure spontanée dans notre système. Ceci a en effet été prédit et mesuré dans des conditions simillaires aux notres, où ne asymmétrie entre les deux feuillets constituant la membrane existe du fait de l'exposition de chacun des feuillets à une solution contenant des espèces chimiques différentes [12]. Cependant, il est à noter que pour des vésicules contenant une solution aqueuse de sucrose et immergée dans une solution aqueuse de glucose, des mesures expérimentales ont rapporté l'existence d'une courbure spontanée positive (la membrane préfère courber vers l'extérieur) [104], tandis que toutes nos mesures et observations suggèrent une courbure spontanée de signe opposé (négative). Ceci peut toutefois être expliqué par la différence de méthode de fabrication ainsi que de composition en lipides des membranes formant les vésicules.

Engloutissement autonome de particules actives

Après avoir étudié les transitions de morphologie induites par une particule piégée optiquement sur une vésicule géante à faible tension, nous nous sommes penchés sur l'étude de particules actives. Ces particules actives synthétiques sont a priori capables d'exercer une force sur la membrane grâce à leur mécanisme (actif) de nage, de manière analogue à une particule piégée optiquement, à la différence que la direction dans laquelle s'exerce la force dépend de l'orientation de la particule. Pour ce faire, nous avons introduit un système de particules Janus Cu@SiO_2 capables de se déplacer dans une solution aqueuse de glucose sous

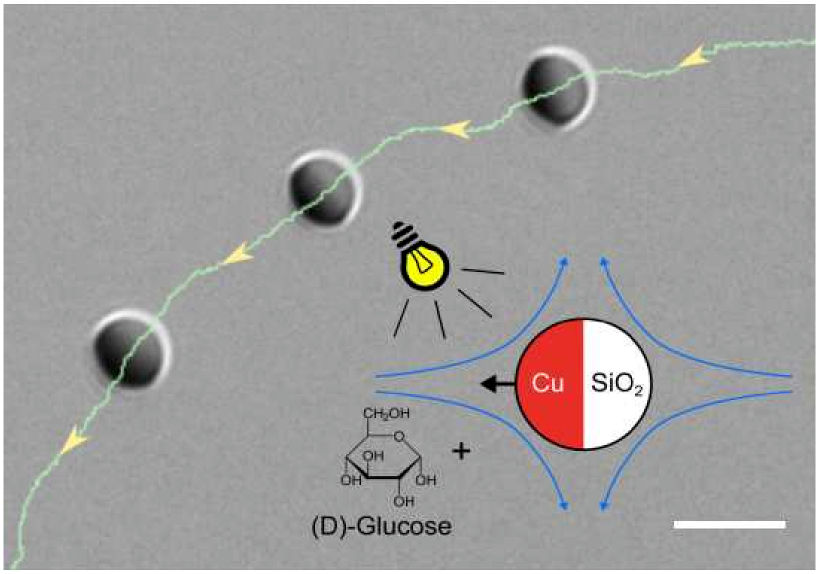

Figure 7.4: Image en microscopie en champ clair et trajectoire (en vert) d'un nageur Janus Cu@SiO_2 dans une solution de glucose à 100 mM. L'encart illustre le mécanisme de mouvement actif et l'écoulement de fluide le plus probable dans le référentiel du nageur (puller). L'échelle correspond à 5 µm.

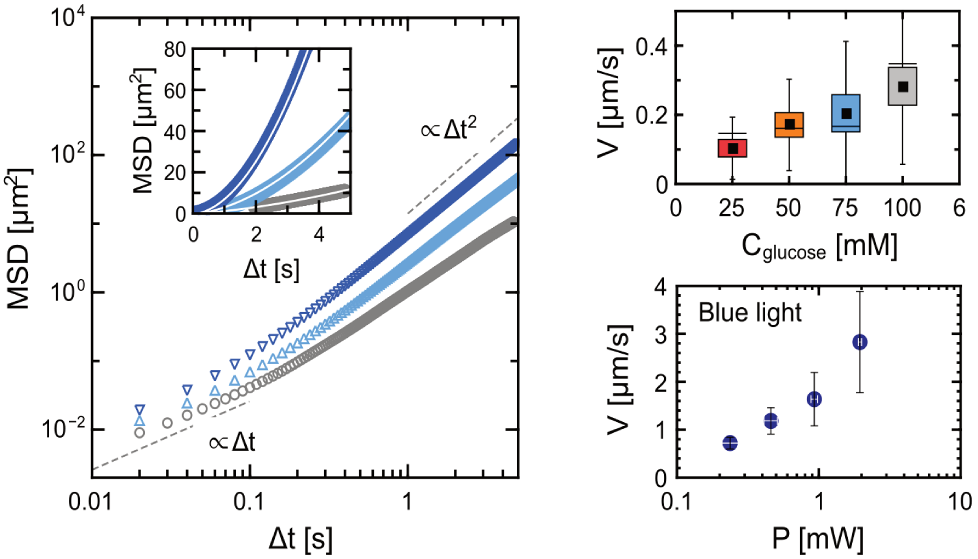

Figure 7.5: *(gauche)* Déplacement quadratique moyen en fonction du temps de retard en échelle logarithmique pour trois trajectoires représentatives de particules immergées dans une solution de glucose à 100 mM avec uniquement de la lumière blanche (cercles gris), de la lumière blanche et une irradiation de lumière bleue de 0.46 mW (triangles bleus clairs pointant vers le haut) et de la lumière blanche et une irradiation de lumière bleue de 1.96 mW (triangles bleus foncés pointant vers le bas). L'encart montre une représentation en échelle linéaire avec des ajustements (lignes blanches pleines) permettant d'extraire la vitesse projetée en utilisant l'équation 1. Pour ces trois cas, l'ajustement donne $V = 0.48$ μm.s^{-1}, $V = 1.23$ μm.s^{-1} et $V = 2.33$ μm.s^{-1} (de bas en haut). *(droite)* Vitesse active projetée V extraite des ajustements MSD pour des particules immergées dans des solutions de glucose de concentration croissante dans des conditions d'illumination normale. Les carrés noirs représentent des moyennes sur 10 trajectoires. Vitesse active projetée mesurée pour des particules immergées dans une solution de glucose à 100 mM sous différentes puissances d'illumination bleue.

irradiation lumineuse visible. Le cuivre est converti en oxydes de cuivre photocatalytiques lorsque les particules sont dispersées dans l'eau. En raison de leur structure asymétrique Janus, elles ont la capacité intrinsèque de se déplacer dans n'importe quelle direction indépendamment de la source lumineuse, ce qui nous permet d'observer des interactions complexes avec l'environnement. En particulier, les interactions avec les interfaces fluides telles que les membranes de phospholipides représentent une situation de confinement rencontrée dans de nombreux processus. Il a été observé que les nageurs Janus sont capables de déformer des vésicules géantes lorsqu'ils sont enfermés à l'intérieur [89], une réponse qui a également été confirmée pour la matière active biologique [151] et par des considérations théoriques [152, 153]. Cependant, les particules Janus nageant librement à l'extérieur de la vésicule ont montré des interactions qui ressemblent aux interactions génériques de la matière active avec des obstacles solides [154, 69, 155]. Pour les nageurs de type "pusher" (générant un champ de vitesse du fluide environnant qui pousse le fluide devant et derrière lui), un mouvement orbital persistant des nageurs Janus autour des vésicules géantes a été rapporté [71], et le transport actif des vésicules par une seule particule a pu être réalisé uniquement après l'application de forces importantes [86]. À notre connaissance, aucun autre comportement n'a été rapporté lors de l'interaction de particules Janus actives nageant librement avec des compartiments de biomimétiques. Alors que dans les expériences précédentes, les particules Janus étaient généralement fabriquées à partir de Platine déposé sur une hémisphère de colloides commerciaux de silice ($Pt@SiO_2$), qui nagent dans la direction opposée de l'hémisphère métallique et sont généralement considérées comme des "pushers" [63], nous utilisons une nouvelle combinaison de particules constituées de particules commerciales de silice semblables, sur lesquelles une couche de cuivre est déposée. Immergées dans une solution aqueuse de glucose en concentration physiologique (25-150 mM) et illuminées par la lumière visible du système d'illumination du microscope, ces particules deviennent activent et naviguent de manière autonome dans un plan proche du substrat solide, comme montré dans l'image de microscopie en champ clair de la Figure 7.4.

L'activité de ces particules Janus dans du glucose sous illumination par de la lumière visible peut être démontrée et quantifiée en utilisant le déplacement quadratique moyen (ou MSD pour mean squared displacement en anglais). La dépendence quadratique de ce dernier avec le décalage temporel Δt aux temps longs, visible sur les graphes présentés sur la Figure 7.5, est la signature du comportement ballistique à ces échelles de temps et permettent d'extraire une vitesse moyenne projetée V. Il est possible de montrer qu'en augmentant la concentration de glucose dans le milieu ou l'intensité de l'illumination de l'échantillon, cette vitesse projetée V augmente, ce qui suggère que ces deux ingrédients sont impliqués dans le mécanisme menant à la locomotion de la particule Janus (voir Figure 7.5). Il est cependant à noter que les particules Janus de $Cu@SiO_2$ immergées dans du glucose présentent une dynamique orientationnelle riche, et que par conséquent le vecteur associé à la vitesse d'autopropulsion de la particule présente des composantes non nulles hors du plan d'observation durant une grande partie du temps. La vitesse moyenne projetée V ainsi extraite de l'ajustement d'une courbe de MSD reflètant une moyenne sur l'ensemble d'une trajectoire de plusieurs secondes ne représente donc pas la vitesse active réelle de la particule, mais la moyenne temporelle de sa projection dans le plan d'observation.

Tout comme les particules Janus Cu alimentées avec du peroxyde d'hydrogène [92, 65, 66], ces nageurs immergés dans du glucose se dirigent vers l'hémisphère catalytique, ce qui peut

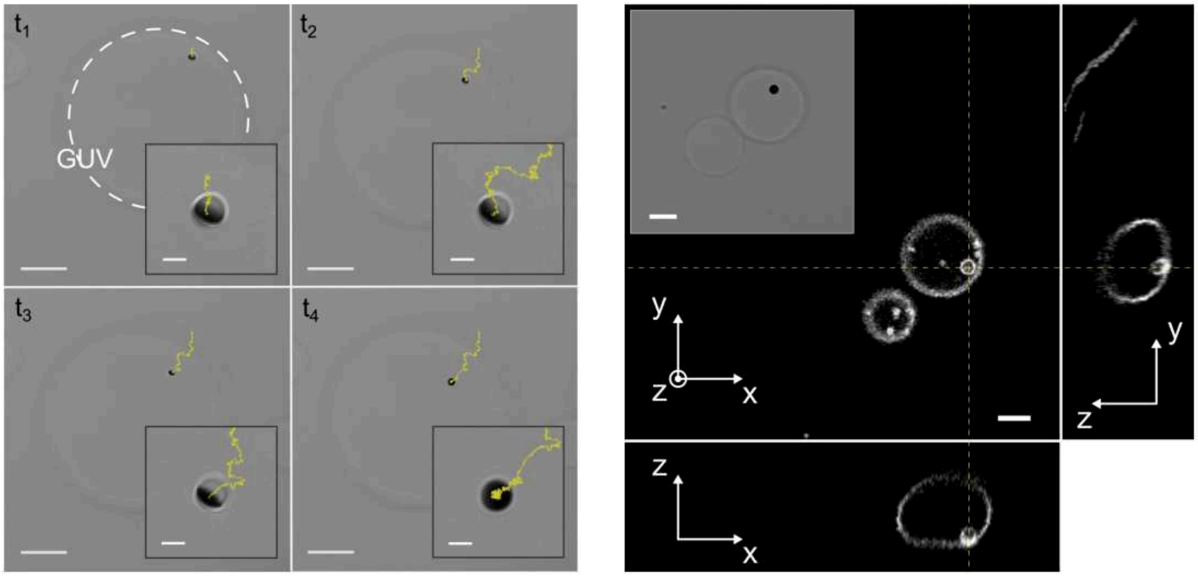

Figure 7.6: *(gauche)* Instantanés d'une acquisition de microscopie en champ clair montrant l'enveloppement d'une particule Janus Cu@SiO$_2$ par une GUV de POPC. La trajectoire rétrograde est montrée en jaune. *(droite)* Images de microscopie confocale montrant les plans xy, zy et zx permettant de montrer le signal de fluorescence des lipides correspondant à la GUV et à la particule enveloppée. L'encart montre l'image en champ clair correspondante.

être interprêté comme une signature de la nature "puller" du nageur. Ce mode de nage différent permet d'autres types d'interactions avec les vésicules et permet notamment d'observer des comportements semblables à l'endocytose, où la particule est complètement enrobée par la membrane d'une vesicule lipidique.

En effet, en étudiant la dynamique translationnelle ainsi que rotationnelle de la particule au cours de l'approche et aux débuts de l'interaction avec une vésicule géante à faible tension sédimentée proche du substrat solide, l'on peut mettre en évidence l'existence d'interactions hydrodynamiques attractives maintenant l'hémisphère de cuivre orientée vers la membrane. Ce type d'interaction attractives ont été prédites pour des nageurs pullers en présence d'un obstacle solide sphérique, et il a été prédit qu'elles mènent à l'adsorption de la particule sur une interface solide [156]. Ici, à défaut d'être complètement adsorbée et immobile, la position et l'orientation de la particule continue de fluctuer de manière Brownienne tout en étant confinée spatialement au périmètre de la vésicule et orientationellement avec le cuivre pointant vers le centre de masse projeté de la vésicule. Après un temps de contact t_c de l'ordre de quelques dizaines de secondes, un mouvement radial soudain peut être observé correspondant à l'enrobage complet de la particule par la vésicule géante (voir Figure 7.6, gauche). Cet engloutissement peut être confirmé grâce à de la microscopie confocale en fluorescence (voir Figure 7.6, droite), et sa dynamique étudiée plus en détail dans la situation particulière où la particule se trouve exactement en-dessous de la vésicule. Dans ce cas, la transition d'enrobage partiel à complet se traduit par un changement d'intensité de fluorescence collectée de la région où se trouve la particule (la particule est complètement enrobée de lipies fluorescents), et on mesure un temps de transition de l'ordre de la seconde. Une modélisation de la situation avec les énergies associées à la déformation locale de la membrane permet de mettre en évidence le rôle crucial joué par la partie libre (la partie qui n'est pas en contact avec la paticule) de la membrane lors de la transition vers l'enrobage complet. En effet, l'énergie associée à ce segment de la membrane augmente avec le degré d'engloutissement de la particule pour une membrane de courbure spontanée négative [20], puis possède une énergie quasi-nulle lorsque l'enrobage de la particule est complet, ce qui mène à l'existence d'une instabilité.

Dynamique de particules englouties ou confinées proche d'une membrane

Un dernier axe de recherche dans mes travaux de thèse a consisté à étudier la dynamique des particules dans différents régimes d'interactions et états d'engloutissements afin de sonder leur environnement et ainsi obtenir des informations sur la structure connectant la particule enrobée à la membrane ou la membrane elle-même.

Le premier cas est celui des particules englouties. En effet, la façon dont l'énergie thermique est dissipée dans l'environnement de la particule a une influence sur la dynamique de cette dernière, et dépend de son environnement. Les trajectoires expérimentales de microparticules isotropes et Janus enrobées après leur enloutissement complet par des vésicules, soit entraînées par des pinces optiques, soit en conditions actives, ont donc permis de recueillir des informations sur la dissipation. La situation dans laquelle ont été effectuées ces mesures est schématisée sur la Figure 7.7, avec la définition des paramètres physiques importants. Nous avons montré que les particules englobées subissent des dissipations dues au couplage de leur mouvement avec le mouvement de la structure les reliant à la vésicule mère (le col), comme montré dans la Figure 7.8. En effet, la friction translationelle ζ_t mesurée pour des particules en état d'enrobage complet dans une vésicule lipidique a été mesuré comme étant entre 3 et 4 fois supérieures aux valeurs théoriques prédites par l'équation de Stokes-Einstein ($\zeta_{t,b} = 6\pi\eta R_P$) pour des particules sphériques dans le volume. L'utilisation de différentes

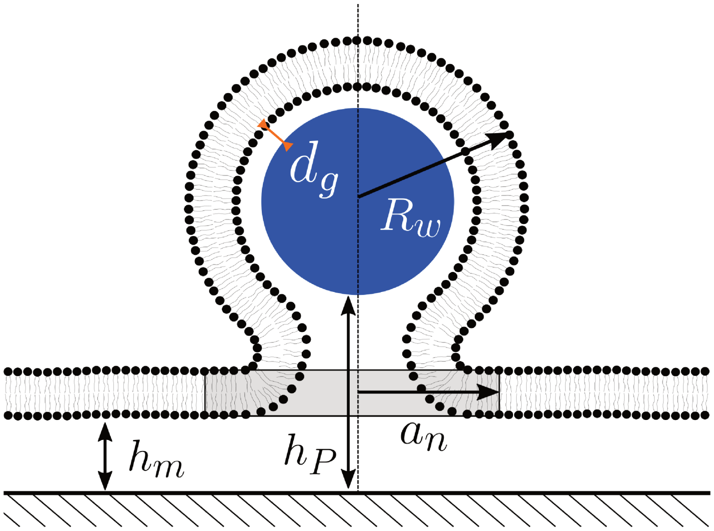

Figure 7.7: Représentation schématique de la situation de la particule enveloppée avec définition du rayon effectif R_w, du rayon équivalent du disque a_n, et de l'épaisseur du film d_g, ainsi que des distances de séparation membrane-particule h_m et h_P, respectivement.

tailles de particules et la comparaison de nos données avec des modèles simples existants ont indiqué que l'augmentation mesurée pouvait s'expliquer par les mécanismes dissipatifs associés à la translation du col dans la membrane fluide, s'il est considéré comme étant solidaire de la particule enrobée. La cohérence de la traînée réduite mesurée $\zeta_t/\zeta_{t,b} \approx 3$ pour des particules isotropes (voir Figure 7.8) de $R_P \approx 1\,\mu\text{m}$ et des particules Janus englobées avec différents mécanismes de propulsion suggère une certaine universalité dans les propriétés de diffusion de la structure finale. L'étude de la dynamique d'une particule engloutie permet donc de confirmer ou infirmer certaines hypothèses quant à la nature et aux propriétés de diffusion de la structure connectant la particule engloutie à la vésicule mère.

Par la suite, en contrôlant la tension de la vesicule mère à l'aide de la micropipette, nous avons pu montrer que la diffusion d'une particule engloutie est ralentie par l'augmentation de la tension de la vésicule mère. Ce phénomène a été mesuré dans le cas d'une particule engloutie libre (c'est à dire n'étant soumis à aucune force externe en plus de la membrane l'enrobant), comme décrit dans la Figure 7.9, mais aussi pour une particule piégée optiquement à l'équateur. En effet, en augmentant soudainement la tension de la vésicule, on mesure une augmentation de la friction ressentie par la particule, ce qui se traduit par une décroissance de la pente du déplacement quadratique moyen en fonction de l'intervalle de temps Δt, voir Figure 7.9. Peu de travaux ont rapporté l'existence d'une dépendence de la diffusion sur la tension d'une interface et a fortiori d'une membrane lipidique. Les quelques travaux décrivant de tels effets rapportent un comportement inverse: une diffusion apparente crois-

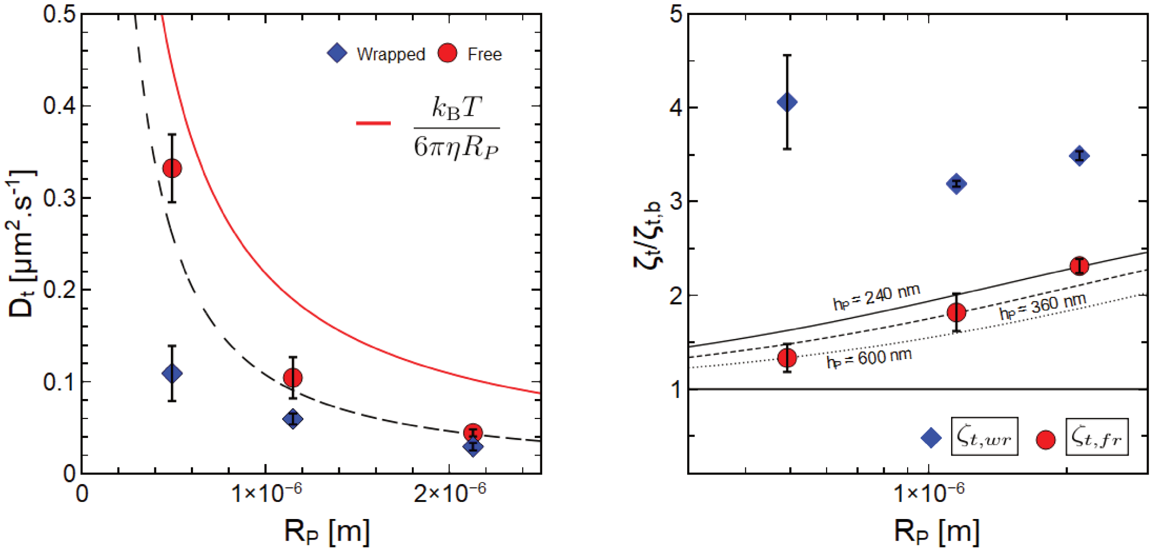

Figure 7.8: *(gauche)* D_t expérimental moyen en fonction de la taille de la particule R_P calculé à partir de $N \geq 5$ trajectoires de différentes particules englouties dans différentes vésicules pour chaque point. Les barres d'erreur représentent l'écart type. La ligne rouge pleine représente la prédiction en volume selon la relation de Stokes-Einstein, et la ligne noire en pointillés représente la traînée modifiée résultant de la présence d'une paroi solide (le substrat) à une distance de séparation h_P=200 nm calculée par les équations de Fàxen [180] *(droite)* Traînée réduite expérimentale $\zeta_t/\zeta_{t,b}$ en fonction de la taille des particules pour les cas libres (disques rouges) et enveloppés (diamants bleus) avec des prédictions théoriques de Faxén pour trois distances de séparation différentes.

sante pour une une tension croissante. C'est le cas par exemple pour des protéines inclues dansla membrane d'une vésicule géante et induisant une courbure locale de la membrane en son voisinage [188].

Pour déterminer l'origine de ce phénomène dissipatif, nous nous sommes penchés sur l'étude de la dynamique de particules de silice isotropes passives optiquement piégées, confinées proche d'une membrane de vésicule aspirée par une micropipette. Des actuateurs piézoélectriques permettent un contrôle précis de la distance relative entre la particule et la membrane et la dynamique de la particule est suivie et analysée pour comprendre la les interactions et les dissipations à l'oeuvre. Les résultats montrent que lorsque la membrane est proche de la particule, celle-ci se déplace de sa position d'équilibre dans le piège optique, indiquant une force exercée par la membrane. Cette force modifie la position d'équilibre et augmente la raideur du puit de potentiel dans lequel la particule évolue. En analysant ce potentiel de manière expérimentale, nous avons pu montrer que l'étude de la raideur du potentiel permettrait d'inférer des propriétés élastiques de la membrane, comme la tension

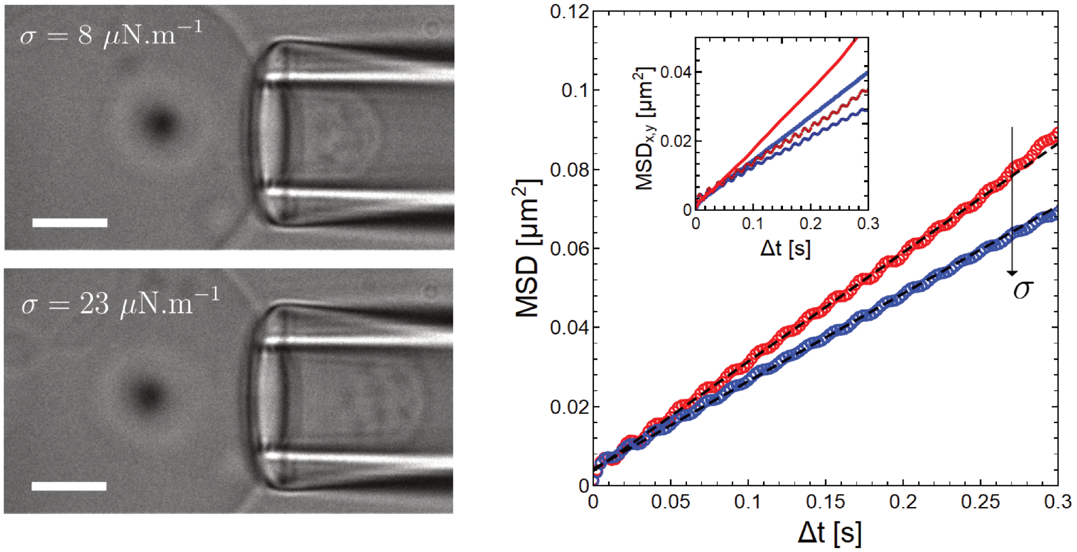

Figure 7.9: *(gauche)* Images de microscopie en champ clair d'une GUV aspirée par une micropipette, avec une particule englobée de $R_P = 1.15$ µm (hors de la focale) apparaissant comme un point sombre flou. L'échelle est de 5 µm. *(droite)* MSD bidimensionnelle $\langle (x(t+\Delta t) - x(t))^2 \rangle + \langle (y(t+\Delta t) - y(t))^2 \rangle$ pour la particule englobée à deux tensions membranaires différentes. La courbe rouge (en haut) correspond à la membrane avec une tension plus faible, tandis que la plus tendue est en bleu (en bas). Les lignes noires en pointillés sont des ajustements donnant $D_t = 0.068$ µm^2/s pour la membrane à faible tension (rouge) et $D_t = 0.055$ µm^2/s (bleu) pour la vésicule plus tendue. L'encadré montre les deux composantes du mouvement séparées et indique que le mouvement le long de la micropipette a une diffusion plus lente que celui perpendiculaire. Les deux composantes sont cependant impactées de manière similaire par l'augmentation de la tension.

de la membrane dans le cas d'une membrane tendue, ou le module de courbure dans le cas d'une vésicule à tension quasi nulle.

Enfin l'étude de la dynamique translationelle de la particule parallèle à la membrane, notament en traçant la densité spectrale de puissance des positions, a permis d'établir que la proximité de la membrane n'introduit que très peu de dissipation supplémentaire selon ce mode de déplacement puisque la friction mesurée reste presque inchangée (inférieur à la précision de la mesure), ce qui est cohérent avec les résultats précédents rapportés dans la littérature.

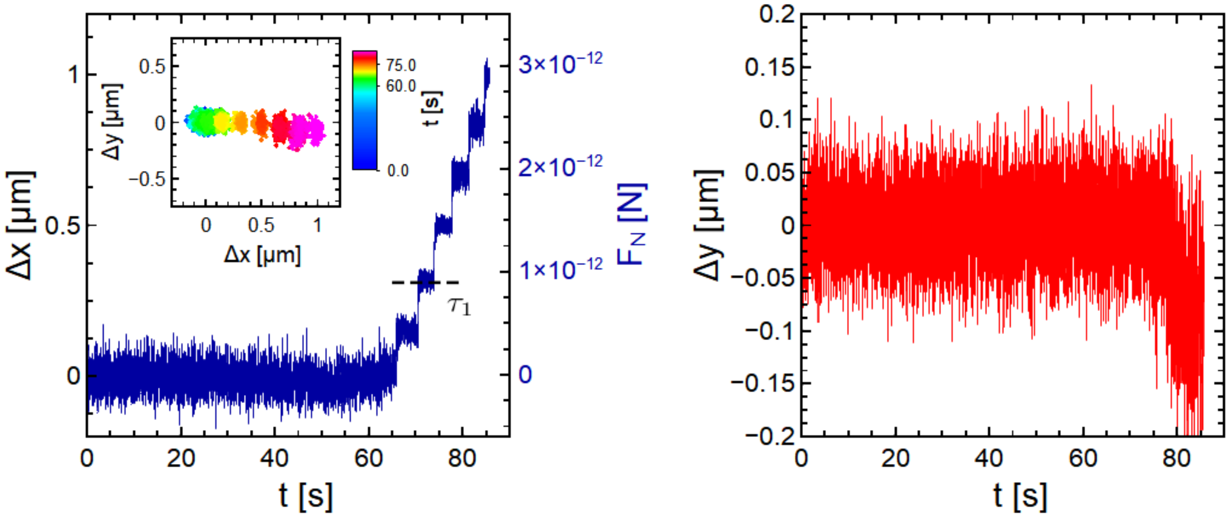

Figure 7.10: Trajectories extracted from the experiment in Figure 5.13 acquired at 200 fps. *(left)* Temporal evolution of the relative position $\Delta x(t) = x(t) - x_0$, where x_0 is the center of the optical trap, upon step-wise approach of an optically trapped $R_P = 1.15$ µm SiO_2 particle as shown in Figure 5.13. Note that the axis x corresponds to the direction perpendicaular to the membrane. Inset shows the two dimensional trajectory with the color map allowing to visualize the time evolution. *(right)* Evolution of $\Delta y(t) = y(t) - y_0$.

Conclusion

Les processus cellulaires comme l'endocytose nécessitent une déformation continue de la membrane. Le paysage énergétique et la dynamique de ces processus sont influencés par les interactions entre les particules et la membrane, ainsi que par la dynamique couplée des deux entités. Dans cette thèse, nous avons employé des techniques expérimentales pour étudier l'enveloppement de particules sous contrainte en utilisant un système modèle. Nous avons utilisé des pinces optiques pour sonder les forces impliquées dans l'enveloppement des particules sous une force externe dirigée, en examinant l'influence de divers paramètres physiques et la réversibilité du processus. Nous avons démontré que l'enveloppement complet et stable d'une particule active peut se produire de manière autonome, même en l'absence de machinerie biologique.

Dans un premier temps, nous avons étudié l'entrée forcée de microparticules sphériques dans des vésicules géantes unilamellaires en utilisant des pinces optiques dans des conditions d'adhésion quasi-nulle. Nos études ont révélé une instabilité dans la forme du segment de membrane non lié, conduisant à un enveloppement stable. Nous avons mis en évidence le rôle de la surface excédentaire de la membrane stockée dans les réservoirs de surface de la vésicule, qui contribuent à la tension membranaire de manière similaire à la tension interfaciale dans les interfaces liquides. En pénétrant successivement des particules dans une même vésicule, nous avons montré que ce régime de tension constante est limité par la disponibilité du réservoir de surface de la membrane, et que la tension peut augmenter de manière significative avec une consommation minime de la surface de la membrane, comme décrit par les théories établies. En variant la taille des particules, nous avons trouvé un minimum de force pour des tailles de particules comparables à la longueur bendocapillaire de la membrane. En utilisant l'aspiration par micropipette, nous avons sondé le degré de réversibilité du processus d'enveloppement et quantifié la tension membranaire nécessaire pour rouvrir le col, montrant une variabilité dans le degré de réversibilité probablement due à des différences de courbure spontanée.

Ensuite, nous nous sommes penchés sur un système modèle qui imite de manière autonome les premières étapes de l'endocytose, où des particules Janus actives peuvent approcher, déformer et être enveloppées par des vésicules géantes en utilisant la lumière visible et des concentrations physiologiques de glucose. Nous avons étudié les interactions physiques responsables de l'enveloppement stable dans cette situation où la dynamique des interactions, en particulier à grande distance, est dictée par la dynamique stochastique de la particule active et les interactions à longue portée avec l'hôte. Nos résultats ont montré que des temps de contact prolongés, plutôt que de maximiser la vitesse des particules, sont cruciaux pour un enveloppement réussi, surtout en présence d'adhésion et de courbure spontanée négative. Les interactions hydrodynamiques à longue portée aident à maintenir le contact entre la particule et la membrane, permettant l'adhésion et le franchissement des barrières énergétiques. Enfin, nous montrons que, de manière similaire au cas de l'enveloppement des particules sous l'action des pinces optiques, la stabilité de l'état totalement enveloppé est assurée par le coût énergétique élevé associé au segment de membrane non lié pour les états d'enveloppement intermédiaires.

Enfin, une dernière partie de mon travail a été dédiée à l'analyse de la dissipation et des interactions des microparticules avec les bicouches lipidiques. Nous avons étudié la diffusion de particules isotropes et Janus complètement enveloppées par des vésicules molles, montrant que les particules englouties subissent une dissipation due au couplage avec la structure du col. Nos données ont suggéré une augmentation universelle de la traînée, avec une dépendance significative à la taille des particules et à la tension membranaire. Cela contraste avec les rapports précédents sur les protéines induisant la courbure et nécessite de nouvelles explications théoriques. En effet, nos résultats ont indiqué que les particules englouties pouvaient subir une traînée jusqu'à 10 fois la prédiction en vrac de la loi de Stokes pour les membranes tendues, et nous avons montré que cette augmentation de la traînée translationnelle ne pouvait pas être due uniquement à la proximité de la bicouche et du substrat solide. Nous concluons qu'un autre chemin de dissipation existe dans cette géométrie particulière d'une particule enveloppée connectée à une vésicule mère par un col.

De manière générale, les résultats obtenus au cours de cette thèse fournissent des informations sur les critères physiques nécessaires pour l'enveloppement stable de particules entraînées par des vésicules lipidiques grâce à une force directionnelle externe, ou dans le contexte de particules autopropulsées naviguant de manière autonome. Ces résultats sont significatifs pour comprendre d'un point de vue physique les processus biologiques qui aboutissent à l'absorption de particules inertes ou de nageurs par des unités biologiques. Des applications potentielles pourraient être envisagées dans des domaines allant de la délivrance de médicaments, de la nanomédecine ou de l'infection microbienne, à la conception de micromoteurs dans des contextes de traitement des eaux usées.

Chapter 8

Appendix

8.1 Detailed micropipette fabrication and filling procedure

The capillaries used are borosilicate glass capillaries with an inner diameter of 0.78 or 0.58 mm and an outer diameter of 1 mm (Ref. GC100-10 Harvard Apparatus). The machine used to heat the capillary locally with a heating filament and subsequently pull it at high speed is the Sutter Instruments Co. P-97 Pipette Puller, see Figure 8.1 *(left)*. This machine allows the user to modify many parameters to obtain the desired micropipette shape. For the manipulation and mechanical characterization of GUVs, the goal is to achieve a cylindrical tip with an inner diameter of around 5 microns. Note that both thick-walled and thin-walled capillaries can be used, but they will require different parameters on the pulling machine to obtain the desired shape. Thick-walled capillaries, however, are expected to be more robust during the microforging step and less likely to break unexpectedly. If the pipette puller has not been used for a long time, a RAMP test must be performed to determine the HEAT value at which the glass capillary starts to melt locally. To perform a RAMP test, turn on the machine, select any program, press clear, choose “NO” to access the function, then press 1 to start the ramp test (a glass capillary must be in place, tightly screwed and passing through the heating filament as shown in Figure 8.1 *(middle)*). This RAMP test heat value will be the basis for tuning the HEAT parameter.

Once the capillary is pulled, it results in two raw micropipettes Figure 8.1 *(right)* (each being one half of the initial capillary). These micropipettes must undergo microforge manipulation to ensure the inner diameter is correct, the micropipette is cut perfectly straight,

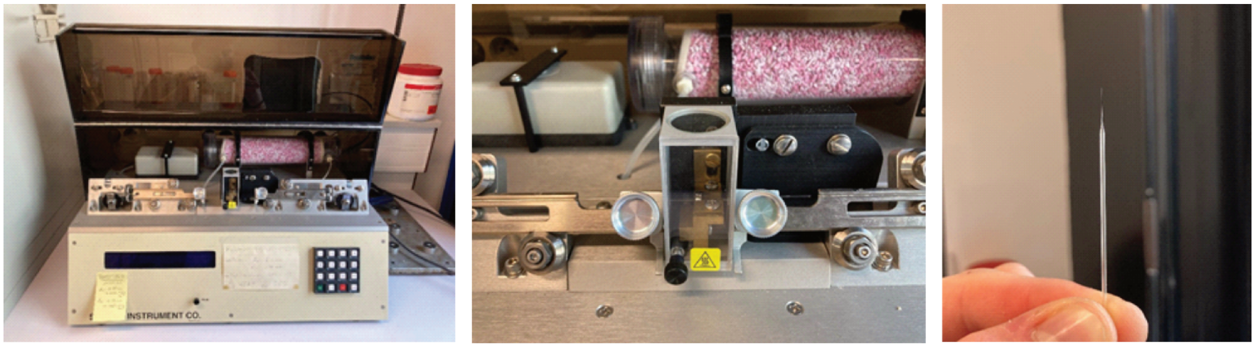

Figure 8.1: *(left)* Micropipette Puller Sutter Instruments Co. P-97. *(middle)* Position of the capillary before pulling. The capillary should be well centred in order to obtain two micropipettes with the same size. *(right)* ”Raw” micropipette after being pulled.

and the tip is cylindrical (the cylindrical nature is determined by the pulling step and cannot be adjusted in the microforge step).

We use a homemade microforge designed by A. Schroder for this purpose [198, 199]. The setup consists of a tungsten filament on which we deposit some powder of Sodium Tetraborate Decahydrate, a micropipette holder, and micrometric screws to move the micropipette around and bring it into contact with the filament, see Figure 8.2 *(left)*. This setup includes a protected Nikon 40x microscope objective with a large working distance and a BW Sony camera to image the manipulation on a screen. The filament is connected to a tunable current source, allowing it to be heated to melt the powder previously placed on it. The objective should be protected to avoid any damage from heating the nearby filament (see Figure 8.2).

By bringing the pipette into contact with the heated filament, one can shorten the pipette to the desired inner diameter by melting the glass on the filament if it is hot enough, see Figure 8.2 *(right)*. At lower filament heating temperatures, the melted powder will rise by capillarity in the micropipette when brought into contact. If the current source is suddenly switched off, the system cools down, leading to the spontaneous straight breaking of the pipette at the level where the melted powder rose, see Figure 8.3. This procedure should result in a clean cut of the micropipette edge at the desired inner diameter suitable for GUV manipulation. The pipette should be as cylindrical as possible (see Figure 8.3).

Once the pipette is cut to the desired diameter, straight, and cylindrical, it is suitable for manipulating GUVs. An additional step can be added to bring the tip of the micropipette

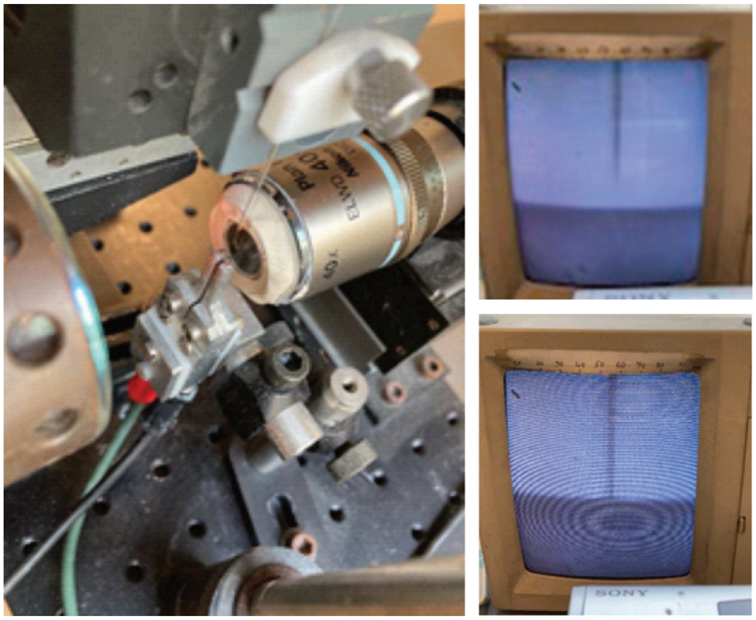

Figure 8.2: *(left)* Microforge setup with a pulled capillary held in place on top of the filament. *(right)* Melting of the thin part of the pulled capillary on the hot filament. This has to be done until the pipette diameter is the desired one.

close to the hot filament again to smooth the edges where it broke, avoiding unexpected behaviors when manipulating sensitive objects such as GUVs. The finished micropipettes can be stored in a petri dish held in place with Vitrex to avoid any contact with the fragile tip.

To fill the micropipette, dip it in the liquid medium, which should be the same as the sample to be studied (mostly glucose solutions for us), see Figure 8.4 *(left)*. The liquid will rise in the pipette by capillarity but only to a certain point. To fill it completely, take it out of the liquid and use a tiny pipette tip to inject liquid from the top, see the pipette

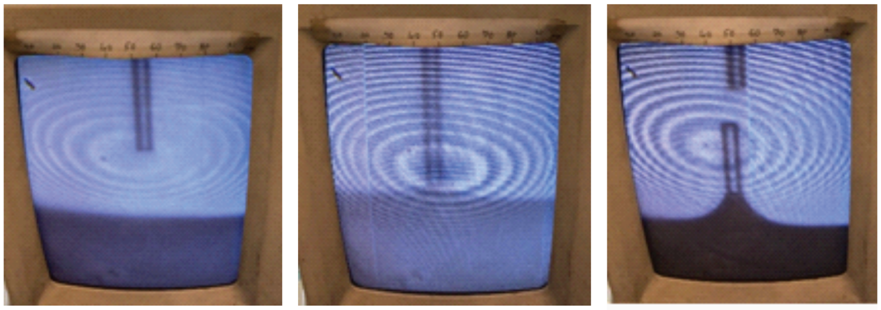

Figure 8.3: Rise of the melted powder in the pipette leading to the breaking of the capillary at the level of the meniscus when the current is switched off and the filament (and pipette) cool down.

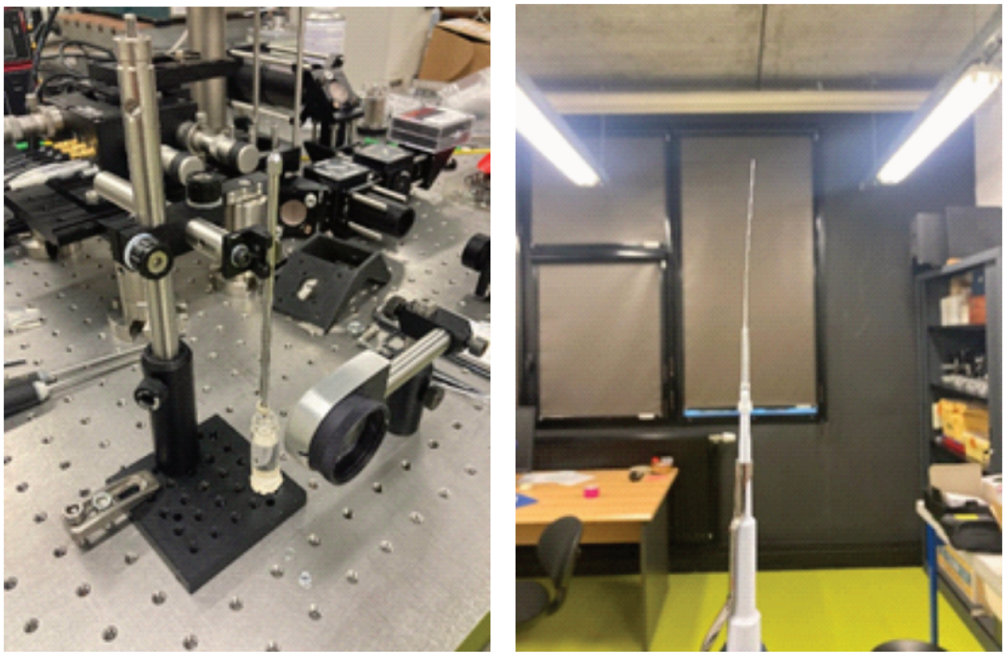

Figure 8.4: *(left)* Dipping of the pipette tip in the medium (usually glucose solutions if the GUVs are sedimented in glucose solutions) using a homemade holding setup. *(right)* Eppendorf pipette tip that is thin and long enough to penetrate the capillary from the top.

tip used in Figure 8.4 *(right)*. This step is crucial since any air bubble during filling might dramatically impact the suction pressure control applied by the pipette on the GUVs. A magnifying glass can be used to see and control the filling of the pipette. If a bubble is created inside the pipette, restart filling from the bottom to make the bubble escape from the top of the capillary.

Once the micropipette is filled, connect it to the hydrostatic setup using the PTFE tube, allowing to induce hydrostatic pressure thanks to the height difference between the water tank and micropipette tip. The principle of this hydrostatic setup is simple: a water container is connected to the pipette, and the container can be moved up and down with a micrometric screw Figure 8.5 *(left)*. The height difference between the container top and the pipette tip will create hydrostatic pressure. Before connecting the filled micropipette to the pipette holder (a long metallic piece supporting the micropipette), ensure the container is higher than the holder's tip to avoid introducing any air bubble when connecting them.

Once the micropipette is filled and connected, place it in the sample cell and find the zero-pressure height of the hydrostatic device water container (no liquid flux in the micropipette). Clean the entire hydrostatic setup (tank, tube, and metallic holder) thoroughly before each

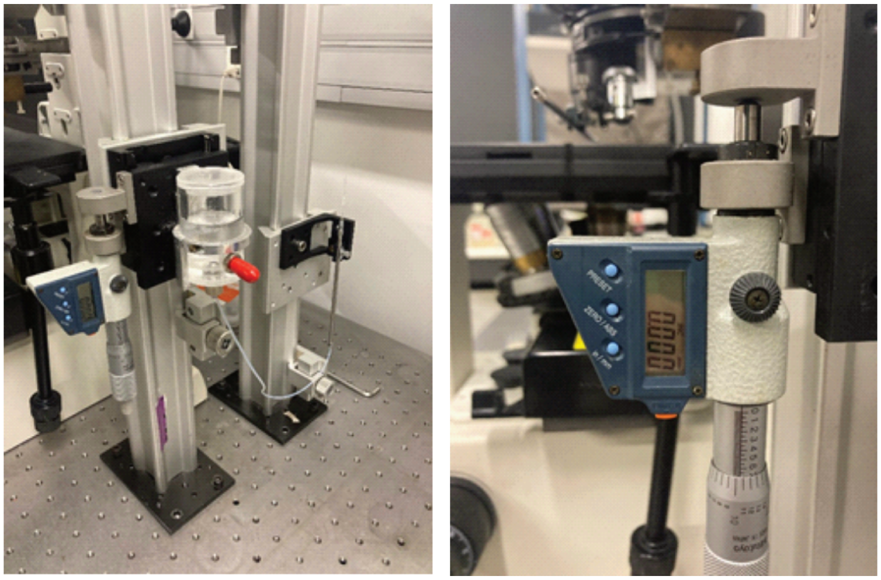

Figure 8.5: *(left)* Hydrostatic setup with the water container, a PTFE tube linking it to the pipette holder and micrometric screw. *(right)* Digital screen allowing to display the height difference with the zero-pressure height.

use by flowing ethanol and then MilliQ water through it for a few minutes to remove air bubbles and dirt. The most convenient sample cells to use with the micropipette consist of a regular sample cell with a red self-adhering silicon spacer on regular glass slides. Place the spacer close to the edge of the glass slide and cut it to allow the introduction of the micropipette inside the sample. The opening should be wide enough for the micropipette to fit in but not too wide to avoid excessive evaporation.

8.2 ImageJ Macro for orientation determination

The following Macro can be applied to a stack of images (movie) on which a pre-treatment was performed (filters and binarization, as detailed in the main text). Each image should therefore be a binary image with the projection of the cap having maximal pixel value and 0 elsewhere. The provided macro asks the user to select a point at the start of the algorithm. This point should be choose by the user slightly on the left of the cap to be tracked for the ”wand” tool to find the contour of the cap for the first image. The code then adjusts the starting point for the next images using the coordinates of the previous images coordinates and no further input from the user is necessary. Note that for the output text file to contain the desired information about area and ellipse long axis angle with a reference axis, the ”Area” and ”Fit ellipse” features in ”Set measurements...” should be ticked in the ImageJ software (Analyze>Set measurements...).

```
setSlice(1);
setTool("multipoint");
waitForUser("Clik on starting point for wand tool");
getSelectionCoordinates(x, y);

print(x[0],y[0])

X=x[0]
Y=y[0]

setTool("wand");

for (i=1; i<nSlices;i++) {
  run("Select None");
  doWand(X,Y);
  run("Measure");
  X=getValue("X")-30;
  Y=getValue("Y");
  run("Next Slice [>]");
  wait(10);
}
```

8.3 Influence of relative motion speed on engulfment force profiles

The relative speed imposed between the particle and the lipid vesicle unavoidably has an influence on the force exerted on the bead. The friction force acting on the bead due to the motion of the surrounding fluid has the form $F_{stokes} = \zeta_t v_{rel}$ with $\zeta_t = 6\pi\eta R_P$ for a spherical particle in an unbound fluid at low Reynolds number. The presence of the lipid bilayer slightly increases the drag felt by the particle [190] both in the radial and tangential direction upon approach of the vesicle (less than 10%). In Figure 8.6 we show the force profiles as a function of piezo stage displacement for different relative speeds. Note that the vertical dashed lines correspond to the moment the stage stops its motion, meaning that the x axis after that should be read as a temporal evolution, as d stays constant from there. It appears that at higher velocities, a non zero force is measured before contact ($d = 0$), which corresponds to the friction force F_{stokes} mentioned earlier. We can check the consistency by checking that using the bulk prediction for the friction $F_{stokes} = 6\pi\eta R_P v_{rel} = 0.21$ pN is comparable to the 0.2 pN force measured.

The overall shape of the force peak, showing an increase with two distinct slopes and an abrupt drop at the full wrapping transition, remains similar for all velocities shown here. The penetration depth at which the transition occurs however seems to decrease with decreasing speed. It also appears clearly that the force measured after the force drop, which is constant as it only depends on the membrane bending modulus κ_b, tension σ and spontaneous curvature m, has a higher amplitude relatively to the resting phase (no motion, after the vertical dashed line) captured by the quantity ΔF_v. This evidences a non-negligible contribution of an additional dissipative process associated to the dynamical pulling of the

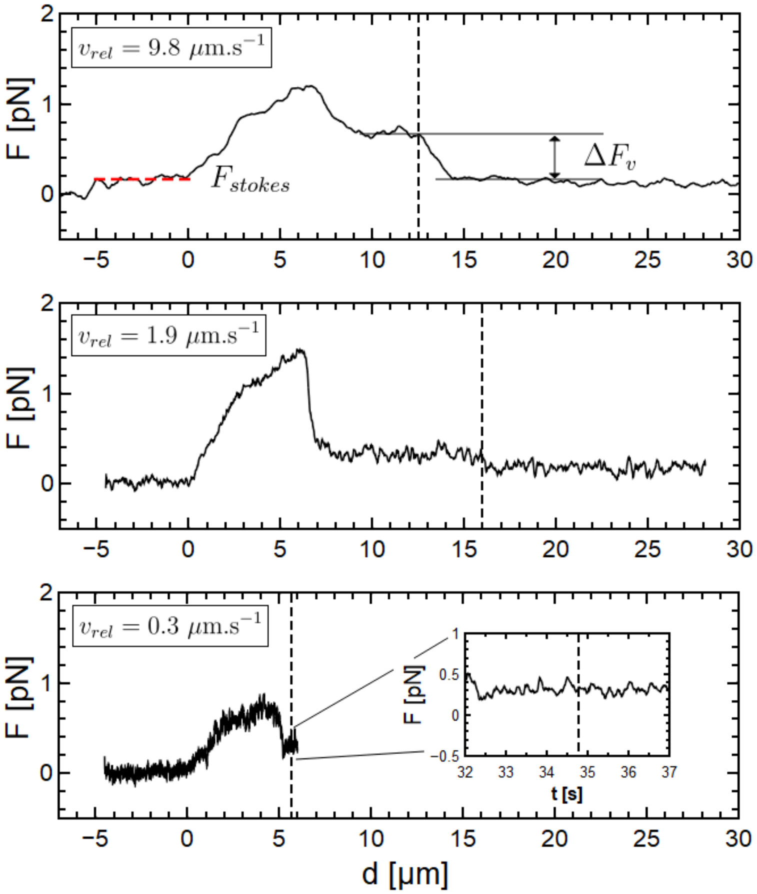

Figure 8.6: Force profiles upon forced entry of $R_P = 1.15$ μm particles performed at different imposed velocities. The vertical dashed lines stand for the distance at which the relative motion is stopped, and the abscissa scale d should therefore not be considered as a distance but as a time of the experiment.

membrane tether. Only for the lowest velocity ($v_{rel} = 0.3\,\mathrm{\mu m\,s^{-1}}$) $\Delta F_v = 0$ pointing to the fact that the tube is pulled slowly enough to avoid the additional dissipations. We conclude that in order to probe equilibrium properties and avoid artefacts associated to bringing the system too far from equilibrium, forced entry should be performed at relative speeds in the range $v_{rel} = 0.3\,\mathrm{\mu m\,s^{-1}}$. We will therefore use $v_{rel} = 0.3\,\mathrm{\mu m\,s^{-1}}$ in the first Chapter of the thesis.

8.4 Bud containing a particle and a large volume of fluid

We show here in Figure 8.7 a rare situation where a large volume of solution of the exterior fluid (glucose aqueous solution) was enclosed upon wrapping driven by optical tweezers. The left panel of Figure 8.7 shows a bright field microscopy image right after the neck closure of a $R_P = 1.15\,\mathrm{\mu m}$. The fact that the neck closed in this situation is an additional proof that adhesion is so small in our system that it has no influence on the shape of the vesicle and on the nucleation and stability of the neck. Conversely, the fact that a large volume of the exterior solution was enclosed is the signature that the closure of the neck is due to an instability of the membrane segment behind the particle.

Upon applying tension to the vesicle through aspiration pressure with the micropipette in this case, the neck can open and the particle is expelled as reported in 40 % of the cases in our system, as discussed in Section 3.3. This is shown on the *(right)* panels of Figure 8.7 (b,c), where the same vesicle as in Figure 8.7 (a) is aspirated. Again, one can measure an increase of the projected tongue length inside the micropipette ΔL which should relate to the surface area of the spherical A_{bud} bud as:

$$\Delta L = \frac{A_{\mathrm{bud}}}{2\pi R_{\mathrm{pip}}} = \frac{2R_{\mathrm{bud}}^2}{R_{\mathrm{pip}}} \tag{8.1}$$

where R_{pip} is the inner radius of the cylindrical micropipette and R_{bud} is the radius of the bud if considered to be spherical. Measuring R_{pip} and R_{bud} from the microscopy images one gets $\Delta L = 2.2\,\mathrm{\mu m}$ which is in accordance with the measurable value of ΔL ($\Delta L = 2.35\,\mathrm{\mu m}$)

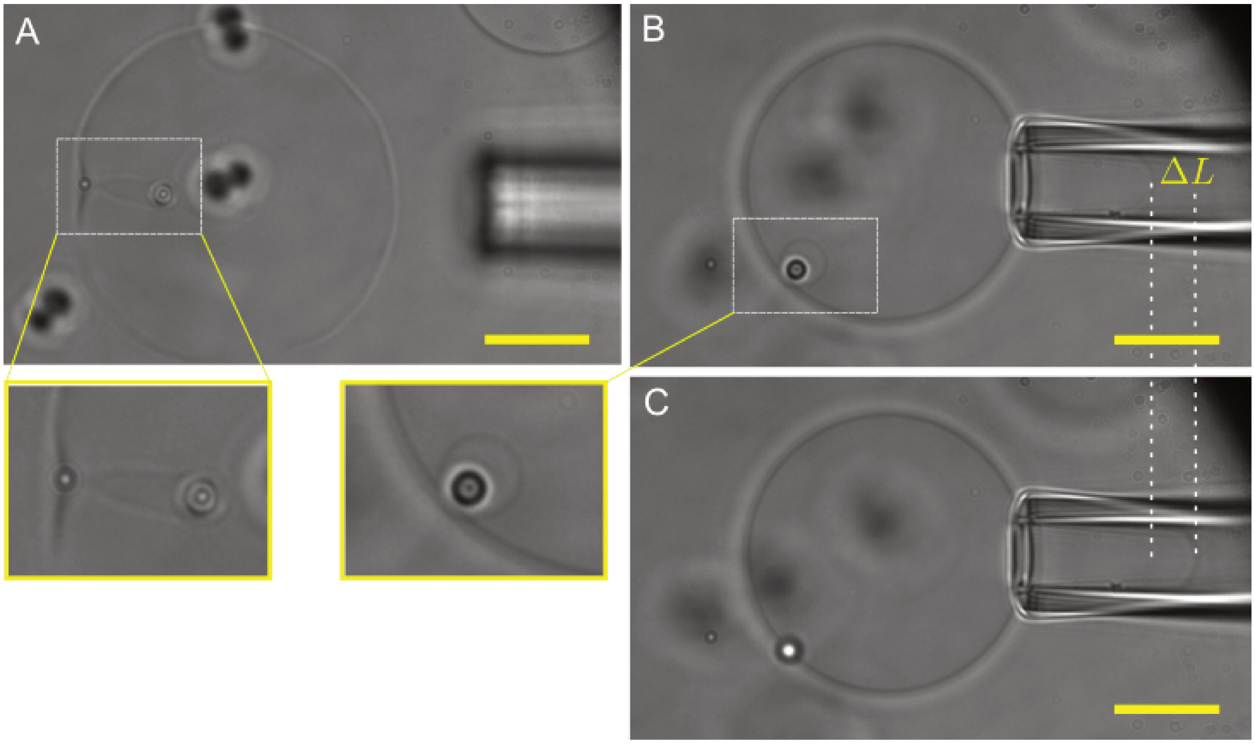

Figure 8.7: *(left)* (a) Bright field microscopy image of a $R_P = 1.15\,\mu\text{m}$ particle that was forced to enter a POPC GUV. One clearly sees that a large volume of fluid is enclosed in the bud together with the particle. The dark spots at the middle of the vesicle are particles laying underneath the vesicle and are not wrapped by the vesicle. Scale bars are $10\,\mu\text{m}$. *(right)* (b) Same vesicle with the bud containing the particle and a large volume of fluid. Here, a tension is applied with the micropipette, and one clearly see the change of shape of both the vesicle and the inside bud as both became spherical. (c) Expulsion of the particle at some critical applied tension. Zoom on the area showing the membrane bud containing the particle and fluid show the change in shape after appling pressure.

8.5 Influence of white light illumination intensity on the projected velocity of Cu@SiO$_2$ particles in glucose solutions

For a given concentration of glucose, changing the intensity of the white light illumination of the microscope also appears to have an impact on particles activity. The measured projected active velocity V from MSD fits with Equation 4.1 where D_t and V are fit parameters shows a clear increase of V upon illumination intensity increase. We show in Figure 8.8 that the average V extracted for $N = 10$ particles increase with increasing illumination intensity, as it was the case for blue light (see main text). Note that unless otherwise stated, the

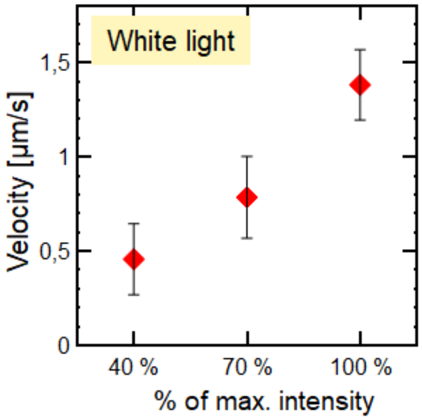

Figure 8.8: Average (on $N=$ 10 trajectories) measured values for projected velocity V for different illumination intensities (in percentage of maximum illumination intensity) at 100 mM glucose concentration.

experiments conducted in this work were performed at low white light illumination intensity (40% of maximum intensity) to avoid heating of the sample and drifts due to temperature gradients as much as possible.

The light source for sample illumination on the microscope used for this set of experiments (Nikon TE-2000 Eclipse) is a 12V 100W halogen lamp (LHS-H100P-1 12V100W) from Nikon. Determination of optical power output or optical intensity in the case of such light source after attenuation by filters etc. is tedious, which is the reason why we stick with a percentage of maximum achievable light intensity to quantify the light intensity.

8.6 Faxén's predictions for the drag of a sphere close to a no-slip boundary

The Stokes equation for a translating sphere close to a plane wall (with no-slip boundary conditions) have to be solved numerically in order to obtain exact solutions, which is computationally very costly [200, 181, 201]. Considering a spherical particle of radius R_P whose surface is separated from a bounding wall from a distance d and translating at velocity U parallel to the wall, Faxén derived approximate solutions which provides an expression for the drag experienced by the particle in this case [180]. From his solution, the drag force $F_{\parallel}$ exerted on the particle translating parallel to the wall can be written as [180]:

$$\frac{F_{\parallel}(d)}{\zeta_{t,b}U} = \left(1 - \frac{9}{16}\left(\frac{R_P}{R_P+d}\right) + \frac{1}{8}\left(\frac{R_P}{R_P+d}\right)^3 - \frac{45}{256}\left(\frac{R_P}{R_P+d}\right)^4 - \frac{1}{16}\left(\frac{R_P}{R_P+d}\right)^5\right)^{-1} \tag{8.2}$$

where $\zeta_{t,b} = 6\pi\eta R_P$ is the Stokes drag. This expression provides values for the modified drag in good agreement with exact numerical calculations only for $d/R_P > 0.01$ [181]. For $R_P \sim 1\,\mu\text{m}$ as in our systems, it means that Equation 8.2 is valid for gaps $d > 10\,\text{nm}$.

8.7 Translational diffusion of active Cu@SiO$_2$ microparticles from MSD fits

Using equation Eq. 4.1 from the main text, we can extract both the projected active velocity and the translational diffusion coefficient D_t of the Janus particles in active conditions. Values for the extracted projected velocity V are reported in the main text and V increases with increasing glucose concentration. Here, Figure 8.9 shows the average for the extracted values for D_t as a function of the glucose concentration.

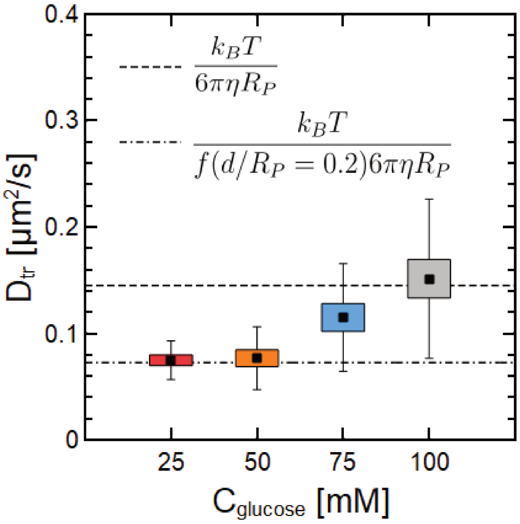

Figure 8.9: Average (over N= 10 trajectories for each point) of the values extracted from MSD fits for D_t for different illumination intensities (in percentage of maximum illumination intensity) at 100 mM glucose concentration. Error bars account for the standard deviation

It appears that for lower glucose concentrations, the values are in agreement with Fàxen predictions of the diffusion coefficient of a particle close to a solid wall at a distance $d = 0.2R_P = 300$ nm [202], as described in Appendix 8.6. For increasing glucose concentrations, D_t increases and becomes closer to the Stokes-Einstein prediction of the diffusion coefficient valid in the bulk. One interpretation would be that the particle activity (depending on glucose concentration) has an impact on the equilibrium swimming distance of the particle from the substrate. However, recent investigations, as reported in Section 6.1 suggest that Eq. 4.1 does not properly describe the dynamics in our system due to complex dynamics of the out-of-plane orientation of Cu@SiO$_2$. One should therefore be careful when interpreting this increase in apparent diffusion as variations in height, as additional noises due to the particle activity might result into higher effective thermal diffusion coefficients using the model of Eq. 4.1.

8.8 Free energy variation associated to rotational motion during capture

In the following, we will relate the in-plane orientation range explored by an active Cu@SiO$_2$ Janus particle during the *capture* phase to the energy variations associated to this degree of freedom due to adhesive contact with the membrane in the Janus geometry.

We recall that by defining the adhesion energy $E_w = wA_b$ with A_b the adhered membrane area, w is negative when there is an affinity between the two surfaces. Taking into account the Janus geometry of our particle pinned with the Cu cap facing towards the membrane, a variation of φ implies bringing a Copper region of the particle initially in contact with the membrane in contact with water and a SiO$_2$ region initially exposed to water in contact with the membrane. If one considers the change in free energy associated to a change in orientation is solely imputed to surface energy contributions, the energy variation associated to the maximum angular variation range φ^* can be written as:

$$\Delta E\left(\varphi^*\right) = 2R_P^2\varphi^*[(\sigma_{\mathrm{SiO_2,m}} - \sigma_{\mathrm{SiO_2,aq}}) + (\sigma_{\mathrm{Cu,aq}} - \sigma_{\mathrm{Cu,m}})] = 2\pi R_P^2\varphi^*(w_{\mathrm{Si}} - w_{\mathrm{Cu}}) \tag{8.3}$$

as we can define $w_{\mathrm{Cu}} = \sigma_{\mathrm{Cu,m}} - (\sigma_{\mathrm{Cu,aq}} + \sigma)$ and $w_{Si} = \sigma_{\mathrm{Si,m}} - (\sigma_{\mathrm{Si,aq}} + \sigma)$ where σ is the membrane tension. In thermal equilibrium, the degree of freedom associated to φ is attributed $1/2k_BT$ energy so that one can write $\Delta E(\varphi) = 1/2k_BT$. From there, the adhesion energy density difference $(w_{\mathrm{Si}} - w_{\mathrm{Cu}})$ that would correspond to such an orientational confinement can be extracted and yields $(w_{Si} - w_{Cu}) = k_B T / 4R_P^2 \varphi^* \approx 10^{-9}$ N.m^{-1} during the capture phase. However, we measured that at equilibrium, $w_{\mathrm{Cu}} > 10^{-7}$ N.m^{-1} and $w_{\mathrm{Si}} < 10^{-9}$ N.m^{-1} which means that $|(w_{\mathrm{Si}} - w_{\mathrm{Cu}})| \gg 10^{-9}$ N.m^{-1}. In other terms, the adhesion strength are much weaker during the capture phase, which is an additional proof that far-field hydrodynamic interactions are responsible for the orientation confinement of φ during capture, rather than surface adhesion between copper and the membrane.

8.9 Particle-wall distance calculation from double layer electrostatic/gravitational forces

At thermal equilibrium, a spherical SiO_2 bead immersed in a fluid will sediment at the bottom of the observation cell as it is denser than the surrounding fluid due to gravity. A particle may find a finite equilibrium distance from the substrate around which it might fluctuate due to thermal Brownian motion. This equilibrium distance results from the sum of the two main forces acting on the particle, which are the gravitation attraction and the double layer electrostatic repulsion with the substrate. The latter repulsion is due to the particle and substrate surfaces being negatively charged in water. The van der Waals interaction

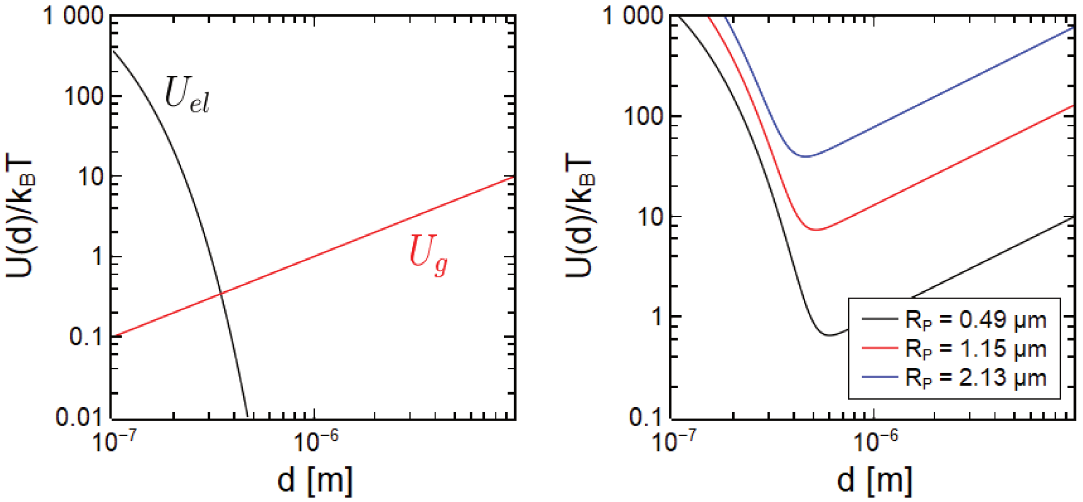

Figure 8.10: *(left)* Graph showing the distance dependent components of the potential U_{el} for double layer repulsion and U_g for gravity for a spherical SiO_2 particle with $R_P = 0.49\,\mu$m. *(right)* Sum of the two components forming the total potential as in Eq. 8.4 as a function of separation distance d and for the three particle radii considered in Section 5.2.1. We use here $Z_{part} = -25\,\mathrm{m\,V}$ (see 2.4), $Z_{wall} = -75\,\mathrm{m\,V}$ and $\lambda_D = 50\,\mathrm{nm}$. Using representative values in this range (Z_{wall} and λ_D were not determined experimentally), one systematically obtains a minimum at smaller distance d for larger particles.

contributions are expected to be negligible in these conditions where the gap d between the particle and the substrate is relatively large [203]. The total potential energy landscape therefore reads [203, 204, 157]:

$$\frac{U_{tot}(d)}{k_B T} = \begin{cases} Be^{-\frac{d}{\lambda_D}} + d\frac{\Delta\rho V g}{k_B T}, & \text{for } d > 0 \\ +\infty, & \text{for } d \leq 0 \end{cases} \tag{8.4}$$

where $\Delta\rho$ is the particle-fluid mass density difference and V the volume of the spherical colloid $V = 4/3\pi R_P^3$, g the gravitational acceleration, the Debye length λ_D, and with:

$$B = 64\pi\epsilon_0\epsilon_f R_P \left(\frac{k_B T}{e}\right)^2 \tanh\left(\frac{eZ_{\text{wall}}}{k_B T}\right) \tanh\left(\frac{eZ_{\text{part}}}{k_B T}\right), \tag{8.5}$$

where ϵ_0 is the vacuum permittivity, ϵ_f the relative dielectric constant of the fluid, Z_{wall} the zeta potential of the substrate and Z_{part} the zeta potential of the particle.

Note that the Debye length λ_D can be written as:

$$\lambda_D^{-1} = \sqrt{\frac{2e^2 C_{\text{s}}}{\epsilon_0\epsilon_f k_B T}}. \tag{8.6}$$

where C_s is the ionic strength. In absence of added salt (as in our case), this should only account for a contribution from the pH of the solution. In absence of salt, the Debye length should therefore be large $> 100\,\text{nm}$, however due to impurities, it is not rare to have a smaller Debye length ($\lambda_D \approx 50\,\text{nm}$) even in the absence of salt.

Note that the electrostatic charge and Debye length in our system are not measured, but by using values used in the literature for similar systems [157], we can plot the potential as a function of the distance for each contribution U_{el} and U_g of U_{tot} in Figure 8.10 *(left)*. The total potential for different particle sizes is plotted in Figure 8.10 *(right)*. We see that these energy considerations allow to explain the average distance d from the wall of few hundreds of nanometers as inferred from Faxén's predictions using experimental results in Section 5.2.1. Additionally, the fact that larger particles have smaller equilibrium distance d is also captured by these considerations. Still, more precise determination of the distance d using these theoretical predictions would require more precise knowledge of λ_D, Z_{wall} and Z_{part} to be compared with the experimental values.

Bibliography

[1] Valentin Jaumouillé and Clare M. Waterman. Physical constraints and forces involved in phagocytosis. *Frontiers in Immunology*, 11, 2020.

[2] David M. Richards and Robert G. Endres. The mechanism of phagocytosis: Two stages of engulfment. *Biophysical Journal*, 107:1542–1553, 2014.

[3] Erin Weddle and Hervé Agaisse. Principles of intracellular bacterial pathogen spread from cell to cell. *PLOS Pathogens*, 14(12):1–8, 2018.

[4] Jennifer R. Robbins, Angela I. Barth, Hélène Marquis, Eugenio L. de Hostos, W. James Nelson, and Julie A. Theriot. Listeria monocytogenes Exploits Normal Host Cell Processes to Spread from Cell to Cell . *Journal of Cell Biology*, 146(6):1333–1350, 1999.

[5] Jangsun Hwang, Daheui Choi, Seora Han, Se Yong Jung, Jonghoon Choi, and Jinkee Hong. Potential toxicity of polystyrene microplastic particles. *Scientific reports*, 10(1):7391, 2020.

[6] Ole G Mouritsen and Luis A Bagatolli. *Life-as a matter of fat: lipids in a membrane biophysics perspective.* Springer, 2015.

[7] Gerrit Van Meer, Dennis R Voelker, and Gerald W Feigenson. Membrane lipids: where they are and how they behave. *Nature reviews Molecular cell biology*, 9(2):112–124, 2008.

[8] G. Cevc and D. Marsh. *Phospholipid Bilayers: Physical Principles and Models.* Cell Biology: A Series of Monographs. Wiley, 1987.

[9] Rumiana Dimova and Carlos Marques. *The giant vesicle book.* CRC Press, 2019.

[10] Rumiana Dimova. Giant vesicles and their use in assays for assessing membrane phase state, curvature, mechanics, and electrical properties. *Annual Review of Biophysics*, 48(Volume 48, 2019):93–119, 2019.

[11] W Helfrich. Elastic properties of lipid bilayers: Theory and possible experiments.

Zeitschrift für Naturforschung C, 28(11-12):693–703, 1973.

[12] R Lipowsky and H.-G Döbereiner. Vesicles in contact with nanoparticles and colloids. *Europhysics Letters (EPL)*, 43(2):219–225, 1998.

[13] Reinhard Lipowsky. Remodeling of membrane shape and topology by curvature elasticity and membrane tension. *Advanced Biology*, 6, 2022.

[14] W Rawicz, K C Olbrich, T Mcintosh, D Needham, and E Evans. Effect of chain length and unsaturation on elasticity of lipid bilayers. *Biophysical journal*, 2000.

[15] E Evans and W Rawicz. Entropy-driven tension and bending elasticity in condensed-fluid membranes. *Phys. Rev. Lett.*, 64:17, 1990.

[16] E. Evans, W. Rawicz, and B. A. Smith. Concluding remarks back to the future: Mechanics and thermodynamics of lipid biomembranes. *Faraday Discussions*, 161:591–611, 2012.

[17] W Helfrich and R.-M. Servuss. Undulations, steric interaction and cohesion of fluid membranes. *Il Nuovo Cimento D*, 3(1):137–151, 1984.

[18] MB Schneider, JT Jenkins, and WW Webb. Thermal fluctuations of large quasi-spherical bimolecular phospholipid vesicles. *Journal de Physique*, 45(9):1457–1472, 1984.

[19] Reinhard Lipowsky. Spontaneous tubulation of membranes and vesicles reveals membrane tension generated by spontaneous curvature. *Faraday Discussions*, 161:305–331, 2012.

[20] Jaime Agudo-Canalejo. Particle engulfment by strongly asymmetric membranes with area reservoirs. *Soft Matter*, 17:298–307, 2021.

[21] Tripta Bhatia, Jaime Agudo-Canalejo, Rumiana Dimova, and Reinhard Lipowsky. Membrane nanotubes increase the robustness of giant vesicles. *ACS Nano*, 12(5):4478–4485, 2018.

[22] P G Saffman and M Delbrück. Brownian motion in biological membranes. *Proceedings of the National Academy of Sciences*, 72(8):3111–3113, 1975.

[23] P. G. Saffman. Brownian motion in thin sheets of viscous fluid. *Journal of Fluid Mechanics*, 73(4):593–602, 1976.

[24] B. D. Hughes, B. A. Pailthorpe, and L. R. White. The translational and rotational drag on a cylinder moving in a membrane. *Journal of Fluid Mechanics*, 110:349–372, 1981.

[25] Jurgen F. Klingler and Harden M. McConnell. Brownian motion and fluid mechanics of lipid monolayer domains. *The Journal of Physical Chemistry*, 97(22):6096–6100, 1993.

[26] Vincent L. Thoms, Tristan T. Hormel, Matthew A. Reyer, and Raghuveer Parthasarathy. Tension independence of lipid diffusion and membrane viscosity. *Langmuir*, 33(43):12510–12515, 2017.

[27] Winchil L.C. Vaz, Federico Goodsaid-Zalduondo, and Ken Jacobson. Lateral diffusion of lipids and proteins in bilayer membranes. *FEBS Letters*, 174(2):199–207, 1984.

[28] Rumiana Dimova. Recent developments in the field of bending rigidity measurements on membranes. *Advances in Colloid and Interface Science*, 208:225–234, 2014.

[29] E. Evans, A. Yeung, R. Waugh, and J. Song. Dynamic coupling and nonlocal curvature elasticity in bilayer membranes. In *The Structure and Conformation of Amphiphilic Membranes*, pages 148–153. Springer Berlin Heidelberg, 1992.

[30] U. Seifert and S. A. Langer. Viscous modes of fluid bilayer membranes. *Europhysics Letters*, 23(1):71, jul 1993.

[31] F.M. Hochmuth, J.Y. Shao, J. Dai, and M.P. Sheetz. Deformation and flow of membrane into tethers extracted from neuronal growth cones. *Biophysical Journal*, 70(1):358–369, 1996.

[32] Saša Svetina, Boštjan Žekš, RE Waugh, and RM Raphael. Theoretical analysis of the effect of the transbilayer movement of phospholipid molecules on the dynamic behavior of a microtube pulled out of an aspirated vesicle. *European biophysics journal*, 27:197–209, 1998.

[33] E. Evans and A. Yeung. Hidden dynamics in rapid changes of bilayer shape. *Chemistry and Physics of Lipids*, 73(1):39–56, 1994.

[34] R.M. Raphael and R.E. Waugh. Accelerated interleaflet transport of phosphatidylcholine molecules in membranes under deformation. *Biophysical Journal*, 71(3):1374–1388, 1996.

[35] W.K. den Otter and S.A. Shkulipa. Intermonolayer friction and surface shear viscosity of lipid bilayer membranes. *Biophysical Journal*, 93(2):423–433, 2007.

[36] Stefano Villa, Giuseppe Boniello, Antonio Stocco, and Maurizio Nobili. Motion of micro- and nano- particles interacting with a fluid interface. *Advances in Colloid and Interface Science*, 284, 2020.

[37] E. M. Purcell. Life at low Reynolds number. *American Journal of Physics*, 45(1):3–11, 1977.

[38] Sho C. Takatori and Amaresh Sahu. Active contact forces drive nonequilibrium fluctuations in membrane vesicles. *Physical Review Letters*, 124, 2020.

[39] Michael Allen. Algae ‘breaststroke’ is synchronized from within. *Physics World*, 2015.

[40] Kyriacos C. Leptos, Kirsty Y. Wan, Marco Polin, Idan Tuval, Adriana I. Pesci, and Raymond E. Goldstein. Antiphase synchronization in a flagellar-dominance mutant of chlamydomonas. *Phys. Rev. Lett.*, 111:158101, 2013.

[41] Raphaël Jeanneret, Dmitri O Pushkin, Vasily Kantsler, and Marco Polin. Entrainment dominates the interaction of microalgae with micron-sized objects. *Nature communications*, 7(1):12518, 2016.

[42] Katherine Villa and Martin Pumera. Fuel-free light-driven micro/nanomachines: Artificial active matter mimicking nature. *Chemical Society Reviews*, 48:4966–4978, 2019.

[43] Hong Wang and Martin Pumera. Micro/nanomachines and living biosystems: From simple interactions to microcyborgs. *Advanced Functional Materials*, 28, 2018.

[44] Hong Wang and Martin Pumera. Fabrication of micro/nanoscale motors. *Chemical Reviews*, 115:8704–8735, 2015.

[45] Dong Liu, Ting Wang, and Yuan Lu. Untethered microrobots for active drug delivery: From rational design to clinical settings. *Advanced Healthcare Materials*, 11, 2022.

[46] Michael Kuron, Patrick Kreissl, and Christian Holm. Toward understanding of self-electrophoretic propulsion under realistic conditions: From bulk reactions to confinement effects. *Accounts of Chemical Research*, 51(12):2998–3005, 2018.

[47] Varun Sridhar, Byung-Wook Park, and Metin Sitti. Light-driven janus hollow mesoporous tio2–au microswimmers. *Advanced Functional Materials*, 28(25):1704902, 2018.

[48] Hong-Ren Jiang, Natsuhiko Yoshinaga, and Masaki Sano. Active motion of a janus particle by self-thermophoresis in a defocused laser beam. *Phys. Rev. Lett.*, 105:268302, 2010.

[49] Sébastien Fayolle, Thomas Bickel, and Alois Würger. Thermophoresis of charged colloidal particles. *Phys. Rev. E*, 77:041404, 2008.

[50] Bian Qian, Daniel Montiel, Andreas Bregulla, Frank Cichos, and Haw Yang. Harnessing thermal fluctuations for purposeful activities: the manipulation of single microswimmers by adaptive photon nudging. *Chem. Sci.*, 4:1420–1429, 2013.

[51] Xing Ma, Kersten Hahn, and Samuel Sanchez. Catalytic mesoporous janus nanomotors for active cargo delivery. *Journal of the American Chemical Society*, 137(15):4976–4979, 2015.

[52] Wei Gao, Allen Pei, Renfeng Dong, and Joseph Wang. Catalytic iridium-based janus micromotors powered by ultralow levels of chemical fuels. *Journal of the American Chemical Society*, 136(6):2276–2279, 2014.

[53] Wei Gao, Allen Pei, Xiaomiao Feng, Camille Hennessy, and Joseph Wang. Organized self-assembly of janus micromotors with hydrophobic hemispheres. *Journal of the American Chemical Society*, 135(3):998–1001, 2013.

[54] Jonathan R. Howse, Richard A. L. Jones, Anthony J. Ryan, Tim Gough, Reza Vafabakhsh, and Ramin Golestanian. Self-motile colloidal particles: From directed propulsion to random walk. *Physical Review Letters*, 99(4), 2007.

[55] Andrei Honciuc. *Amphiphilic Janus Particles at Interfaces*, pages 95–136. Springer International Publishing, Cham, 2019.

[56] Muhammad Safdar, Shahid Khan, and Janne Jänis. Progress toward catalytic micro- and nanomotors for biomedical and environmental applications. *Advanced Materials*, 30:1703660, 2018.

[57] Clemens Bechinger, Roberto Di Leonardo, Hartmut Löwen, Charles Reichhardt, Giorgio Volpe, and Giovanni Volpe. Active particles in complex and crowded environments. *Rev. Mod. Phys.*, 88:045006, 2016.

[58] Saverio E. Spagnolie and Eric Lauga. Hydrodynamics of self-propulsion near a boundary: predictions and accuracy of far-field approximations. *Journal of Fluid Mechanics*, 700:105–147, 2012.

[59] William Gilpin, Vivek N Prakash, and Manu Prakash. Vortex arrays and ciliary tangles underlie the feeding–swimming trade-off in starfish larvae. *Nature Physics*, 13(4):380–386, 2017.

[60] Eric Lauga and Thomas R Powers. The hydrodynamics of swimming microorganisms. *Reports on Progress in Physics*, 72(9):096601, 2009.

[61] Takuji Ishikawa. Suspension biomechanics of swimming microbes. *Journal of The Royal Society Interface*, 6(39):815–834, 2009.

[62] Knut Drescher, Jörn Dunkel, Luis H. Cisneros, Sujoy Ganguly, and Raymond E. Goldstein. Fluid dynamics and noise in bacterial cell–cell and cell–surface scattering. *Proceedings of the National Academy of Sciences*, 108(27):10940–10945, 2011.

[63] Andrew I Campbell, Stephen J Ebbens, Pierre Illien, and Ramin Golestanian. Experimental observation of flow fields around active janus spheres. *Nature communications*, 10(1):3952, 2019.

[64] Knut Drescher, Raymond E. Goldstein, Nicolas Michel, Marco Polin, and Idan Tuval. Direct measurement of the flow field around swimming microorganisms. *Phys. Rev. Lett.*, 105:168101, 2010.

[65] Priyanka Sharan, Zuyao Xiao, Viviana Mancuso, William E. Uspal, and Juliane Simmchen. Upstream rheotaxis of catalytic janus spheres. *ACS Nano*, 16:4599–4608, 2022.

[66] Priyanka Sharan, Abdallah Daddi-Moussa-Ider, Jaime Agudo-Canalejo, Ramin Golestanian, and Juliane Simmchen. Pair interaction between two catalytically active colloids. *Small*, 19(36):2300817, 2023.

[67] Ramin Golestanian, TB Liverpool, and A Ajdari. Designing phoretic micro-and nano-swimmers. *New Journal of Physics*, 9(5):126, 2007.

[68] Giovanni Volpe, Ivo Buttinoni, Dominik Vogt, Hans-Jürgen Kümmerer, and Clemens Bechinger. Microswimmers in patterned environments. *Soft Matter*, 7:8810–8815, 2011.

[69] Juliane Simmchen, Jaideep Katuri, William E. Uspal, Mihail N. Popescu, Mykola Tasinkevych, and Samuel Sánchez. Topographical pathways guide chemical microswimmers. *Nature Communications*, 7, 2016.

[70] Daisuke Takagi, Jérémie Palacci, Adam B. Braunschweig, Michael J. Shelley, and Jun Zhang. Hydrodynamic capture of microswimmers into sphere-bound orbits. *Soft Matter*, 10:1784–1789, 2014.

[71] Vaibhav Sharma, Elise Azar, Andre P. Schroder, Carlos M. Marques, and Antonio Stocco. Active colloids orbiting giant vesicles. *Soft Matter*, 17:4275–4281, 2021.

[72] Allison P. Berke, Linda Turner, Howard C. Berg, and Eric Lauga. Hydrodynamic attraction of swimming microorganisms by surfaces. *Physical Review Letters*, 101, 2008.

[73] Saverio E. Spagnolie, Gregorio R. Moreno-Flores, Denis Bartolo, and Eric Lauga. Geometric capture and escape of a microswimmer colliding with an obstacle. *Soft Matter*, 11:3396–3411, 2015.

[74] Sambeeta Das, Astha Garg, Andrew I. Campbell, Jonathan Howse, Ayusman Sen, Darrell Velegol, Ramin Golestanian, and Stephen J. Ebbens. Boundaries can steer active janus spheres. *Nature Communications*, 6, 2015.

[75] O. Sipos, K. Nagy, R. Di Leonardo, and P. Galajda. Hydrodynamic trapping of swimming bacteria by convex walls. *Phys. Rev. Lett.*, 114:258104, 2015.

[76] Aidan T Brown, Ioana D Vladescu, Angela Dawson, Teun Vissers, Jana Schwarz-Linek, Juho S Lintuvuori, and Wilson C K Poon. Swimming in a crystal †. *Soft Matter*, 12:131, 2016.

[77] Hendrik T. Spanke, Robert W. Style, Claire François-Martin, Maria Feofilova, Manuel Eisentraut, Holger Kress, Jaime Agudo-Canalejo, and Eric R. Dufresne. Wrapping of microparticles by floppy lipid vesicles. *Phys. Rev. Lett.*, 2020.

[78] Christian Dietrich, Miglena Angelova, and Bernard Pouligny. Adhesion of latex spheres to giant phospholipid vesicles: Statics and dynamics. *Journal de Physique II*, 7:1651–1682, 1997.

[79] Hendrik T. Spanke, Jaime Agudo-Canalejo, Daniel Tran, Robert W. Style, and Eric R. Dufresne. Dynamics of spontaneous wrapping of microparticles by floppy lipid membranes. *Phys. Rev. Res.*, 4:023080, 2022.

[80] Stijn van der Ham, Jaime Agudo-Canalejo, and Hanumantha Rao Vutukuri. Role of shape in particle-lipid membrane interactions: From surfing to full engulfment. *ACS Nano*, 18(15):10407–10416, 2024.

[81] Markus Deserno. Elastic deformation of a fluid membrane upon colloid binding. *Physical Review E - Statistical, Nonlinear, and Soft Matter Physics*, 69, 2004.

[82] Jaime Agudo-Canalejo and Reinhard Lipowsky. Critical particle sizes for the engulfment of nanoparticles by membranes and vesicles with bilayer asymmetry. *ACS Nano*, 9:3704–3720, 2015.

[83] Amir Houshang Bahrami, Reinhard Lipowsky, and Thomas R. Weikl. The role of membrane curvature for the wrapping of nanoparticles. *Soft Matter*, 12:581–587, 2016.

[84] Jaime Agudo-Canalejo and Reinhard Lipowsky. Uniform and janus-like nanoparticles in contact with vesicles: energy landscapes and curvature-induced forces. *Soft Matter*, 13:2155–2173, 2017.

[85] Eleanor J. Ewins, Koohee Han, Bhuvnesh Bharti, Tom Robinson, Orlin D. Velev, and Rumiana Dimova. Controlled adhesion, membrane pinning and vesicle transport by janus particles. *Chemical Communications*, 58:3055–3058, 2022.

[86] Vaibhav Sharma, Carlos M. Marques, and Antonio Stocco. Driven engulfment of janus particles by giant vesicles in and out of thermal equilibrium. *Nanomaterials*, 12, 2022.

[87] Jared T. Wiemann, Zhiqiang Shen, Huilin Ye, Ying Li, and Yan Yu. Membrane poration, wrinkling, and compression: deformations of lipid vesicles induced by amphiphilic janus nanoparticles. *Nanoscale*, 12:20326–20336, 2020.

[88] Lucas Le Nagard, Aidan T. Brown, Angela Dawson, Vincent A. Martinez, Wilson C. K. Poon, and Margarita Staykova. Encapsulated bacteria deform lipid vesicles into flagellated swimmers. *Proceedings of the National Academy of Sciences*, 119(34):e2206096119, 2022.

[89] Hanumantha Rao Vutukuri, Masoud Hoore, Clara Abaurrea-Velasco, Lennard van Buren, Alessandro Dutto, Thorsten Auth, Dmitry A Fedosov, Gerhard Gompper, and Jan Vermant. Active particles induce large shape deformations in giant lipid vesicles. *Nature*, 586(7827):52–56, 2020.

[90] Andreas Meinel, Benjamin Tränkle, Winfried Römer, and Alexander Rohrbach. Induced phagocytic particle uptake into a giant unilamellar vesicle. *Soft Matter*, 10:3667–3678, 2014.

[91] Pengyu Chen, Ziyang Xu, Guolong Zhu, Xiaobin Dai, and Li Tang Yan. Cellular uptake of active particles. *Phys. Rev. Lett.*, 124, 2020.

[92] Ke Xiao, Rui Ma, and Chen-Xu Wu. Force-induced wrapping phase transition in activated cellular uptake. *Physical Review E*, 106, 2022.

[93] A. Einstein. Über die von der molekularkinetischen theorie der wärme geforderte bewegung von in ruhenden flüssigkeiten suspendierten teilchen. *Annalen der Physik*, 322:549–560, 1905.

[94] Masao Doi. *Soft Matter Physics*. Oxford University Press, 2013.

[95] Peter J. W. (Peter Josef William) Debye. *Polar molecules*. The Chemical Catalog Company, inc., New York, 1929.

[96] Arthur Ashkin, James M Dziedzic, John E Bjorkholm, and Steven Chu. Observation of a single-beam gradient force optical trap for dielectric particles. *Optics letters*, 11(5):288–290, 1986.

[97] Arthur Ashkin. History of optical trapping and manipulation of small-neutral particle, atoms, and molecules. *IEEE Journal of Selected Topics in Quantum Electronics*, 6(6):841–856, 2000.

[98] Kirstine Berg-Sørensen and Henrik Flyvbjerg. Power spectrum analysis for optical tweezers. *Review of Scientific Instruments*, 75(3):594–612, 2004.

[99] Miglena I. Angelova and Dimiter S. Dimitrov. Liposome electroformation. *Faraday Discuss. Chem. Soc.*, 81:303–311, 1986.

[100] Dirk van Swaay and Andrew deMello. Microfluidic methods for forming liposomes. *Lab Chip*, 13:752–767, 2013.

[101] Jeanne C Stachowiak, David L Richmond, Thomas H Li, Allen P Liu, Sapun H Parekh, and Daniel A Fletcher. Unilamellar vesicle formation and encapsulation by microfluidic jetting. *Proceedings of the national academy of sciences*, 105(12):4697–4702, 2008.

[102] Andreas Weinberger, Feng Ching Tsai, Gijsje H. Koenderink, Thais F. Schmidt, Rosângela Itri, Wolfgang Meier, Tatiana Schmatko, André Schröder, and Carlos Marques. Gel-assisted formation of giant unilamellar vesicles. *Biophysical Journal*, 105:154–164, 2013.

[103] Hammad A. Faizi, Annie Tsui, Rumiana Dimova, and Petia M. Vlahovska. Bending rigidity, capacitance, and shear viscosity of giant vesicle membranes prepared by spontaneous swelling, electroformation, gel-assisted, and phase transfer methods: A comparative study. *Langmuir*, 38:10548–10557, 2022.

[104] Tripta Bhatia, Simon Christ, Jan Steinkühler, Rumiana Dimova, and Reinhard Lipowsky. Simple sugars shape giant vesicles into multispheres with many membrane necks. *Soft Matter*, 16:1246–1258, 2020.

[105] Yong Woon Kim and Wokyung Sung. Membrane curvature induced by polymer adsorption. *Phys. Rev. E*, 63:041910, 2001.

[106] Bing Li and Steven M. Abel. Shaping membrane vesicles by adsorption of a semiflexible polymer. *Soft Matter*, 14:185–193, 2018.

[107] Miao, Lingzhan, Song Guo, Zhilin Liu, Songqi Liu, Guoxiang You, Hao Qu, and Jun Hou. Effects of nanoplastics on freshwater biofilm microbial metabolic functions as determined by biolog eco microplates. *International Journal of Environmental Research and Public Health*, 16:4639, 2019.

[108] Hui Xu and Leah Casabianca. Probing driving forces for binding between nanoparticles and amino acids by saturation-transfer difference nmr. *Scientific Reports*, 10, 2020.

[109] Robert Vogel, Anoop K. Pal, Siddharth Jambhrunkar, Pragnesh Patel, Sachin S. Thakur, Eduardo Reátegui, Harendra S. Parekh, Paula Saá, Adonis Stassinopoulos, and Murray F. Broom. High-resolution single particle zeta potential characterisation of biological nanoparticles using tunable resistive pulse sensing. *Scientific Reports*, 7, 2017.

[110] Haiyang Su, Shunxiang Li, Guang Zhong Yang, and Kun Qian. Janus micro/-nanorobots in biomedical applications, 2023.

[111] Mauricio D. Carbajal-Tinoco, Ricardo Lopez-Fernandez, and José Luis Arauz-Lara. Asymmetry in colloidal diffusion near a rigid wall. *Phys. Rev. Lett.*, 99:138303, 2007.

[112] Maxime Lavaud, Thomas Salez, Yann Louyer, and Yacine Amarouchene. Stochastic inference of surface-induced effects using brownian motion. *Physical Review Research*, 3, 2021.

[113] Arindam Banerjee and Kenneth D. Kihm. Experimental verification of near-wall hindered diffusion for the brownian motion of nanoparticles using evanescent wave microscopy. *Physical Review E - Statistical, Nonlinear, and Soft Matter Physics*, 72, 2005.

[114] Greg Welch and Gary Bishop. An introduction to the kalman filter. *Proc. Siggraph Course*, 8, 2006.

[115] Bruce Lucas and Takeo Kanade. An iterative image registration technique with an application to stereo vision (ijcai). *Proceedings of the 7th International Joint Conference on Artificial Intelligence*, 81, 1981.

[116] Minghao Li, Oussama Sentissi, Stefano Azzini, Gabriel Schnoering, Antoine Canaguier-Durand, and Cyriaque Genet. Subfemtonewton force fields measured with ergodic brownian ensembles. *Phys. Rev. A*, 100:063816, 2019.

[117] Xavier Michalet and Andrew J. Berglund. Optimal diffusion coefficient estimation in single-particle tracking. *Phys. Rev. E*, 85:061916, 2012.

[118] Rémi Goerlich, Minghao Li, Samuel Albert, Giovanni Manfredi, Paul-Antoine Hervieux, and Cyriaque Genet. Noise and ergodic properties of brownian motion in an optical tweezer: Looking at regime crossovers in an ornstein-uhlenbeck process. *Phys. Rev. E*, 103:032132, 2021.

[119] Vaibhav Sharma, Florent Fessler, Fabrice Thalmann, Carlos M. Marques, and Antonio Stocco. Rotational and translational drags of a janus particle close to a wall and a lipid membrane. *Journal of Colloid and Interface Science*, 652:2159–2166, 2023.

[120] Markus Deserno. When do fluid membranes engulf sticky colloids? *Journal of Physics: Condensed Matter*, 16(22):S2061, 2004.

[121] Aurora Dols-Perez, Victor Marin, Guillermo J. Amador, Roland Kieffer, Daniel Tam, and Marie Eve Aubin-Tam. Artificial cell membranes interfaced with optical tweezers: A versatile microfluidics platform for nanomanipulation and mechanical characteriza-

tion. *ACS Applied Materials and Interfaces*, 11:33620–33627, 2019.

[122] Yareni A. Ayala, Ramin Omidvar, Winfried Römer, and Alexander Rohrbach. Thermal fluctuations of the lipid membrane determine particle uptake into giant unilamellar vesicles. *Nature Communications*, 14, 2023.

[123] Gerbrand Koster, Angelo Cacciuto, Imre Derényi, Daan Frenkel, and Marileen Dogterom. Force barriers for membrane tube formation. *Physical Review Letters*, 94, 2005.

[124] Imre Derényi, Frank Jülicher, and Jacques Prost. Formation and interaction of membrane tubes. *Physical Review Letters*, 88:4, 2002.

[125] Vasiliy Kantsler, Enrico Segre, and Victor Steinberg. Critical dynamics of vesicle stretching transition in elongational flow. *Physical Review Letters*, 101, 2008.

[126] Dinesh Kumar, Channing M. Richter, and Charles M. Schroeder. Conformational dynamics and phase behavior of lipid vesicles in a precisely controlled extensional flow. *Soft Matter*, 16:337–347, 2020.

[127] Dinesh Kumar and Charles M. Schroeder. Nonlinear transient and steady state stretching of deflated vesicles in flow. *Langmuir*, 37:13976–13984, 2021.

[128] Vadim A. Frolov, Vladimir A. Lizunov, Antonina Ya Dunina-Barkovskaya, Andrey V. Samsonov, and Joshua Zimmerberg. Shape bistability of a membrane neck: A toggle switch to control vesicle content release. *Proceedings of the National Academy of Sciences of the United States of America*, 100:8698–8703, 2003.

[129] Raktim Dasgupta and Rumiana Dimova. Inward and outward membrane tubes pulled from giant vesicles. *Journal of Physics D: Applied Physics*, 47, 2014.

[130] Raktim Dasgupta, Markus S. Miettinen, Nico Fricke, Reinhard Lipowsky, and Rumiana Dimova. The glycolipid gm1 reshapes asymmetric biomembranes and giant vesicles by curvature generation. *Proceedings of the National Academy of Sciences*, 115(22):5756–5761, 2018.

[131] Thomas R Powers, Greg Huber, and Raymond E Goldstein. Fluid-membrane tethers: minimal surfaces and elastic boundary layers. *Physical review E*, 65(4):041901, 2002.

[132] B. Ashok and G. Ananthakrishna. Dynamics of intermittent force fluctuations in vesicular nanotubulation. *Journal of Chemical Physics*, 141, 2014.

[133] T. Roopa and G. V. Shivashankara. Nanomechanics of membrane tubulation and dna assembly. *Applied Physics Letters*, 82:1631–1633, 2003.

[134] Ilya Koltover, Joachim O. Rädler, and Cyrus R. Safinya. Membrane mediated attraction and ordered aggregation of colloidal particles bound to giant phospholipid vesicles. *Physical Review Letters*, 82(9):1991–1994, 1999.

[135] Dinesh Kumar, Channing M. Richter, and Charles M. Schroeder. Double-mode relaxation of highly deformed anisotropic vesicles. *Physical Review E*, 102, 2020.

[136] Ramin Omidvar, Yareni A. Ayala, Annette Brandel, Lukas Hasenclever, Martin Helmstädter, Alexander Rohrbach, Winfried Römer, and Josef Madl. Quantification of nanoscale forces in lectin-mediated bacterial attachment and uptake into giant liposomes. *Nanoscale*, 13:4016–4028, 2021.

[137] Marcelina Cardoso Dos Santos, Cyrille Vézy, and Rodolphe Jaffiol. Nanoscale characterization of vesicle adhesion by normalized total internal reflection fluorescence microscopy. *Biochimica et Biophysica Acta - Biomembranes*, 1858(6):1244–1253, 2016.

[138] Amir H. Bahrami, Michael Raatz, Jaime Agudo-Canalejo, Raphael Michel, Emily M. Curtis, Carol K. Hall, Michael Gradzielski, Reinhard Lipowsky, and Thomas R. Weikl. Wrapping of nanoparticles by membranes. *Advances in Colloid and Interface Science*, 208:214–224, 2014.

[139] Gaetano Napoli and Alain Goriely. Elastocytosis. *Journal of the Mechanics and Physics of Solids*, 145:104133, 2020.

[140] Jaime Agudo-Canalejo and Reinhard Lipowsky. Stabilization of membrane necks by adhesive particles, substrate surfaces, and constriction forces. *Soft Matter*, 12:8155–8166, 2016.

[141] YG Smirnova and M Müller. How does curvature affect the free-energy barrier of stalk formation? small vesicles vs apposing, planar membranes. *European Biophysics Journal*, 50:253–264, 2021.

[142] B. del Rosal, P. Haro-González, W. T. Ramsay, L. M. Maestro, K. Santacruz-Gómez, M. C. Iglesias de la Cruz, F. Sanz-Rodríguez, J. Y. Chooi, P. Rodríguez-Sevilla, D. Choudhury, A. K. Kar, J. García Solé, L. Paterson, and D. Jaque. Heat in optical tweezers. *Optical Trapping and Optical Micromanipulation X*, 8810:88102A, 2013.

[143] Jonathan R. Howse, Richard A. L. Jones, Anthony J. Ryan, Tim Gough, Reza Vafabakhsh, and Ramin Golestanian. Self-motile colloidal particles: From directed propulsion to random walk. *Phys. Rev. Lett.*, 99:048102, 2007.

[144] Wei Gao, Allen Pei, Renfeng Dong, and Joseph Wang. Catalytic iridium-based janus micromotors powered by ultralow levels of chemical fuels. *Journal of the American*

Chemical Society, 136(6):2276–2279, 2014.

[145] Linda Feuerstein, Carl Georg Biermann, Zuyao Xiao, Christian Holm, and Juliane Simmchen. Highly efficient active colloids driven by galvanic exchange reactions. *Journal of the American Chemical Society*, 143(41):17015–17022, 2021.

[146] Martin Wittmann, Maximilian Voigtmann, and Juliane Simmchen. Active bivo4 swimmers propelled by depletion gradients caused by photodeposition. *Small*, 19(15):2206885, 2023.

[147] Yefei Wu, Renfeng Dong, Qilu Zhang, and Biye Ren. Dye-enhanced self-electrophoretic propulsion of light-driven tio2–au janus micromotors. *Nano-Micro Letters*, 9(3):30, 2017.

[148] Qilu Zhang, Renfeng Dong, Yefei Wu, Wei Gao, Zihan He, and Biye Ren. Light-driven au-wo3@c janus micromotors for rapid photodegradation of dye pollutants. *ACS Applied Materials & Interfaces*, 9(5):4674–4683, 2017.

[149] Martin Wittmann, Sandra Heckel, Felix Wurl, Zuyao Xiao, Thomas Gemming, Thomas Strassner, and Juliane Simmchen. Microswimming by oxidation of dibenzylamine. *Chem. Commun.*, 58:4052–4055, 2022.

[150] Qinglong Wang, Renfeng Dong, Chun Wang, Shuyu Xu, Decheng Chen, Yuying Liang, Biye Ren, Wei Gao, and Yuepeng Cai. Glucose-fueled micromotors with highly efficient visible-light photocatalytic propulsion. *ACS Applied Materials & Interfaces*, 11(6):6201–6207, 2019.

[151] Lucas Le Nagard, Aidan T Brown, Angela Dawson, Vincent A Martinez, Wilson CK Poon, and Margarita Staykova. Encapsulated bacteria deform lipid vesicles into flagellated swimmers. *Proceedings of the National Academy of Sciences*, 119(34):e2206096119, 2022.

[152] Sophie Y Lee, Philipp WA Schönhöfer, and Sharon C Glotzer. Complex motion of steerable vesicular robots filled with active colloidal rods. *Scientific Reports*, 13(1):22773, 2023.

[153] Priyanka Iyer, Gerhard Gompper, and Dmitry A Fedosov. Non-equilibrium shapes and dynamics of active vesicles. *Soft matter*, 18(36):6868–6881, 2022.

[154] Stanislaw Makarchuk, Vasco C Braz, Nuno AM Araújo, Lena Ciric, and Giorgio Volpe. Enhanced propagation of motile bacteria on surfaces due to forward scattering. *Nature Communications*, 10(1):4110, 2019.

[155] Carolina van Baalen, William E Uspal, Mihail N Popescu, and Lucio Isa. Transition

from scattering to orbiting upon increasing the fuel concentration for an active janus colloid moving at an obstacle–decorated interface. *Soft Matter*, 19(45):8790–8801, 2023.

[156] Eric Lauga. *The Fluid Dynamics of Cell Motility.* Cambridge Texts in Applied Mathematics. Cambridge University Press, 2020.

[157] Stefania Ketzetzi, Joost De Graaf, and Daniela J. Kraft. Diffusion-based height analysis reveals robust microswimmer-wall separation. *Physical Review Letters*, 125, 2020.

[158] Edward R. Block. Hydrogen peroxide alters the physical state and function of the plasma membrane of pulmonary artery endothelial cells. *Journal of Cellular Physiology*, 146(3):362–369, 1991.

[159] Guro Valen, Anders Sondén, Jarle Vaage, Elisabeth Malm, and B.Thomas Kjellström. Hydrogen peroxide induces endothelial cell atypia and cytoskeleton depolymerization. *Free Radical Biology and Medicine*, 26(11):1480–1488, 1999.

[160] Jianwu Dai, H Ping Ting-Beall, and Michael P Sheetz. The secretion-coupled endocytosis correlates with membrane tension changes in rbl 2h3 cells. *J. Gen. Physiol*, 110, 1997.

[161] Bruno Pontes, Pascale Monzo, and Nils C. Gauthier. Membrane tension: A challenging but universal physical parameter in cell biology. *Seminars in Cell and Developmental Biology*, 71:30–41, 2017.

[162] Florent Fessler, Vaibhav Sharma, Pierre Muller, and Antonio Stocco. Entry of microparticles into giant lipid vesicles by optical tweezers. *Phys. Rev. E*, 107:L052601, 2023.

[163] Joachim O Radier, Toni J Feder, Helmut H Strey, and Erich Sackmann. Fluctuation analysis of tension-controlled undulation forces between giant vesicles and solid substrates. *Phys. Rev. E*, 51, 1995.

[164] I. Cantat, K. Kassner, and C. Misbah. Vesicles in haptotaxis with hydrodynamical dissipation. *European Physical Journal E*, 10:175–189, 2003.

[165] A. L. Bernard, M. A. Guedeau-Boudeville, L. Jullien, and J. M. Di Meglio. Strong adhesion of giant vesicles on surfaces: dynamics and permeability. *Langmuir*, 16:6809–6820, 2000.

[166] Hendrik T. Spanke, Jaime Agudo-Canalejo, Daniel Tran, Robert W. Style, and Eric R. Dufresne. Dynamics of spontaneous wrapping of microparticles by floppy lipid membranes. *Phys. Rev. Res.*, 4:023080, 2022.

[167] Reinhard Lipowsky and Udo Seifertt. Adhesion of membranes: A theoretical perspective. *Langmuir*, page 7, 1991.

[168] Thomas Gruhn, Thomas Franke, Rumiana Dimova, and Reinhard Lipowsky. Novel method for measuring the adhesion energy of vesicles. *Langmuir*, 23:5423–5429, 2007.

[169] Jan Steinkühler, Jaime Agudo-Canalejo, Reinhard Lipowsky, and Rumiana Dimova. Modulating vesicle adhesion by electric fields. *Biophysical Journal*, 111(7):1454–1464, 2016.

[170] Travers H. Anderson, Younjin Min, Kim L. Weirich, Hongbo Zeng, Deborah Fygenson, and Jacob N. Israelachvili. Formation of supported bilayers on silica substrates. *Langmuir*, 25(12):6997–7005, 2009.

[171] Benjamin Klasczyk, Volker Knecht, Reinhard Lipowsky, and Rumiana Dimova. Interactions of alkali metal chlorides with phosphatidylcholine vesicles. *Langmuir*, 26(24):18951–18958, 2010.

[172] Xiankai Jiang, Jinjin Zhang, Bo Zhou, Pei Li, Xiaojuan Hu, Zhi Zhu, Yanwen Tan, Chao Chang, Junhong Lü, and Bo Song. Anomalous behavior of membrane fluidity caused by copper-copper bond coupled phospholipids. *Scientific Reports*, 8, 2018.

[173] Matthew F. Poyton, Anne M. Sendecki, Xiao Cong, and Paul S. Cremer. Cu2+ binds to phosphatidylethanolamine and increases oxidation in lipid membranes. *Journal of the American Chemical Society*, 138:1584–1590, 2016.

[174] Ke Xiao, Rui Ma, and Chen-Xu Wu. Force-induced wrapping phase transition in activated cellular uptake. *Phys. Rev. E*, 106:044411, 2022.

[175] Hans Günther Döbereiner, Olaf Selchow, and Reinhard Lipowsky. Spontaneous curvature of fluid vesicles induced by trans-bilayer sugar asymmetry. *European Biophysics Journal*, 28:174–178, 1999.

[176] M. Deserno and T. Bickel. Wrapping of a spherical colloid by a fluid membrane. *Europhysics Letters*, 62(5):767, 2003.

[177] Qingfen Yu, Sameh Othman, Sabyasachi Dasgupta, Thorsten Auth, and Gerhard Gompper. Nanoparticle wrapping at small non-spherical vesicles: curvatures at play. *Nanoscale*, 10:6445–6458, 2018.

[178] Peter Hänggi, Peter Talkner, and Michal Borkovec. Reaction-rate theory: fifty years after kramers. *Rev. Mod. Phys.*, 62:251–341, 1990.

[179] Travers H. Anderson, Younjin Min, Kim L. Weirich, Hongbo Zeng, Deborah Fygen-

son, and Jacob N. Israelachvili. Formation of supported bilayers on silica substrates. *Langmuir*, 25(12):6997–7005, 2009.

[180] H Faxen. Die bewegung einer starren kugel langs der achse eines mit zaner flusigkeit gefullten rohres. *Arkiv. Mat. Astron. Fys*, 17:1–28, 1923.

[181] Howard Brenner. The slow motion of a sphere through a viscous fluid towards a plane surface. *Chemical Engineering Science*, 16(3):242–251, 1961.

[182] Evan Evans and Erich Sackmann. Translational and rotational drag coefficients for a disk moving in a liquid membrane associated with a rigid substrate. *Journal of Fluid Mechanics*, 194:553–561, 1988.

[183] S. A. Rogers, M. Lisicki, B. Cichocki, J. K.G. Dhont, and P. R. Lang. Rotational diffusion of spherical colloids close to a wall. *Physical Review Letters*, 109, 2012.

[184] Manfred Wimmer. Experiments on a viscous fluid flow between concentric rotating spheres. *Journal of Fluid Mechanics*, 78(2):317–335, 1976.

[185] Howard A Stone and Armand Ajdari. Hydrodynamics of particles embedded in a flat surfactant layer overlying a subphase of finite depth. *J. Fluid Mech*, 369:151–173, 1998.

[186] Yegor A. Domanov, Sophie Aimon, Gilman E. S. Toombes, Marianne Renner, François Quemeneur, Antoine Triller, Matthew S. Turner, and Patricia Bassereau. Mobility in geometrically confined membranes. *Proceedings of the National Academy of Sciences*, 108(31):12605–12610, 2011.

[187] Y Gambin, R Lopez-Esparza, M Reffay, E Sierecki, N S Gov, M Genest, R S Hodges, and W Urbach. Lateral mobility of proteins in liquid membranes revisited. *Proceedings of the National Academy of Sciences*, 103, 2006.

[188] François Quemeneur, Jon K. Sigurdsson, Marianne Renner, Paul J. Atzberger, Patricia Bassereau, and David Lacoste. Shape matters in protein mobility within membranes. *Proceedings of the National Academy of Sciences of the United States of America*, 111:5083–5087, 2014.

[189] Rossana Rojas Molina, Susanne Liese, and Andreas Carlson. Diffusion on membrane domes, tubes, and pearling structures. *Biophysical Journal*, 120(3):424–431, 2021.

[190] Felix Jünger, Felix Kohler, Andreas Meinel, Tim Meyer, Roland Nitschke, Birgit Erhard, and Alexander Rohrbach. Measuring local viscosities near plasma membranes of living cells with photonic force microscopy. *Biophysical Journal*, 109:869–882, 2015.

[191] J Elgeti, R G Winkler, and G Gompper. Physics of microswimmers—single particle

motion and collective behavior: a review. *Reports on Progress in Physics*, 78(5):056601, 2015.

[192] Ivo Buttinoni, Giovanni Volpe, Felix Kuemmel, Giorgio Volpe, and Clemens Bechinger. Active brownian motion tunable by light. *Journal of Physics: Condensed Matter*, 24(28), 2012.

[193] Stefania Ketzetzi, Joost de Graaf, Rachel P. Doherty, and Daniela J. Kraft. Slip length dependent propulsion speed of catalytic colloidal swimmers near walls. *Phys. Rev. Lett.*, 124:048002, 2020.

[194] Xu Zheng, Borge ten Hagen, Andreas Kaiser, Meiling Wu, Haihang Cui, Zhanhua Silber-Li, and Hartmut Loewen. Non-gaussian statistics for the motion of self-propelled janus particles: Experiment versus theory. *Physical Rev. E*, 88(3), 2013.

[195] Nick Oikonomeas-Koppasis, Stefania Ketzetzi, Daniela J. Kraft, and Peter Schall. Power-law intermittency in the gradient-induced self-propulsion of colloidal swimmers. *Soft Matter*, pages –, 2024.

[196] Melissa Rinaldin, Ruben W. Verweij, Indrani Chakraborty, and Daniela J. Kraft. Colloid supported lipid bilayers for self-assembly. *Soft Matter*, 15:1345–1360, 2019.

[197] Vincent T. Moy, Yuekan Jiao, Thomas Hillmann, Horst Lehmann, and Takeshi Sano. Adhesion energy of receptor-mediated interaction measured by elastic deformation. *Biophysical Journal*, 76(3):1632–1638, 1999.

[198] Georges Weber, Thierry Charitat, Maurício S. Baptista, Adjaci F. Uchoa, Christiane Pavani, Helena C. Junqueira, Yachong Guo, Vladimir A. Baulin, Rosangela Itri, Carlos M. Marques, and André P. Schroder. Lipid oxidation induces structural changes in biomimetic membranes. *Soft Matter*, 10:4241–4247, 2014.

[199] N. Fa, C. M. Marques, E. Mendes, and A. P. Schröder. Rheology of giant vesicles: A micropipette study. *Phys. Rev. Lett.*, 92:108103, 2004.

[200] M. E. O'Neill. A slow motion of viscous liquid caused by a slowly moving solid sphere. *Mathematika*, 11(1):67–74, 1964.

[201] John Happel and Howard Brenner. *Low Reynolds number hydrodynamics: with special applications to particulate media*, volume 1. Springer Science & Business Media, 2012.

[202] A J Goldmans, R G Cox, and H Brenner. Slow viscous motion of a sphere parallel to a plane wall-1 motion through a quiescent fluid. *Chemical Engineering Science*, 22:637651, 1967.

[203] Scott G. Flicker and Stacy G. Bike. Measuring double layer repulsion using total internal reflection microscopy. *Langmuir*, 9(1):257–262, 1993.

[204] Aidin Rashidi and Christopher L. Wirth. Motion of a Janus particle very near a wall. *The Journal of Chemical Physics*, 147(22):224906, 2017.

Florent Fessler

Driven microparticles interacting with lipid vesicles: from wrapping by optical tweezers to autonomous active particle engulfment

Résumé

Les interactions entre des corps de taille micro- ou nanométrique et les membranes lipidiques, agissant comme des barrières à l'échelle cellulaire, régissent de nombreux mécanismes se produisant lors de phénomènes allant de l'infection virale et la propagation intercellulaire à la délivrance de médicaments et l'exposition des cellules aux microplastiques. La déformation de ces membranes molles et fluctuantes par une particule, soit sous l'effet d'une force externe, soit par la force de propulsion de la particule, peut entraîner des transitions de forme de la membrane dans des processus biologiques élémentaires tels que l'endocytose, même en l'absence de machinerie biologique. Dans cette thèse, les principes physiques régissant les transitions de forme menant à l'endocytose dans un système modèle, sans interactions spécifiques, sont étudiés en provoquant l'engloutissement avec des pinces optiques ou en utilisant des particules Janus actives.

Mots clés : Pinces optiques, colloïdes Janus actifs, autopropulsion, vésicules lipidiques, engloutissement, endocytose

Résumé (english)

Interactions between micro- or nanometric-sized entities and lipid membranes, acting as barriers at the cellular scale, govern many mechanisms occurring during phenomena ranging from viral infection and intercellular spread to drug delivery and cell exposure to microplastics. The deformation of these soft fluctuating membranes by a particle, either driven by an external force or by the particle's propulsion force, can lead to membrane shape transitions taking place in elementary biological processes such as endocytosis, even in the absence of biological machinery. In this thesis, the physical principles governing the shape transitions leading to endocytosis in a model system without specific interactions are investigated by driving the engulfment with optical tweezers or using active Janus particles.

Keywords: Optical tweezers, active Janus colloids, self-propulsion, lipid vesicles, engulfment, endocytosis